MEASURING THE SUNYAEV-ZEL'DOVICH EFFECTS WITH CURRENT AND FUTURE OBSERVATORIES

A Dissertation

Presented to the Faculty of the Graduate School

of Cornell University

in Partial Fulfillment of the Requirements for the Degree of

Doctor of Philosophy

by

Eve Marie Vavagiakis

August 2021

MEASURING THE SUNYAEV-ZEL'DOVICH EFFECTS WITH CURRENT AND FUTURE OBSERVATORIES

Eve Marie Vavagiakis, Ph.D.

Cornell University 2021

Increasingly precise measurements of the cosmic microwave background (CMB) continue to shape our understanding of our universe's origin, evolution, and contents. Measurements with ground-based observatories like the Atacama Cosmology Telescope (ACT) and satellite missions such as *Planck* have been able to precisely constrain the 6-parameter cosmological constant (Λ) Cold Dark Matter (CDM) model of cosmology and probe the growth of structure over cosmic time. Future observatories like CCAT-prime and the Simons Observatory will produce higher signal-to-noise data sets covering large areas on the sky, which will enable unprecedented measurements of the CMB and the Sunyaev-Zel'dovich effects. This data will inform our theoretical models of galaxy evolution and feedback mechanisms, provide insight into dark energy, and constrain the sum of the neutrino masses.

Pursuit of these science goals necessitates the deployment of large numbers of sensitive superconducting detectors in novel cryogenic receivers. In this thesis we present the design of a first light instrument for the Fred Young Submillimeter Telescope (FYST), Mod-Cam, which will be used to deploy the first light microwave kinetic inductance detector array for the CCAT-prime project. Mod-Cam will also serve as a single-module cryogenic testbed for Prime-Cam, the first-generation science instrument for the FYST. We discuss the cryogenic design, initial instrument modules, and science goals for the Prime-Cam receiver.

Developing the superconducting detector and readout technologies for these upcoming experiments requires laboratory testing to tune the fabrication process to the required parameters. We present measurements of transition edge sensors (TESes) and superconducting films that informed the fabrication process for the Simons Observatory (SO), which will field ~70,000 TES bolometers in six spectral bands centered between 27 and 280 GHz, and CMB-S4, the future ground-based CMB project that will push measurements of the CMB to cosmic variance limits. We also measure the magnetic sensitivity of TESes and the superconducting quantum interference devices (SQUIDs) required to amplify and read out the TES signals, and discuss how these measurements inform the magnetic shielding requirements for successful deployment of the components for future observatories such as SO.

Maps of the CMB from observations with ACT, which relies on AlMn TESes like the ones measured in this thesis, have been combined with data from *Planck* to yield maps with superior depth and resolution to either data product alone. By using these maps in conjunction with optical data from the Sloan Digital Sky Survey, we present increasingly precise measurements of the thermal and kinematic Sunyaev-Zel'dovich (SZ) effects. We compare independent estimates of halo optical depth from these effects to explore the potential for thermal SZ measurements to serve as input for the measurement of kinematic SZ pairwise velocity curves which can constrain cosmology. By probing the optical depth of these galaxy halos, we also probe their baryon content, and make progress towards defining an empirical relationship between optical depth and Compton-y. This relationship will inform simulations of galaxy evolution and enable future precise cosmological constraints.

BIOGRAPHICAL SKETCH

Eve Vavagiakis was born in Manhattan and grew up in Rockland County, New York, where she graduated from Suffern High School in 2010. She was awarded the Tony Alt Memorial Foundation Scholarship to attend Cornell University, where she majored in Physics with an Astronomy concentration. She completed her Bachelor of Arts degree in 2014. Eve received the Cranson W. and Edna B. Shelley Award in 2013 for her work in designing a cryogenic scanning Fabry-Perot interferometer for mid-IR to sub-millimeter astronomical observations. Her research in Gordon Stacey's group in the Astronomy Department cemented her interest in instrumentation and astronomy.

In 2014, Eve was awarded a National Science Foundation Graduate Research Fellowship, under which she engaged with the diverse array of research projects available in Michael Niemack's group at Cornell. As a part of the Atacama Cosmology Telescope (ACT), CCAT-prime, CMB-S4, and Simons Observatory (SO) Collaborations, Eve's research has included cryogenics design and operation, superconducting materials and device testing, and analysis of maps of the cosmic microwave background. As a remote observer, Eve took shifts remotely operating ACT, and screened superconducting devices later deployed in the ACTPol receiver. She also analyzed ACT maps to measure the Sunyaev-Zel'dovich effects. Eve's cryogenic measurements of materials and devices for SO and CMB-S4 helped inform the fabrication process for these projects' detectors. Her work in developing and operating several cryogenic systems prepared her to design the cryogenics for the the instrument module testbed and first-light receiver for the CCAT-prime project, Mod-Cam.

Throughout her time at Cornell, Eve has worked to make science accessible to all through her education and public engagement activities. She has given

lectures, science workshops and demos to the community, organized and participated in events for local high schools, given tours of the campus particle accelerator, and helped manage the social media for ACT and SO. Eve has participated in groups of physicists focused on education, public engagement, and equity, diversity and inclusion initiatives. In the lab, she enjoyed mentoring undergraduate students. Interested in communicating science to a broad audience, Eve blogged for and then co-directed the high energy physics reader's digest blog, ParticleBites, which summarizes particle physics experiments at an undergraduate level. Her first in a series of illustrated science children's books, *I'm a Neutrino*, will be published by Candlewick and MIT Press under their new collaborative imprint, MIT Kids Press, in 2022, followed by *I'm a Black Hole* in 2023.

Outside of research and science communication, Eve enjoys exploring the Finger Lakes Region on foot, by boat, or on two wheels. She loves lifting weights, reading, cooking and baking, and delights in her seasonal local Community Supported Agriculture vegetable boxes. She hopes we can be good stewards of this planet, so we can keep looking skyward and pursuing the answers to our biggest questions for a long time to come.

To my mother, Ilze Lemesis, for everything.

ACKNOWLEDGEMENTS

I would first like to thank my advisor, Michael Niemack, for enabling this research. Thank you Mike, for the years of mentorship, leadership, and guidance. Thank you also to Maren, Linnea and Juliana, for helping to make this lab feel like a family. Thank you to Rachel Bean and Nick Battaglia for the collaborative work on our SZ projects. Terry Herter, Gordon Stacey, Thomas Nikola, Steve Parshley, and George Gull, thank you for the years of collaboration and mentorship, and for enabling the CCAT-prime work presented in this thesis. Thank you to Peter Wittich and Liam McAllister for serving on my committee and giving me valuable advice over the years. To everyone at the Cornell Physics and Astronomy departments who I have worked with, conversed with, and attended seminars with, you have all made Cornell an excellent place to pursue a PhD. Kacey Acquilano, Debra Hatfield, and Craig Wiggers, thank you for everything you've done for the physics department.

I had the gift of participating in a supportive, vibrant, and close-knit research group here. Shawn Henderson (and Rina, Liana, Miles, Macademia), thank you for all of your mentorship, V-ϕ curves drawn on white boards, practice exams, advice, friendship, and support. Thank you Francesco de Bernardis (and Nikhita) for your friendship and for first teaching me the basics of SZ analysis. To my office and lab mates, Brian, Pato (and Ale), Jason (and Nicole), Nick (and Jenn and Pharaoh), Cody (and Hope, Arlo and Yama), Zach, Paul, Noah, Pra, Sarah Marie, Willow, Kshama, Jesse, Kaiwen, Steve, Yaqiong, and all the summer and undergraduate students, I have learned so much from all of you.

To everyone I've worked with in the Atacama Cosmology Telescope, CCAT-prime, CMB-S4, and Simons Observatory Collaborations, thank you for enabling this research, for welcoming and supporting me as a young researcher,

and for improving my papers and presentations. Each one of our collaboration meetings left me feeling refreshed and grateful to work in such a large community of talented and passionate people. Thank you to my collaborators at Princeton, UC Berkeley, Argonne National Laboratory, Fermilab, and NIST for supplying much of the hardware tested in this thesis. To my ACT collaborators, thank you for all of the work that made analyzing our maps possible, from scanning to stacking.

Friends, near and far, PhDs would not be nearly as fun without you. Mari, Josue, Meagan, Sabrina, Smaranda, Sammy, Naomi, Gaël, Mike, Michelle, Berit, Sara, Nick G., Amit, Christopher, thank you. Bonus thanks to anyone showing up at the Big Red Barn after another long week of work. Thank you also to my college friends, Kevin, Josh, Ben, Robbie, Dylan, Izzy, Christine, Iain, Christian, Abby, Mike, Cody L., Veronica. Special thanks to Kevin Tharratt, Josh Burt, Nick Cothard, Shawn Beckman, Flip Tanedo, Thomas Bachlechner, Alise Muok, John Groh, Frankie Zhu, and Adrienne Chang for all the years of support, friendship, and adventures.

This thesis feels like the culmination of an education that started many years ago. Thank you to my high school physics teachers, Bill Ballerine and Jim Marina, who encouraged me to first pursue the subject. Your encouragement to aim high, try early, and risk failure among supportive instructors and peers is advice I routinely give students today. Thank you to Angela Greer, Kathy Farrow, Elizabeth Coletta, and Sarah Kern, for your example and tutelage. Thank you also to Annmarie McAnany and everyone at the Sloatsburg Public Library for making it a wonderful place to learn and work. To my high school classmates, our experiences completing problem sets and homeworks together introduced me to the camaraderie I would need to get me through all the rest of my career

as a student. Em, thank you for traveling all of those miles in 2014.

Finally, thank you to my mother and family for your unwavering support. This work would not have been possible without you.

TABLE OF CONTENTS

LIST OF TABLES

LIST OF FIGURES

CHAPTER 1

INTRODUCTION

The perception of electromagnetic (EM) radiation is a cornerstone of our ability to interact with and understand our physical world. As modern science has progressed, we extended our reach into the EM spectrum beyond visual sight and infrared sensation, using light with wavelengths spanning over 20 orders of magnitude to traverse length scales in our universe from the sub-atomic to the cosmic. As light travels over these vast distances, it also allows us to look back in time, by carrying signals imprinted both at its origin and also along its journey through space-time. Through the development of telescopes and cameras, detectors and readout systems, and the interpretation of the data these collect, we can look back towards the beginnings of our universe, and probe the highest energy and largest distance scales accessible to us. These measurements shape our understanding of our nature and our origins.

1.1 The Cosmic Microwave Background

The discovery of a background of microwave light of wavelength 7.4 cm (4.1 GHz) from all parts of the sky opened this window for the first time in 1964. Bell Labs scientists Arno Penzias and Robert A. Wilson were working with cryogenic receivers and the Holmdel Horn Antenna, used to detect radio waves from passive and active communications satellite experiments. In seeking to eliminate interfering signals, Penzias and Wilson discovered the cosmic microwave background (CMB), in the form of an excess antenna temperature of ~3.5 K for which they could not account, and thus attributed correctly to an extragalactic origin [189]. Concurrently, physicists Dicke, Peebles, Wilkinson and Roll at Princeton

University had theorized the existence of relic radiation from the Big Bang theory of cosmology. Thus, the era of experimental cosmology had begun, with experiments making increasingly precise measurements of the CMB over the next half century.

The CMB has the spectrum of a blackbody: that of an opaque, isothermal, and non-reflecting object, with a brightness temperature of 2.725 ± 0.001 K and a peak frequency of 160.4 GHz [165]. The nature of this blackbody spectrum supports the conjectures arising from the Big Bang theory. If the early universe were a hot, dense plasma, opaque due to the ionized nature of the gas, it would be expected to emit blackbody radiation. As the universe expanded, cooling and decreasing in density, there would come a point at which the universe would become transparent to photons, allowing them to stream freely in all directions after protons and electrons combined to form neutral hydrogen. Measurements of the CMB relic radiation support this "recombination" occurring about ~380,000 years after the Big Bang, when the last-scattered photons were able to travel freely and reach us here on Earth today, largely undisturbed. As we look back in time as we look into the sky, with objects further away communicating older light, the CMB represents the most ancient EM radiation we can detect.

1.1.1 Primary Anisotropies

Probing the early universe's history, observations of the CMB can help address some of the most compelling questions in modern physics. The CMB radiation comes from all directions, and is surprisingly uniform in temperature: isotropic

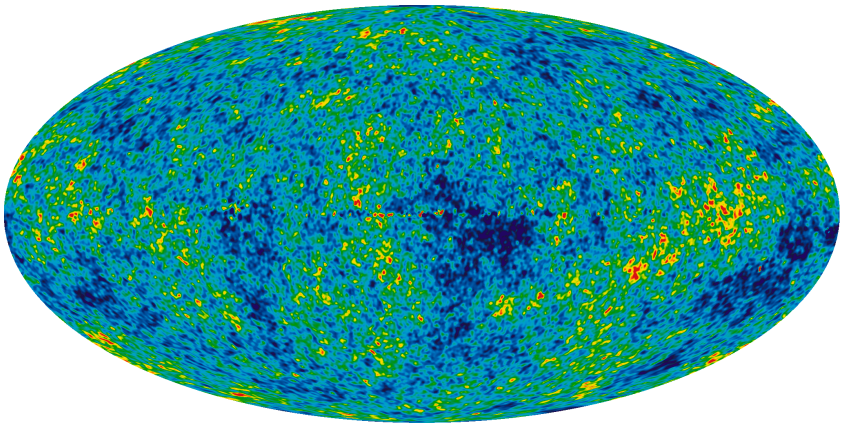

Figure 1.1: The anisotropies of the Cosmic Microwave Background (CMB) as observed by the Wilkinson Microwave Anisotropy Probe (*WMAP*) over seven years, visible at the plotted temperature range of $\pm 200\,\mu$K. The CMB is isotropic at 2.73 K to roughly one part in 10^5. The correlation of the overall temperature and temperature anisotropies of the CMB at large scales presents a problem when combined with knowledge of the comparatively small ($\sim 1^\circ$) causally connected regions of sky, addressed by the inflationary paradigm in the standard model of cosmology. Figure is from the NASA/*WMAP* Science Team [133].

to roughly 1 part in 10^5 (Figure 1.1) [129]. The fact that the temperature is so homogeneous, and that the anisotropies we do observe appear to be correlated on large scales, are curious when one considers the causal structure of our universe.

Our universe is well described by the Friedmann-Lemaître-Robertson-Walker metric,

$$\mathrm{d}s^2 = -\mathrm{d}t^2 + a^2(t)\mathrm{d}\mathbf{x}^2, \tag{1.1}$$

in natural units where $c = 1$. The dimensionless scale factor $a(t)$ characterizes the expansion of our universe over time. The metric provides a solution to Einstein's field equations consistent with the large-scale matter distribution in the universe, and describes a universe that is flat (a beam of light emitted will not

eventually make its way back to its source), homogenous (has constant density) and isotropic (the same in all directions) [188, 29]. The comoving distance measure,

$$D_C = \frac{1}{H_0} \int_0^z \frac{dz'}{\sqrt{\Omega_M(1+z)^3 + \Omega_k(1+z)^2 + \Omega_\Lambda}}, \tag{1.2}$$

factors out the expansion of the universe to leave a distance that does not change in time due to the expansion of space. At a time t in the universe's history after the initial singularity at $t = 0$, the maximum comoving distance a particle could have traversed would be

$$r_H = \int_0^t \frac{\mathrm{d}t'}{a(t')}, \tag{1.3}$$

where r_H denotes the radius of the particle horizon [188]. During this early radiation-dominated phase of the universe's history, $a(t) \propto t^{1/2}$. The horizon at the surface of last scattering (from which we receive CMB photons, at a redshift of $z \sim 1000$) could thus only be ~ 100 Mpc in size, subtending an angle of about 1 degree on the sky. This would indicate that areas on the CMB which are separated by more than one degree could not have been in causal contact, yet they are correlated in both temperature and observed temperature fluctuation. Inflation suggests a solution to this problem which extends conformal time to negative values, introducing a period of decreasing comoving Hubble radius such that all points observed in the CMB originate from a causally connected region of space.

Beyond this remarkable isotropy, the small anisotropies present in the CMB are also of interest. These anisotropies point towards galaxies and clusters grow-

ing via gravitational instabilities from seeds planted by initial perturbations. The history of the universe onwards from 10^{-10} seconds is based on fundamental laws of high energy physics and general relativity, which help to explain the growth of structure from these fluctuations. The structure problem asks for an explanation for the origin of these perturbations. The standard Big Bang model of cosmology predicts no such inhomogeneities, but inflation combined with quantum mechanics offers a source for primordial fluctuations in the very early universe [188]. During inflation, an equation of state with negative pressure necessitates an era during which the universe was dominated by a cosmological constant. The solutions to the Friedmann equation,

$$H^2 = \frac{8\pi G}{3}\rho - \frac{k}{a^2}, \tag{1.4}$$

in this case all evolve towards the exponential $k = 0$ solution,

$$a(t) \propto e^{Ht}, \tag{1.5}$$

known as de Sitter space. An event horizon can be defined for de Sitter space,

$$r_{EH} = \int_{t_0}^{\infty} \frac{\mathrm{d}t}{a(t)}, \tag{1.6}$$

which states that the distance that particles can travel between a time t_0 and $t = \infty$ is finite. The proper radius of the horizon is given by $a_0 r_{EH} = 1/H$. The exponential expansion makes distant regions of space fall out of causal contact with one another due to their moving apart faster than the speed of light. A picture of thermal Hawking radiation can be constructed based on this horizon,

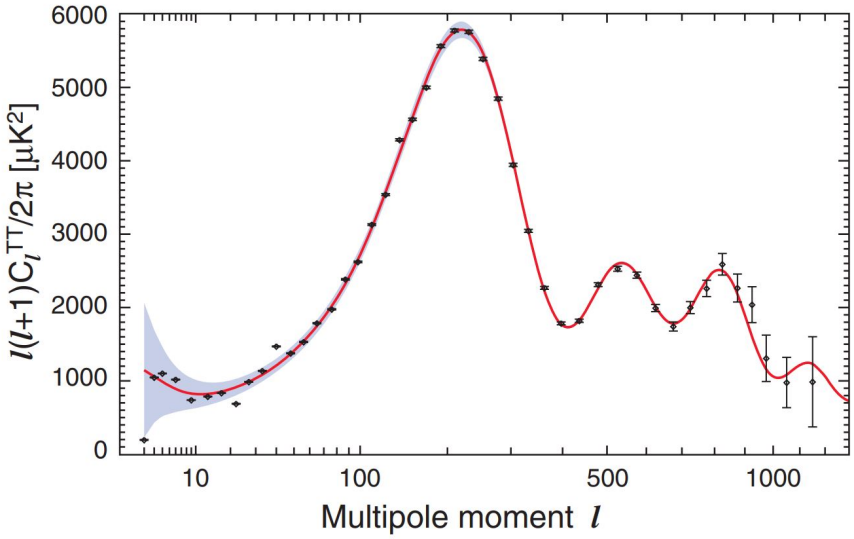

Figure 1.2: The temperature angular power spectrum of the primary anisotropies of the CMB, as measured by the Wilkinson Microwave Anisotropy Probe (*WMAP*) [33] over 7 years. The measurements are consistent with a flat universe that is expanding at the rate of $71.0 \pm 2.5 \mathrm{km \cdot s^{-1} Mpc^{-1}}$. The data provide limits on the ΛCDM model of cosmology. Figure is from Larson et al. 2011 [151].

and it is these quantum fluctuations that provide the seeds for what we now observe as galaxies and clusters. If this is true, there should exist a background imprint of gravitational waves left in the CMB as a relic of inflation, from modes of fixed comoving wavelength that are expanded to sizes $\gg 1/H$ and forced by causality to become frozen as classical amplitudes which seed large-scale structure [188]. Many modern cosmology experiments seek to measure this signal, and, if observed, the amplitude would be a signature of inflation that would teach us about the nature of the very early universe. Beyond this signal, a wealth of information waits to be extracted from careful measurements of the CMB.

The temperature anisotropies of the CMB can be expressed in the basis of spherical harmonics (Y_{lm}) as

$$\frac{\Delta T}{T_{CMB}}(\theta, \phi) = \sum_{lm} a_{lm} Y_{lm}(\theta, \phi), \tag{1.7}$$

where (θ, ϕ) indicates a location on the sky [99]. The coefficients a_{lm} are determined by the underlying density perturbations, and can be described statistically, with the angular power spectrum C_l,

$$\langle a^*_{lm} a_{l'm'} \rangle \equiv C_l \delta_{l'l} \delta_{m'm} \tag{1.8}$$

encapsulating the predictions of a given cosmological model through an ensemble average over the directional index m (Figure 1.2). Measuring the angular power spectrum of the CMB thus returns us information about the physics underlying our universe.

The largest anisotropy present in the CMB is a kinematic dipole arising from the motion of the Earth relative to the average reference frame of the CMB [229]. After this dipole, three physical processes generate most of the temperature fluctuations in the CMB: gravitational red/blue shifts known as the Sachs-Wolfe effect [211], acoustic oscillations in the plasma of the early universe, and diffusion damping of photons at small scales [242].

At the surface of last scattering, the place where CMB photons were scattered by electrons for the last time before free streaming through the universe, the photons were redshifted if they needed to climb out of a larger potential well (a region with higher density). Since curvature and gravitational potential perturbations are frozen on the super-horizon scale, this Sachs-Wolfe effect provides a dominant contribution to the primordial temperature anisotropies at

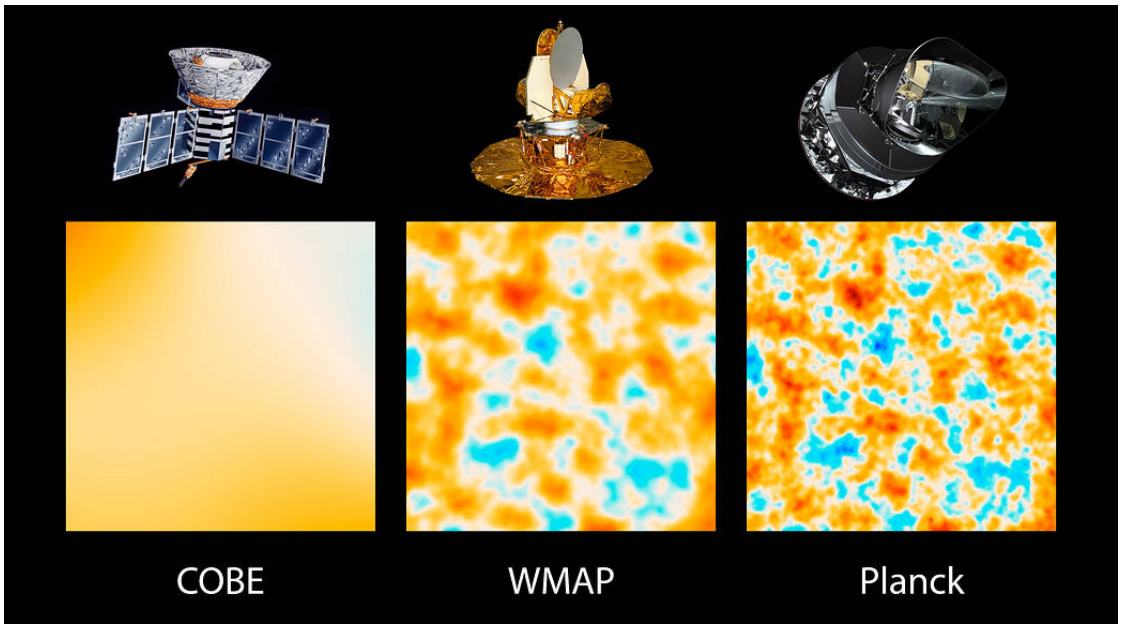

Figure 1.3: Improved measurements of the CMB over time have produced improved constraints on the power spectrum of the CMB anisotropies, and thus the model of cosmology that describes our universe. This graphic shows the improvement in resolution in 10 square degree submaps of the microwave sky from three generations of CMB satellite experiment: COBE [82], *WMAP* [33], and *Planck* [194]. Figure is from [177].

scales larger than the angular size of the horizon scale at recombination (Equation 1.3), (about 2 degrees) [212].

Before recombination, protons, electrons, and photons were coupled in a plasma that can be treated as a mixed compressive fluid, inside which density fluctuations are acoustic waves. These perturbations start to oscillate as acoustic waves once they cross the sound horizon, and we can measure these baryon acoustic oscillations (BAO) in the CMB within the angular scale corresponding to that horizon: $\theta_s = 0.80°$ [242]. The first peak of the CMB power spectrum corresponds to the scale at which acoustic oscillations are reaching their maximum amplitude at the surface of last scattering, while latter peaks occur at scales of subsequent antinodes and nodes (Figure 1.2). For a given cosmological model,

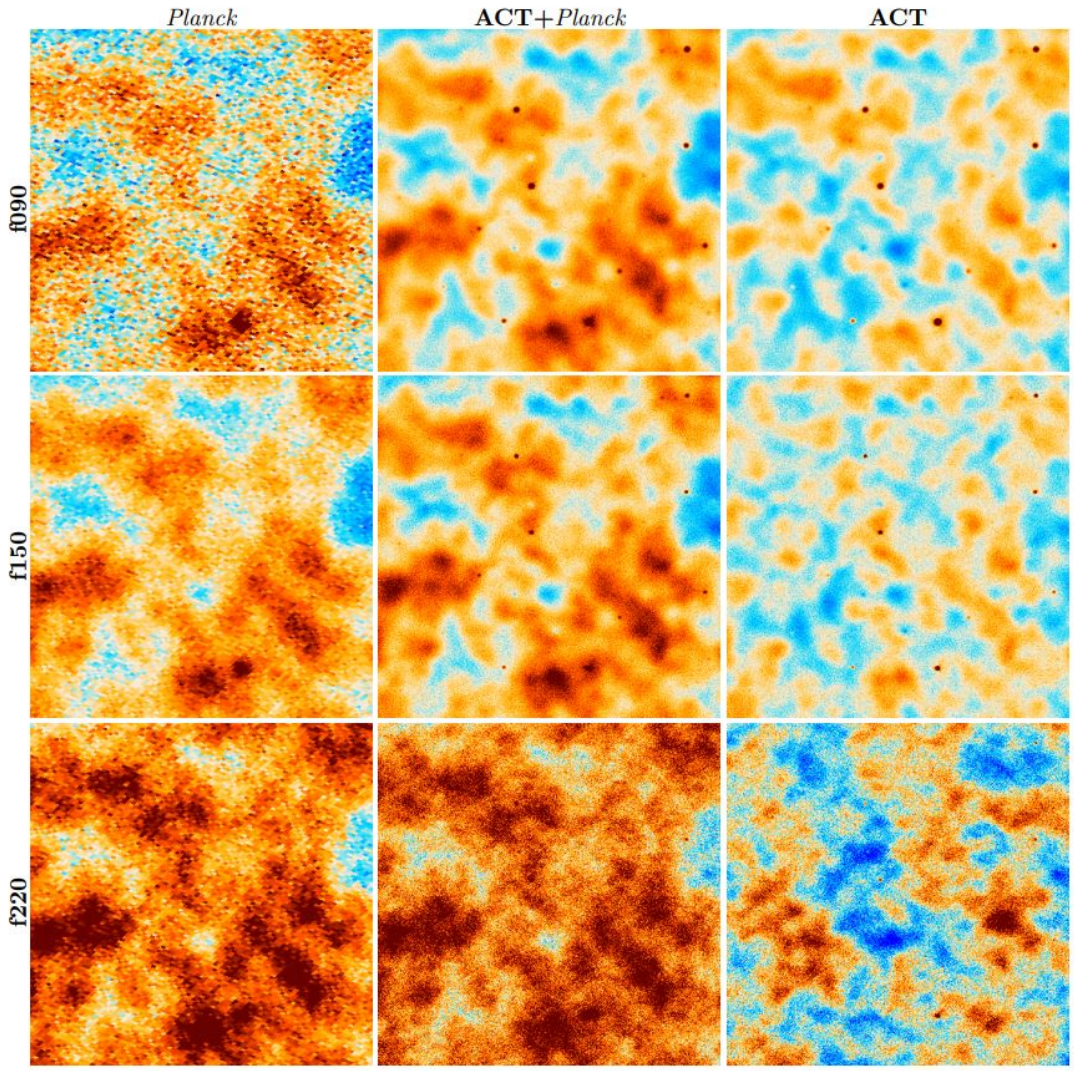

Figure 1.4: A comparison of Atacama Cosmology Telescope (ACT), *Planck*, and ACT+*Planck* data in a 3 square degree patch of sky across three frequencies (band centers at ~98, 150, and 224 GHz). The combination of ACT and *Planck* data is an improvement over *Planck* data alone in resolution and depth thanks to ACT's larger 6-meter mirror and more sensitive detector arrays. The combined maps also include the larger scales that *Planck* is better at measuring. Figure is from [175].

the location of the first peak in the CMB informs Ω_m, the universe's total matter density. Measurements of the subsequent peaks can give us more insight into the matter content of our universe [99].

On smaller scales, these fluctuations decrease in amplitude due to photon diffusion: random walks of photons between collisions with electrons that reduce the pressure in the fluid, resulting in a decrease of the acoustic wave amplitude. This damping effect, often called Silk damping [224], suppresses the fluctuations in the CMB on scales less than a few arcminutes.

After the first discovery of these primary CMB anisotropies by the COBE Differential Microwave Radiometers (DMR) [82], the experimental cosmology community has made increasingly precise measurements (Figure 1.2) of this angular power spectrum to inform our cosmological model as it stands today. The sound velocity in the baryon-photon fluid depends on the baryon density of our universe (Ω_b), impacting the amplitude of the BAO peaks in the CMB power spectrum. The Hubble constant, H_0, which paramterizes the time-dependent expansion of spacetime, also impacts the amplitude of these peaks. The power spectrum also depends on the dark matter density of our universe (Ω_c), which affects not only the amplitude of the BAO peaks but also their location, as the matter to radiation ratio controls the age of the universe at recombination and thus how far sound can travel. The amplitude of matter fluctuations on 8 Mpc scales, σ_8, influences the growth of fluctuations in the early universe, and depends on Ω_m. The curvature of the universe, Ω_k, modifies the apparent angular size, and thus the acoustic peaks and damping scale of the power spectrum. The spectrum depends also on the initial parametrizing power law spectral index, n_s, where $n_s = 1$ corresponds to scale invariant initial fluctuations, and current

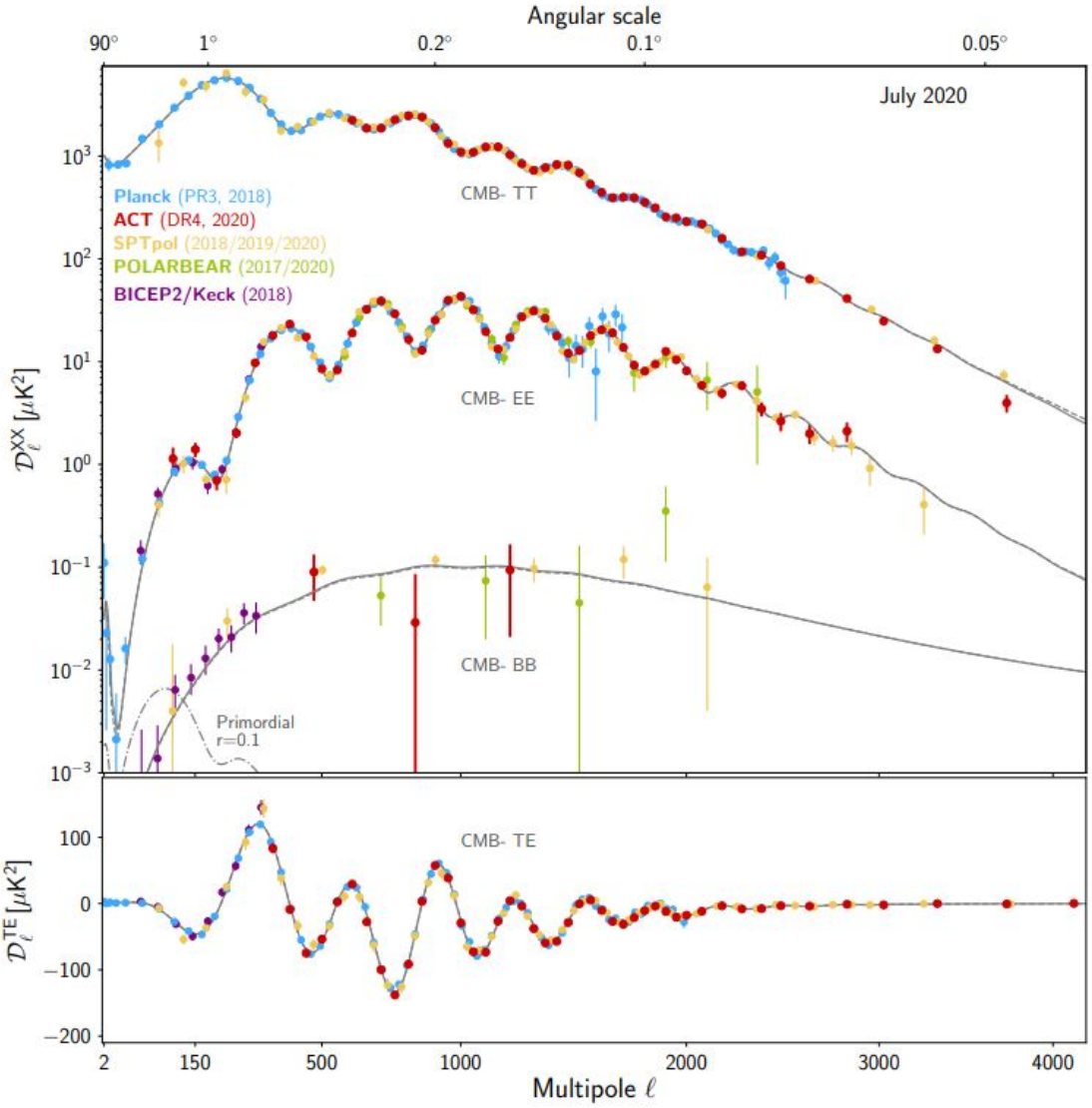

Figure 1.5: The primary temperature anisotropies and polarization of the CMB as measured by recent experiments: ACT [56], SPT [123, 215, 100], Polarbear/Simons Array [15, 199], BICEP2/Keck [38], and *Planck* [194]. The solid grey line is the ACT plus *WMAP* cosmological model and the dashed grey line is the *Planck* cosmology. One sigma error bars are plotted on each point. Figure is from [56].

values just below 1 are consistent with inflationary models. Altogether, these parameters describe the cosmology of our universe, and our confidence in their values grows as we improve our measurements of the CMB through higher signal-to-noise and complimentary datasets (Figures 1.3 and 1.4). An example of this progress is shown in Figure 1.5, where measurements of the temperature and polarization power spectra by ACT are presented alongside those from other experiments. The cosmological parameters from the ACT data agree with ΛCDM with $H_0 = 67.6 \pm 1.5$ km/s/Mpc. Analysis of current and future data from ACT, and that from upcoming experiments like the Simons Observatory, will continue to improve our understanding of cosmology.

1.1.2 Secondary Anisotropies

Photons from the CMB arrive on Earth only after a long journey through our universe, and as such they bear the signatures of their particular paths to our telescopes. At small angular scales of at or below a few arcminutes, secondary temperature fluctuations due to interactions with matter after z ~1100 dominate over the primary anisotropies discussed in Section 1.1.1. These secondary anisotropies must be accounted for to meet the science goals necessitating precise measurements of the primordial fluctuations. The secondary anisotropies also hold their own wealth of physical information and can inform us about the local properties of the universe, such as the evolution of structure. One person's foreground is another person's science goal. Other foregrounds that can contaminate both the primary and secondary anisotropies of the CMB include radio and infrared emission from our galaxy, extragalactic radio and infrared sources such as galaxies and active galactic nuclei, and bright point sources.

Measuring, constraining, simulating and separating these effects present in the CMB is thus necessary to extract the full suite of science information present in observed maps of the microwave sky.

Secondary anisotropies arise from two main types of CMB photon interactions: gravitational effects, such as gravitational lensing, and scattering with free electrons, such as inverse Compton scattering.

Photons from the CMB are affected by gravitational potentials as they travel from the surface of last scattering, which changes the temperature of these photons when they are observed by our telescopes. In the integrated Sachs-Wolfe (ISW) effect [211, 135], the photons traverse the gravitational potential evolving with the evolution of large scale structure. The CMB photon temperature change due to the ISW from time-variable metric perturbations is frequency independent, as are the other gravitational effects, and thus cannot be separated by primary anisotropies from spectral information alone. The ISW is correlated with tracers of large scale structure, is of interest to study at larger angular scales (at or above ~10 degrees), and its detection can provide information about the equation of state and clustering properties of dark energy (Section 1.4) [17, 135].

In the Rees-Sciama (RS) effect [204], corresponding to angular scales of 5-10 arcminutes, CMB photons are affected by their traversing a non-linear gravitational potential. This is generally associated with gravitational collapse, if the photon crossing time is large enough compared to the timescale of the structure formation. The RS effect can contaminate primary anisotropies and has the potential to become a limiting background for CMB polarization measurements [17, 204].

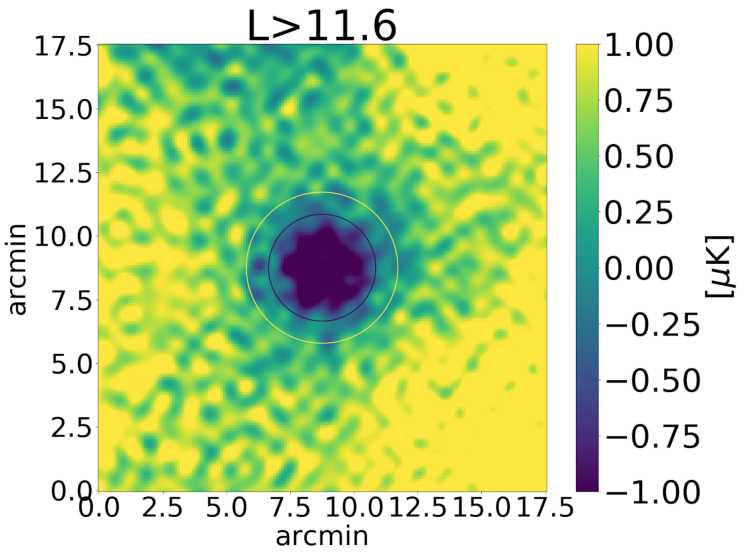

Figure 1.6: An example of the thermal SZ effect (Section 1.2.1) in a map of the CMB [264]. A weighted average of submaps taken from a 150 GHz ACT+Planck CMB map [175] centered on 23,504 sources from the BOSS DR15 galaxy catalog [18] with luminosities above $11.6 \times 10^{10} L_{\odot}$ (more details in Section 5.3.4). CMB photon interactions with the electrons in the galaxy halos create a temperature decrement at the observed frequency relative to what the CMB would look like without this secondary anisotropy present.

Gravitational lensing of the CMB by the large scale structure of our universe (wherever there is a gravitational potential) redistributes power towards smaller scales, with significant effects below a few arcminutes. Accounting for lensing at large scales becomes important when seeking to measure the B-mode power spectrum. Reconstructing the projected mass distribution of our universe via maximum likelihood estimators or quadratic statistics in temperature and polarization can clean this effect from the CMB power spectrum, reduce the mixing between the E and B components of CMB polarization, provide a map of the structure lying between us and the surface of last scattering, and probe neutrino mass (Section 1.3.4) and dark energy equation of state parameters (Section 1.4) [17, 156, 6, 259, 61].

In the Sunyaev-Zel'dovich (SZ) effects, CMB photons interact with the electrons present in ionized gas along the line of sight (Figure 1.6). The SZ effect is discussed in Section 1.2. The SZ effect is frequency-dependent, unlike the secondary anisotropies from gravitational effects, but shares commonality with these anisotropies in its usefulness to learn about the complicit matter structures, neutrino mass, and dark energy equation of state parameters (Sections 1.3.4, 1.4).

Measuring the secondary anisotropies of the CMB provides a complementary picture of the lower-redshift universe to that probed by other tools, such as galaxy surveys. Large scale structure surveys such as BOSS [67], DES [11], DESI [155], Euclid [73], LSST [160] and WFIRST [231] provide independent maps of mass distribution and galaxy clustering at optical wavelengths. Cross-correlations between these and CMB datasets can improve systematics and resulting constraints on parameters of interest such as neutrino mass [6]. Similarly, using optical catalogs to trace galaxy groups and clusters in maps of the CMB can enable high signal-to-noise SZ measurements and enable this probe of cosmology and galaxy evolution (Section 1.2).

1.2 The Sunyaev-Zel'dovich Effects

The Sunyaev-Zel'dovich (SZ) effects are a consequence of cosmic microwave background (CMB) photons inverse-Compton scattering off electrons in hot, ionized gas, especially that in the intra-cluster medium (ICM) of late-time galaxy clusters and groups. This scattering results in a shift in the blackbody spectrum observable as a secondary anisotropy in maps of the CMB [271, 243].

The leading order effects are the thermal SZ (tSZ) and kinematic SZ (kSZ) effects, caused by CMB photon interactions with electrons in the hot gas or Doppler shifts of the scattered photons due to the line-of-sight motion of the gas, respectively. The kSZ effect has a different spectral signature and is an order of magnitude smaller in amplitude than the tSZ signal, making it significantly more difficult to detect in maps of the CMB. Together, the SZ effects encode rich information about the structure and composition of our universe, including neutrino mass, dark energy, and galaxy groups and clusters.

1.2.1 The Thermal SZ Effect

A small fraction of the photons from the CMB passing through the hot gas present in galaxy groups and clusters will undergo Compton scattering by colliding with electrons in that gas, leaving a characteristic frequency-dependent distortion on the spectrum of the CMB. This is the tSZ effect [271, 243].

The distortion from the tSZ effect depends on the optical depth of the gas,

$$\bar{\tau} = \sigma_{\mathrm{T}} \int_{\mathrm{LOS}} n_e dl, \tag{1.9}$$

where σ_{T} is the Thompson cross-section, n_e is the electron number density, and dl is the integral along the line of sight (LOS) away from the observer [188, 27]. A larger optical depth represents a higher chance of photons interacting with the electrons within that gas. The tSZ effect also depends on the electron temperature, T_e, in its proportionality to the dimensionless Compton-y parameter via

$$\frac{\delta T_{\rm tSZ}(\theta)}{T_{\rm CMB}} = f_{\rm SZ}\, y(\theta), \tag{1.10}$$

where $y(\theta)$ is the Compton parameter at a projected angle θ from the cluster center. In the non-relativistic limit, $f_{\rm SZ}$ depends on observed radiation frequency,

$$f_{\rm SZ} = \Big(x\frac{e^x+1}{e^x-1} - 4\Big), \tag{1.11}$$

where $x = h\nu/k_B T_{\rm CMB}$ [137].

The Compton-y parameter is

$$y = \int_{\rm LOS} \sigma_{\rm T} n_e \frac{kT_e}{m_e c^2} dl = \frac{\sigma_{\rm T}}{m_e c^2} \int_{\rm LOS} P_e dl, \tag{1.12}$$

where m_e is the electron mass, T_e is the electron temperature, and P_e is the electron pressure [27, 188]. The fractional change in temperature of the CMB photons due to the tSZ effect can then equivalently be expressed as simply $\tau(kT_e/m_e c^2) \sim \tau(v_{thermal}/c)^2$ [218].

The resulting frequency-dependent shift in the blackbody spectrum of the CMB due to the tSZ effect appears as a decrement in the intensity of the CMB at frequencies below ~218 GHz, and as an increment at higher frequencies (Figure 1.7).

In its sensitivity to the cluster's integrated line-of-sight pressure profile, the tSZ effect is a valuable, largely redshift-independent probe of gas in the intracluster medium. The characteristic frequency dependence of the tSZ effect can be isolated through the use of multi-frequency measurements of the CMB.

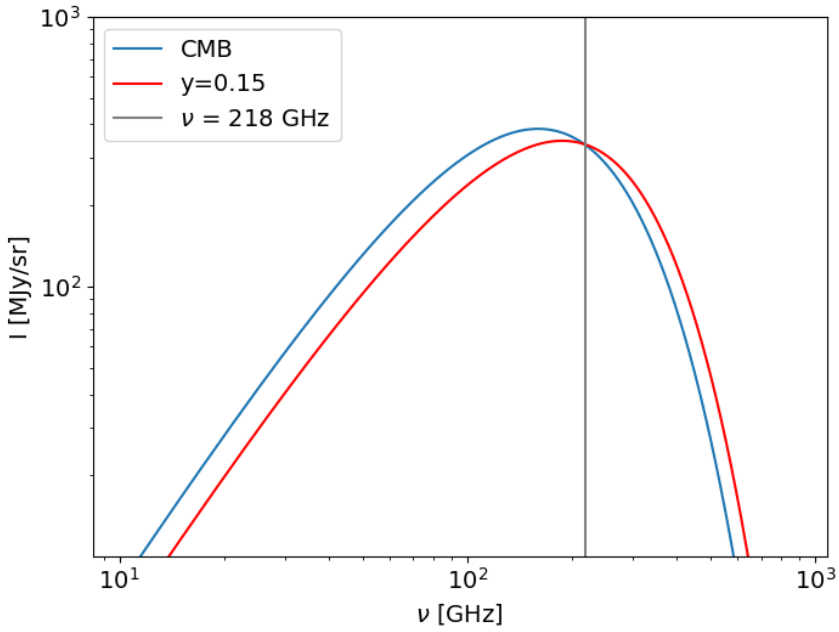

Figure 1.7: The spectral distortion of the CMB due to the tSZ effect via Equations 1.10 and 1.11 for a cluster that is >1000 times more massive than a typical cluster, to more easily visualize the (generally small) shift. The undistorted CMB blackbody spectrum is the blue line and the distorted spectrum is the red line. The tSZ effect causes a decrease in CMB intensity at frequencies below 218 GHz and an increase above this point. At ~218 GHz, no shift is observed, which can be useful for systematics checks in tSZ analyses.

Measurements of the tSZ effect allow us to study the thermodynamics of the cluster gas, including processes such as active galactic nuclei (AGN) feedback, star formation, radiative cooling, and cluster merger histories. The tSZ effect can also give us information about the shapes and extents of cluster gravitational potential wells and dark matter halos [25, 170]. By tracing the electron distribution within groups and clusters, the tSZ effect is sensitive to the poorly understood spatial distribution of ionized gas and the baryon content.

We are able to estimate the optical depth, τ, of the gas within halos by combining tSZ measurements with cosmological hydrodynamic simulations (Sec-

tion 5.3.2) [25]. In the case of the "missing baryon" problem, observations suggest that this gas contains fewer baryons than would be predicted by mass-density profile models neglecting heating processes [92, 178, 223, 203, 54]. These baryons are thought to be located at the outskirts of groups in the diffuse warm-hot intergalactic medium, where they are not easily measured by X-ray observations or the tSZ effect [92, 216, 130, 205, 50, 53].

To use tSZ measurements to probe cluster properties, we must extract the tSZ signal from the microwave sky at high significance. Cleaning the tSZ signal from sources of contamination such as competing astrophysical and cosmological signals, instrumentation and atmospheric noise, and dusty galaxy and synchrotron emission can be a challenge. Recent efforts by the Atacama Cosmology Telescope (ACT) [164, 116, 128, 16], South Pole Telescope (SPT) [236, 41], and *Planck* Collaborations [194] have produced measurements of the tSZ effect in CMB data. Many tSZ analyses use single frequency (especially 150 GHz) CMB maps and rely on matched filters. Heritage for both tSZ stacking and multifrequency dust reconstruction in ACT data includes multiple recent publications [93, 105, 239]. Our recent work with multi-frequency ACT data is detailed in Chapter 5.

1.2.2 The Kinematic SZ Effect

The kinematic SZ effect arises from Doppler shifts in the scattered CMB photons due to the radial peculiar motion of the interacting gas halos relative to the CMB rest-frame, rather than the Doppler shifts due to the thermal motion of the gas electrons as in the tSZ effect. The kSZ effect is typically an order of magnitude

smaller than the tSZ effect and has a spectrum that is similar to the CMB blackbody, making it challenging to detect and separate from contaminating tSZ and dust emission foregrounds. The fractional shift in the CMB temperature signal due to this Doppler-shifting kSZ effect depends on the peculiar velocity, $\hat{v}_p$, of the gas halo along the line of sight:

$$\frac{\delta T_{\rm kSZ}(\theta)}{T_{\rm CMB}} = \int_{\rm LOS} \sigma_{\rm T} n_e \frac{\hat{\mathbf{v}}_{\mathbf{p}} \mathbf{e}^{-\tau}}{c} dl, \tag{1.13}$$

where $\sigma_{\rm T}$ is the Thompson cross-section, c is the speed of light, n_e is the electron number density, $T_{\rm CMB}$ is the temperature of the CMB, and the integral is along the LOS away from the observer [243, 27]. The fact that the galaxy groups commonly being analyzed, like those in our recent work with ACT data (Chapter 5), have optical depths that are at or below the $\sim 1 \times 10^{-4}$ level means we can set $e^{-\tau}$ in Equation 1.13 to ~1. This then simplifies the fractional shift in CMB temperature to the more intuitive $-\tau v_p/c$, where v_p is the free electron bulk LOS velocity and τ is the optical depth of the galaxy group [218]. We see that the kSZ signal, like the tSZ signal, is dependent on the optical depth of the gas in question (Equation 1.9).

Techniques to extract the kSZ effect from the dominating primary CMB fluctuations and tSZ effect (Figure 1.8) include velocity reconstruction [217], projected fields [125, 86], cross-correlation of angular redshift fluctuations [53], cluster stacking [248], and a pairwise correlation statistic, which we have used to measure the kSZ effect in data from the Atacama Cosmology Telescope (Chapter 5).

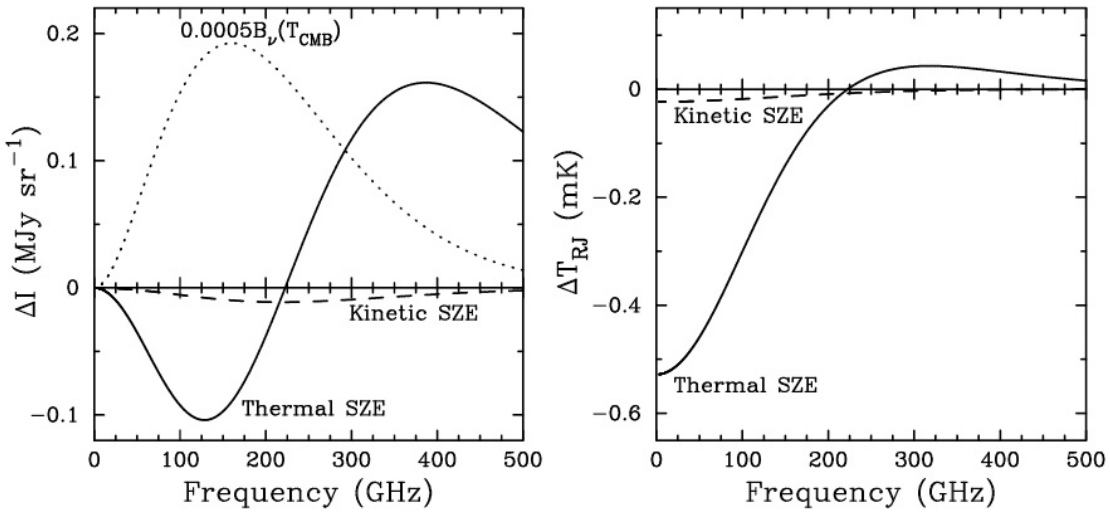

Figure 1.8: The intensity (left) and Rayleigh Jeans brightness temperature (right) of the thermal (solid line) and kinematic (dashed line) SZ effect distortions of the CMB. The 2.7 K thermal spectrum of the CMB is scaled by 0.0005 in the dotted line for reference (left), illustrating the comparatively small magnitude of the SZ effects. The cluster properties used to calculate the plotted spectra are T_e = 10 keV, Compton-y = 10^{-4}, and v_p = 500 km/s. Figure is from [48].

The Pairwise kSZ Effect

When separated by distances on the order of ~25-50 Mpc, clusters and groups of galaxies, on average, move towards each other due to the attractive force of gravity. This pairwise trend in gas motion can be used to extract the kSZ effect, and the statistical nature of the approach relies on large numbers of tracer sources to measure the small signal. A pairwise correlation statistic [65] to extract the kSZ signal depends on pairwise differences of measured temperatures on the sky at the positions of galaxies, and thus averages out contaminating signals like the tSZ signal and dust emission without needing to model them in detail.

The pairwise estimator,

$$p_{est}(r) = \frac{\Sigma_{i<j}(\mathbf{p}_i \cdot \mathbf{r}_i - \mathbf{p}_j \cdot \mathbf{r}_j)c_{ij}}{\Sigma_{i<j}c_{ij}^2}, \tag{1.14}$$

computes the mean pairwise momentum of a sample of galaxies through their line-of-sight components: here, $\mathbf{r}_i$ is the comoving distance (Equation 1.2) to the ith object, calculated assuming a given cosmology and optical catalog redshift of the galaxy [68]. The measured kSZ signal (Equation 1.13) from a given halo is proportional to this line-of-sight momentum (as traced by galaxy i of the catalog), $-\mathbf{p}_i \cdot \mathbf{r}_i$. The pairwise momentum estimator is a function of r, the comoving separation distance between galaxy pairs i and j, $r = |\mathbf{r}_{ij}| = |\mathbf{r}_i - \mathbf{r}_j|$. The factor c_{ij} in Equation 1.14 is a geometrical factor accounting for the alignment of a given pair of galaxies i and j along the line of sight:

$$c_{ij} = \mathbf{r}_{ij} \cdot \frac{\mathbf{r}_i + \mathbf{r}_j}{2} = \frac{(r_i - r_j)(1 + \cos\theta)}{2(r_i^2 + r_j^2 - 2r_i r_j \cos\theta)} \text{ [68].} \tag{1.15}$$

Here, θ is the angular separation between the two galaxies i and j relative to the line of sight.

Because of its sensitivity to the motion of gas on large scales, the pairwise kSZ estimator has the potential to probe the growth rate of large scale structure (LSS), providing insights into the evolution of dark energy, equations of modified gravity, and constraints on the sum of the neutrino masses (Sections 1.3.4,1.4) [71, 36, 147, 46, 172, 171, 91].

Optical galaxy surveys can provide bright tracer galaxies to identify and locate the clusters and groups for which we measure the pairwise kSZ effect [143, 142, 88, 154, 241]. The first measurement of the pairwise kSZ signal was made by Hand et al. [113] by estimating the mean pairwise cluster momentum

with ACT data from 2008 to 2010 and a sample of galaxies from the Sloan Digital Sky Survey Data Release 9 (SDSS DR9) catalog. This measurement has since been improved with a 4.1σ measurement in the mass-averaged optical depth, $\bar{\tau}$, using data from ACT DR3 and SDSS DR11 [68], and a 5.4σ measurement using data from ACT DR4 and DR5 and SDSS DR15 [47].

While the amplitude of the kSZ effect is proportional to both the total cluster gas mass and the cluster's line-of-sight velocity, it is independent of the gas temperature. When both the tSZ and kSZ effects are measured for the same sample of sources and the optical depth (and thus the total cluster gas mass) is modeled from the tSZ data, the combination can be used to convert the pairwise momentum [113] measured from the kSZ effect into pairwise velocity. The pairwise velocity can then be used to constrain cosmological parameters, such as the sum of the neutrino masses (Section 1.3.4) [172, 171].

1.3 Neutrinos, the Early Universe, and Large Scale Structure

Measurements of the CMB can turn the universe itself into a laboratory for fundamental particle physics. Cosmological probes are independent from and complementary to Earthly laboratory experiments, providing a useful method for studying particles like neutrinos.

1.3.1 Neutrino Mass

Neutrinos, once thought to be massless, are now known through oscillation experiments to have small masses: many orders of magnitude smaller than

those of charged fermions. Understanding the mechanism of neutrino mass could explain this deviation, as well as answer open questions about the matter-antimatter asymmetry problem and whether lepton number is a symmetry of nature [107].

Neutrinos could be Dirac particles ($\nu \neq \bar{\nu}$), in which case lepton number would be conserved. The Dirac mass term couples left- and right-handed chiral states, and charged fermions (like electrons and quarks) can only have a Dirac type mass. The existence of sterile (solely gravitationally interacting), right-handed chiral neutrinos would allow for a Dirac type mass.

If neutrinos are instead Majorana particles ($\nu = \bar{\nu}$), a mass term can be constructed in which the charge conjugate of the Majorana field is the same as the field itself, meaning antineutrinos would be identical to neutrinos. Because the Majorana mass term couples the antineutrino and neutrino components, interactions involving Majorana neutrinos do not conserve lepton number [39].

In the presence of a Majorana mass term, the seesaw mechanism provides an explanation for the neutrino's tiny mass. The seesaw mechanism produces the three known light neutrino flavors, and three heavy counterparts (which have yet to be observed). The potential existence of these heavy particles enables a hypothetical process that produced an asymmetry between leptons and antileptons in the very early universe: leptogenesis [107].

The baryon asymmetry of the universe, or why we see more baryonic matter in our universe than antibaryonic matter, is not yet understood. If neutrinos are Majorana particles, violation in lepton number conservation of the heavy sterile neutrinos early in the universe's history would manifest in a violation in baryon

number conservation. In this way, leptogenesis could address the missing antimatter problem. It is known that quarks violate CP-symmetry, the combination of charge symmetry and parity symmetry, but not enough to account for the disparity between matter and antimatter in the universe. CP violation in the decays of heavy sterile neutrinos could bridge that gap [191]. CP violation is thus interesting to study in the oscillations of light neutrinos, even though there is not a direct connection to CP violation in the heavy neutrinos. Determining the nature of neutrino mass is central to investigating whether neutrinos may explain the baryon asymmetry of our universe [110].

One of the unresolved issues surrounding neutrino mass in the Standard Model is determining the mass hierarchy. This will serve as a critical input to more accurate cosmological and astrophysical models and help to interpret the results of future neutrinoless double beta decay experiments. Neutrinoless double beta decay ($0\nu\beta\beta$) is a lepton number violating decay of a nucleus with electron emission, but without neutrino emission: $(A, Z) \rightarrow (A, Z + 2) + 2e^{-}$. An observation of 0ν would indicate that neutrinos are Majorana fermions. Two orderings (hierarchies) of the three known neutrino masses are possible. In the normal hierarchy (NH), ν_3 is the heaviest mass eigenstate, whereas in the inverted hierarchy (IH), it is the lightest (Figure 1.9) [187].

1.3.2 Thermal History

The thermal history of the universe and the origins of the cosmic neutrino background dictate what we can learn about the sum of the neutrino masses from cosmological measurements. In the time during the early universe's history that

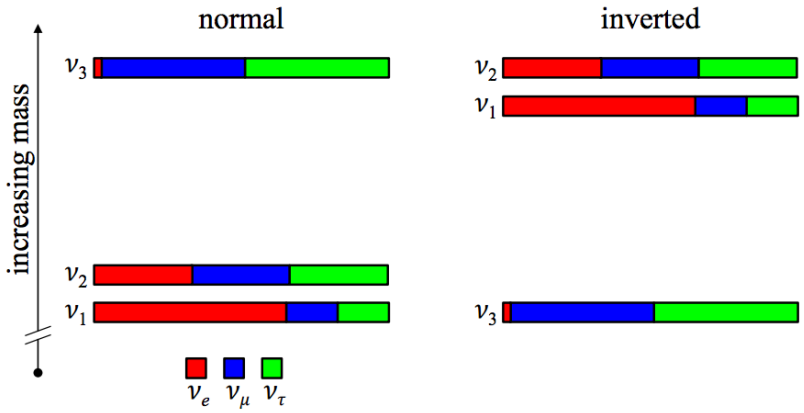

Figure 1.9: Normal and inverted neutrino mass hierarchies. The colors in each bar represent the neutrino flavor eigenstate admixtures present in each mass eigenstate. The sign and magnitude of the solar mass splitting (Δm^2_{21}) has been determined through solar neutrino experiments, but the sign of the atmospheric mass splitting (Δm^2_{32}) is not yet known, resulting in these two possible configurations. Upper limits on the sum of the neutrino masses with input from cosmology can determine the neutrino mass hierarchy. Figure is from [187].

the temperature of the plasma was falling from $\sim 10^{11}$ K to $\sim 10^8$ K, neutrinos decoupled from the rest of the plasma, and electrons and positrons annihilated, heating the photons relative to the neutrinos by a factor of $(11/4)^{1/3}$. The total energy density and entropy density of the early universe during this radiation-dominated period are given by

$$\rho(T) = g_* \frac{\pi^2}{30} T^4, \quad s(T) = \frac{4}{3} g_* \frac{\pi^2}{30} T^3, \tag{1.16}$$

where g_* counts the spin states for all particles and antiparticles, with an extra factor of 7/8 for fermions due to integration over the Fermi-Dirac distribution function [267, 30]. The first law of thermodynamics implies that the comoving entropy density of particles in equilibrium is conserved ($a^3 s(T)$=const.) such that the temperature evolves as the inverse of the scale factor for radiation in free expansion. After the electron positron annihilation, the radiation density of

the universe was

$$\rho_r = \frac{\pi^2}{15}\left[1 + \frac{7}{8}\left(\frac{4}{11}\right)^{4/3}\right] N_{eff} T_\gamma^4, \tag{1.17}$$

where T_γ is the photon temperature and N_{eff} is a quantity which represents the effective number of neutrino species. Big Bang nucleosynthesis predicts $N_{eff} = 3.05$ [6]. The current estimate predicts $N_{eff} = 2.99 \pm 0.17$ [267, 30, 196].

1.3.3 Structure Formation

The energy density in nonrelativistic neutrinos contributes to the matter budget of the universe today, but the fact that neutrinos were relativistic for much of the history of the universe means that their gravitational clustering is different from that of cold dark matter (CDM) particles.

The angular power spectrum of the CMB (Section 1.1.1) at small angular scales is sensitive to the radiation content of the early universe, parametrized by N_{eff}, introduced in Section 1.3.2 as a measure of the energy density of the cosmic neutrino background. More generally, N_{eff} receives contributions from all forms of radiation present in the early universe apart from photons. Cosmic neutrinos (and other light relics which would increase N_{eff}) contribute to the total energy in radiation which controls the expansion history and affects the damping tail of the power spectrum, as well as producing a shift in the phase of the acoustic peaks due to their fluctuations.

The neutrino energy density is given by

$$\rho_\nu = \sum_i \int \frac{d^3\mathbf{p}}{(2\pi)^3} \frac{\sqrt{p^2 + m_{\nu i}^2}}{e^{ap/T_{\nu 0}} + 1}, \tag{1.18}$$

where $m_{\nu i}$ are the three neutrino mass eigenstates and the density depends on the Fermi-Dirac momentum distribution [267, 30]. In early times, the neutrino energies are dominated by their momenta and the total energy density behaves like radiation ($\rho_\nu \propto a^{-4}$) while for later times, the energy density behaves like matter ($\rho_\nu \propto a^{-3}$). For a neutrino of mass $m_{\nu i}$, this transition ($k_B T_\nu(a) \sim m_{\nu i} c^2$) occurs at redshift $z_{nr} \sim 300(m_{\nu i}/0.05\text{eV})$. The fractional energy density in neutrinos today can then be written as[6]

$$\Omega_\nu \approx \frac{\sum_i m_{\nu i}}{93\text{eV}}. \tag{1.19}$$

Using current information from CMB and BAO measurements [194], an upper limit on the contribution of neutrinos to the cosmic energy budget can be placed at 0.003 [194], and from neutrino mixing results, an upper limit of $\Omega_\nu \leq 0.0012$ is placed [107].

Because they started as relativistic particles, neutrinos do not participate in gravitational collapse until late times when they became nonrelativistic. Before this, the neutrinos free streamed out of gravitational wells, damping primordial fluctuations in the neutrino density on scales smaller than the horizon at z_{nr}. This scale corresponds to the wave number

$$k_{nr} \equiv a_{nr} H(a_{nr}) \approx 0.003 \left(\frac{\Omega_m}{0.3} \frac{m_\nu}{0.05\text{eV}}\right)^{1/2} h/\text{Mpc}. \tag{1.20}$$

The neutrino free streaming scale is defined in comoving coordinates as

$$k_{fs}(a) \equiv \sqrt{\frac{3}{2}}\frac{aH(a)}{v_\nu(a)} \approx 0.04a^2\sqrt{\Omega_m a^{-3} + \Omega_\Lambda}\left(\frac{m_\nu}{0.05\text{eV}}\right)h/\text{Mpc}. \tag{1.21}$$

On scales larger than k_{nr}, perturbations in the density of neutrinos, baryons, and CDM can be described by a single perturbation to the total matter density. On smaller scales, only the perturbations to the CDM and baryons remain, and they grow more slowly because the neutrino energy density contributes only to the expansion rate. This causes a suppression in the amplitude and the growth rate of matter perturbations with wavenumbers $k > k_{fs}$ relative to a universe with massless neutrinos. The net change in the amplitude of perturbations with $k > k_{nr}$ depends on the fractional energy density in massive neutrinos and on the neutrino mass sum (Figure 1.10) [6, 267, 30].

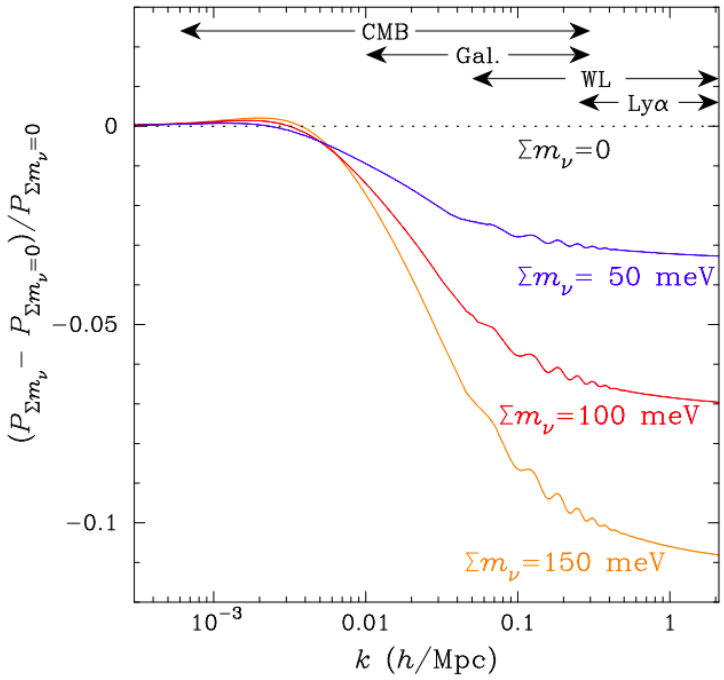

Figure 1.10: The fractional change in the matter density power spectrum as a function of comoving wavenumber k for various values of $\sum m_\nu$, along with ranges of experimental sensitivity from the CMB, galaxy surveys, weak lensing of galaxies, and the Lyman-α forest. CMB lensing involves an integral over this power spectrum and is also sensitive to neutrino mass. Figure is from [8].

1.3.4 Cosmological Probes

The signature of massive neutrinos is present in the energy density Ω_ν (Equation 1.18). Probes of the matter power spectrum are sensitive to the sum of the neutrino masses and can place upper limits on the sum (Figure 1.11). The lowest possible value of $\sum m_\nu$ depends on the mass hierarchy and is determined by the results of the oscillation experiments: the lowest value for the inverted hierarchy is $\sum m_\nu \sim 0.1$ eV, and the lowest value for the normal hierarchy is $\sum m_\nu = 0.058$ eV. Therefore, an upper limit below $\sum m_\nu = 0.1$ eV would disfavor the inverted hierarchy and determine the neutrino mass ordering [184].

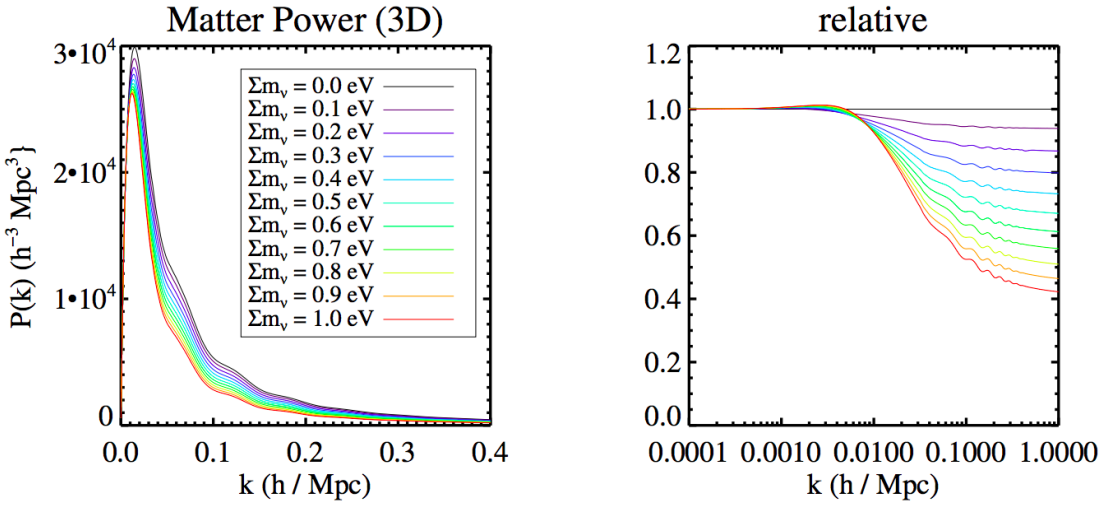

Figure 1.11: Suppression in the matter power spectrum at small scales due to neutrino mass. Figure is from [6].

Gravitational lensing of the CMB directly measures the matter distribution along the line of sight. As CMB photons travel to the Earth from the surface of last scattering, they are deflected by matter which distorts the CMB anisotropies and their statistical properties. In this way, CMB lensing encodes statistical information about the large scale structure (LSS) mass distribution [6].

Beyond CMB lensing, external LSS datasets are sensitive to the scale of the neutrino masses through the suppression of the matter power spectrum (inferred from weak gravitational lensing, fluctuations in galaxy abundance, or changes in the opacity of intervening gas) and the change in the growth rate of matter perturbations, inferred from redshift-space distortions. The suppression of the matter power spectrum is the same effect tested by CMB lensing, but galaxy surveys measuring the effect are probing structure at multiple epochs in the universe's history whereas CMB lensing provides a map of the integrated mass distribution. The LSS information thus contains more information than galaxy surveys [6].

Galaxy clusters form from high peaks in the matter density field, out of a regions smaller than the neutrino free streaming scale. The neutrino free streaming therefore slows the growth of structure on galaxy cluster scales, suppressing the abundance of galaxy clusters.

Galaxy clusters can be identified and probed in CMB data via the thermal Sunyaev-Zel'dovich (tSZ) effect (Section 1.2.1). The kinematic SZ effect, an order of magnitude smaller effect due to the velocity of the galaxy clusters in which these photons interact, can be used to constrain cosmology including the neutrino mass sum (Section 1.2.2). A variety of methods of extracting the kSZ signal from CMB maps are currently being pursued, with promising results (Section 1.2.2). Forecasts for kSZ measurements in combination with Planck primordial CMB priors provide constraints on the sum of neutrino masses with a precision of up to 0.09 eV for the current generation of CMB experiments [173]. When combined with laboratory experiments, CMB-S4 will be able to disfavor the inverted mass hierarchy if $m_\nu \lesssim 0.1$ eV [6].

The Lyman-α forest and 21 cm surveys are other approaches to probe the underlying matter clustering in LSS using neutral hydrogen as a tracer. Input from future 21 cm surveys combined with CMB data will also improve constraints on neutrino mass [184].

The combination of cosmological and terrestrial neutrino mass measurements tests the cosmological neutrino model, with a discrepancy possibly pointing to new physics. Cosmological neutrino mass measurements are also complementary with $0\nu\beta\beta$ experiments. In the absence of a signal in next generation $0\nu\beta\beta$ searches, a cosmological measurement constraining $\sum m_\nu > 0.1$ eV (corresponding to either an IH or a minimum neutrino mass of 0.05 eV) would strongly point to neutrinos being Dirac particles. On the other hand, in the presence of a $0\nu\beta\beta$ signal, in the IH cosmological measurements together with $0\nu\beta\beta$ measurements can constrain one of the Majorana phases. If cosmological and $0\nu\beta\beta$ measurements turn out to be in tension, new physics beyond the model of light Majorana neutrino mediated decay could be suggested [6].

Target thresholds for 2σ and 3σ detections of $\sum m_\nu \approx 0.058$ eV are 0.03 eV and 0.02 eV respectively for a CMB-S4 effort. Reaching these thresholds and making a determination of the mass hierarchy through CMB measurements requires constraints on degenerate parameters τ (optical depth) and $\Omega_m h^2$ [6]. Independent measurements of the optical depth of galaxy halos could also aid kSZ constraints on neutrino mass (Section 1.2.2). Experiments studying neutrino oscillations in matter, in which resonant enhancements enhance oscillations, are expected to make the most significant determination of the neutrino mass ordering [70]. Information from cosmology will serve as an independent and complementary probe.

1.4 Dark Energy

The universe is expanding at an increasing rate, a fact that remains a quagmire and necessitates either a modification to the well-tested theory of general relativity, or the presence of an unknown substance dubbed dark energy. Tests confirming this accelerating expansion include supernova Ia observations ([207, 192]), large scale structure [249, 250], and baryon acoustic oscillations [190, 43] in addition to CMB measurements [232, 194, 115]. Our standard ΛCDM model of cosmology includes the cosmological constant Λ to account for the observed acceleration, but despite the success of the ΛCDM model, the cosmological constant lacks theoretical motivation and is accompanied by several theoretical issues [268, 49]. Many dark energy and modified gravity models have been suggested, and experimental constraints can help distinguish between them.

Our current dark energy-dominated expansion of the universe is more modern than the $z \sim 1100$ CMB, so modifications to gravity or the behavior of dark energy do not have a significant impact on the primordial CMB. Instead, secondary anisotropies in the CMB form the picture of the evolution of large scale structure under the influence of modified gravity or dark energy (Section 1.1.2). Measurements of these anisotropies thus have the potential to constrain and separate the two possible explanations for this extraordinary evolution of our universe.

Cosmological observations of large scale structure include probes of the bending of light due to gravitational potentials (Section 1.1.2) and probes of the velocities of gravitationally bound objects like galaxy clusters and groups as they move within the large scale structure. Probes of peculiar velocities in-

clude the kinematic SZ effect (Section 1.2.2) and redshift space distortions in the galaxy correlation function [141].

The mean pairwise velocity of clusters derived from the kSZ effect (Section 1.2.2) can serve as a probe of large scale structure and thus models of dark energy and modified gravity.

The matter over-density, δ_m, is proportional to the velocity of dark matter particles, v_m. This proportionality links the time evolution of the matter perturbations to the velocity of dark matter, such that tracers of the dark matter velocity distribution (like the velocities of galaxy groups and clusters) can be used to constrain cosmology. Although in many modified gravity models, the background expansion of the universe looks the same as in a ΛCDM universe, the evolution of the density perturbations can look different than standard gravity and thus can be used to distinguish between models. The linear perturbation equations are solved with an equation of the form $\delta_m(x,t) = D_a(t)\delta(x)$, where D_a is the growth factor and contains the time dependence within the equation. The growth rate at a given scale factor a can then be defined as

$$f_g a \equiv \frac{d\mathrm{lnD_a}}{d\mathrm{lna}}, \tag{1.22}$$

the logarithmic derivative of the growth factor [171]. This growth of structure can be approximated by $f_g(a) \sim \Omega_m(a)^\gamma$ where for standard general relativity $\gamma \cong 0.55$ [159, 265]. For a given cosmology, the dark energy equation of state can be written in the Chevallier-Polarski-Linder parametrization [219] as $w(a) = w_0 + (1-a)w_a$, where the equation of state parameters are w_0 and w_a. In this form, the fractional matter density and dark energy density evolve over time as

$$\Omega_m(z) = \Omega_m^0(1+z)^3, \Omega_{\rm DE} = \Omega_{\rm DE}^0(1+z)^{3(1+w_0+w_a)}\exp\Big(-\frac{3w_a z}{1+z}\Big) \tag{1.23}$$

where Ω_m^0 and Ω_{DE}^0 are the matter and dark energy density at $z = 0$ [162]. These equations can be substituted into the Friedmann equation (Equation 1.4) in order to calculate the Hubble expansion and comoving distance $x(z)$. The coming distance increases as w_0 or w_a decreases, and vice versa, since a more negative w_0 or w_a means the Hubble parameter was smaller in the past.

These models involve expansion histories which deviate from that of ΛCDM due to an evolution in the dark energy equation of state. A measurement of pairwise velocity can be used to constrain this growth of structure, and thus the underlying theory of gravity [139, 87]. Figure 1.12 shows the mean pairwise velocity curve and how its amplitude and shape varies when varying the equation of state parameter w_0, growth exponent λ, and the minimum mass of the galaxy sample. While changes in w_0 and λ have degenerate effects on the amplitude of the pairwise velocity and do not impact the shape of the curve, the redshift dependence of these parameters breaks the degeneracy, with $V(z)$ varying with w_0 differently than with λ [171]. High signal-to-noise measurements of these pairwise velocity curves thus have the potential to constrain cosmological models.

A CMB-S4 style survey with high resolution is projected to constrain the growth of structure at $\leq$ 5% in models including a redshift dependent dark energy equation of state, distinguishing dark energy from modified gravity. Improving constraints on the optical depth, τ, of the clusters involved in the pairwise velocity analysis will improve the accuracy of the kSZ pairwise velocity measurements and thus the constraints on gravity and dark energy, as

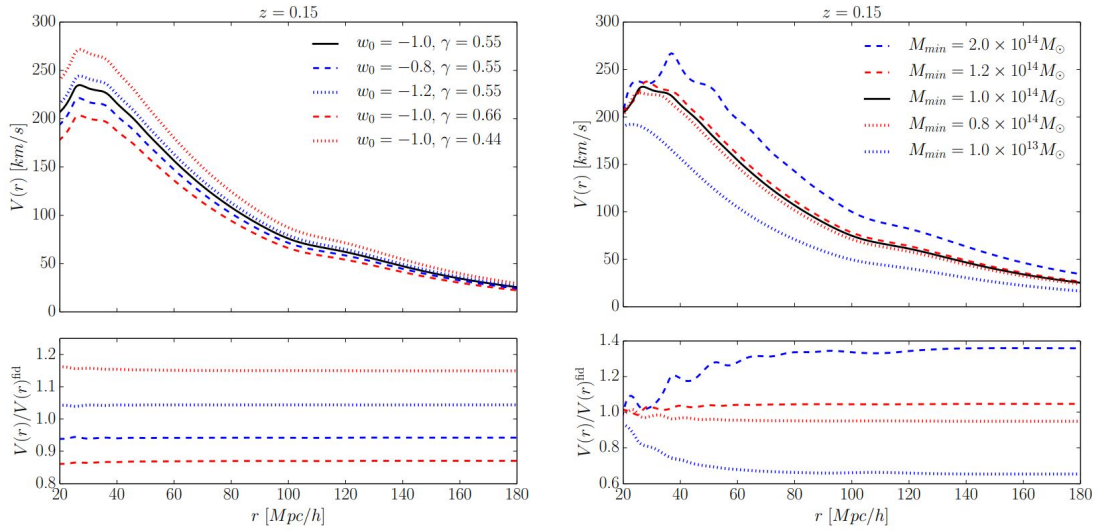

Figure 1.12: Left, above: The mean pairwise cluster velocity V (as discussed in Section 1.2.2) as a function of galaxy separation r differs based on values of the dark energy equation of state parameter w_0 and the modified gravity parameter λ, illustrating the sensitivity of the pairwise statistic to models of dark energy and modified gravity. The pairwise curves are plotted for a redshift of 0.15, and a minimum cluster mass of the sample is taken to be $M_{min} = 1 \times 10^{14} M_\odot$. A more negative w_0 leads to an increase in the amplitude of the mean pairwise cluster velocity (V). A smaller γ increases the growth rate, increasing V, and vice-versa. Left, below: Ratio of the mean pairwise velocity for the different w_0 and γ values to the fiducial model, $V(r)^{\rm fid}$. Right, above: The mean pairwise cluster velocity V for various minimum mass cuts at the same redshift of 0.15. The minimum mass cut affects the shape of the pairwise velocity curve in addition to its amplitude. Higher minimum mass increases mean pairwise velocity, since more massive clusters tend to have higher peculiar velocities. Right, below: Ratio of the mean pairwise velocity for the different minimum mass values to the fiducial model, $V(r)^{\rm fid}$. Figure is from [171].

discussed in Section 1.2.2. These pairwise velocity measurements are complimentary to other tracers of large scale structure, like weak lensing and redshift space distortion measurements, and combining datasets has the potential to improve future constraints [6, 171].

1.5 Instrumentation for Measuring the CMB

The light from the microwave sky can be observed using ground-based telescopes at high altitudes in locations with dry atmospheres, such as in the Atacama Desert in Chile. This is the site for the current and upcoming experiments discussed in this thesis. The telescopes focus light into cryogenic receivers, which cool a series of filters, lenses and optical couplings as well as arrays of low-temperature detectors to measure the light. The signals are read out using multiplexed readout schemes depending on superconducting devices. In the upcoming chapters, some of this instrumentation is discussed in detail. In Chapter 2, cryogenic testbeds to test and deploy these detectors and readout components are presented. In Chapter 3, the fabrication process for transition edge sensors (TESes) for the Simons Observatory and CMB-S4 is informed through laboratory tests of films and devices. In Chapter 4, magnetic sensitivity measurements of TESes and readout superconducting quantum interference devices (SQUIDs) are presented to motivate the magnetic shielding designs for upcoming cryogenic receivers. And in Chapter 5, results from measurements with the Atacama Cosmology Telescope serve as an example of the SZ effect science that can be done using measurements with these superconducting devices.

CHAPTER 2

CRYOGENIC RECEIVER DESIGN

In order to achieve high signal-to-noise measurements of the microwave sky with high mapping speed (a large number of low-noise detectors), cameras need to be designed with cold optics, detectors (Chapter 3) and readout components (Chapter 4) that are densely packed. Modularity and ease of upgrade capability are also design drivers, with the benefits of enabling technical upgrades over the observing lifetime of the receiver without requiring changes to mechanical, thermal, or electrical interfaces or lengthy turn-around times. In this chapter, designs for a first-generation science instrument for the Fred Young Submillimeter Telescope (Section 2.1), Prime-Cam (Section 2.2), are presented, along with a first-light receiver and single instrument module testbed, Mod-Cam (Section 2.3).

2.1 The Fred Young Submillimeter Telescope

The Fred Young Submillimeter Telescope (FYST) is a 6-meter aperture telescope operating from sub-mm to mm wavelengths, currently being built by the CCAT-prime collaboration[1] at 5600 meters elevation on Cerro Chajnantor in the Atacama Desert in northern Chile [233, 251]. Its novel crossed-Dragone optical design will deliver a high throughput, wide field of view capable of illuminating much larger arrays of sub-mm and mm detectors than existing telescopes. First light is expected in early 2023 with Mod-Cam (Section 2.3), a single-instrument module testbed for Prime-Cam (Section 2.2). Prime-Cam will house up to seven

[1]CCAT-prime is an international consortium including researchers from the USA, Canada, Germany, and Chile. www.ccatobservatory.org

instrument modules in a 1.8 meter diameter cryostat, cooled by a dilution refrigerator. The instrument modules can be individually optimized for particular science goals, and will each house metal mesh and alumina filters along with silicon lenses as the refractive optical elements. Planned broadband, polarimetric surveys at five different frequency bands (220, 280, 350, 410, and 850 GHz) along with simultaneous spectroscopic surveys (with $R \sim 100$ from 210 to 420 GHz) will take advantage of FYST's wide field-of-view, low emissivity, and exceptional atmospheric conditions [233, 251, 78]. This wide range of frequencies will allow excellent characterization and removal of galactic foregrounds, which will enable precision measurements of the sub-mm and mm sky. Prime-Cam will be used to constrain cosmology via the Sunyaev-Zel'dovich effects (Section 1.2), map the intensity of [CII] 158 μm emission from the Epoch of Reionization, measure cosmic microwave background polarization and foregrounds, and characterize the star formation history over a wide range of redshifts.

2.2 Prime-Cam

Much of the work presented in this section has been published in E. M. Vavagiakis et al. "Prime-Cam: A first-light instrument for the CCAT-prime telescope," Proc. SPIE 10708:107081U (2018) [260].

As the first-generation science instrument for the FYST, Prime-Cam will enable unique observations that address astrophysical questions ranging from the physics of star formation to Big Bang cosmology. Prime-Cam will simultaneously cover five bands spanning 220 to 850 GHz [55].

The wavelength coverage, sensitivity, spatial resolution, and large field of

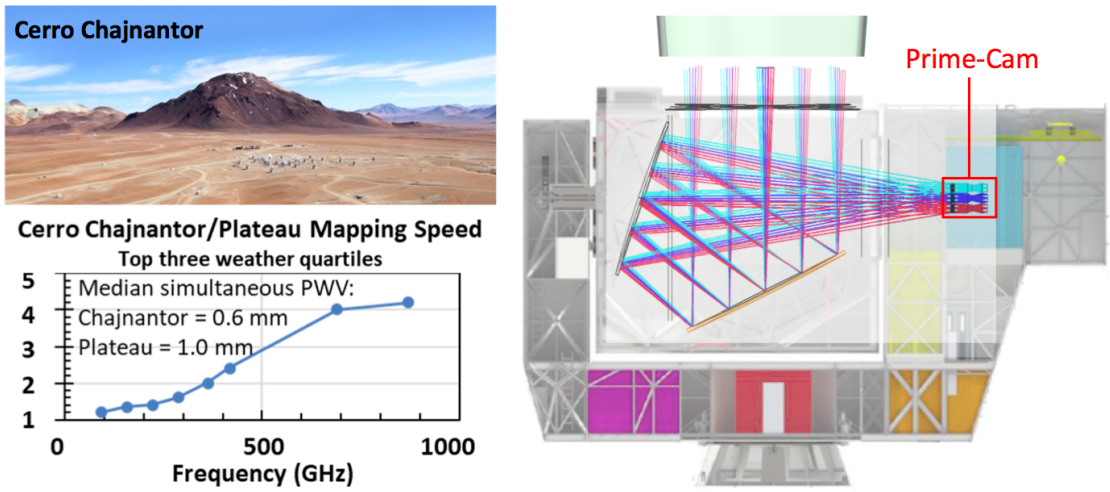

Figure 2.1: *Left*: A photo of the CCAT-prime site, Cerro Chajnantor, and the improvement in sub-mm mapping speed expected at 5600 m relative to that of the ALMA Plateau [202]. *Right*: A cross-section of the FYST including the optics focusing onto the detector arrays of Prime-Cam, which sits in the telescope receiver cabin. Figure is from [260].

view (FoV) of Prime-Cam on the FYST allow for a set of wide-area surveys (between 5 and 15,000 $\deg^2$) to be conducted in order to address the following scientific goals:

1. Trace the formation and large-scale three-dimensional clustering of the first star-forming galaxies during the Epoch of Reionization through wide-field, broadband spectroscopy [148];
2. Constrain dark energy and feedback mechanisms by measuring the physical properties and distribution of galaxy clusters via the Sunyaev-Zel'dovich (SZ) effects (Section 1.2) on the CMB [168, 27];
3. Enable more precise constraints on inflationary gravity waves and light relics by measuring polarized CMB foregrounds and Rayleigh scattering [7, 20];
4. Directly trace the evolution of dusty-obscured star formation in galaxies

since the epoch of galaxy assembly, starting > 10 billion years ago [206].

At first light, Prime-Cam will deploy three modules, a subset of its seven module capacity, installed in a single cryostat. A module for a 280 GHz MKID array (detailed in Section 2.2.2) is currently under construction, and its design is presented in Section 2.3.4. An 860 GHz module and KID array [52], enabled by the very low precipitable water vapor at the CCAT-prime site, will begin the short wavelength early science. The module will be compatible with Mod-Cam, as all Prime-Cam modules are. A third upcoming instrument module for Prime-Cam, the Epoch of Reionization Spectrometer (EoR-Spec) module, will contain a Fabry-Perot Interferometer (FPI) and have spectroscopic capabilities over 210 to 420 GHz. EoR-Spec is described in Section 2.2.4.

The Prime-Cam receiver design is shown in Figure 2.4. The cryostat details and three initial instrument modules designed for first-light observations are discussed in the following sections.

2.2.1 Optics

The modularity of Prime-Cam enables each optical path to be independently optimized for the science requirements of each instrument module (Figure 2.3). Each module within the Prime-Cam receiver contains a series of anti-reflection coated silicon optics, blocking filters, Lyot stop, and focal plane. The module optics are designed to provide diffraction-limited (or near diffraction-limited) image quality across a wide FoV. This instrument module approach has been developed from the ACTPol model [253, 179] in collaboration with the Simons Observatory, which is building a receiver with 13 optics tubes that will all be

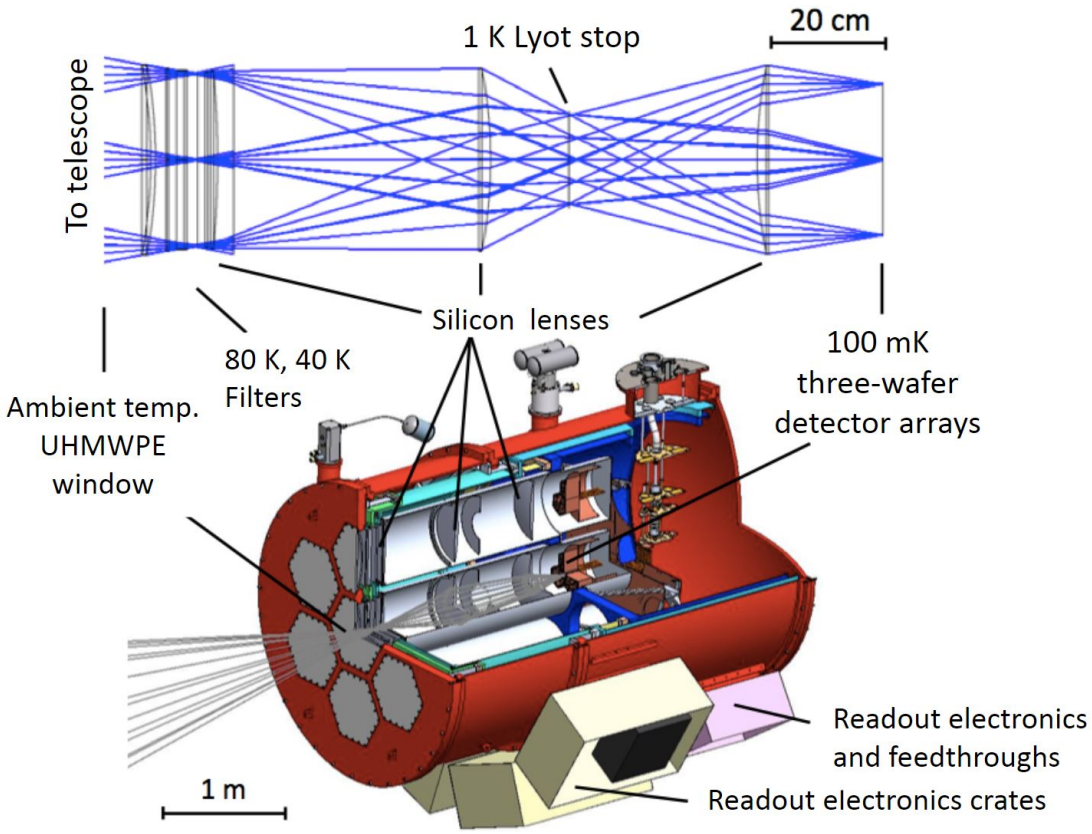

Figure 2.2: Summary of Prime-Cam's optical design. *Top:* Instrument module optics designs provide diffraction-limited image quality across a wide field of view. Cryogenic silicon lenses offer excellent optical performance at these wavelengths. We have previously deployed silicon metamaterial AR coatings with <1% reflection across an octave of bandwidth [63, 97]. *Bottom:* Preliminary design of the Prime-Cam instrument with three first-light instrument modules shown (two in cross-section). See Section 2.2.5 for Prime-Cam instrument mechanical design details. Figure is from [260].

used for broadband detection between 20 and 300 GHz [270, 273, 94, 272].

Several different sizes of optics tubes were studied before converging on the approximately 0.4-m diameter optics tubes, each capable of illuminating three 150-mm detector wafers, used in Prime-Cam. The sizes studied ranged from approximately 0.2-m diameter optics tubes, each illuminating single 150-mm detector arrays, to 0.6-m optics tubes illuminating 7 detector arrays and a single 2-m diameter optics tube illuminating many more detector arrays. In addition

to optical analyses, a sensitivity calculator that included estimates of the loss and emission of each component was used to compare all the configurations [124]. The conclusion of these analyses was that several configurations could provide similar mapping speeds, although, the image quality degrades as the optics tube diameter increases. The 0.4-m diameter optics tube design provides a practical balance between good image quality, high throughput and mapping speed, modularity, manufacturability, and the ability to upgrade with new optics tubes. These qualities led the 0.4-m size to be selected for the primary instruments for both CCAT-prime and SO [74].

Ultra-high-molecular-weight polyethylene (UHMWPE) vacuum windows and a series of approximately 6 infrared-blocking and low-pass filters minimize emission and block undesired radiation in the instrument [255]. The telescope focus is transferred to the detector focal plane of each module by three refractive silicon lenses with metamaterial anti-reflection coatings (four lenses for EoR-Spec) [63]. Silicon is the preferred lens material at Prime-Cam's target wavelengths. High resistivity silicon has extremely low loss ($\tan\delta \sim \times 10^{-5}$ at $T < 40\,\mathrm{K}$, where δ is the loss angle), high thermal conductivity (ensuring lens temperature uniformity and limiting detector background loading), and a high index of refraction, $n \simeq 3.4$ [63].

The baseline design for each instrument module is to target illuminating roughly 5.5 m of the 6.0-m aperture telescope, which provides $f/2.6$ at the telescope focus [186]. The selected optics tube size provides an unobstructed 1.3 deg diameter FoV and keeps the size of the entrance window manageable and within current fabrication capabilities.

This full FoV can be focused onto three detector arrays at $f/2.0$ as shown

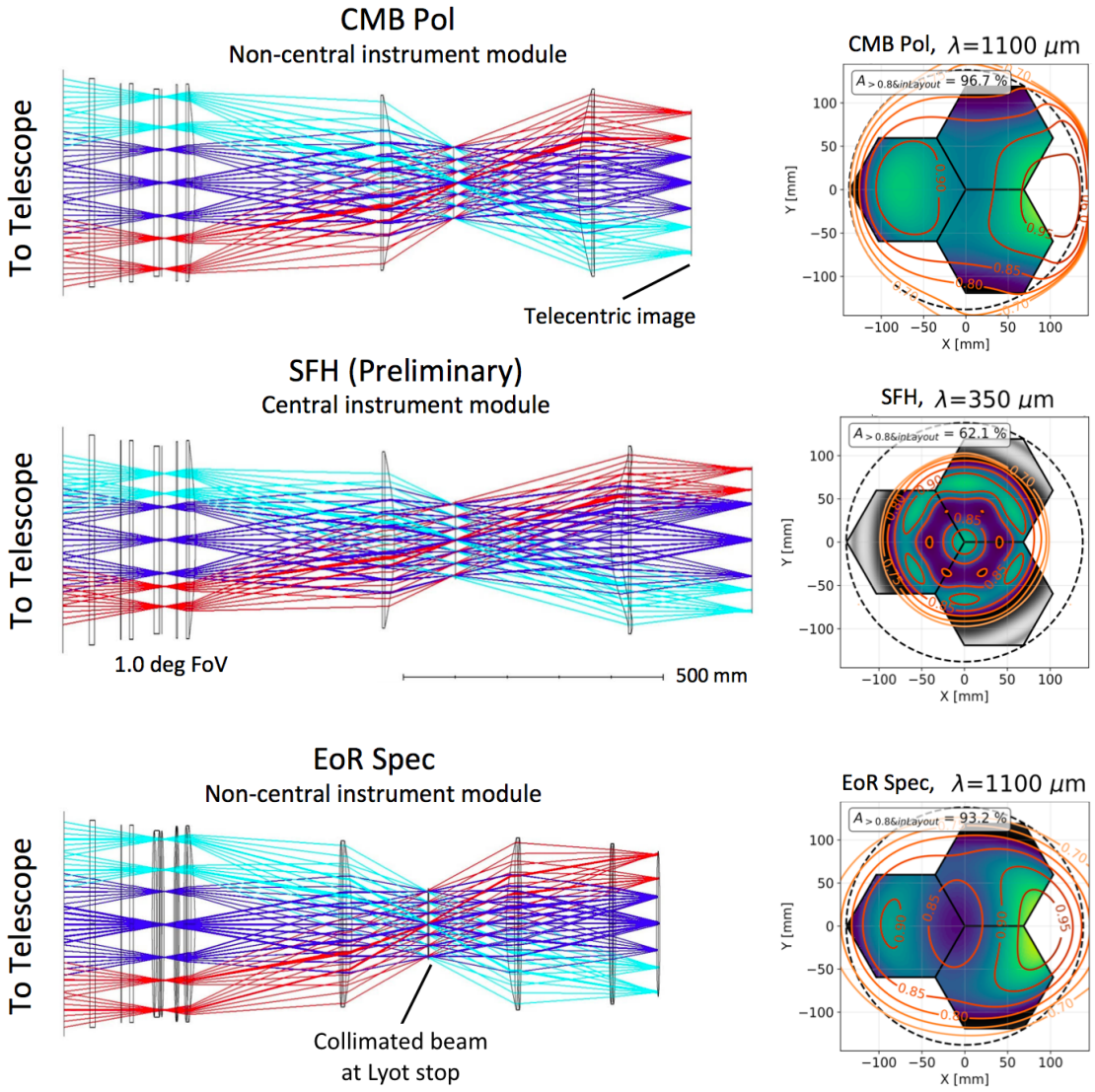

Figure 2.3: Geometrical ray traces for each preliminary optics design for Prime-Cam's three initial instrument modules: the CMB polarization module (CMB Pol); the Epoch of Reionization spectrometer module (EoR-Spec), equipped with an FPI at the 1 K Lyot stop of the module and a four-lens design; and the star formation history (SFH) 860 GHz module, which has a 1.0° diameter FoV instead of the 1.3° diameter FoV of the other modules, providing better image quality at 350 μm. Strehl ratios for each of the optics tubes are shown, with areas corresponding to the fraction of the area with Strehl ratio greater than 0.8 and within a tiled hexagonal pattern at the focal plane of the modules. One rotational degree of freedom, where the angle of the tiled pattern at the focal plane is varied to allow maximum coverage, has the ability to be optimized in the future [96]. Figure is from [260].

in Figure 2.3. This three-lens instrument module optics design was optimized to achieve a telecentric, diffraction-limited image with minimal ellipticity for CMB polarization measurements across a 1.3° diameter FoV [74]. Similar designs have been optimized for use with an FPI, in which a larger optimization weight is given to collimating the light at the Lyot stop so as not to limit the finesse of the interferometer. This approach led to a preliminary design with four lenses instead of three (Figure 2.3) to improve the collimation. For the 860-GHz SFH module, a combination of ray tracing and physical optics calculations are being pursued to optimize the balance between resolution and sensitivity by adjusting the FoV and taking into account practical detector array and feedhorn geometry constraints. At 350 μm, a three lens design with a 1.0° FoV (instead of 1.3°) can provide significantly better (diffraction-limited) image quality. Reducing the FoV changes the effective pixel spacing at 350 μm for the KID arrays, from 1.8 F-λ to 1.4 F-λ, which improves the angular resolution at 350 μm to near the diffraction-limited target of 14″. While the three-lens design would suffice, optimization (including the consideration of a four-lens design) is ongoing for the SFH module to further improve the image quality and resolution.

2.2.2 Detectors

Kinetic Inductance Detectors

The first light array of 280 GHz microwave kinetic inductance detectors (MKIDs) for the CCAT-prime project will be deployed in Mod-Cam (Section 2.3) on the Fred Young Submillimeter Telescope (Section 2.1). Compared to TESes, MKIDs have the advantage of simpler fabrication and readout. While MKIDs

are a less mature technology than TESes, their performance in laboratory measurements and millimeter-wave experiments combined with their relative simplicity makes them an attractive candidate for future surveys.

KIDs, like TESes, rely on the principle of superconductivity. When photons hit the superconducting material of a KID, they break the Cooper pairs in the material, creating excess quasiparticles that change the inductance of the superconductor. This superconducting inductor is combined with a capacitor to form a microwave resonator, such that the increased kinetic inductance from photon absorption registers as a signal via a shift in the resonant frequency. The energy and arrival time of the incident photons can be reconstructed by recording the frequency shifts in this resonance. [166].

Because of this effect, while TESes are read out using time-division multiplexing (TDM) or frequency-division multiplexing (FDM) using SQUID amplifiers, MKIDs do not require any additional cold multiplexers. Because MKIDS are resonators in and of themselves, they can be intrinsically frequency-multiplexed by tuning the individual resonator parameters during fabrication. This feature relegates the majority of the readout complexity to room temperature electronics, leaving RF lines, attenuators, and low noise amplifiers at the cryogenic stages, rather than the SQUID readout components required for TESes [78].

First Light Array

At first light on the FYST, we will deploy Mod-Cam's (Section 2.3) instrument module currently under development (Section 2.3.4) with at least one

280 GHz MKID array operated at 100 mK. Additional detector arrays and instrument modules are under development for deployment simultaneously or shortly after this 280 GHz module in Prime-Cam, including an additional broadband module centered on 850 GHz, and the spectrometer module EoR-Spec [78, 122, 58]. KIDs increase the number of detectors in the EoR-Spec module by a factor of 2 over TESes, approximately doubling the mapping speed, although they will need to be optimized for the low loading conditions of the spectrometer [58].

The initial 280 GHz MKID array for Mod-Cam contains 3,456 feedhorn-coupled, polarization-sensitive TiN MKIDs on a hexagonal 550-μm thick, 15 cm diameter silicon-on-insulator wafer [78]. The feedhorn array, including all choke structures, is being machined out of aluminum based on a spline profile [23]. The array is optimized for background-limited observations at 280 GHz with a ~60-GHz wide band [56]. Fabrication of the first array was recently completed by the Quantum Sensors Group at the National Institute of Standards and Technology (NIST) in Boulder, CO, and designs drew heavily on the heritage from the BLAST-TNG [75, 95] and TolTEC [23, 24] receivers. The first light array resonators share the same design as the 280 GHz detectors designed for TolTEC, with minor adjustments in the absorber geometry to account for CCAT-prime's slightly lower atmospheric loading [78].

Scaling from the first light array design and assuming a multiplexing factor of ≤580 per microwave feedline, when the seven tubes are fully populated, Prime-Cam will house 60,000 polarimetric KIDs at 220/280/350/410 GHz, 31,000 KIDS at 250/360 GHz coupled with FPIs 2.2.4, and 21,000 polarimetric KIDs at 850 GHz. These figures include detector spacings at $\geq 1.1F\lambda$.

Optimization studies of different frequency bands are ongoing to hone these designs in order to maximize science returns [55].

2.2.3 Readout Electronics

Readout electronics for both testing and deploying the 280 GHz MKID array will feature a reconfigurable FPGA-based design. The 280 GHz array (Section 2.2.2) contains 6 networks, each requiring 576 resonators (Section 4.1.2) between 500 MHz and 1 GHz to be read out with a single RF feedline.

Our current readout approach is evolving from the second generation Reconfigurable Open Architecture Computing Hardware (ROACH-2), including firmware developed for BLAST-TNG [102] and TolTEC [78]. This approach presents challenges in scaling up to the full deployment of Prime-Cam with 21 KID arrays. Since each ROACH-2 system requires about two units of rack space and 100 W of power, and a single array requires six individual ROACH-2 systems, it would prove difficult to deploy the necessary number of ROACH-2 systems for a fully populated instrument, even if multiplexing factors could be significantly improved. Because of this challenge, work towards porting the ROACH-2 firmware to the Xilinx ZCU111 RFSoC evaluation board [226] is ongoing. These next generation systens would be capable of reading out $\sim 5,000$ KIDs, which would enable significant reductions in readout hardware requirements [78, 55].

2.2.4 Epoch of Reionization Spectrometer

One instrument module for Prime-Cam will contain a spectrally/spatially multiplexing Fabry-Perot Interferometer (FPI): the Epoch of Reionization Spectrometer (EoR-Spec) module. EoR-Spec is designed to measure the 158 μm [CII] line intensity from galaxies at redshifts between 3.5 and 8 (observed frequency from 210 to 420 GHz) [58].

The epoch of reionization (EoR) is a yet poorly understood period of the universe's evolution ($\sim 6<z<11$) during which the neutral hydrogen in our universe began to be re-ionized by the ultraviolet light of star formation and/or black hole accretion. Understanding this process of reionization requires probing a multitude of faint sources, which are difficult to detect individually. EoR-Spec will overcome this challenge by measuring the spatial fluctuations of large-scale structure spectroscopically at low spatial resolution, using spectral [CII] line imaging of the aggregate signal (line intensity mapping).

By performing this large-scale intensity mapping of the [CII] emission, EoR-Spec will probe cosmology by shedding light on the growth of density fluctuations and the primordial power spectrum. These probes could eventually place constraints on models of inflation, dark energy, and the sum of the neutrino masses with sufficiently high signal-to-noise datasets, which will complement similar constraints through CMB and SZ measurements. Measurements with EoR-Spec will also be complementary with other intensity mapping probes like 21 cm, Hα, H, OIII, Lyα and CO, working in synergy to reveal information about young massive stars, the growth of ionization, the production of metals, and the evolution of reionization bubbles in our universe [58]. Spectroscopic measurements between 210-315 will overlap with the 220 GHz "zero crossing" of

the thermal Sunyaev-Zel'dovich (SZ) effect spectrum to improve SZ measurements (Section 1.2). This will open a new frontier in the SZ spectral separation and extraction of cluster parameters like temperature and peculiar velocities, which will be complementary to our broadband measurements using multiple frequency modules (Section 1.2).

EoR-Spec's cryogenic scanning FPI will rely on metamaterial silicon substrate-based mirrors and operate at a resolving power of 100. Our previous generations of FPIs are based on free-standing metal mesh screens [198, 234, 152, 153, 45, 182, 77, 150], where the screen geometry results in a finesse that is a strong function of frequency ($F \propto \nu^{-2.5\,\mathrm{to}\,3}$). To avoid losses which would limit efficiency over the octave bandwidth of operation we require, we will use the silicon substrate based (SSB) mirror designs developed at Cornell [97, 59]. The FPI will be installed at the Lyot stop of the instrument module (Figure 2.4), which is cooled to 1 K. The optics of the module (Figure 2.2) are optimized to provide a well-collimated beam at the stop. The FPI will be scanned to shift the resonant bandpasses across the three broadband MKID arrays, enabling spectroscopic measurements using two orders of the FPI simultaneously. Fabrication and testing of the FPI and EoR-Spec MKID arrays is underway.

2.2.5 Cryogenics

The Prime-Cam cryogenic receiver will consist of a two-section 6061-T6 aluminum vacuum shell, 1.8 m in diameter, and 2.8 m in length (Figure 2.4). The seven optics tube receiver design has evolved from the larger thirteen tube cryogenic design for the Simons Observatory LATR [94, 272]. Hexagonal UHMWPE

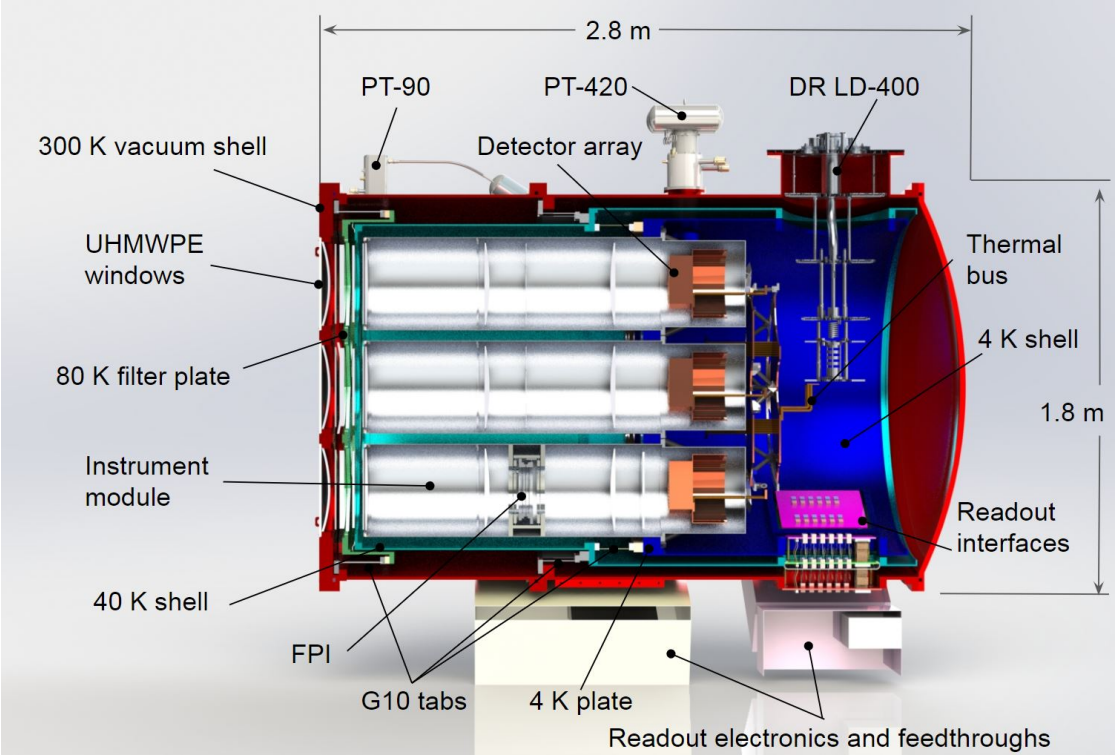

Figure 2.4: A rendered cross section of the Prime-Cam cryogenic receiver design. The two-section 6061-T6 Aluminum vacuum shell is shown in red. An 80 K filter plate and ring is shown in green, followed by a 40 K plate and shell in light blue, a 4-K plate and shell in dark blue, and thermal buses in copper. The temperature stages are supported by a series of G10 tabs. The DR, two pulse tubes, three instrument modules, and detector arrays of the initial three tube deployment are shown. Figure is from [260].

vacuum windows on the front plate will begin the optical chain of the instrument. Within the vacuum shell, several cooling stages provide thermal isolation for the optics tubes and detector arrays. The temperature and stability requirements for the cryostat interior are derived from the requirements for the SO LATR [273, 270, 183, 57]. In addition to the temperature requirements, the cryostat must be mechanically stable under the roughly 0.1-g load encountered during execution of the nominal science scan modes of the telescope.[2]

[2]The design of a small cryogenic testbed preceding Prime-Cam and Mod-Cam is shown in Appendix A.

80 K and 40 K temperature stages will hold optical filters. A short 80 K shield will be located at the front of the receiver. A 40 K shield will surround the interior of the receiver. A series of G10 tabs will support the assembly of thermal shields and provide thermal isolation as well as resilience against mechanical shocks and vibration. Inside the 40 K shield, the three optics tubes for initial deployment will be mounted on the 4 K temperature stage of the cryostat. A 4 K shield will surround the back end of the optics tubes. Cryomech PT-90 and PT-420 pulse tubes, each providing 90 W of cooling power at 80 K (PT-90), 55 W at 40 K (PT-420), and 2 W at 4 K (PT-420), along with a Bluefors LD-400 dilution refrigerator (DR) providing 400 μW of cooling power at 100 mK, will be used to cool the receiver. The PT-90s will be located at the front of the receiver, and will cool the 80 K plate and shield. The PT-420s will be located towards the rear of the cryostat, and will cool the 40 K shield and 4 K plate. The DR will be located at the rear of the cryostat, and will cool the detector arrays to 100 mK and the final optical lenses to 1 K through thermal buses. Around the exterior of the vacuum shell will lie supports for room temperature readout electronics. The fully loaded receiver, including seven optics tubes and all readout components, will weigh about 2.8 metric tons.

2.3 Mod-Cam

The CCAT-prime project's first light array will be tested and deployed in Mod-Cam, a single-module cryogenic testbed for Prime-Cam [260, 55] and first light instrument for the FYST (Figure 2.1). Mod-Cam's 89-cm diameter cryostat (Figure 2.5 described in Section 2.3.1) is cooled by a Bluefors LD-400 dilution refrigerator (DR) and enables efficient swapping of instrument modules by means of

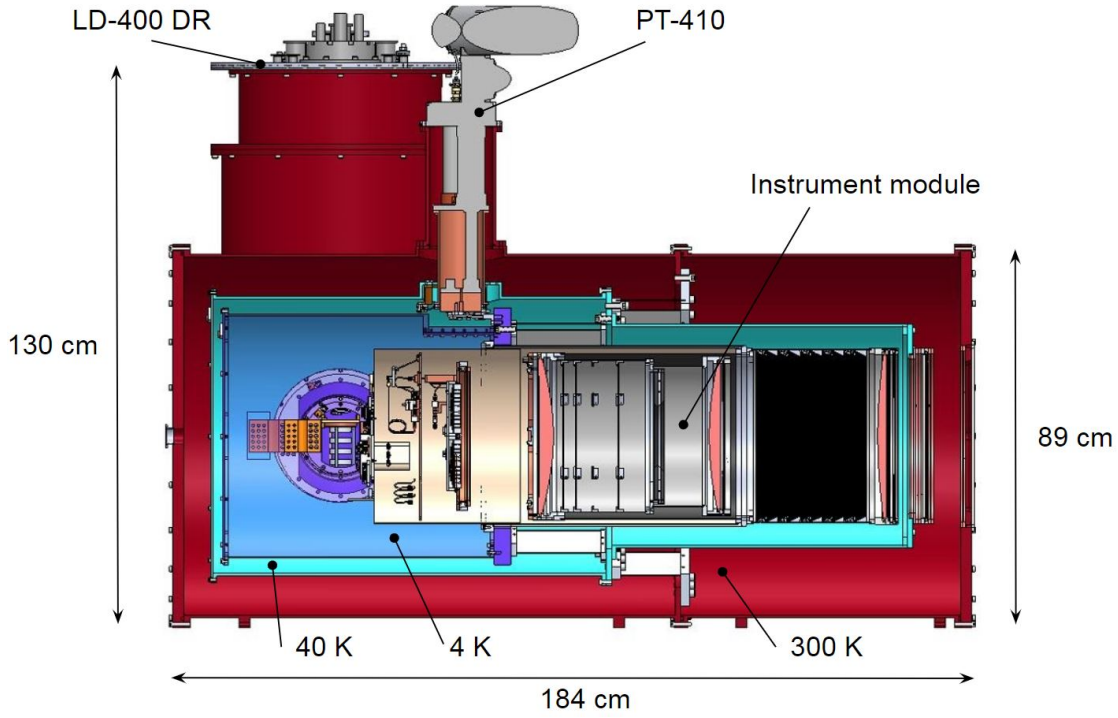

Figure 2.5: Labeled schematic overview of Mod-Cam.

its side-car DR design. The instrument modules are installed from the back of the cryostat and are cantilevered off of the 4 K stage. Each instrument module tested or deployed in Mod-Cam will be optimized for a specific subset of the overall Prime-Cam science goals and be able to hold up to three 100 mK detector arrays along with silicon lenses and filter stacks at 1 K and 4 K.

The modules themselves allow for up to a 36-cm diameter aperture and are based on the optics tube designs for the Simons Observatory's large aperture telescope receiver [260, 272, 74]. In this design, light enters the instrument module after passing through the 300 K ultra-high-molecular-weight polyethylene (UHMWPE) vacuum window and 40 K infrared-blocking filters. The light is additionally filtered by a series of absorbing alumina filters [74], metal-mesh infrared-blocking filters [255], and low pass edge filters to block unwanted ra-

diation, and it is re-imaged onto the focal plane by three meta-material anti-reflection-coated silicon lenses [64].

2.3.1 Cryogenics

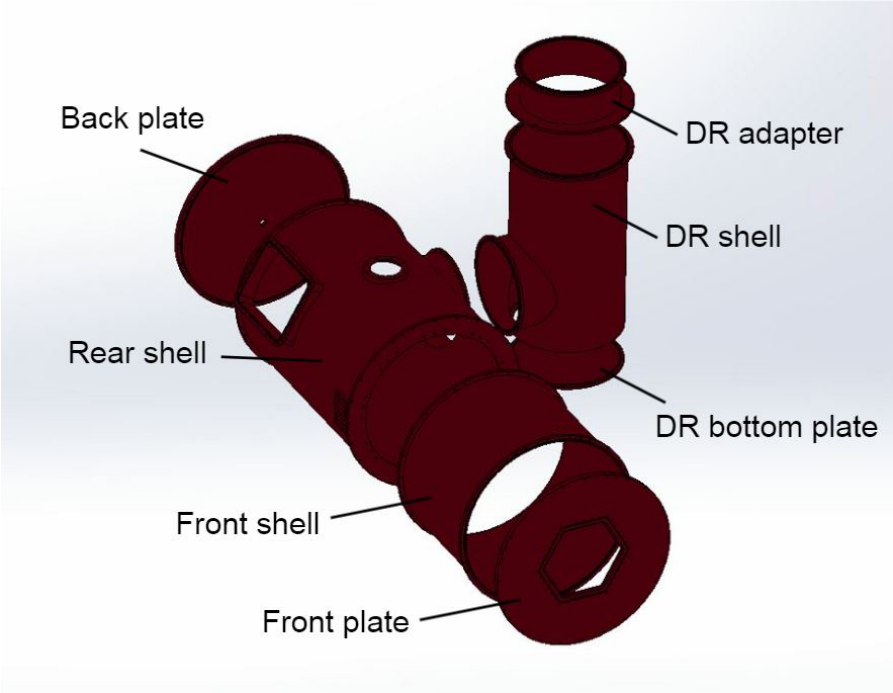

Figure 2.6: An exploded view of the 6061-T6 Al Mod-Cam vacuum shell. The main shells consist of a front and rear shell, a front plate onto which is mounted an UHMWPE window and double-sided infrared blocking filter, and a back plate which includes a vacuum flange. The rear shell includes interfaces for readout plates (rectangular cutout), a pulse tube (top cutout), and the DR shells. The DR shell consists of the main shell, a bottom plate, and an adapter to mate to the Bluefors 300 K DR plate.

Mod-Cam is designed to serve as a scaled-down version of the much larger Prime-Cam cryostat (Section 2.2.5) for significantly faster testing of individual instrument modules prior to deployment. It has an 89-cm diameter exterior aluminum vacuum shell (Figure 2.6), along with additional aluminum shells

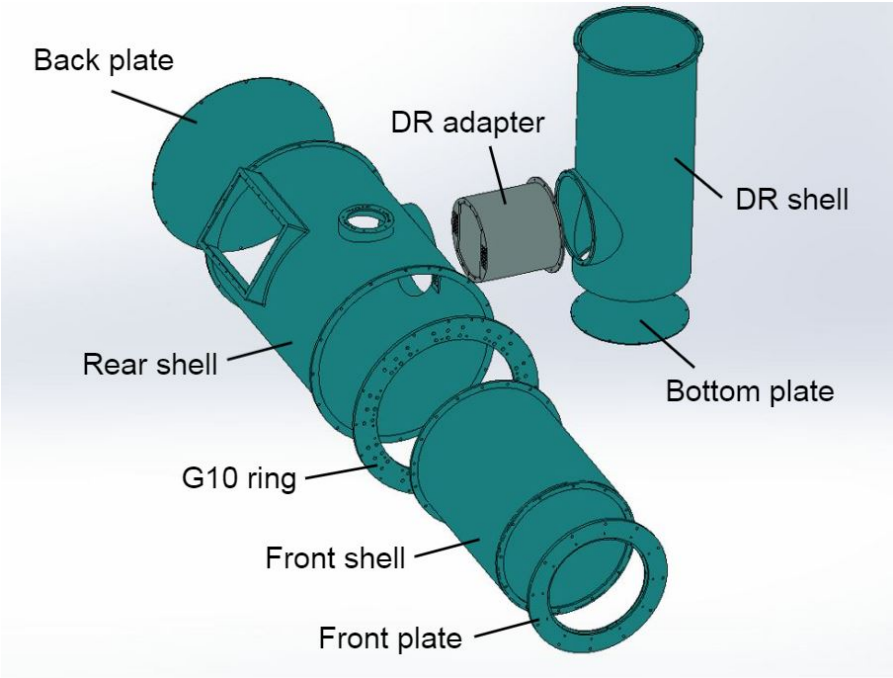

Figure 2.7: An exploded view of the 40 K Mod-Cam shells and plates. All are fabricated of 6063-T5 Al except for the DR shell bottom plate. The front plate mounts a filter stack including double-sided infrared blockers and an alumina filter. The front and rear shells mount to the G10 ring which supports the 40 K main shells from the 300 K shell and the 4 K shells from the 40 K shells (Figure 2.9). The rear shell includes interfaces for readout plates (rectangular cutout), a pulse tube 40 K thermal connection (top cutout), and the 40 K DR adapter and potential thermal connection. The 40 K DR adapter is mounted onto the DR shell, which is mounted on the 40 K shell of the Bluefors DR. When the DR shells are connected to the main shells, the 40 K DR adapter floats in the side cutout of the rear shell, and its position is offset due to predicted thermal contractions in order to be centered when cold (Section 2.3.3).

at 40 K (2.7) and 4 K (2.8) supported by a series of G10 tabs (Figure 2.9). The cryostat was fabricated by Precision Cryogenics. A model of the LD-400 300, 40, and 4 K plates was designed and fabricated to ensure the alightment of the DR shells with the main Mod-Cam shells. The side-mounted DR can provide cooling to the 40 and 4 K stages, and/or an optional Cryomech PT-420 or PT-410 (currently installed) pulse tube can provide cooling power at 40 K and 4 K,

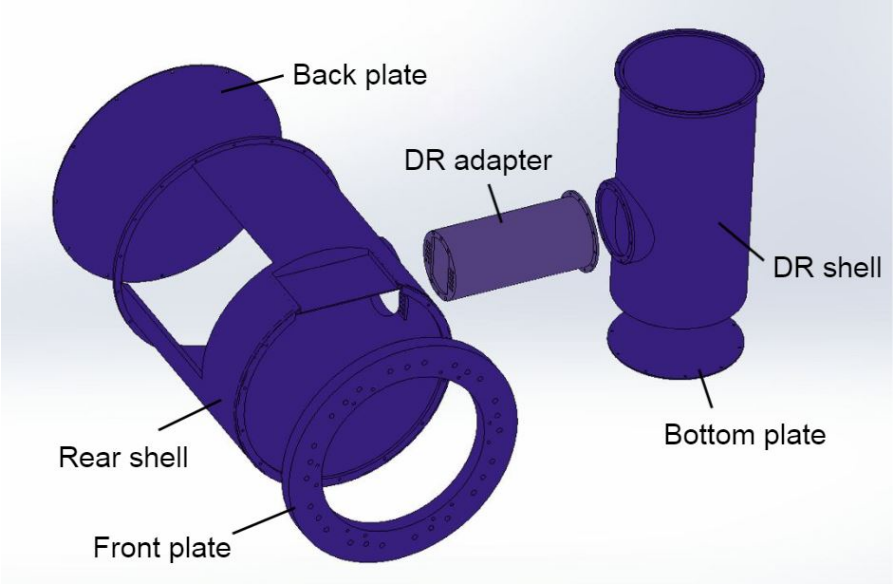

Figure 2.8: An exploded view of the 6061-T6 Al 4 K Mod-Cam shells and plates. The front plate is mounted onto the 40 K G10 ring through a pattern of G10 tabs (Figure 2.9). The instrument module (Figure 2.12) is mounted through the rear of the 4 K shell onto the front plate. The 4 K stage of a pulse tube is accommodated by a recess in the 4 K shell and thermally couples to the 4 K plate. The rear shell includes interfaces for readout plates (rectangular cutout) and the 4 K DR adapter and potential thermal connection. The 4 K DR adapter is mounted onto the DR shell, which is mounted on the 4 K shell of the Bluefors DR. When the DR shells are connected to the main shells, the 4 K DR adapter floats in the side cutout of the rear shell, and its position is offset due to predicted thermal contractions in order to be centered when cold (Section 2.3.3).

through custom OFHC braided straps from TAI[3] or from straps made in house. In the preliminary testing reported in Section 2.3.5, the only custom thermal strap is a clamped OFHC copper strip assembly between the 40 K PT-410 stage and the 40 K rear shell.

All thermometry and RF signals are read out through a custom modular harness that is installed on the opposing side to the DR. The modularity of the harness design allows for flexible and upgradable readout options. This ar-

[3]https://www.techapps.com/

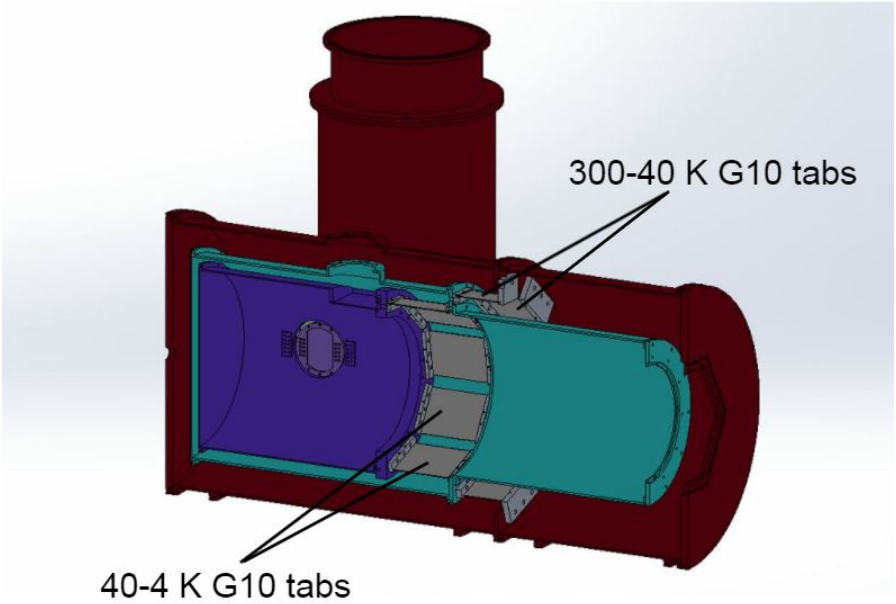

Figure 2.9: The G10 tabs, 9 in each circular pattern, which support the 4 (purple) and 40 K (light blue) stages of the Mod-Cam main shells while thermally isolating them from one another. The tabs are of the same geometry used in Prime-Cam and in the LATR [273] and are comprised of G10 rectangles epoxied into aluminum mounting feet.

rangement is what leaves the rear of Mod-Cam relatively clear for removal of both individual detector arrays and entire instrument modules. The first optics module for Mod-Cam is discussed in Section 2.3.4. The mounting scheme for the first light MKID array and readout components is currently being designed. The thermometry plan for Mod-Cam is presented in Section 2.3.2.

2.3.2 Thermometry

The thermometry plan for Mod-Cam involves 18 temperature sensors distributed through the cryostat at important thermal interfaces, locations on plates and shells to probe potential gradients, and within the instrument modules to

Stages	Thermometers
40 K	6
4 K	7
1 K	2
100 mK	3
Total	18

Table 2.1: Planned number of thermometers for each stage in Mod-Cam. Six 40 K thermometers will measure temperature at the 40 K PT stage, 40 K DR adapter, and across the 40 K shells and plates. Seven 4 K thermometers will measure temperature at the 4 K PT stage, 4 K DR adapter, 4 K instrument module components, and across the 4 K shells and plates. Two 1 K and three 100 mK thermometers will measure temperatures in the instrument module. Cernox sensors will be used at 1 K and above, while ROXs will be used at 100 mK.

monitor temperatures. The number of sensors at each temperature stage is presented in Table 2.1. Cernox[4] 1080 thin film resistance cryogenic temperature sensors are selected for the 40 K stage, Cernox 1050 for the 4 K stage, Cernox 1030 for the 1 K stage, and Ruthenium oxide sensors (ROXs) for the 100 mK stage. While testing in the lab, LEMO connectors are used for four-lead sensor measurement and read out using Lakeshore resistance bridges. Custom cables for the thermometry will be acquired for deployment.

2.3.3 Shell Thickness

The temperature gradient along the 40 K DR shell (Figure 2.7), which mounts to the 40 K DR plate, is estimated to determine the thickness of the shell walls.

The original design of the 40 K DR shell included 6061-T6 Al (with a thermal conductivity at 40 K of 52 W/m·K) and a thickness of 0.25". The length of the shell is 36.7 inches, and the cross-sectional area of the shell in meters if is 0.008

[4]shop.lakeshore.com/temperature-products/temperature-sensors/cernox.html

m^2. The power of the PT-420, which cools the 40 K DR plate coupled to this shell, is 55 W at 45 K. To estimate the radiative loading on the shell (for more details see Appendix A), we assume the view factor to be unity, the 300 K shell is a blackbody with emissivity $\epsilon = 1$, the 40 K shell is a grey body with $\epsilon = 0.07$ and that a 20 layer wrapping of MLI produces a factor of 3 reduction in the 40 K emissivity [101]. The estimated radiative loading on the 40 K shell is then

$$W_{300\,K \rightarrow 40\,K} = \sigma A_1 F_{12} \frac{\epsilon_1 \epsilon_2}{\epsilon_1 + \epsilon_2 - \epsilon_1 \epsilon_2} (T_1^4 - T_2^4) = \boxed{13\text{W.}} \tag{2.1}$$

This loading leads to an estimated gradient between the ~45 K top of the DR shell and the bottom of the DR shell of

$$13\text{W} = \frac{k}{l} A (T_2 - T_1) \rightarrow T_2 = \boxed{73\,\text{K.}} \tag{2.2}$$

With a thinner, 0.19 inch thick shell, $T_2 = 82$ K. To reduce this gradient, the material choice of 6063-T5 Al was motivated, which reduces T_2 to 52 K, balancing a reduction in gradient with a desire for ease of fabrication with the thinner shell. The thermal conductivities of the other parts in the 40 K chain were estimated and compared to the conductivity of the 40 K DR shell, such that no thickness was reduced enough to drop the part conductivity below 20% better than this lowest conductivity part in the chain. A similar approach was taken to define the thicknesses and Al alloys for the 4 K thermal chain.

Thermal Contraction Estimate

Due to the sidecar design of the DR shells, a thermal contraction estimate was necessary to design the position of the DR 40 and 4 K shells relative to the 40 and 4 K main shell mating flanges. As the shells contract as they cool, the flanges on the DR shells will move upward towards the DR cold plates, and the corresponding openings in the 40 and 4 K main shells will move towards the window of the receiver. The positions of the elements contracting are shown in Figures 2.10 and 2.11.

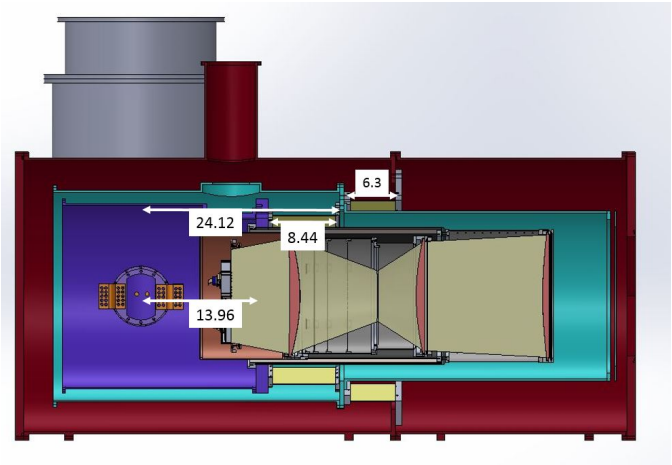

Figure 2.10: The 40 K DR shell (light blue) and the 4 K DR shell (purple) are subject to contraction towards the DR plates. The distances to the center of the 40 and 4 K DR adapters extending into the main shells of Mod-Cam are labeled in inches.

From [83], at 4 or 40 K, $\Delta L/L(\%)_{\mathrm{Al}} = 0.4$ and $\Delta L/L(\%)_{\mathrm{G10}} = 0.75$. Considering the annotated distances in Figures 2.10 and 2.11, and assuming the 300-40 K G10 tabs contract half as much due to the thermal gradient, the vertical/horizontal offset for the 40 K adapter is designed to be 0.11"+0.10" clearance/0.12"+0.10" clearance, and the vertical/horizontal offset for the 4 K adapter is designed to be 0.06"+0.10" clearance/0.14"+0.10" clearance. These offsets are built into the

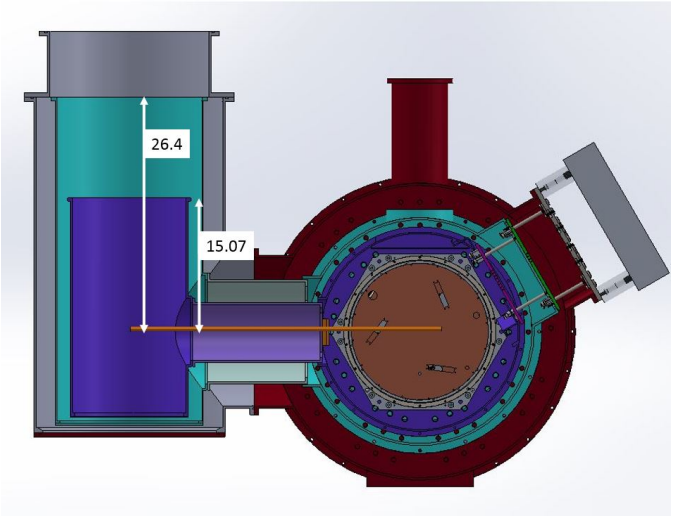

Figure 2.11: The cutouts in the 40 (light blue) and 4 K (purple) main shells through which the 40 and 4 K DR adapters extend are subject to contraction towards the center of the main shells. The critical dimensions for this contraction are annotated in inches.

mechanical design, such that when cold, the DR adapters should be centered in the cutouts in the main 40 and 4 K shells of Mod-Cam.

2.3.4 280 GHz Instrument Module

The first instrument module designed, assembled and tested in Mod-Cam will be the 280 GHz module, which will house the first MKID array for the project, described in Section 2.2.2 and [78]. The instrument module designs are based off of the optics tube designs for the Simons Observatory LATR [270, 273], and are self-contained assemblies of filters, lenses, and detector arrays, mounted on the 4 K plate of Mod-Cam (and compatible with Prime-Cam) at and below 4 K. Each module is approximately 40 cm in diameter and 130 cm long, and mounts through the rear of Mod-Cam, requiring minimal dissasembly of the cryostat. A schematic of an instrument module and its components is shown

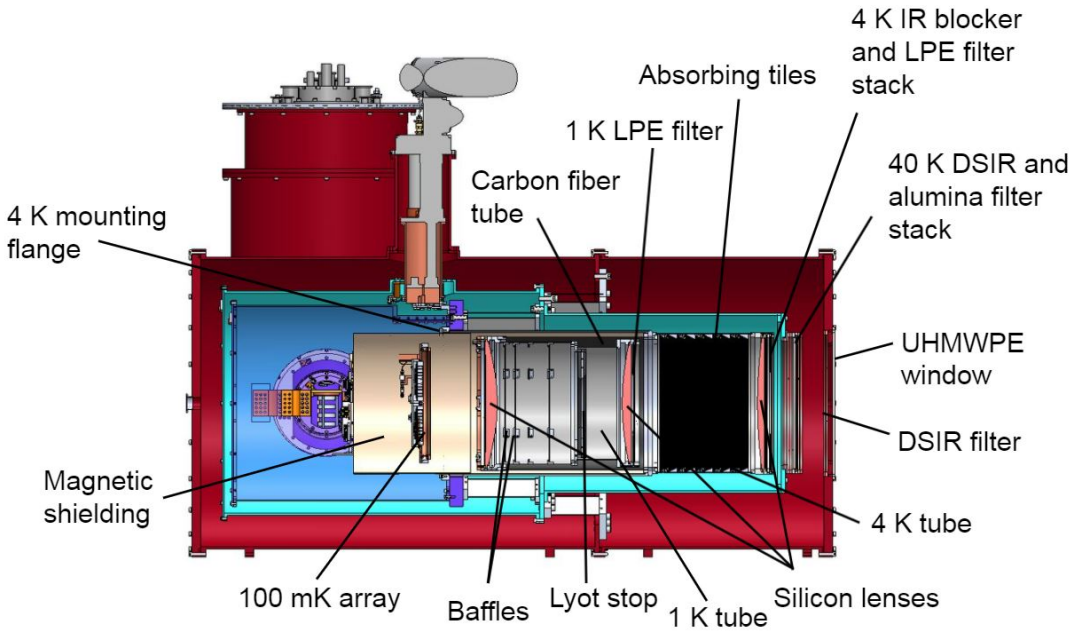

Figure 2.12: A schematic of an instrument module inside of Mod-Cam. The module is inserted through the rear of the main shells (left), and mounts to the 4 K plate. A series of infrared blocking and low pass edge filters are installed on the 300 K and 40 K front plates (right) where light enters the module, as well as in the 4 K and 1 K instrument module lens cells. A series of metamaterial coated silicon lenses focus the light from the telescope onto the 100 mK detector array. The array and cold readout components will mount to the 1 K tube (not shown). Metamaterial absorbing black tiles and baffles [272] line the interior of the 4 K and 1 K tubes. The Lyot stop at 1 K is labeled. A carbon fiber tube suspends the 1 K module components from the 4 K tube. Magnetic shielding at 4 K surrounds additional shielding at 1 K (not shown) to protect the detectors and cold readout components from spurious fields (Chapter 4). The first instrument module for Mod-Cam is currently being designed and fabricated.

in Figure 2.12. The 4 K stage of the instrument modules is cooled through the thermal and mechanical coupling to the 4 K plate of Mod-Cam (or Prime-Cam), and the components at 1 K and below are cooled by the 1 K and 100 mK stages of the LD-400 DR. The 280 GHz module is currently being fabricated at Cornell. Other modules for Prime-Cam currently in development include the EoR-Spec module [52] and 860 GHz module [122].

Stage	40 K [W]	4 K [W]	1 K [mW]	100 mK [μW]
Shell radiation	9.4	0.07	0.002	0.2
Support structure	3.6	0.12	0.755	16.1
Wiring	5.4	0.29	0.121	3.1
Beam radiation	11.8	0.03	0.029	31.2
Total	28.4	0.51	0.907	50.6
Available power	95	3	24	400

Table 2.2: Loading estimates for each stage of Mod-Cam from each source estimated. The cooling power at 40 K and 4 K is supplied by a PT-420 and backup PT-410, and the cooling power at 1 and 0.1 K is supplied by the DR still and mixing chamber stages respectively. Our estimated cooling power is more than sufficient to meet our estimated needs at all stages for an SO-style instrument module.

2.3.5 Status and Laboratory Testing

In considering the thermal loads for Prime-Cam and Mod-Cam, we scaled from the SO LATR thermal model [273]. This thermal model combines material properties and radiation estimates with custom Python estimates of the optical filter elements. The thermal loading estimates for Mod-Cam are presented in Table 2.2.

Mod-Cam is currently assembled in the lab and undergoing initial rounds of testing (Figure 2.13). After successful vacuum tests, cooldowns were run in a number of configurations to test the thermal performance of Mod-Cam's 40 and 4 K stages, as well as the DR performance. As a first step towards a thermal model, a rough three-block model to begin cooldown time estimates is presented. Heat applied to the 40 and 4 K stages informs our estimates of the thermal conductivities of the system, and the results of those initial measurements are shown in this section.

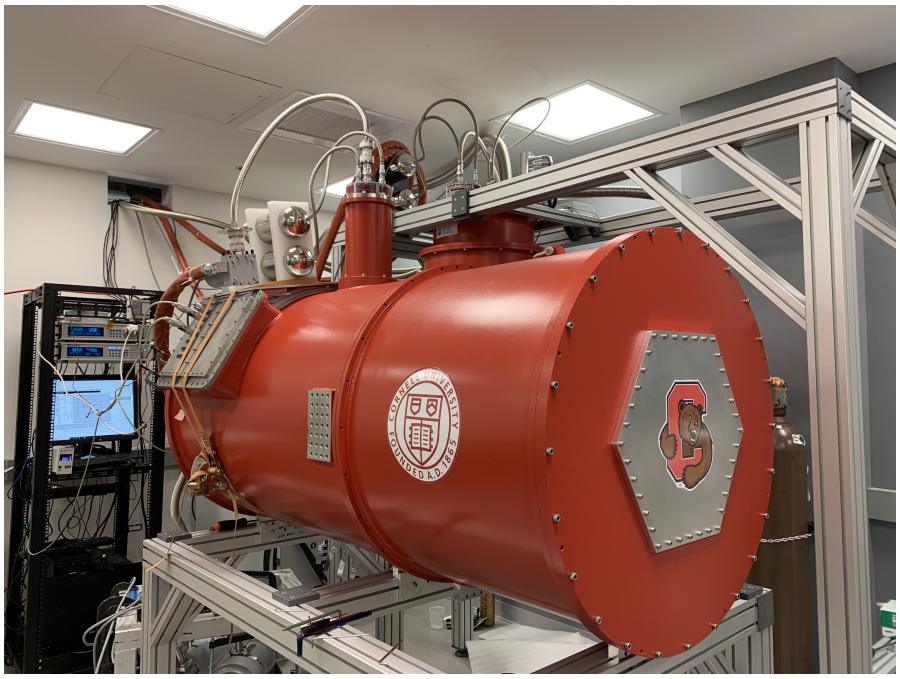

Figure 2.13: The current status of Mod-Cam at Cornell. Cryogenic tests are performed using an LD-400 DR and PT-410.

DR Performance

The performance of the LD-400 was tested in the configuration with the PT-410 coupled to the 40 and 4 K main shells of Mod-Cam, and the 40 and 4 K DR adapters uncoupled such that the DR was not cooling the main shells. this configuration is of interest to study because we might be able to cool only the 1 K and 100 mK instrument module components with the DR if the backup PT can handle the 40 and 4 K shell cooling. DR load curves were taken, and shown in Figure 2.14. In this configuration, the DR mixing chamber achieves over 400 μW of cooling power at 100 mK, which is more than sufficient for one LATR-style instrument module [270]. Load curves will be taken again in future configurations to test this performance.

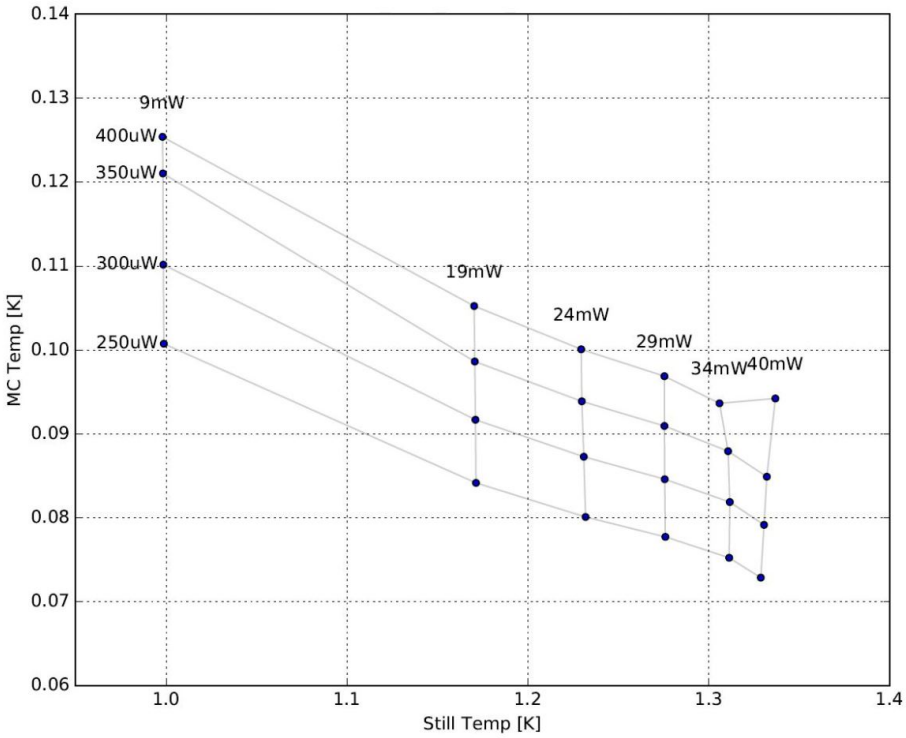

Figure 2.14: Load curves with the LD-400 DR show the temperature of the mixing chamber plate and still plate with various applied still and mixing chamber powers. We achieve over 400 μW of cooling power at 100 mK in the configuration without thermal coupling between the DR shells and the Mod-Cam main shells.

A Three-Block Thermal Model

As a first step towards a cooldown model for Mod-Cam, and a check of our assumed conductivities and capacities, we adopted a rough three-capacity model for the 40 K Mod-Cam shell and compared it with measurements from our first cooldown of the shell (Figure 2.15). We assume that the bath temperature is fixed to the value of the 40 K DR plate at t=0, 63.5 K. From our cooldown logs at this point in time, C1 is taken to be at 175 K, G1 and C2 at 173 K, G2 and C3 at 170 K, and G3 at 135 K (Figure 2.16).

The mass of each capacity block (C1, C2, C3) is estimated using the Solid-

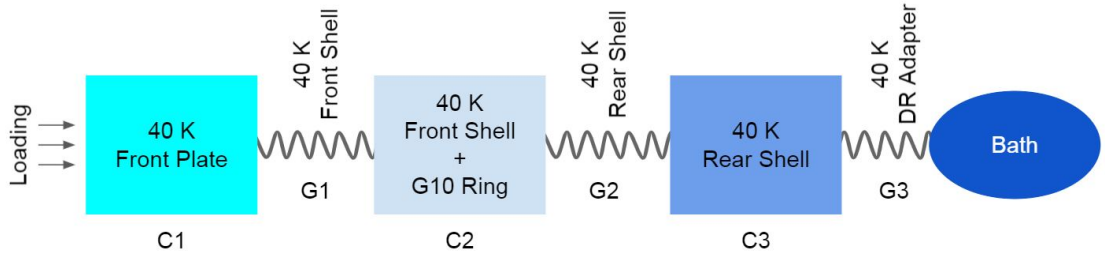

Figure 2.15: Rough three-block model of the Mod-Cam 40 K shell, including three conductivities (G1, G2, G3) and three capacities (C1, C2, C3) as well as loading from 300 K radiation onto the 40 K front plate and the 40 K DR stage bath temperature. Additional loading at C2 is assumed in the model plotted in Figure 2.16.

Works CAD model. Each block is fabricated of 6063-T5 Al. The specific heat capacity of 6063-T5 Al is taken to be 900 J/kg·K.[5] The capacities for each block are then:

$$\begin{aligned} c\rho|_{C1} &= 900\frac{\mathrm{J}}{\mathrm{kg}\cdot\mathrm{K}}\cdot 4\,\mathrm{kg} = 3600\,\mathrm{J/K}, \\ c\rho|_{C2} &= 900\frac{\mathrm{J}}{\mathrm{kg}\cdot\mathrm{K}}\cdot 26\,\mathrm{kg} = 23400\,\mathrm{J/K}, \\ \text{and } \mathrm{c}\rho|_{C3} &= 900\frac{\mathrm{J}}{\mathrm{kg}\cdot\mathrm{K}}\cdot 33\,\mathrm{kg} = 29700\,\mathrm{J/K}. \end{aligned} \tag{2.3}$$

The thermal conductivity of each link is calculated using the equation for low-temperature conductivity of 6063-T5 Al provided by NIST,[6] through

$$\begin{aligned} \frac{\mathrm{kA}}{l}\Big|_{G1} &= k(175.0\,\mathrm{K})\frac{\mathrm{W}}{\mathrm{m}\cdot\mathrm{K}}\cdot 0.015\mathrm{m} = 2.9\,\mathrm{W/K}, \\ \frac{\mathrm{kA}}{l}\Big|_{G2} &= k(173\,\mathrm{K})\frac{\mathrm{W}}{\mathrm{m}\cdot\mathrm{K}}\cdot 0.03\mathrm{m} = 5.9\,\mathrm{W/K}, \\ \text{and } \frac{\mathrm{kA}}{\mathrm{l}}\Big|_{\mathrm{G3}} &= \mathrm{k}(170.0\,\mathrm{K})\frac{\mathrm{W}}{\mathrm{m}\cdot\mathrm{K}}\cdot 0.0035\mathrm{m} = 0.6\,\mathrm{W/K}. \end{aligned} \tag{2.4}$$

[5] http://www.matweb.com/
[6] https://trc.nist.gov/cryogenics/materials/

The loading on the 40 K front plate from the 300 K shell is estimated in the cooldown configuration without MLI installed. We assume that the outer shell is a blackbody with $\epsilon_{\text{shell}} = 1$, the inner 40K shell is a grey body with $\epsilon_{\text{Al}} = 0.07$, the view factor is unity, and the area to be that of the front plate, 0.22 square meters. Then,

$$\begin{aligned} W_{\text{Loading}} &\sim \sigma A_1 \frac{\epsilon_1 \epsilon_2}{\epsilon_1 + \epsilon_2 - \epsilon_1 \epsilon_2} (T_1^4 - T_2^4) \\ W_{\text{Loading}} &\sim \sigma \cdot 0.22\text{m}^2 \cdot 0.07 \cdot (293^4 - 175^4) \sim 26\,\text{W}, \end{aligned} \tag{2.5}$$

where σ is the Stefan-Boltzmann constant. This is an oversimplification of the real geometry due to the potential of radiation entering the MLI layers which are not taped down around the front of the 40 K plate. An additional 10 W of loading on the 40 K shell is adopted into the model ($W_{\text{Loading 2}}$). To estimate the change in temperature of each block over one hour while taking the assumptions outlined above, we solve the following equations:

$$\begin{aligned} \Delta T|_{C1} = (T_{C1_i} - T_{C1}) &= \left(\frac{\text{kA}}{l}\Big|_{G1} (T_{C1} - T_{C2}) - W_{\text{Loading}}\right) \cdot (1\text{ hour}) \cdot \frac{1}{c\rho|_{C1}}, \\ \Delta T|_{C2} = (T_{C2_i} - T_{C2}) &= \left(\frac{\text{kA}}{l}\Big|_{G2} (T_{C2} - T_{C3}) - W_{\text{Loading 2}}\right) \cdot \frac{1}{c\rho|_{C2}}, \\ \text{and } \Delta \text{T}|_{\text{C3}} = (\text{T}_{\text{C3}_\text{i}} - \text{T}_{\text{C3}}) &= \frac{\text{kA}}{\text{l}}\Big|_{\text{G3}} (\text{T}_{\text{C3}} - \text{T}_{\text{bath}}) \cdot (1\text{ hour}) \cdot \frac{1}{\text{c}\rho|_{\text{C3}}}. \end{aligned} \tag{2.6}$$

Solving these equations for T_{C1}, T_{C2} and T_{C3} iteratively in python returns a primitive cooldown model that we can compare with our cooldown plot. The thermal conductivity estimate for C3 was found to be an overestimate when compared to our cooldown data, returning a faster cooldown rate than observed, so G_3 is degraded by a factor of 2 to better compare with the data. This deviation

from expectation may be explained by the inclusion of multiple thermal joints in reality versus in the simple model. The model with degraded G_3 is overplotted on the data in Figure 2.16 and is found to be a rough estimate for the observed cooldown rate.

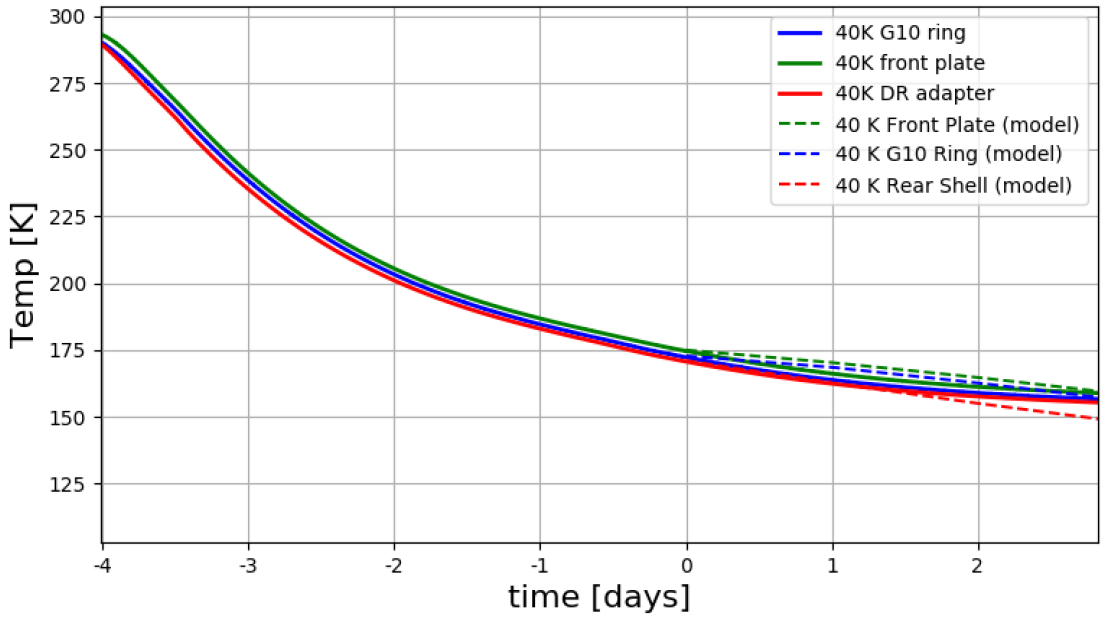

Figure 2.16: Cooldown plot from the first Mod-Cam cooldown along with three-block model cooldown estimates. At t=0, the 40 K DR stage was at 63.5 K, and the temperatures of the other stages are recorded for the model (Figure 2.15). The model includes 26 W of loading on the 40 K Front Plate and 10 W loading on the 40 K shell. The thermal conductivity of the third conductive block needed to be decreased by a factor of 2 to better estimate the cooldown data, indicating that the performance of this conductive block was lower than expected.

Gradient Estimates

Applying loads to various stages of the cryostat through resistive heaters allows us to estimate the performance of the system. In the second Mod-Cam cooldown, a PT-410 cooled the main 40 K shell, no 4 K shell was installed, and the 40 and 4 K DR stages were not coupled to the main shell of the cryostat. MLI

was installed over the 40 K front plate. Heat was applied to the front plate, and temperatures are recorded at the front plate, G10 plate, and on the 40 K shell side of a copper strap coupled to the PT 410's 40 K stage (Figure 2.17).

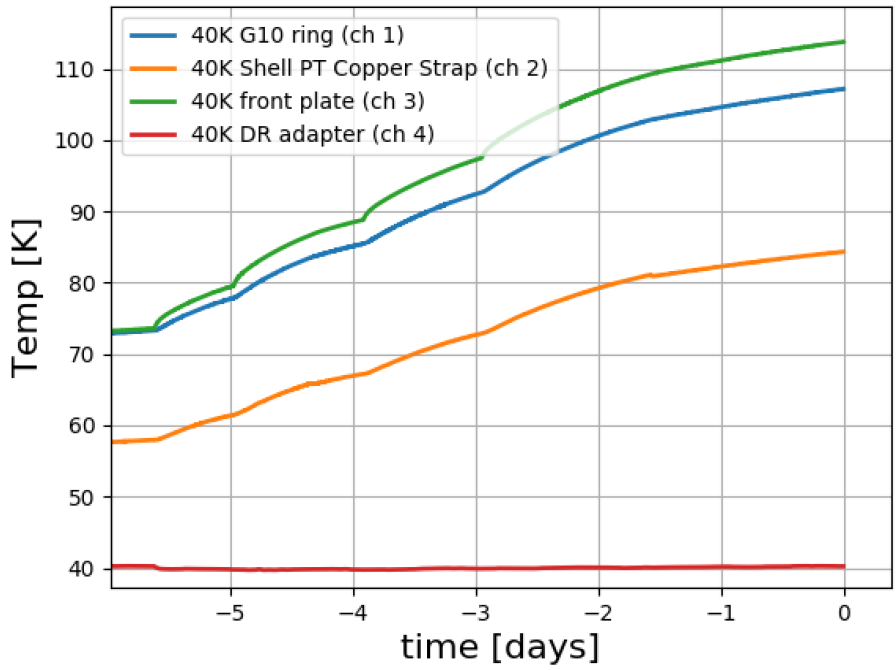

Figure 2.17: Applying 0, 2.5, 5, 7.5, and 10 W to the MLI-covered front plate during our second cooldown in which the DR shells are uncoupled from the main shells, and a PT 410 cools the 40 K shell through a copper strap assembly. Gradients are seen across the 40 K stages.

From our curves in Figure 2.17, applying heat to the MLI covered 40 K front plate, we can estimate:

$$\sim 10\,\mathrm{W} = \mathrm{G} \cdot (113 - 107)\,\mathrm{K} \rightarrow \mathrm{G}_1 \sim 2\,\mathrm{W/K} \tag{2.7}$$

which is lower than our estimated ~3 W/K, and if we fix our estimated A/l, would represent a material conductivity of k=133 W/mK. This could be accounted for by reduced Al conductivity or poor thermal joints. From Figure

2.17, comparing the gradient over the 40 K Front Shell with and without load applied, we can ascertain that the ambient load on the front plate has been improved from the estimated 26 W without MLI to approximately half a Watt. When the optical filters are installed on this plate, based on estimates from the Simons Observatory LATR performance, we will expect to see about 10 W on the front plate.

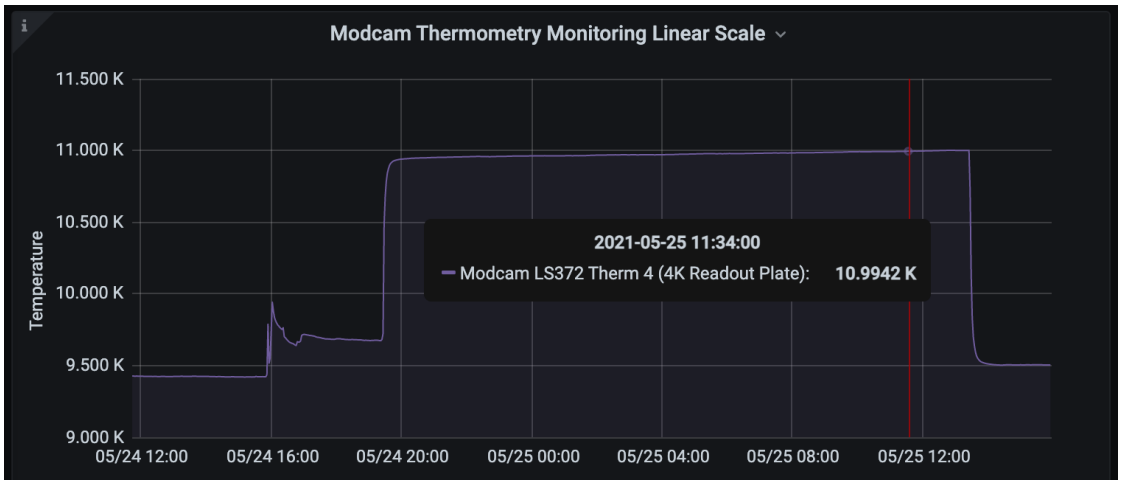

Figure 2.18: Applying 0, 50, and 120 mW to the readout plate of the 4 K shell, as monitored using Grafana. 120 mW of power increases the temperature of the readout plate from 9.42 K to 10.99 K and can be used to estimate the loading and thermal conductivities present in the system.

During our third cooldown, the 4 K main shell and plate are installed, and coupled through a OFHC braided copper strap from TAI to the 4 K stage of the PT 410. The DR shells remain thermally uncoupled from the main shells. A 200 Ohm resistive heater is installed on the 4 K readout plate on the 4 K shell, and up to 120 mW of power is applied to the readout plate, increasing its temperature from 9.42 K to 10.96 K. A plot of the effect is shown in Figure 2.18. The plot is generated using Grafana[7], an open source web application to visualize and analyze time series data, used by the Simons Observatory for online remote

[7]https://grafana.com/

systems monitoring [146]. The recording and logging of temperatures for this cooldown and following cooldowns will rely on Grafana in conjunction with a distributed control system developed for SO: Observatory Control System (ocs) [146]. The application of 120 mW on the 4 K readout plate increases the PT 410 4 K cold head temperature by about 0.27 K, which is what would be expected from the capacity curve for the cryocooler (Figure A.3), and the gradient present between the readout plate and the cold head suggests a thermal conductivity of G ~ 0.09, which is reasonable when comparing to the estimated G ~ 0.06 of the 4 K shell. We expect up to ~300 mW of loading on the 4 K readout plate when fully populated with readout wiring components.

2.4 Future Directions

Mod-Cam and Prime-Cam's modular receiver design offers flexibility for future upgrades. Adding more instrument modules can provide new measurement capabilities or reduce integration time by improving sensitivity. KID arrays will realize the full sub-millimeter capabilities of the instruments. Observations at new frequencies, including 90 GHz, 150 GHz, 750 GHz, and 1.5 THz would be valuable for both complementing the current science goals [84, 168] and enabling new goals.

Beyond broadband surveys, additional spectrometers could be deployed, with the possibility of including up to seven spectroscopic modules to fill the Prime-Cam receiver. Such an approach, or one including on-chip spectrometers, could dramatically improve future measurements of [CII] from the Epoch of Reionization or other spectroscopic measurements [138]. Beyond Prime-Cam,

CMB-S4 is the natural extension of the approach of deploying more detectors and instrument modules, and would benefit from the development of an even larger diameter cryostat for CCAT-prime with the capability to hold up to 19 Prime-Cam or SO-style optics tubes, or even more smaller-diameter optics tubes [13].

CHAPTER 3

DEVELOPMENT AND CHARACTERIZATION OF TRANSITION EDGE SENSORS

3.1 Transition Edge Sensors

Low-temperature detectors are widely used to measure radiation across a wide range of frequencies to achieve a large span of science goals, including x-ray, gamma ray, neutrino and dark matter experiments. Current CMB experiments rely on the use of low-temperature detectors such as superconducting transition-edge sensors (TESes) that are individually background-limited, or limited in sensitivity by the random arrival of background photons to improve sensitivity and mapping speed.

TESes are a mature superconducting detector technology, which has been demonstrated to perform well across a range of bands and applications. Present and upcoming Stage-III ground-based CMB experiments such as Advanced ACTPol [118], BICEP/Keck Array [144], CLASS [114], the Simons Array [79], and SPT-3G [34], balloon-borne experiments like EBEX [81] and SPIDER [108], and satellite experiment LiteBIRD [240] all are fielding or plan to field large arrays of TES bolometers. The maturity of the technology and the fact that TES bolometers have been thoroughly demonstrated to achieve CMB science goals make TESed bolometers coupled to Superconducting Quantum Interference Device (SQUID)-based readout systems the planned detector technology for the CMB-S4 experiment. TESes are also scalable, enabling the order of magnitude higher detector counts required by CMB-S4.

Laboratory tests of superconducting films and prototype devices guide and inform the fabrication processes required to meet experiment goals. In this chapter, four-lead measurements of films (Sections 3.2,3.3) and TDM measurements (Section 4.1) of devices for the Simons Observatory and CMB-S4 inform the fabrication process for these experiments' detectors.

3.1.1 Transition Edge Sensor Theory

In its essence, a transition edge sensor is a device that relies on the principle of superconductivity to read out a relatively large change in resistance from a relatively small change in temperature, due to the steep superconducting phase transition in resistance vs. temperature. This property makes the TES a useful tool to make sensitive measurements of photon energy when electrically biased on its transition at low temperatures while coupled to a cryogenic bath. TESes are often referred to as TES bolometers, as bolometers are devices that measure incident electromagnetic radiation through the heating of a material with a resistance that depends on temperature.

The superconducting phase transition is a rapid transition from nonzero resistance (characteristic of the superconducting material at temperatures above T_c, the critical temperature), to zero resistance (below T_c) (Figure 3.1). T_c is chosen to suit the cryogenic system in which the TES is operating, such that it can be biased on this transition. The total power into the TES can then be expressed as

$$P_{\mathrm{TES}} = P_{\mathrm{el}} + P_{\gamma} - P_{\mathrm{bath}}, \tag{3.1}$$

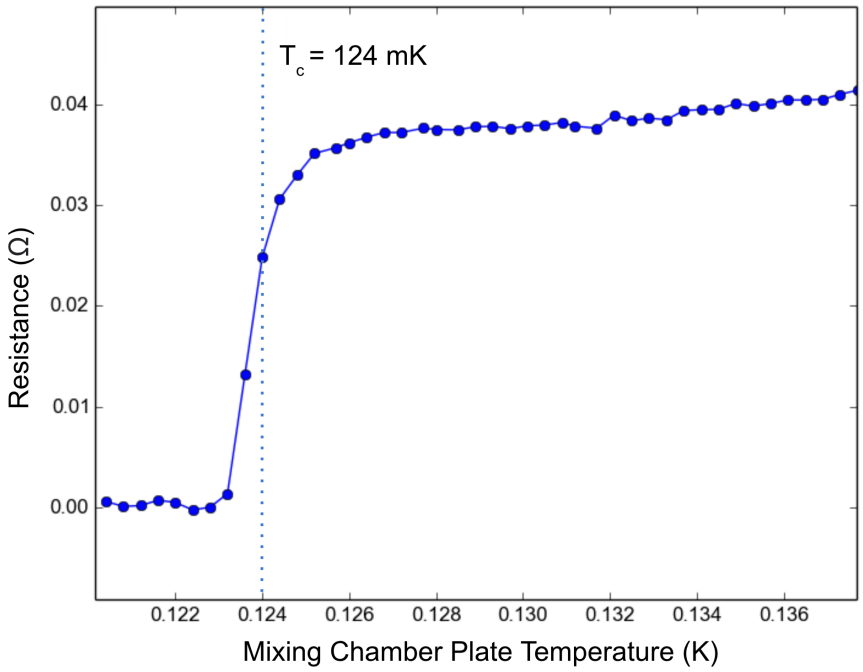

Figure 3.1: The superconducting transition of an AlMn 2500 ppm sample fabricated at U.C. Berkeley as measured using a four-lead measurement board (Section 3.2) in a Bluefors dilution refrigerator. The critical temperature is recorded to be 124 mK, indicating the temperature at which the material undergoes a rapid change in resistance from normal resistance (R_N) to no resistance (superconducting state).

where P_{el} is the power into the TES due to its voltage bias, P_γ is the power into the TES from the photons being measured, and P_{bath} is the power flowing into the cryogenic temperature bath [136]. In equilibrium, $P_{\text{TES}} = 0$, such that $P_{\text{el}} + P_\gamma = P_{\text{bath}}$. The saturation power of the device, P_{sat}, is equivalent to $P_{\text{el}} + P_\gamma$ when biased near the top of the transition. In cryogenic laboratory testbeds closed to light, $P_\gamma \approx 0$. We define P_{sat} to be the bias power that drives the TES to 90% of its normal resistance, R_N, or the resistance the device has above the superconducting transition. The measured P_{sat} values can be fit to the model

$$P_{sat} = K(T_c^n - T_{bath}^n), \tag{3.2}$$

where P_{sat} is related to the bath temperature T_{bath} and the critical temperature (T_c) of the device. K is a constant related to the thermal conductivity, G, of the device, [136]:

$$G = \frac{dP_{sat}}{dT_c} = nKT_c^{n-1}, \tag{3.3}$$

which links the heat capacity C to the cryogenic bath, and n is an exponent that is typically ~ 3. The total power into the TES can be expressed in terms of this heat capacity via $P_{\mathrm{TES}} = CdT/dt$, which yields a differential equation with a thermal time constant solution,

$$\tau = C/G. \tag{3.4}$$

This natural thermal time constant dictates the exponential decay of the increased temperature of the TES due to power input back to the bath temperature. Negative electrothermal feedback typically speeds up the device time constants considerably during operation [60].

3.1.2 AlMn Transition Edge Sensors

One technique of fabricating TES bolometers uses thin films of aluminum doped with manganese impurities to reduce the T_c of the film from ~1K to ~100 mK. This approach has advantages in the simplicity of fabrication and appears to result in reduced sensitivity to magnetic fields when compared to molybdenum and copper bilayer fabrication techniques [72, 262]. AlMn films also bypass an issue in the Mo-Cu bilayers used in ACTPol of small deposition rate variations

in the thin Mo layers required for dilution refrigerator temperature targets affecting T_c and therefore detector saturation power and sensitivity [157]. AlMn TESes can be fabricated on single wafers with high uniformity, and are currently being used for Advanced ACTPol (AdvACT) [118] and POLARBEAR-2/Simons Array [79]. These features along with demonstrated performance in the field make AlMn TESes an attractive choice for next generation CMB experiments, enabling simple film manufacturing and highly uniform distributions of targeted device parameters over large arrays [157, 132].

The geometries and fabrication methods of the devices are tuned to meet specifications through iterative rounds of fabrication and testing (Section 3). The amount of manganese doping in the aluminum affects the T_c of the superconducting films, as does the thickness of the films [42, 157]. Baking of the films then tunes the T_c in a predictable manner that is easily scaled and reproduced. Baking also protects the film from subsequent changes in T_c due to heating during fabrication [157].

3.1.3 Magnetic Sensitivity

Theoretical models of the physics governing the superconducting phase transition of TES bolometers are under continued development [257]. Experiments have shown that the critical current of square thin-film TESes depends upon the TES geometry and temperature, which can be described in terms of longitudinal proximity effects in the weak-link model of TES films [213]. The proximity effect describes the consequences of placing a superconductor in contact with a non-superconducting material. Because the electrons of the superconducting

material are paired into Cooper pairs and act differently than electrons in non-superconductors, putting the two types of metals in contact results in a transitional regime in both the materials. The superconductor becomes weaker near the transition, and the paired state of the superconductor spreads into the normal metal until the coherence of the pairs is destroyed. The TES superconductor material is connected to superconducting leads that have transition temperatures sufficiently above the transition temperature of the TES material, acting like a normal metal. Because of this, superconductivity is induced longitudinally into the TES material via the proximity effect, and they may be modeled as SS'S or SN'S weak links [213].

The critical current of these TESes has been observed to show Fraunhofer-like oscillations in applied magnetic fields, similar to those observed in Josephson junctions, which are two or more superconductors coupled by a weak link: a small portion of insulator, non-superconducting metal, or weakened section of superconductivity [213, 1]. A Ginzburg-Landau model can be used to explain oscillations in measurements of $I_c(T)$ for TESes considered to be SN'S proximity induced weak-links, measured in bath temperatures near T_c [213, 1, 228]. These measurements have previously been made for MoAu and MoCu bilayers, among others [256].

3.2 Transition Edge Sensors for the Simons Observatory

The Simons Observatory (SO) is a CMB survey experiment with three small-aperture telescopes and one large-aperture telescope, which will observe from the Atacama Desert in Chile. In total SO will field ~70,000 transition-edge sensor

(TES) bolometers in six spectral bands centered between 27 and 280 GHz in order to achieve the sensitivity necessary to measure or constrain numerous cosmological quantities. The densely packed SO Universal Focal Plane Modules (UFMs) each contain a 150 mm diameter TES detector array, horn or lenslet optical coupling, cold readout components, and magnetic shielding [158].

3.2.1 Four-lead Measurements

Laboratory measurements of AlMn films and devices informed the fabrication process for the SO AlMn TES bolometers. Prototypes tested at Cornell include samples and devices from NIST, U.C. Berkeley, and HYPRES/SeeQC, and our measurements iteratively advanced the SO TES development. Presented here are four-lead measurements of AlMn samples from U.C. Berkeley which motivated the AlMn doping level and annealing temperature to meet the critical temperature target of 165 mK. For further details on measurements and development of the TESes for SO, see [237, 238, 247, 246].

Four-lead measurements precisely measure low resistance values by eliminating the lead and contact resistances from the measurements (Figure 3.2).

Four-lead measurements of 2500 ppm AlMn samples fabricated at U.C. Berkeley's Marvell NanoLab were performed for eight annealing temperatures ranging from 180 to 240 degrees Celcius. The samples were mounted to a four-lead measurement board (shown in Figure 3.2) and cooled in a Bluefors dilution refrigerator to 100 mK. Sample critical temperatures were determined by measuring the resistance value of the films at bath temperatures varying from below to above T_c for each film. The excitation current for the films was chosen to pro-

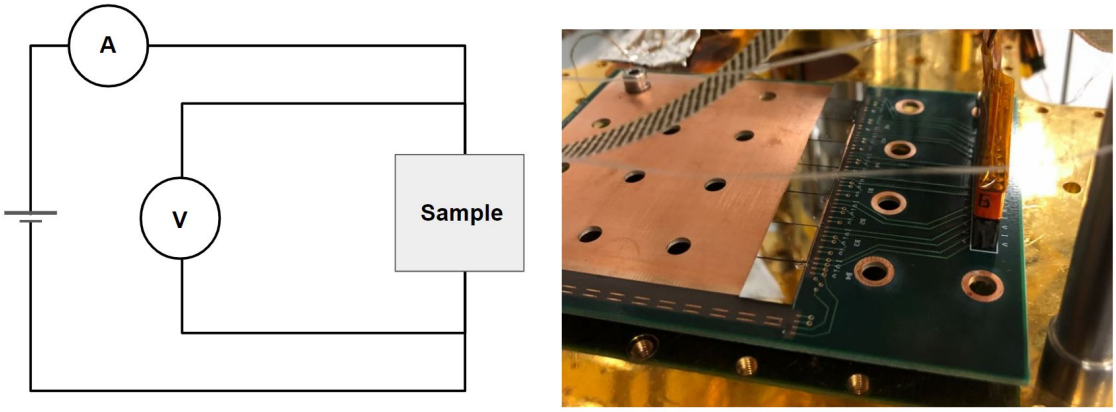

Figure 3.2: Left: A circuit diagram of a four-lead measurement (also known as four-terminal sensing) which provides precision measurements of small resistances by eliminating the lead and contact resistances from the measurement. Right: Berkeley AlMn samples affixed to a four-lead measurement board by a small amount of rubber cement, then mounted to the 100 mK plate of a Bluefors dilution refrigerator before cooling down and measuring the critical temperature of the superconducting films.

vide a balance of low current and low noise. The lower the excitation current, the larger the statistical error bar of the measurement, and the higher the excitation current, the lower the measured T_c will be, because the excitation current heats the film (Section 3.1). An example of this effect is shown in Figure 3.3. The excitation current for the measurements presented here was chosen to be 3.16 μA.

3.2.2 Results

Plots of critical temperature and residual-resistivity ratio (RRR, the ratio of the resistivity of the film at room temperature to at 4 K) versus annealing temperature are shown in Figure 3.4. The results confirm that the annealing temperature range met the desired critical temperature target, with an annealing temperature of 210 degrees Celcius resulting in a T_c of 180 mK. The curve was steeper

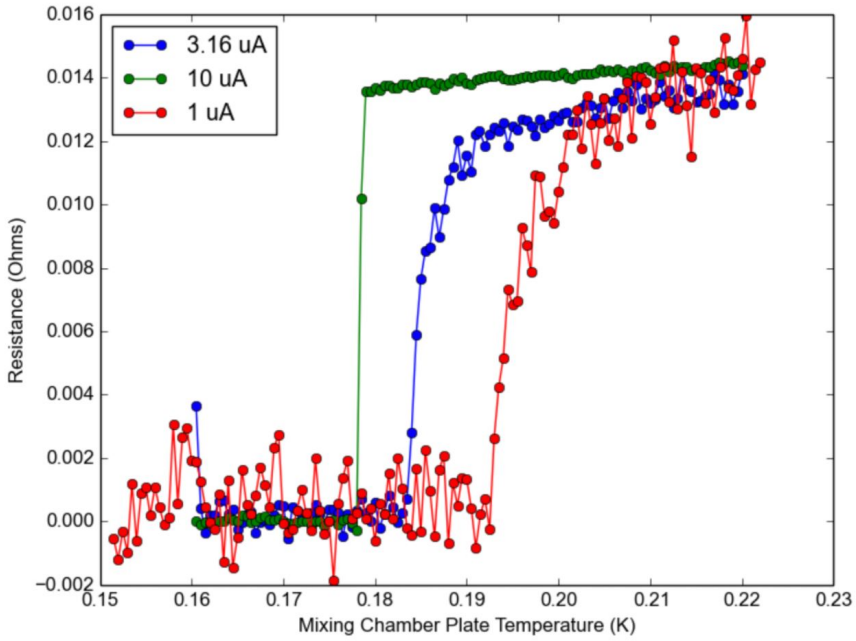

Figure 3.3: Resistance versus temperature plot from four-lead measurements of a U.C. Berkeley AlMn TES. Excitation currents 1, 3.16 and 10 μA were compared. Higher excitation currents reduce T_c as expected, while lower excitation currents produce noisier measurements. The excitation current for testing is selected based on the lowest excitation current possible to measure T_c within 2 mK.

than expected, and follow-up efforts with smaller steps in annealing temperature were conducted after seeing these plots. The RRR values and trends were consistent with expectations, rising with annealing temperature as expected. These results confirmed that the target of 2500 ppm Mn doping was satisfactory, and subsequent tests proceeded to inform the current fabrication process for the SO TESes.

3.3 AlMn Films for CMB-S4

The work presented in this section has been published in E. M. Vavagiakis, N. F. Cothard, J. R. Stevens, et al., "Developing AlMn Films for Argonne TES fab-

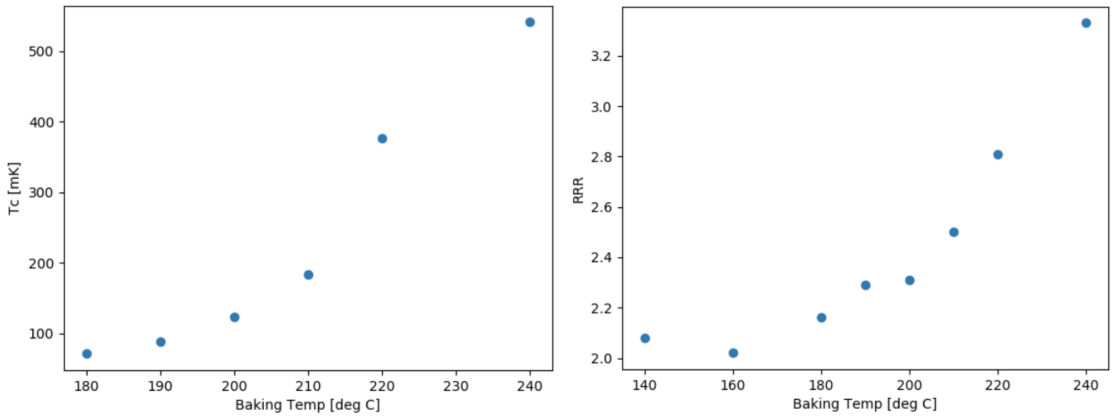

Figure 3.4: Left: Critical temperature as a function of annealing temperature for the tested U.C. Berkeley 2500 ppm AlMn films. T_c increases with increasing annealing temperature, as expected, but the curve is steeper than expected in the region of interest (around 210 degrees Celsius). This result motivated the selection of the 2500 ppm target and the subsequent analysis of films annealed at finer step temperatures. Right: RRR versus annealing temperature. RRR increases with increasing annealing temperature as expected.

rication," Journal of Low Temperature Physics 199, 408–415 (2020) [261].

CMB-S4 is a proposed "Stage-4" ground-based CMB experiment that will map the polarization of the CMB in multiple frequency bands to nearly the cosmic variance limit. The reference design for CMB-S4 relies on large arrays of AlMn Transition-Edge Sensors (TESes) coupled to Superconducting Quantum Interference Device (SQUID)-based readout systems to reach its sensitivity targets [14, 10].

Monolithic arrays of multichroic TESes have previously been fabricated at Argonne National Laboratory and deployed in the South Pole Telescope's SPT-3G camera [200]. These Ti/Au bolometers have a critical temperature of T_c = 420 mK and a normal resistance of R_N = 2Ω. To meet the experiment design requirements for CMB-S4, current $AlMn_{2000ppm}$ TES fabrication targets a $T_c \sim$ 150-200 mK and an $R_N \sim$ 10-20 mΩ. While SPT-3G used a ^{4}He-^{3}He-^{3}He absorption

refrigerator with a bath temperature of ~250 mK, CMB-S4 uses dilution refrigerators with bath temperatures <100 mK [230]. Reducing the bath temperature reduces the devices' thermal fluctuation noise. Reducing R_N will optimizes the detector arrays for TDM or microwave-SQUID multiplexing (μMUX) readout. The fabrication process at Argonne therefore needs to be tuned to achieve these new device parameters. Variables in the fabrication process such as the Mn concentration, thickness and geometry of films, thermal annealing temperature, and presence of additional material layers all affect the AlMn device parameters and are tuned to meet specifications through repeated rounds of fabrication and testing [221, 157].

3.3.1 Fabrication

Film samples and devices for testing were fabricated at Argonne National Laboratory and tested at Cornell University to develop Argonne's fabrication process. Bare film studies were performed to investigate the impact of substrate choice and Ti (or Mo) buffer layer between AlMn and Au depositions. A film stack of 2000ppm AlMn on SiO2 with a Ti15nm/Au15nm top layer was chosen based on good critical temperature repeatability and was derived from the Ti/Au SPT-3G array fabrication (Fig. 3.5). The top layer of Au was chosen to prevent oxidation and protect the underlying films, while remaining conductive to connect leads to the device. Patterned films were then tested to predict device T_c and R_N.

The thickness and aspect ratio of the film stacks were iterated to target the desired R_N. Baking time and temperature were selected to target T_c. A lift-

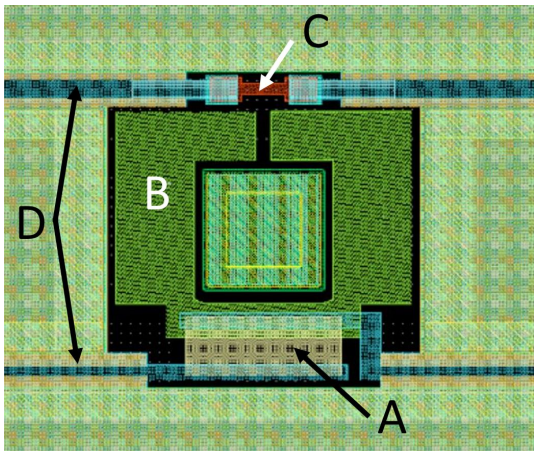

Figure 3.5: A modified SPT-3G TES island, where (A) is the AlMn TES film, (B) is Pd for heat capacity stabilization, (C) is a load resistor, and (D) are the Nb leads. The AlMn200nm/Ti15nm/Au15nm TES film is 15 μm long by 80 μm wide. Figure is from [261].

off process was used for TES patterns, which could potentially lead to tapered edges and interaction between the Al and Au layers, and thus to poor transitions for thicker films. Furthermore, direct contact of Al and Au leads to the formation of intermetallic compounds and variation in superconducting properties. Such effects as well as proximity effects were considered while iterating patterned film and TES designs.

3.3.2 Testing

Four-lead Measurements

Samples were wire bonded and affixed with rubber cement to a printed circuit board (PCB) and mounted to the coldest (100 mK) stage of a dilution refrigerator with an internal 300 K magnetic shield. Four-lead measurements were taken of the samples once cold (Section 3.2). Temperature was varied as resistances were

logged via a Lakeshore AC resistance bridge, reading out the superconducting transition and measuring T_c and R_N. For each transition T_c was taken to be the temperature value at 50% R_N, where R_N is the resistance value measured at 2 mK above the last superconducting data point in the resistance versus temperature curve (Figure 3.6). Excitation currents were varied to ensure their choice didn't significantly affect the measured T_c. Based on the noise in the obtained curves due to temperature fluctuations and Lakeshore measurements, the total uncertainty on T_c is estimated to be 2 mK, and the uncertainty on R_N to be 0.2 $m\Omega$.

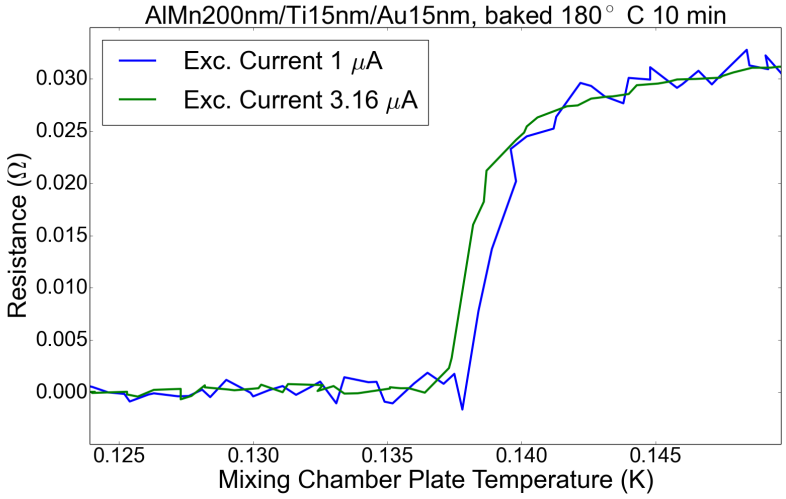

Figure 3.6: Example of the four-lead R vs. T measurement of a film superconducting transition. Choice of excitation current influences results, and T_c is recorded for an excitation current which has been reduced enough to keep T_c consistent within 2 mK. Figure is from [261].

TDM Measurements

Fabricated TESes of two different leg lengths (865 μm, "long" and 446 μm, "short") of equal cross-sectional area (21 μm wide, 1μm SiN + 0.3 μm Nb + 0.5 μm SIO2 thick), were mounted to a PCB on the cold stage of the dilution refrig-

erator, and read out using the same time division multiplexing (TDM) system used in AdvACT with NIST SQUIDs [121] (Section 4.1.1). TDM measurements of current-voltage (IV) curves at various bath temperatures were aquired for the "long" and "short" leg length TES bolometers. The geometry of the legs control the thermal conductance to the bath. We define P_{sat} to be the bias power which drives the TES to 90% of its normal resistance, R_N. The measured P_{sat} values are fit to the model in Equation 3.2, where P_{sat} is related to the bath temperature T_{bath} and the critical temperature (T_c) of the device (Section 3.1). Because K is degenerate with n in our fits, we hold n fixed at a range of values while fitting the other parameters, and finally determine the best fit n by plotting n vs χ^2 and obtaining the minimum χ^2. The thermal conductivity, G, of the device is then given by Equation 3.3.

The temporal response of a given TES can be approximated by a one-pole filter with an effective time constant $f_{3\mathrm{dB}} = 1/2\pi\tau_{\mathrm{eff}}$, where τ_{eff} is the effective time thermal constant of the TES operated under negative electrothermal feedback:

$$f_{3\mathrm{dB}} = f_{\mathrm{nat}}\left(1 + \frac{\mathscr{L}}{1+\beta}\right) = \frac{G}{2\pi C}\left(1 + \frac{1}{(1+\beta)}\frac{\alpha P_{\mathrm{bias}}}{T_c G}\right) \tag{3.5}$$

Here, $f_{\mathrm{nat}} = 1/2\pi\tau_{\mathrm{nat}} = G/2\pi C$ is the natural thermal time constant (Equation 3.4), $\mathscr{L} = \alpha P_{\mathrm{bias}}/T_c G$ is the loop gain, and $\alpha = \frac{\mathrm{d}\log R}{\mathrm{d}\log T}$ is the TES sensitivity to small changes in temperature [136]. To measure $f_{3\mathrm{dB}}$, a small amplitude square wave is added to the DC detector voltage bias. The detector response is sampled quickly at ~1600 Hz. The time constant, τ_{eff}, is extracted by fitting the response to a single pole exponential. These measurements are performed at multiple bath temperatures and at several different points on the superconducting transition [145]. Similar measurements were pursued to characterize TESes for the Simons

Film Label	Material
A	Ti5nm/AlMn$_{1200ppm}$100nm/Ti5nm/Au20nm
B	AlMn$_{1200ppm}$100nm/Mo10nm/Au20nm
C	AlMn$_{2000ppm}$100nm/Ti15nm/Au15nm
D	AlMn$_{2000ppm}$80nm
E	AlMn$_{2000ppm}$550nm/Ti15nm/Au15nm
F*	AlMn$_{2000ppm}$200nm/Ti15nm/Au15nm
G*	AlMn$_{2000ppm}$380nm/Ti15nm/Au15nm
H*	AlMn$_{2000ppm}$550nm/Ti15nm/Au15nm
I*	AlMn$_{2000ppm}$200nm/Ti15nm/Au15nm
J	AlMn$_{2000ppm}$200nm/Ti15nm/Au15nm

Table 3.1: Samples tested using four-lead measurements, with various materials and geometries (listed here). The different bake times, temperatures, and resulting critical temperatures and normal resistances are listed in Table 3.2. *TES devices. Film information is from [261].

Observatory [60, 238]. The bias step measurement results from the two tested Argonne devices are plotted in Figure 3.8.

3.3.3 Four-lead Measurement Results

The critical temperature and normal resistance measurements for TESes and films varying in material and geometry (Table 3.1), and bake time and temperature are given in Table 3.2.

Baking was found to shift T_c, and the films showed evidence of annealing, where T_c doesn't change again after the first bake. Thicker and wider geometries lowered R_N to approach the target value, and aspect ratios were also found to influence T_c (Fig. 3.7).

Film	Heating C	T_c [mK]	R_N [Ω]
A	0	196	0.86
A	180/10 min	153	0.80
A	180/10 min,90/2 min,110/2 min	141	0.77
B	0	371	0.27
B	180/10 min	399	0.37
C	0	223	0.43
C	0	159	1.65
C	180/10 min	181	1.45
C	180/10 min,90/2 min, 110/1.5 min	180	1.46
C	0	179	0.09
C	180/10 min	193	0.05
C	180/10 min,90/2 min, 110/1.5 min	172	0.05
C	0	167	3.31
C	180/10 min	160	3.06
D	0	335	2.10
E	0	151	0.22
E	0	146	0.11
E	180/10 min	66	0.11
E	180/20 min	67	0.11
F*	0	127	0.03
F*	180/10 min	129	0.04
F*	180/10 min	140	0.04
G*	180/10 min	179	0.02
H*	180/10 min	167	0.02
H*	0	219	0.02
H*	180/20 sec + 10 min	88	0.01
H*	180/60 sec + 10 min	86	0.01
I	180	89	0.03
I	210	125	0.03
I	240	174	0.03
Film	**Length [μm] x Width [μm]**	T_c	R_N
J	5x80	201	0.01
J	20x200	126	0.01
J	5x140	172	0.01
J	10x200	146	0.01

Table 3.2: Critical temperatures and normal resistances for samples tested using four-lead measurements, varying in material and geometry (given in Table 3.1), and bake time and temperature. *TES devices. Results are from [261].

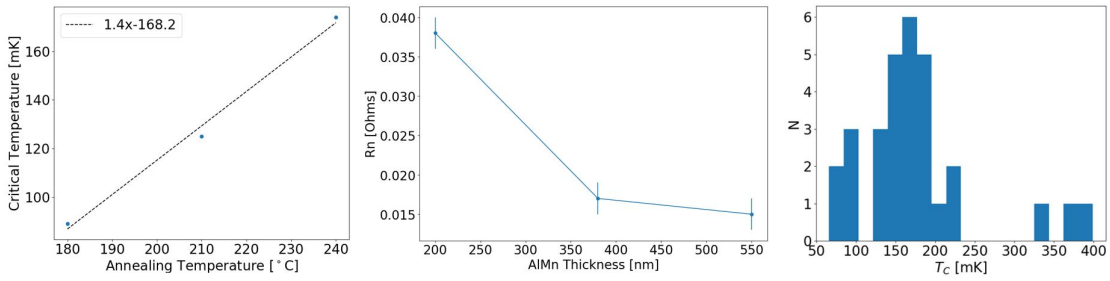

Figure 3.7: *A:* Critical temperature vs. annealing temperature for three $AlMn_{2000ppm}$200nm/Ti15nm/Au15nm films along with linear fit showing the effect of baking on T_c. *B:* Normal resistance vs. AlMn thickness in nm for three film samples, showing R_N decreasing with increasing material thickness. *C:* Histogram of all Argonne sample critical temperatures measured at Cornell, highlighting a trend of narrowing in on the desired critical temperature of 150-200 mK for CMB-S4. Figure is from [261].

Parameter	**Leg Length 865 μm Fit**	**Leg Length 446 μm Fit**
T_c	122 mK	136 mK
G	0.013 pW/mK	0.024 pW/mK
k	4.6e-7 pW/mK^n	1.5e-6 pW/mK^n
R_N	21.9 mΩ	21.7 mΩ

Table 3.3: Parameter fits to P_{sat} measurements (Eqs. 3.2, 3.3), for two Argonne devices of different leg length and identical leg cross-sectional area. The best fit values for these data were $n = 2.76$ and $n = 2.91$ for the short and long leg lengths respectively. Table is from [261].

3.3.4 TDM Measurement Results

The results of P_{sat} fits for two Argonne devices are shown in Table 3.3. We observed a large decrease in time constant as the detectors are biased lower on the superconducting transition, which is consistent with previous AlMn TES measurements (Figure 3.8) [145].

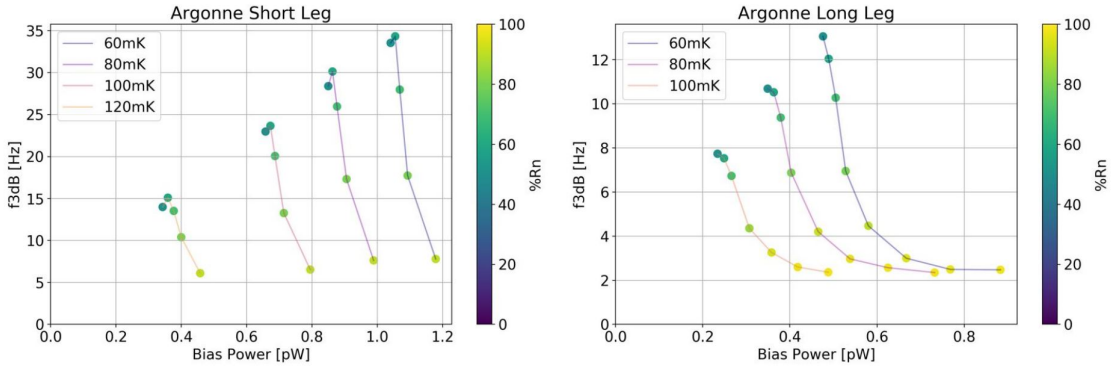

Figure 3.8: The results of bias step measurements for the short leg length (446 μm) TES (left) and the long leg length (865 μm) TES (right). $f_{3\mathrm{dB}}$ is plotted versis bias power in pW for four bath temperatures. Figure is from [261].

3.3.5 Summary

Measurements of T_c, G, k, f_{3dB}, and R_N for two Argonne AlMn TESes, and T_c and R_N for various film stacks, motivated the selection of materials, thickness, geometry, and bake time and temperature for the Argonne fabrication process. The targeted parameters for devices used for precision measurements of the CMB in the next-generation CMB experiment, CMB-S4, include a critical temperature of 150-200 mK and normal resistance of 10-20 mΩ.

3.4 Behavior In Magnetic Fields

The work presented in this section and Sections 4.2 to 4.3 has been published in E. M. Vavagiakis, S. W. Henderson, K. Zheng, et al. 2018. "Magnetic Sensitivity of AlMn TESes and Shielding Considerations for Next Generation CMB Surveys," Journal of Low Temperature Physics 193, 288–297 (2018) [262].

3.4.1 TES Critical Temperatures

In these Sections, we test TESes from ACTPol chips [104], AdvACT 150 GHz (HF) chips, AdvACT 30 GHz (LF) chips [79], TES test chips with AlMn films of varying geometries, and POLARBEAR TES test chips [245] with varying leg lengths for magnetic sensitivity. We take resistance measurements of TESes varying in geometry, material, doping, manufacturer, and leg length using four-lead measurements (Section 3.2, Figure 3.2). The TES chips were mounted to the 100 mK stage of a dilution refrigerator (DR). A set of 1 m diameter Helmholtz coils applied DC magnetic fields up to 10.5 Gauss to the outside of the DR. The fields were attenuated by a 30 cm diameter, 85 cm long half-open cylindrical room temperature mu-metal magnetic shield inside the DR. Shielding factors were measured by using a gaussmeter to measure the field between the coils with and without the shield in place, and were determined to be 380 ± 20 in the horizontal direction (for the SQUID and weak-link-like behavior measurements) and 2.9 ± 0.2 in the vertical direction (for the four-lead measurements) at the locations of our detectors. The series array modules used for TDM readout are additionally shielded in a niobium box. Resistance vs. temperature data was acquired for each TES at various values of applied magnetic field, using a lakeshore AC resistance bridge with a low-noise preamplifier and ruthenium oxide thermometry with low magnetic field-induced errors.

We chose excitation currents for the four-lead measurements to balance noise reduction in the measurements with minimizing power dissipation through the TES bolometers (Table 3.4). For each device and at each applied magnetic field value, we took T_c to be the temperature value at 50% R_N, where R_N is the resistance value measured 2 mK above the last superconducting datapoint in the

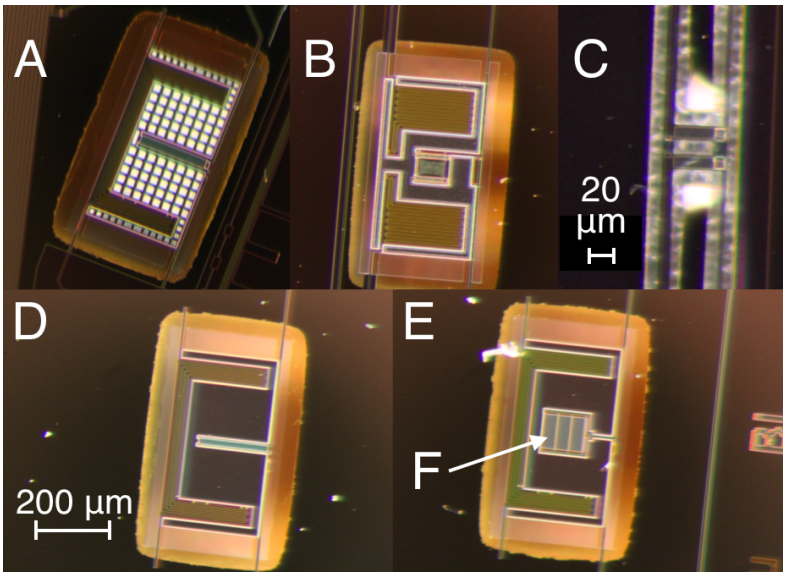

Figure 3.9: Images of tested TESes. A: POLARBEAR AlMn TES. B: AdvACT AlMn TES. C: ACTPol MoCu TES. D: AdvACT AlMn test TES, 16.5μm wide, E: AdvACT AlMn test TES, 37.5μm wide, F: location of AlMn film. Figure is from [262].

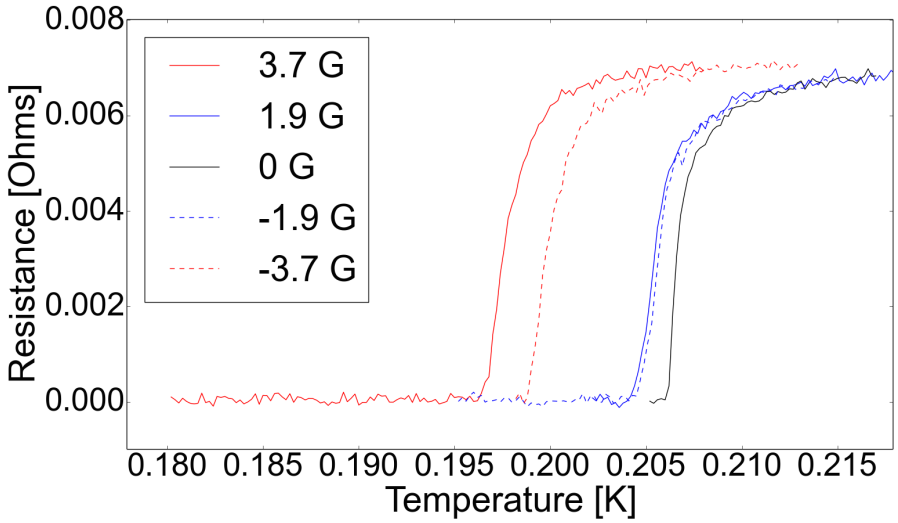

Figure 3.10: Resistance vs. temperature plot for a TES at 10μA excitation current when exposed to various values of magnetic field. T_c is determined for each applied field value and plotted as a function of magnetic field in Figure 3.11. Figure is from [262].

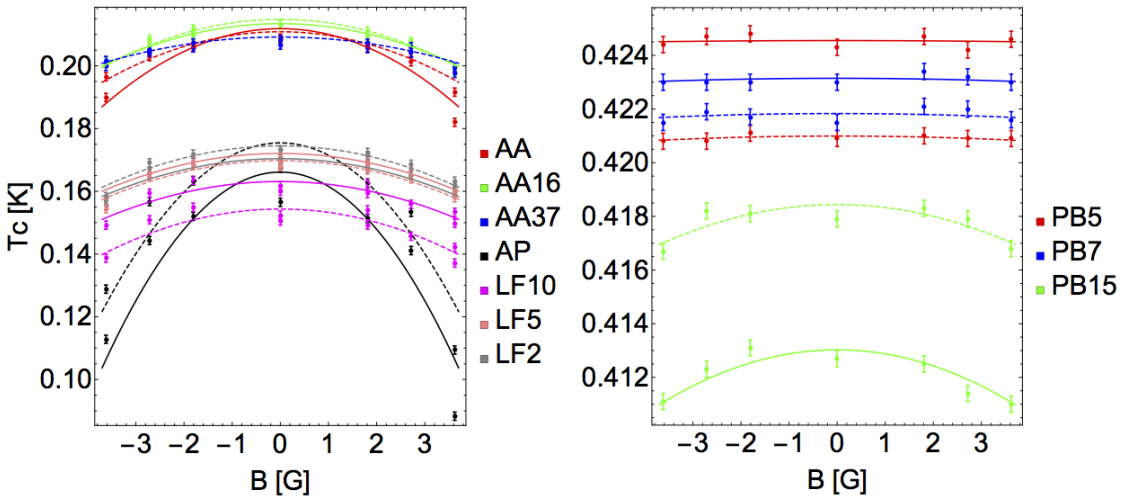

Figure 3.11: T_c vs. B for tested TESes (AdvACT (AA), ACTPol (AP), POLARBEAR (PB), AdvACT LF (LF)) and parabolic fits to the data points. Dashed and solid lines indicate measurements of different devices of the same type. Coefficients from parabolic fits are listed in Table 3.4. Figure is from [262].

resistance vs. temperature curve at zero applied magnetic field. A plot of T_c vs. applied magnetic field for the tested bolometers is shown in Figure 3.11 along with parabolic fits to the points. Parameters from the parabolic fits are listed in Table 3.4. The error bars on T_c are chosen to be 1.3 mK, the standard deviation of a Gaussian fit to the differences in recorded T_c between 18 otherwise identical data points taken over the course of two separate cooldowns for the AdvACT LF chips.

3.4.2 Weak-link-like Behavior in AlMn TESes

In this section we present observations of weak-link-like behavior in AlMn TESes (Section 3.1.3). Using the same experimental field setup described in Section 3.4.1, magnetic fields are applied perpendicular to the plane of the TES films. The TES devices tested were most similar to the AdvACT HF TESes (B. in

TES	Leg w x l [μm]	AlMn Area	Ex. Curr.	$T_{C,B=0}[K]$	$w[\frac{K}{G^2}]$	$\frac{dI_0}{dB}[\frac{\mu A}{G}]$
PB5	4, 10 x 500	610 μm^2	100 nA	0.423	7.3e-6	4e-5
PB7	4, 10 x 700	610 μm^2	100 nA	0.423	9.7e-6	5e-5
PB15	4, 10 x 1500	610 μm^2	100 nA	0.416	1.3e-4	5e-4
AdvACT	15 x 61	6200 μm^2	10 μA	0.211	1.2e-3	1e-1
AA16	20 x 61	3300 μm^2	10 μA	0.214	1.1e-3	1e-1
AA37	20 x 61	11250 μm^2	10 μA	0.208	0.6e-3	1e-1
ACTPol	20 x 61	9000 μm^2	10 μA	0.171	4.2e-3	5e-1
AA LF	10 x 1000	6200 μm^2	10 μA	0.159	1.0e-3	2e-2
AA LF	10 x 500	6200 μm^2	10 μA	0.171	0.9e-3	3e-2
AA LF	10 x 220	6200 μm^2	10 μA	0.173	0.9e-3	5e-2

Table 3.4: AdvACT (AA), ACTPol (AP), and POLARBEAR (PB) TESes, leg lengths, AlMn (or MoCu for ACTPol) areas, and excitation currents, with parabolic fits in the form of $y = T_{C,B=0} - wx^2$ to T_c vs. B data for each type of tested TES. AA16 indicates an AdvACT test TES with a width of 16.5 μm, and AA37 indicates a width of 37.5 μm. PB TESes have one leg which is 4 μm wide and one which is 10 μm wide. Errors on parameters are taken to be 1.3 mK due to scatter in otherwise identical data points during separate cooldowns, and 20% of sensitivity fit mK/G^2 due to fitting error. Estimates of dI_0/dB should be regarded as comparative figures only and are based on an approximation of the sensitivity at B = 0.05 G as described in Section 4.3. Table is from [262].

Figure 3.9). The TESes are read out using the same TDM readout system used in AdvACT (Section 4.1.1) with NIST SQUIDs similar to those in [121]. At each value of applied magnetic field or each value of temperature, we perform voltage ramps to get a reading of the critical current I_c at which the TES transitions from superconducting to normal.

Plots of I_c vs. B are shown for three devices in Figure 3.12. This data was acquired for the TESes at bath temperatures near T_c where the Ginzburg-Landau model would apply for the AlMn films (3.1.3). A plot of I_c vs. T for the three devices is shown in Figure 3 along with fits to the data where the Ginzburg-Landau model applies. The fits take the form $I_c(T) = a\sqrt{T/T_c - 1}e^{-b\sqrt{T/T_c - 1}}$, where a is proportional to the width of the device film and b is proportional

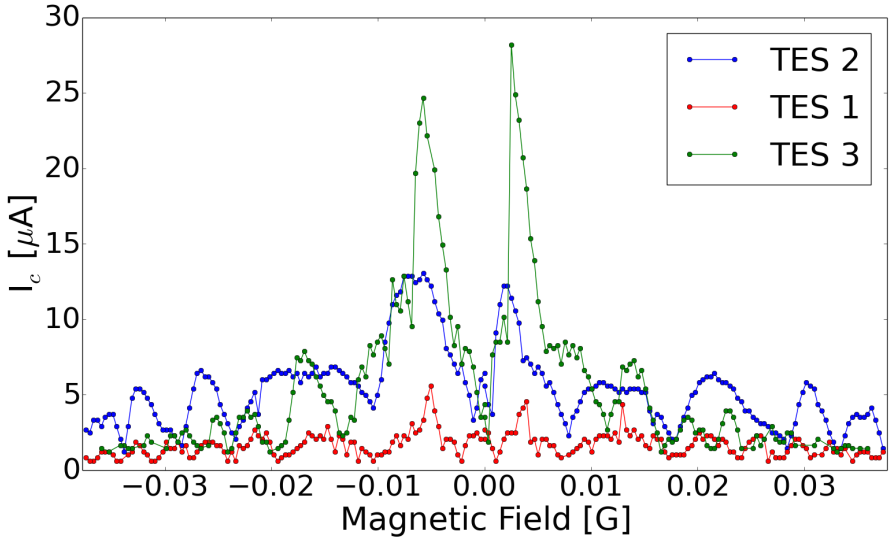

Figure 3.12: I_c vs. B for three AlMn TES films, similar to B. in Figure 3.9. We observe Fraunhofer-like oscillations in the data. The period of the oscillations is irregular, as is their decay. The lack of a central peak requires further study. Figure is from [262].

to the length [213]. We observe a trend in a consistent with the theory, with $a = 0.50 \pm 0.01 \times 10^6$ μA for the 16.5 μm wide AlMn device ("TES 2") and $a = 1.00 \pm 0.05 \times 10^6$ μA for the 25 μm wide devices ("TES 1" and "TES 3").

We observe Fraunhofer-like oscillations in all three tested devices, though the observed oscillations are not consistent in period or decay. The absence of the central peak in the oscillations requires further study. The ability of the Ginzburg-Landau model to describe the high temperature data suggests that the behavior observed in these devices agrees with the weak-link model.

3.4.3 Conclusions

The MoCu ACTPol TESes are the most sensitive to magnetic fields, followed by the AdvACT AlMn TESes, with the POLARBEAR-2 AlMn TESes being the

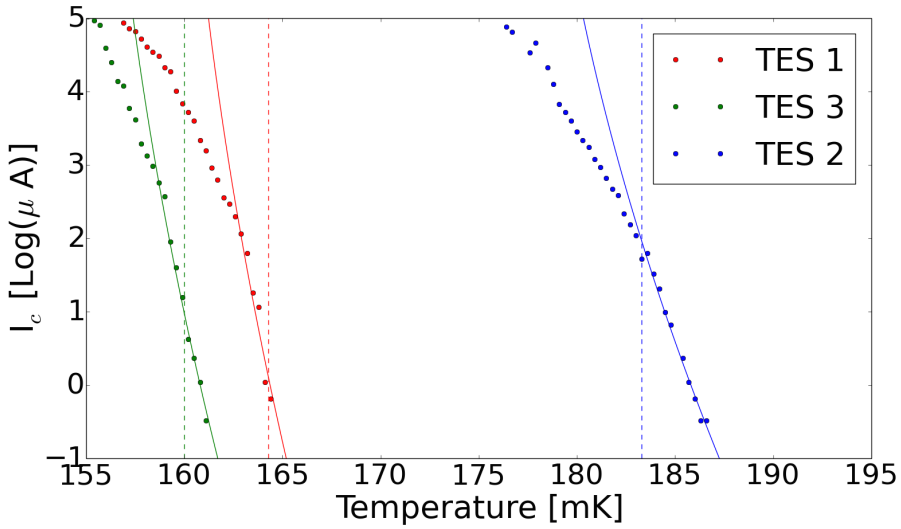

Figure 3.13: I_c vs. T for the three AlMn TES films, along with fits to the high temperature data using the Ginzburg-Landau model. Temperature is held fixed for the measurements of I_c vs. B (Figure 3.12) for each device, indicated by the dashed vertical lines. Figure is from [262].

least sensitive. The primary source of the differences between the sensitivities of the AlMn TESes is not yet clear, though we note that the POLARBEAR2 and AdvACT TESes do have significantly different areas, critical temperatures, doping, and thicknesses. An observation of weak-link-like behavior in AlMn TESes at low critical currents was made. Further study could help inform how this behavior impacts detector parameters.

CHAPTER 4

MAGNETIC SENSITIVITY OF SUPERCONDUCTING READOUT DEVICES

The superconducting devices on which current and future CMB surveys depend are sensitive to magnetic fields (Section 3.1.3). CMB map artifacts introduced from devices improperly shielded from scan-synchronous pickup of Earth's magnetic field, rotating half-wave plates, magnetic components inside of cryostats, and other sources could be difficult to remove and jeopardize science goals. Device performance in the presence of magnetic fields is difficult to compute analytically (Section 3.1.3), and the response of SQUID gradiometers changes with each design iteration and is difficult to simulate [257, 213]. Direct measurements are thus necessary to understand the behavior of these devices. Information about SQUID and TES magnetic sensitivity will motivate magnetic shielding design considerations for future CMB experiments.

The treatment of magnetic shielding currently varies for CMB experiments. Instruments for ACT rely on TDM readout and have used multiple layers of Cryoperm and Amumetal A4K in combination with individual niobium shields for SQUID series arrays [252, 266]. Experiments using MHz FDM readout systems, like POLARBEAR and SPT-3G, have mounted SQUIDs on Nb foil surrounded by a small cryoperm sleeve [201]. Appropriate shielding factors will be motivated by experimental testing of these SQUIDs and TESes combined with simulated telescope observations. This information will be combined with simulations of shield geometries in order to develop mechanical designs for the cryogenic receivers currently under development, including Prime-Cam and Mod-Cam (Sections 2.2, 2.3).

Present and future CMB experiments will rely on multiplexed arrays of AlMn TESes, as discussed in Sections 3.1.2 and 4.1. In this chapter, TDM DC SQUIDs and FDM μMUX rf-SQUIDs are tested for magnetic sensitivity. In Section 4.2 we present upper limits on magnetic sensitivities of TDM DC SQUIDs and μMUX rf-SQUIDs. In Section 4.3 we discuss order of magnitude estimates for required shielding factors based on our measurements. Measurements of μMUX SQUID magnetic sensitivity in various shielding configurations for the Simons Observatory are presented in Section 4.4. We review how these measurements have informed magnetic shielding designs for future experiments in Section 4.5.

4.1 SQUID Multiplexed Readout

The arrays of thousands of TESes relied upon by current and upcoming CMB experiments (Section 3.1) must be multiplexed in order to be read out without overheating the experiments' cryogenic systems. This means that each wire coming from the coldest stages of a cryogenic receiver must carry the signals from many TESes at once. SQUIDs (superconducting quantum interference devices) are sensitive magnetometers constructed of superconducting loops containing Josephson junctions that are used to amplify the TES signals. Multiplexing readout of TESes is currently achieved with either time division multiplexing (TDM) using DC SQUIDs [12] or frequency division multiplexing (FDM) using DC SQUIDs and MHz LC resonators [2] or inductive coupling to GHz frequency rf-SQUIDs (μMUX) [3, 4, 12]. In this section, a brief overview of TDM and μMUX readout is given as an introduction for subsequent measurements.

4.1.1 Time-Division Multiplexing

In Time-Division Multiplexing, each TES is sampled sequentially by reading out one row of a two-dimensional array of bolometers at a time. The rows are addressed sequentially at ~0.5 MHz to read out the entire array of TESes.

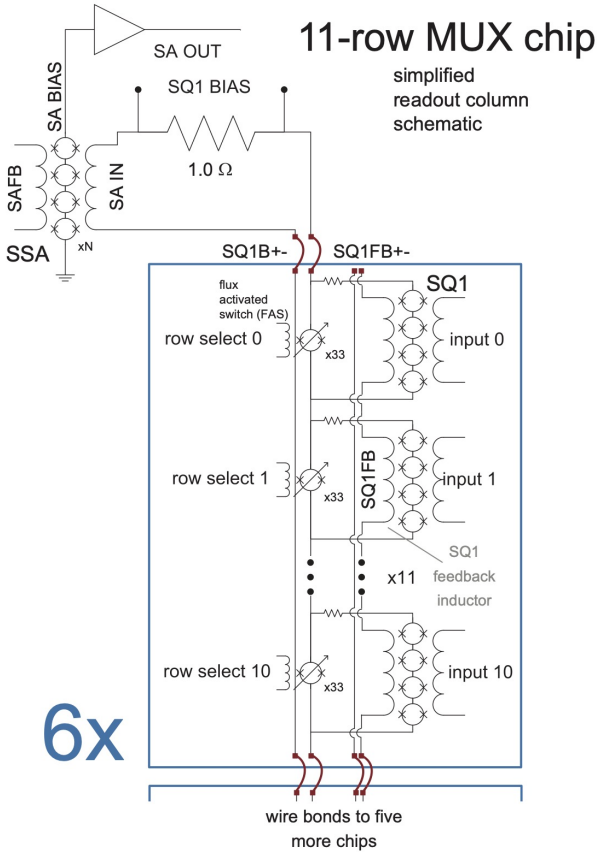

Figure 4.1: A schematic from [121] of 1 of 32 columns of the 64-row TDM SQUID-based multiplexing architecture used to read out the TES arrays for Advanced ACTPol. The design is representative of the TDM architecture used for the laboratory measurements presented in this work. Each TES is inductively coupled to a first stage SQUID series array (SQ1) shunted by a flux activated switch (FAS), connected in series to form 64 rows in a column that are addressed sequentially. Each SQ1 column is biased in parallel and read out through the ~1 K SQUID series array (SSA) using custom Multi-Channel Electronics (MCE) [28, 121]. The blue box represents one TDM MUX chip with 11 rows, and 6 of these chips achieve the 64-row multiplexing (2 rows are not utilized).

TDM readout depends on inductively coupling the TESes to SQUIDs, specifi-

cally DC-SQUIDs, for signal amplification. The superconducting loop of a DC-SQUID contains two Josephson junctions in parallel and functions as a sensitive magnetometer. The DC-SQUID output voltage is a periodic function of applied magnetic flux, where Φ_0, the magnetic flux quantum, is the period. The DC-SQUIDs are inductively coupled to TESes, reading out currents through changes in the SQUID voltage modulated by changes in input magnetic flux from the TES coupling inductors. They also function as switches, as the DC-SQUIDs can be either superconducting or resistive. In the measurements of magnetic sensitivity presented below, the magnetic pickup of a TDM SQUID can be measured by observing the offset of the voltage-flux curve of the SQUID.

A schematic of the TDM architecture used in the laboratory measurements presented in this work (Chapters 3 and 4) and for observations with the Atacama Cosmology Telescope is presented in Figure 4.1. Each TES in the detector array is inductively coupled to a first stage SQUID series array (SQ1). The SQ1 is addressed with a flux-activated switch (FAS), forming a single a channel of the readout, with many channels connected in series to form "columns" of channels. "Rows" of channels across each column are sampled sequentially by connecting the coil of each FAS in series with one other FAS in every column. Each column is then read out by another SQUID series array (SSA) at ~1 K, which amplifies the signals before they are read out using the warm Multi-Channel Electronics (MCE) [121]. The MCE controls the tuning of the various SQUID curves through bias currents and flux offsets, keeping the SQUIDs locked at the desired point in their $V - \phi$ curves and reading out the recorded signals for each TES. The result is a multiplexing (MUX) factor of 64, which requires eight wires per column and two per row.

4.1.2 Frequency-Division Multiplexing with SQUID-coupled GHz Resonators

In contrast with TDM, frequency-division multiplexing (FDM) schemes continuously read out signals from all observing TESes, due to each TES being inductively coupled to a resonator with a resonant frequency tracked over time. SQUID-coupled GHz resonators (μMUX) have been successfully deployed in the MUSTANG2 experiment [235], and the Simons Observatory plans to use μMUX readout to achieve a multiplexing factor of ~1,000 [214].

In μMUX readout schemes, a TES is coupled to a radio frequency (rf-) SQUID, which is in turn coupled to a resonator with a unique resonant frequency (Figure 4.2). A single superconducting transmission line is then able to read out many resonators with different resonator frequencies, densely packed within several GHz of bandwidth. Changes in TES current create a shift in the coupled resonator frequency, which is read out through a phase shift of a probe tone. A feature of μMUX readout which differentiates it from FDM with MHz LC resonators is the addition of "flux-ramp demodulation," the continuous application of a sawtooth signal to the rf-SQUID through a flux ramp line, which linearizes the SQUID response and decreases the $1/f$ readout noise [214].

The warm readout components for the Simons Observatory μMUX readout reside in the SLAC Superconducting Microresonator Radio Frequency (SMuRF) electronics [120]. The SMuRF generates the tones that track the resonators and provide the flux ramp and TES bias signals.

The chips tested for the Simons Observatory are prototype designs for SO, read out using the SMuRF electronics. In our initial measurements, we used

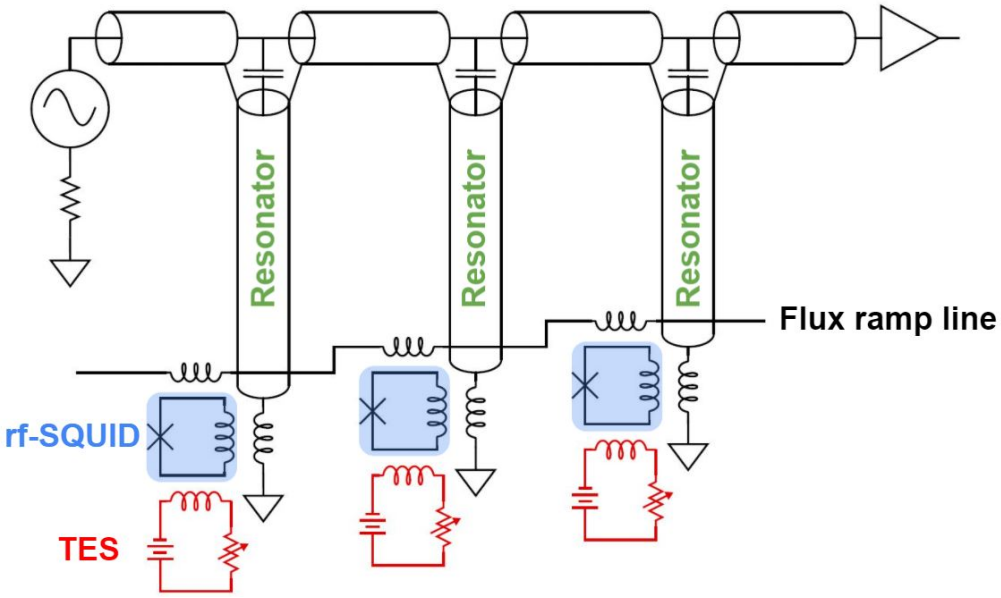

Figure 4.2: A schematic of a section of μMUX readout, with three TESes each coupled to rf-SQUIDs and μMUX resonators. The flux ramp line coupled to the rf-SQUIDs is also shown. The original unlabeled circuit diagram is from [256]

a Reconfigurable Open Architecture Computing Hardware (ROACH) readout system and a vector network analyzer (VNA) to measure the shifts in resonant frequency associated with magnetic field pickup from the rf-SQUID channels. The ROACH system depends on an FPGA board coupled to a DAC/ADC board for generating and measuring probe tones. The VNA traces the resonance frequencies, and the minimum of each frequency can be tracked and measured for offsets from the applied magnetic fields (Section 4.4).

4.2 μMUX and TDM SQUIDs

The work presented in Sections 4.2 to 4.3 and Section 3.4 has been published in E. M. Vavagiakis, S. W. Henderson, K. Zheng, et al. 2018. "Magnetic Sensitivity of AlMn TESes and Shielding Considerations for Next Generation CMB

Surveys," Journal of Low Temperature Physics 193, 288–297 (2018) [262].

To measure the magnetic sensitivity of TDM SQUIDs (Section 4.1.1), magnetic fields were applied perpendicular to the planes of the SQUIDs used for TDM readout for ACT [120]. The SQUIDs were mounted in the same MUX board used to read out AdvACT single pixels on the DR's coldest stage. V-ϕ curves were acquired for various applied field values using the MCE readout electronics (Figure 4.3). The shift in the V-ϕ curves due to the presence of applied fields was averaged for 72 readout channels and for two applied directions of fields (positive and negative normal). We determine the upper bound on measured sensitivities to be 1.2 ϕ_0/Gauss.

To estimate the magnetic sensitivity of μMUX rf-SQUIDs (Section 4.1.2), magnetic fields were applied perpendicular to the planes of 33 rf-SQUIDs on a single NIST μMUX 14a chip and time-ordered data was taken on each rf-SQUID using a ROACH readout system, returning an average phase response of the μMUX channel in radians as a function of applied magnetic field. Data was taken for two different orientations of the chip within the magnetic shield. A gradient in response to the magnetic field was seen across the μMUX chip in the first orientation, with a minimum in sensitivity at the central rf-SQUIDs and maxima at the ends of the chip (Figure 4.4). This slope is thought to be due to the sensitivity of the gradiometric winding of the SQUID coils to gradients in magnetic field as a function of position inside the DR, since the same response was not observed in the second orientation of the chip within the shield. With this single chip we place an upper limit on magnetic sensitivities of 0.3 ϕ_0/Gauss for the μMUX rf-SQUIDs. Many more chips were characterized in the measurements discussed below.

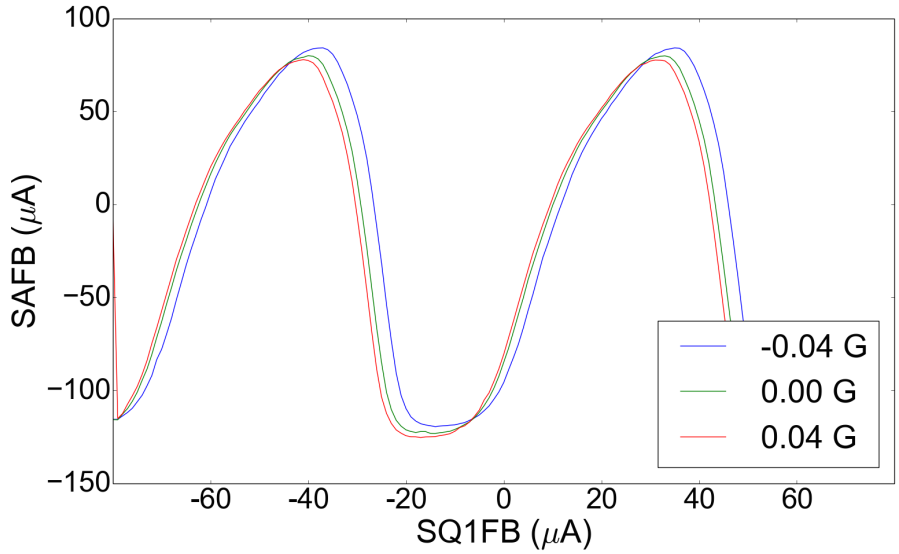

Figure 4.3: An example of shifts in the V-ϕ curve of a single TDM SQUID under the influence of applied magnetic field. Figure is from [262].

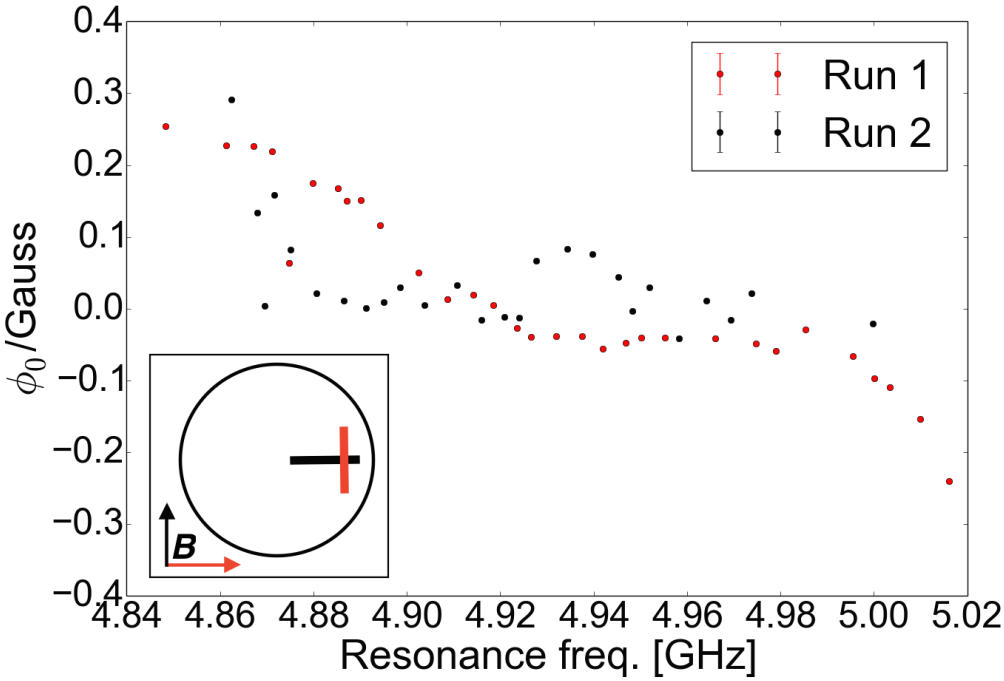

Figure 4.4: ϕ_0/Gauss for resonances on the μMUX chip display a gradient in response across the chip for the Run 1 orientation (red) but not for the Run 2 orientation (black). The top view schematic diagram shows the position of the μMUX chip within the magnetic shield for the two runs along with the applied field directions outside the shield. An upper limit on the magnetic sensitivites of these rf-SQUIDs is taken to be 0.3 ϕ_0/Gauss. Figure is from [262].

4.3 Magnetic Shielding Estimate

Magnetic shielding designs for upcoming CMB experiments should be driven by device sensitivities such as those presented here in order to minimize cost and extent of mechanical design. Using the measurements obtained for our tested TESes and SQUIDs, we can convert detector and readout magnetic sensitivities into estimates of the change in detector bias current per applied magnetic field by using $\frac{\delta I_0}{\delta B} \approx \frac{G(T_c)(-2wB)}{V_0}$, where w is our parameter fit listed in Table 3.4, B is a magnetic field value offset from zero (taken to be 0.05 G, or ~1/10 Earth's magnetic field) and G is the thermal conductance of the TES (eq. 3.3) [5]. Using appropriate values for the types of TESes tested, we obtain sensitivity estimates in detector bias current and list them in Table 3.4 [131, 103, 244, 145]. Because these sensitivities are estimated at an arbitrary value of magnetic field, and the true relationship between dB and dI_0 is more complex than fully represented in this estimate, these numbers should be treated as a comparative guide to relative sensitivities.

A similar calculation can be done to convert the TDM SQUID sensitivity estimate into a predicted detector current response as a function of magnetic fields inside the shielding, using conversion factors particular to our readout setup [5]. For our upper limit sensitivity, 1.2 ϕ_0/Gauss, we estimate $\delta I_{0\ eff}/\delta B \approx 100\ \mu\text{A}/G$, three orders of magnitude larger than the estimates for our TESes. For the μMUX rf-SQUIDS, with an upper limit sensitivity of 0.3 ϕ_0/Gauss due to the gradiometric response of the rf-SQUIDs, $\delta I_{0\ eff}/\delta B \approx 4\ \mu\text{A}/G$.

Based on these measurements, we consider order of magnitude estimates for required shielding factors. These factors would ideally take into account

several phenomena that are not considered here, including the rate at which the instrument is rotated through Earth's field, whether gradients inside the shields result in significantly different pickup levels on different SQUIDs, and how non-common mode magnetic pickup could generate spurious systematics; however, those phenomena are beyond the scope of this study. In this study we consider that the detector white noise level for TDM and μMUX readout is roughly 10^{-10} A/ $\sqrt{\text{Hz}}$ [121]. If we aim to maintain pickup below this noise level and the instrument sweeps through 1/10 of Earth's field (0.05 G) in one second, this would require a shielding factor of roughly 50,000 for TDM and 2,000 for μMUX. If we use a similar scaling approach for the TES pickup in a background DC field comparable to Earth's field, we find smaller required shielding factors for the TESes; however, as described above, the true $\delta I_0/\delta B$ relationship is more complex for TESes than SQUIDs and warrants further study.

Current shielding factors in the field include: ~500 from two A4K shields for AdvACT, with additional localized Nb shielding around the SQUID modules and PCBs [253]; ~150 from two A4K shields for CLASS, with additional magnetic shielding provided by localized Nb shielding around SQUID-based readout components [85]; and ~50,000 from two layers of A4K and two Nb shields for BICEP [220]. Targeted shielding module factors for the Simons Observatory are at or above ~200. As large magnetic field pickup is expected to impede science goals more significantly in the low-l regime (at large angular scales), shielding considerations for the SO SATs will be treated more carefully than for the LATR which is focused on smaller angular scale measurements [19].

4.4 512 Box μMUX SQUIDs for the Simons Observatory

The work presented in this section has been published in E. M. Vavagiakis et al. "The Simons Observatory: Magnetic Sensitivity Measurements of Microwave SQUID Multiplexers," IEEE Transactions on Applied Superconductivity PP(99):1-1 (2021) [263].

The Simons Observatory will use a microwave SQUID multiplexing (μMUX) readout (Section 4.1.2) for its planned ~70,000 TESes (Section 3.2) at an initial multiplexing factor of ~1000. The cold (100 mK) readout components are packaged in a μMUX readout module, which is part of the UFM, and can also be characterized independently [117, 273]. The 100 mK stage TES bolometer arrays and microwave SQUIDs are sensitive to magnetic fields, and their response to changing fields will vary with the local magnetic shielding quality. Each UFM will contain ~1800 μMUX resonators in the 4–8 GHz band, each coupled to a dissipationless radio-frequency superconducting quantum interference device (RF-SQUID), which is in turn inductively coupled to a TES, and read out using a single pair of coaxial cables [214]. The resonators and SQUIDs for SO are developed by NIST (National Institute of Standards and Technology) [76].

We present measurements of the magnetic pickup of test microwave SQUID multiplexers as a study of various shielding configurations for the Simons Observatory. We discuss how these measurements motivated the material choice and design of the UFM magnetic shielding.

4.4.1 Experimental Setup

Readout testing was performed using 512 μMUX resonators and RF-SQUIDs on eight chips installed in the test package referred to as the "512 box." The NIST μMUX chips were of microwave SQUID design uMUX100k v1.0, wafer 1, and covered 4–8 GHz. While the μMUX resonators and RF-SQUIDs may both be sensitive to magnetic fields [90], we cannot yet distinguish between the components' behaviors, and thus refer to the magnetic pickup of each combined channel. 87 channels were chosen for analysis, evenly spaced across the 4–8 GHz frequency range. For each data taking run, the same channels were selected for data taking (as chosen by the closest resonance frequency match).

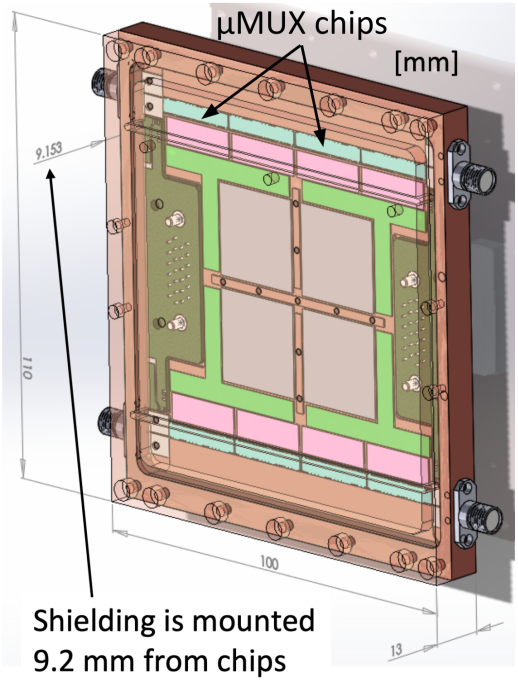

Figure 4.5: Model of the 512 box test package with eight μMUX chips (cyan) mounted in a copper box. Shielding material tested was mounted on the copper cover of the box, 9.2 mm from the chip surface. In the case of a sandwich, shielding material was also mounted on the back of the box, equidistant from the chips. Figure is from [263].

The 512 box (Figure 4.5) was mounted to the cold stage of a Bluefors dilution refrigerator (DR) and cooled to 100 mK (Figure 4.6). Any shielding material tested was placed on one or both sides of the test packaging, 9.2 mm from the chips. Any single layer of shielding material was mounted to the side of the 512 box shown in Fig. 4.5, while sandwiches of material included a layer attached to the back side in Fig. 4.5.

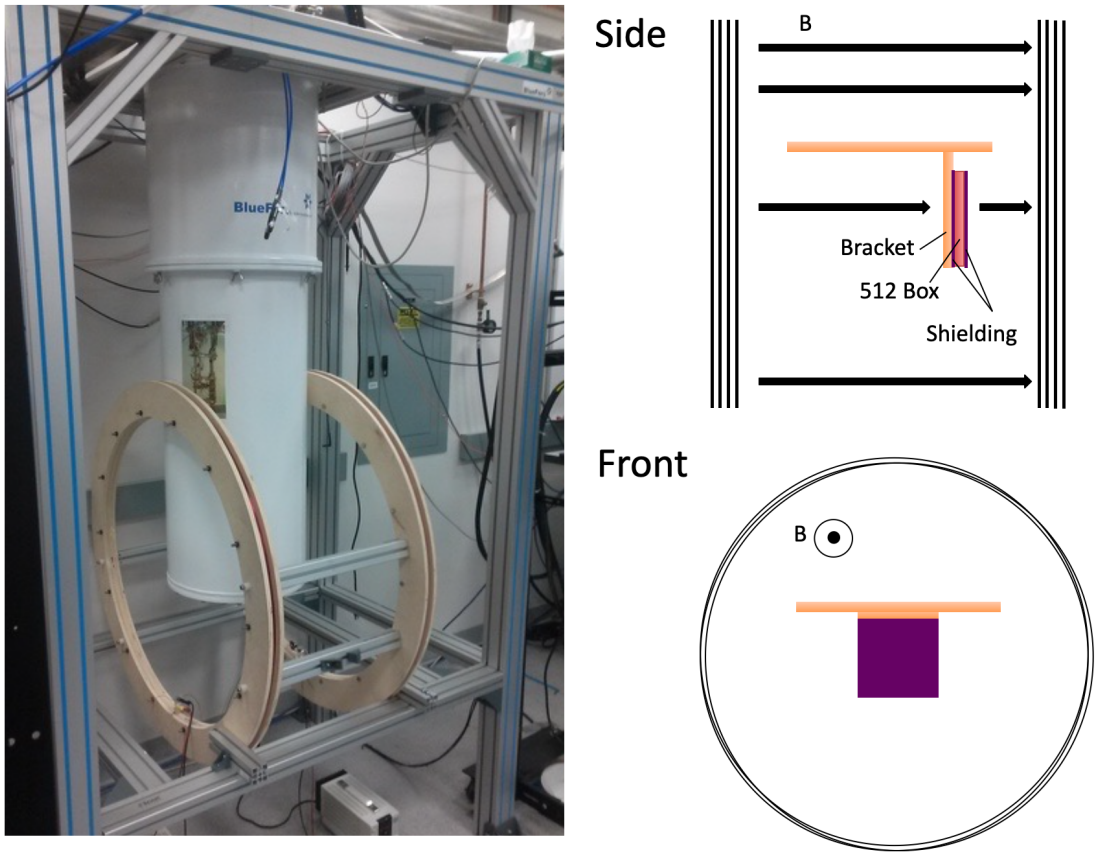

Figure 4.6: Experimental setup for the 512 box magnetic field testing. The 512 box package was mounted to the 100 mK plate of a Bluefors dilution refrigerator. A set of Helmholtz coils apply DC fields perpendicular to the μMUX chips, as shown installed around the DR on the left. On the right, a schematic of the DR mixing chamber plate and mounted 512 box test package is shown along with the coils. The "front" view looks along the z-axis of the coils to the face of the 512 box test package, and the "side" view shows the x-axis of the coils and the edge of the 512 box package. The orientation of the applied magnetic field is annotated "B." Figure is from [263].

An external room temperature mu-metal magnetic shield was placed over the DR while the test chips were cooled to avoid trapping magnetic flux in the chips which would degrade their performance. Once at base temperature, this shield was removed, and a set of Helmholtz coils were positioned outside of the vacuum shell of the DR to apply constant DC magnetic fields perpendicular to the plane of the chips (Fig. 4.6). Fields were not applied parallel to the plane of the chips because uniform magnetic fields applied in this direction should not couple to the SQUIDs or resonators. No additional magnetic shielding beyond the test pieces near the chips was included.

4.4.2 Magnetic Field Application

Upon reaching base temperature, the external mu-metal magnetic shield around the DR was removed, and the Helmholtz coils were installed. The highest field value tested (0.525 G) was applied for approximately one minute, and then removed. DC fields were then applied starting at 0 G for a given polarity, and stepped from 0 to 0.525 G in steps of 0.105 G. Fields were applied by setting a power supply to a given current value (i.e. were set suddenly and not ramped up slowly). The field polarity was then reversed, and data were again taken starting from low to high applied field. The field polarities were not tracked between cooldowns, and small relative asymmetries between the two polarities are expected from Earth's magnetic field.

At each applied field value, a vector network analyzer (VNA) traced S parameters versus frequency, and the frequency (f) of minimum magnitude of S21 was recorded for each applied voltage. Voltage applied to the flux ramp line

was stepped from 0 to 0.5 V in discrete steps of 0.02 V to trace f-Φ curves for the chosen channels (Φ, the flux through the SQUID, is controlled by voltage applied). Seeking only to measure the phase offsets in Φ, a simple sinusoid was fit to the resulting f-Φ curves, where one period is Φ_0, the magnetic flux quantum, in this case 0.39 V. The phase offsets of the sinusoid fits ($d\Phi/\Phi_0$) were recorded for each SQUID (Fig. 4.7).

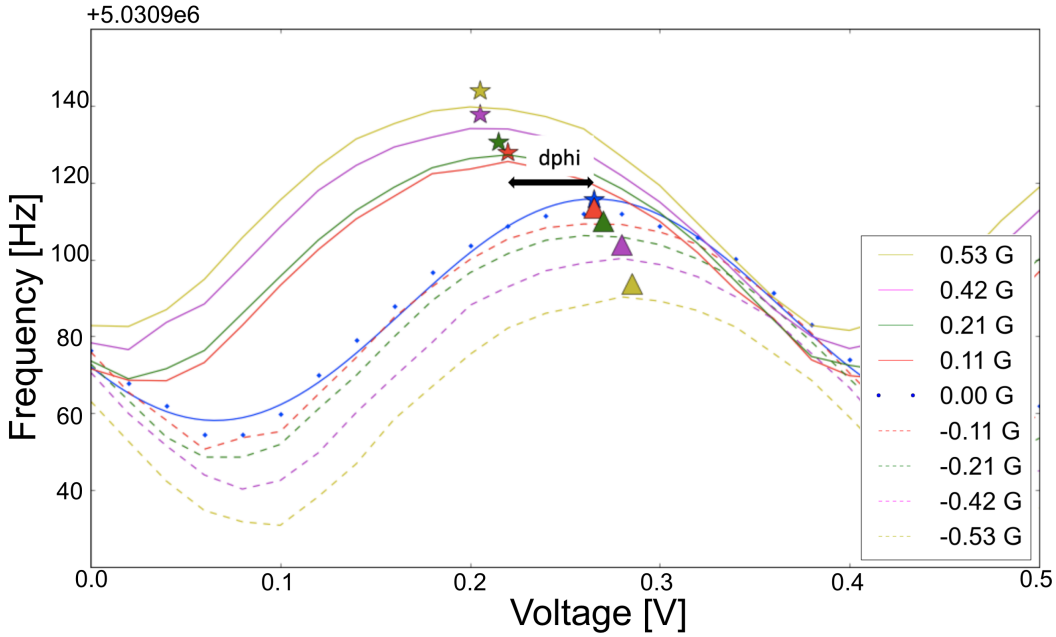

Figure 4.7: Applied field values shift the SQUID f-Φ curves as fit to the data acquired with the VNA. An example of the zero applied field data points are plotted in blue, with the sinusoid curve fit blue line overplotted. The stars and triangles mark the peaks of the fits, which are used to calculate the phase offsets. The offsets in phase ($d\Phi$) are recorded to measure the magnetic pickup in Φ_0/Gauss. Figure is from [263].

The offsets from Earth's magnetic field and the zero-flux phase are accounted for by subtracting the zero applied field $d\Phi/\Phi_0$ from all the data points for each channel, such that $d\Phi/\Phi_0 = 0$ for 0 G applied field. The absolute value of these responses is taken so that one linear fit may be performed to the positive and negative shifts. The best fit sensitivity in Φ_0/G for the tested resonances was

estimated by fitting a line (y = mx, where m = Φ_0/G) to the average absolute value of the f-Φ curve phase shifts as a function of applied magnetic fields.

We found that exposing the chips to the highest value of applied field (0.525 G) had the effect of "settling" the channels such that their measured sensitivity was lower after this exposure as compared to before. This applied field value is larger than the component of Earth's magnetic field running perpendicular to the surface of the chips, which is estimated to be ~0.05 G. This meant that removing the external magnetic shield and taking measurements starting at 0 G to 0.525 G yields a higher pickup estimate than subsequent repeated set of identical measurements (Fig. 4.8). This led us to adopt the approach applying the maximum field value (0.525 G) for ~1 minute before taking the data compared in Fig. 4.9.

With this approach, no hysteresis was observed when taking data from 0 to 0.525 G in steps of 0.105 G, and then again from 0.525 to 0 G in steps of 0.105 G for the test assembly with a single piece of 0.002" Al.

4.4.3 Shielding Materials

The magnetic shielding materials tested included two thicknesses (1/32", 0.002") of 6061-T6 aluminum, 0.002" thick Type 2 annealed niobium from Eagle Alloys, and a hexagonal piece (127.20 ± 0.50 mm corner to corner, × 1 mm thick) of annealed A4K from Amuneal.

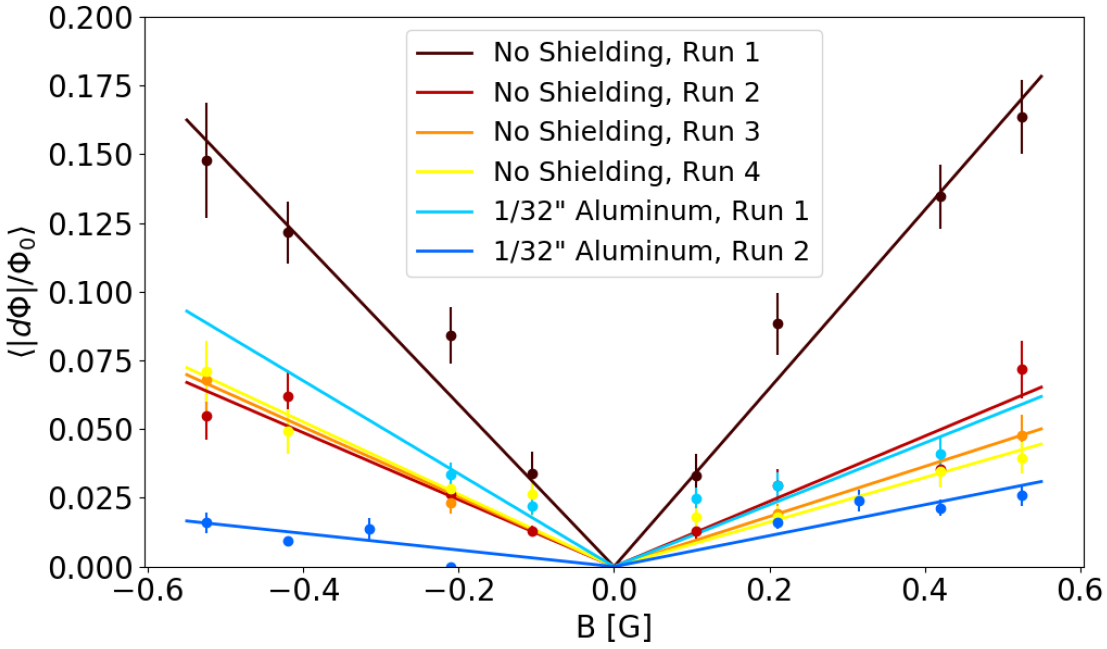

Figure 4.8: "Settling" the μMUX channels by applying a 0.525 G field for 1 minute before data taking (No Shielding, Runs 2, 3 and 4, 1/32" aluminum, Run 2) versus data taking without first applying the 0.525 G field (No Shielding Run 1, 1/32" aluminum Run 1). Error bars shown are standard errors. Linear fits to the average absolute value of $d\Phi/\Phi_0$ for the channels per applied field value are plotted as solid lines. The average response of the channels decreases after the initial magnetic field is applied. Figure is from [263].

4.4.4 512 Box μMUX SQUID Results

Tab. 4.1 lists the average sensitivity results for the data taken in a given magnetic shielding configuration. Average Φ_0/Gauss sensitivities as estimated by linear fits to the average f-Φ phase offsets for the 512 box μMUX channels per applied field value are shown for each material configuration. Uncertainties listed come from the linear fits to the average data point per applied field value. A factor of sensitivity reduction from no shielding material is listed.

With no shielding, the 512 box μMUX channels show a 0.108 ± 0.015 Φ_0/G shift as estimated using the mean linear fit. This fit is a conservative estimate

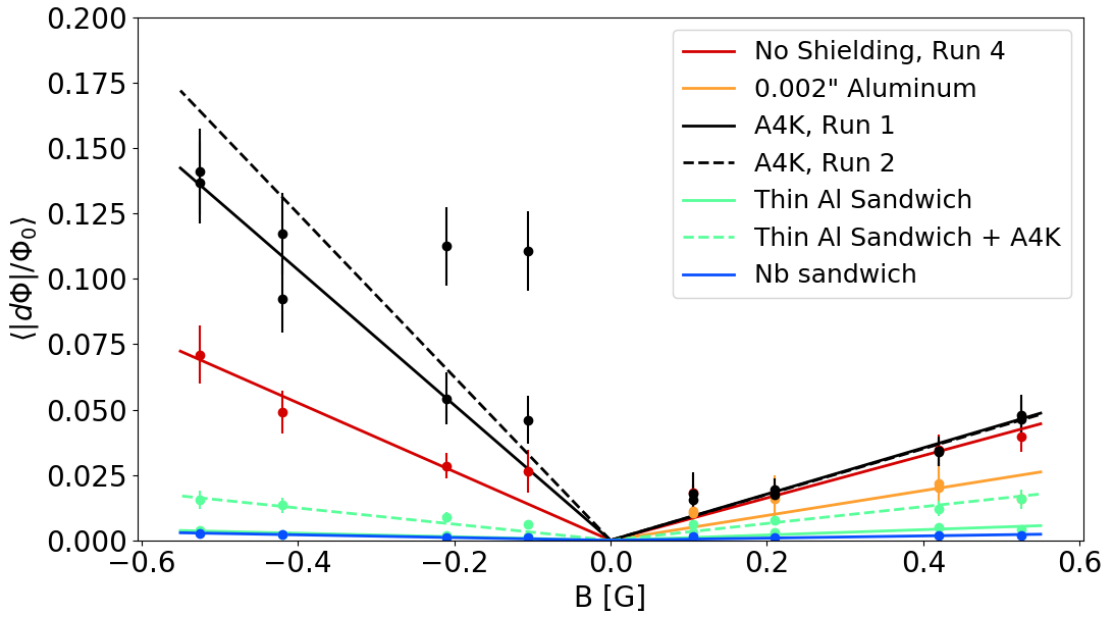

Figure 4.9: Magnetic pickup experienced by the 512 box channels when shielded by a single piece of A4K (black), a thin (0.002") single piece of Al (blue) or a sandwich of the same (green), the thin Al sandwich plus a piece of A4K (dashed green), or a niobium sandwich (orange), compared to no shielding (magenta). The best shielding configurations were the sandwiches of superconductors, and the worst was the single piece of A4K. Figure is from [263].

of the responses, as the distribution of Φ_0/G per channel was not Gaussian, but positively skewed with a lower mode (Fig. 4.10). The best shielding configurations tested were the sandwiches of 0.002" Al or Nb, with a layer of superconductor on either side of the μMUX chips, 9.2 mm from the chip surface. These two shielding configurations reduced the shift by a factor of 12.0 or 21.6, respectively. Single layers of Al were the next most successful, providing a 2.0–2.5 factor reduction in field pickup.

The single layer of annealed A4K yielded higher pickup than no shielding, and introduced a field polarity-dependent asymmetry in sensitivity, repeatable over multiple data-taking runs. To check for asymmetries introduced by the hexagonal shape of the A4K piece, only channels on the central 512 box chips

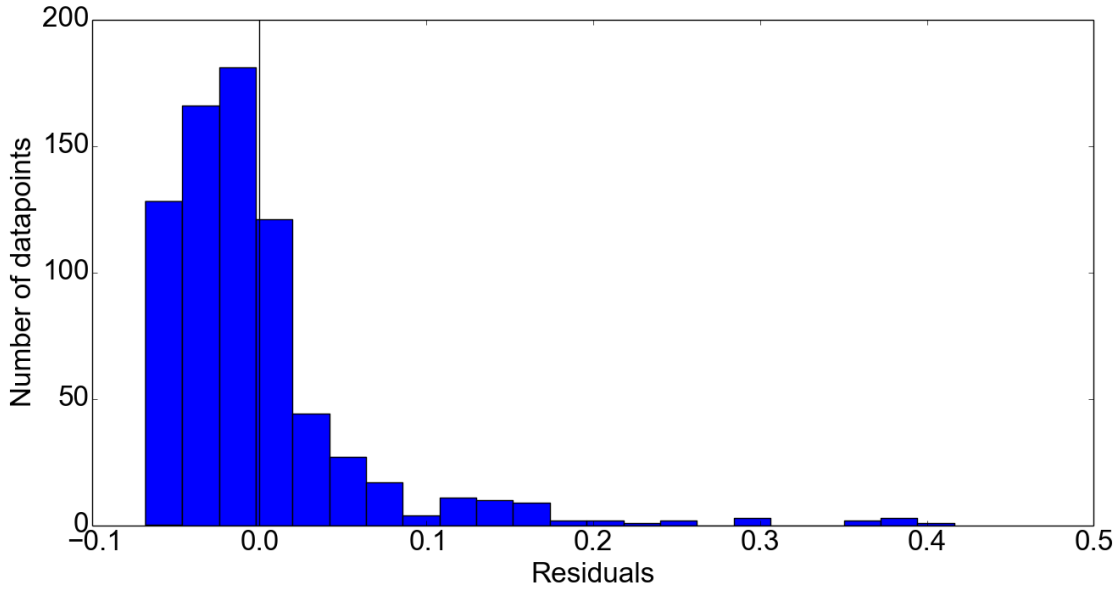

Figure 4.10: Residuals in $|d\Phi|/\Phi_0$ from the linear fit to No Shielding Run 2 (Fig. 4.8). The distribution is typical for all data-taking runs, with most channels showing a lower response than the linear fit to the average, and a small number of channels showing a higher response. Figure is from [263].

(which were farthest from the hexagonal edges of the piece) were analyzed. The behavior was the same for these chips alone. When the piece of A4K was included inside the 0.002" sandwich of Al, the shielding was degraded by a factor of 3.6 as compared to the 0.002" sandwich of Al alone.

4.5 Conclusions

We have made measurements of the magnetic sensitivity of AlMn and MoCu TESes, varying in geometry, leg length and doping, TDM SQUIDs, μMUX rf-SQUIDs, and NIST test chip μMUX resonators and RF-SQUIDs for the Simons Observatory.

The measured unshielded channel sensitivity of 0.108 ± 0.015 Φ_0/G of the

Table 4.1: Magnetic Shielding Results

Material	**Sensitivity [Φ_0/G]**[a]	**Reduction Factor**[b]
None	0.108 ± 0.015	1.0
1/32″ Al	0.044 ± 0.009	2.5
0.002″ Al	0.053 ± 0.007	2.0
A4K	0.199 ± 0.091	0.5
0.002″ Al SW[c]	0.009 ± 0.002	12.0
0.002″ Al SW+A4K[d]	0.033 ± 0.005	3.3
0.002″ Nb SW[e]	0.005 ± 0.001	21.6

[a]Average pickup of the channels for the shielding configuration.
[b]Factor by which sensitivity was reduced compared to no shielding.
[c]A sandwich of 0.002″ Al.
[d]A sandwich of 0.002″ Al + layer of A4K within the top layer of Al.
[e]A sandwich of 0.002″ Nb.

NIST test chip μMUX resonators and RF-SQUIDs for the Simons Observatory in [263] (section 4.4.4) is in agreement with the upper bound of 0.3 Φ_0/G placed on NIST μMUX RF-SQUIDs in [262] (Section 4.2). This pickup equates to a 2 μm^2 effective cross-section, or one part in 2×10^4 of the 40,000 μm^2 SQUID area, and is due to imperfect gradiometry, metal symmetry, and uniformity of applied field. Because Earth's field can produce a magnetic flux quantum through just a 40 μm^2 area, and the SQUIDs are much larger, gradiometry and magnetic shielding must be combined to provide sufficient insensitivity to Earth's field and other sources while scanning and observing. Layers of superconducting materials 6061-T6 Al and Nb reduce the measured pickup by a factor of 2.0-21.6. This behavior agrees with general expectations as both Type I and II superconductors respond to applied magnetic fields by setting up electric surface currents that cancel out these fields. It is notable that single layers of superconductors provided ~5–11 times less shielding than sandwiches of superconductors. The presence of A4K degraded the shielding performance of an Al sandwich by a factor of ~4, and increased the sensitivity of the μMUX SQUIDs when compared

to no shielding at all. The presence of A4K also introduced a large field polarity asymmetry. This motivated the decision not to include A4K in the SO UFM packages.

Instead of canceling out applied magnetic fields like superconductors, A4K redirects them. The details of an A4K shielding geometry may thus have profound effects on the material's shielding ability: single flat layers of A4K may not behave like cylindrical shields or boxes, acting to concentrate, distort, and amplify magnetic fields instead of redirecting and attenuating them. It can also be difficult to simulate the behavior of A4K due to numerical issues when modeling high-permeability materials like A4K directly next to zero-permeability materials like superconductors. Our measured results did not agree with our expectations from simulations using ANSYS Maxwell, which estimated that adding a single hexagonally shaped sheet of A4k to the 0.002" Al sandwich would improve, rather than degrade, the shielding performance of the sandwich by a factor of ~4 (Figure 4.11). The disagreement with this result from simulations highlights the importance of laboratory measurements to accurately predict the effectiveness of magnetic shielding materials and geometries.

Along the same lines, our results may not easily extend to real-world SO UFM shielding designs. Current magnetic shielding tests are being conducted with a more realistic package for an SO μMUX multiplexer assembly with updated NIST microwave SQUID design that includes a 6061-T6 Al cover with holes in it for connectors. Introducing holes in this material may degrade its shielding performance. The best performing sandwiches of continuous layers of superconductors may be difficult to implement within the UFM, so further tests are ongoing to define the UFM shielding design.

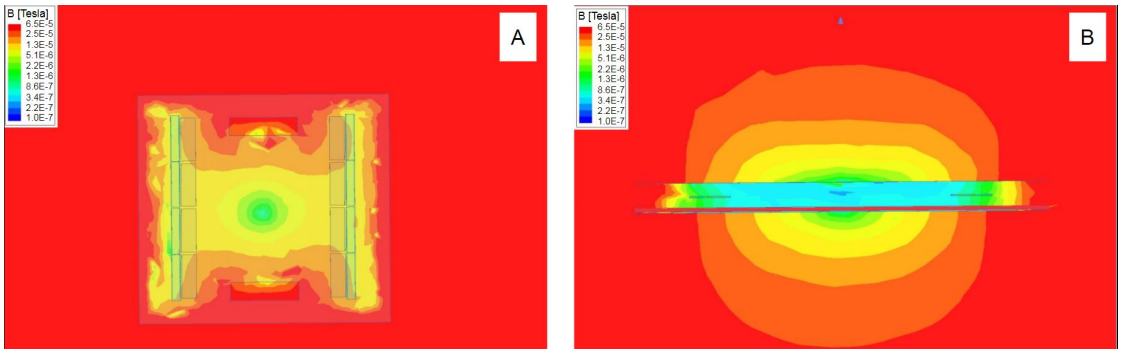

Figure 4.11: Magnetic shielding simulations performed by Aamir Ali using ANSYS Maxwell for two shielding configurations for the 512 box. A: 0.002" Al sandwich including realistic holes for connectors. B: Same as A (0.002" Al sandwich including realistic holes for connectors) with the addition of an A4K hexagon with the same geometry as that tested in the lab (127.20 ± 0.50 mm corner to corner, × 1 mm thick). The shielding factor in configuration A was estimated to be 3-6, which underestimated the observed shielding factor of 12. The shielding factor in configuration B estimated to be 10-20, which disagrees with the measurements in which the addition of A4K degraded the shielding performance of the Al sandwich by a factor of ~4. Simulations and images are courtesy of Aamir Ali.

We used our estimates for AlMn TES, TDM SQUID, and μMUX SQUID magnetic sensitivities from device measurements along with simulations to inform shielding factors that would sufficiently suppress field excursions in upcoming experiments. These results will inform the design of magnetic shielding for future CMB experiment receivers such as those for CCAT-prime, Simons Observatory, and CMB-S4 and thereby help enable precision measurements of the CMB.

CHAPTER 5

SUNYAEV-ZEL'DOVICH MEASUREMENTS WITH THE ATACAMA COSMOLOGY TELESCOPE

By combining high-resolution maps from the Atacama Cosmology Telescope with optical catalogs from BOSS-SDSS, we have made increasingly precise measurements of the kSZ and tSZ effects in maps of the CMB. By measuring both SZ effects using the same datasets, we compare independent estimates of halo optical depth to explore the potential for tSZ measurements to provide optical depth information in order to measure pairwise velocity curves and constrain cosmology. By probing the optical depth of these galaxy halos, we begin to constrain their baryon content, and progress towards an empirical relationship between optical depth and Compton-y which will inform simulations of galaxy evolution and future cosmological constraints.

The majority of the work presented in this chapter has been published in F. De Bernardis, S. Aiola, E. M. Vavagiakis, N. Battaglia, M. D. Niemack et al., "Detection of the pairwise kinematic Sunyaev-Zel'dovich effect with BOSS DR11 and the Atacama Cosmology Telescope," Journal of Cosmology and Astroparticle Physics 03, 008 (2017), and E. M. Vavagiakis, P. A. Gallardo, V. Calafut, S. Amodeo et al. "The Atacama Cosmology Telescope: Probing the Baryon Content of SDSS DR15 Galaxies with the Thermal and Kinematic Sunyaev-Zel'dovich Effects," (2021) (in submission to Physical Review D) [68, 264].

5.1 ACT Data

5.1.1 ACT DR3

In 2011, Hand et al. presented a measurement of the tSZ effect in ACT maps using a matched-filtering method with an assumed galaxy cluster profile [112]. In De Bernardis et al. 2017, henceforth DB17 [68], we used a 600 $\deg^2$ map from ACT Data Release 3 (DR3) with an aperture photometry filter for the kSZ pairwise analysis and a matched filter for the tSZ signal extraction. This map used a combination of data from two seasons of ACT observations [62] and two seasons of nighttime observations with the ACTPol receiver [254] at 148 GHz [174]. The coadded area included the deep patches called D5 and D6, centered at right ascensions (RA) -5° and 35°, as well as the region encompassing D5 and D6, previously called deep56 and now referred to as D56 [69]. The D56 area was observed deeply in 2014 and 2015 and spans roughly from RA of -9° to 43° and declination of -7° to 4° with a total area of about 456 sq. deg [163]. The white noise level in the D56 area from the 2014 observations ranges from 10 to 20 μK·arcmin. Figure 5.1.1 shows the coadded map used in DB17 overlaid with the galaxies from the SDSS DR11 catalog, described in Sec. 5.2, used as tracers in the SZ analysis.

5.1.2 ACT DR4 and DR5

Our 2021 work used two component separated internal linear combination (ILC) maps, referred to as the DR4 ILC maps, covering the same D56 region as in DB17, as well as the BN (1633 sq. deg.) region. The ILC maps are cre-

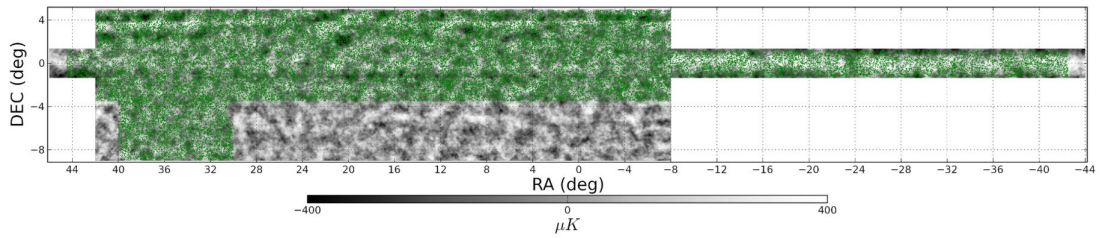

Figure 5.1: The ~600 sq. deg. 148 GHz ACT map used in the DB17 SZ analysis, overlapping with the 67,938 SDSS DR11 sources in green. The longest strip in RA was the region of sky used for the first measurement of the pairwise kSZ effect in Hand et al. 2011 [112]. Figure from [68].

ated using two seasons of observations with the ACTPol receiver (ACT DR4) and public *Planck* satellite data [163]. In Calafut et al. 2021 (C21, [47]), we use the CMB+kSZ DR4 ILC map, and in Vavagiakis et al. 2021 ([264]), we use the Compton-y DR4 ILC map. The ILC approach was designed to account for the anisotropic noise found in ground-based CMB experiments. The ILC method combines multi-frequency data from *Planck* and ACT and constructs wide-area, arcminute-resolution component-separated maps of CMB temperature and the tSZ effect. CIB-deprojected Compton-y maps are also available, but we did not analyze them due to their higher noise. Additionally, we used ACT DR5 single frequency data at 150 and 98 GHz coadded with data from *Planck* at 100 and 143 GHz to cover about 21,100 sq. deg. of sky (3,700 sq. deg. of which overlaps with the SDSS data sample) [175] (Figure 1.4). These maps are referred to as the DR5 f150 and DR5 f090 maps. While the DR5 data has the highest signal-to-noise ratio, the DR4 ILC results serve to check consistency with a map that already combines the multi-frequency information. A higher signal-to-noise ILC map for the DR5 data was not available at the time of analysis, but will be useful for future measurements. The beams have FWHM = 1.3′, 2.1′, and 1.6′ for the DR5 f150, DR5 f090 and DR4 ILC maps, respectively, with associated uncertainties of several percent [175].

The inverse white noise variance map associated with the DR5 data is used for cutting the SDSS data sample (Section 5.2.2) and for weighting (Section 5.3.4). For the ILC analysis, the DR5 f090 inverse white noise variance map is used for weighting as it best estimates the noise properties in the ILC map. Figure 5.2 shows the ACT+*Planck* map overlaid with the selected 343,647 sources from the SDSS DR15 catalog.

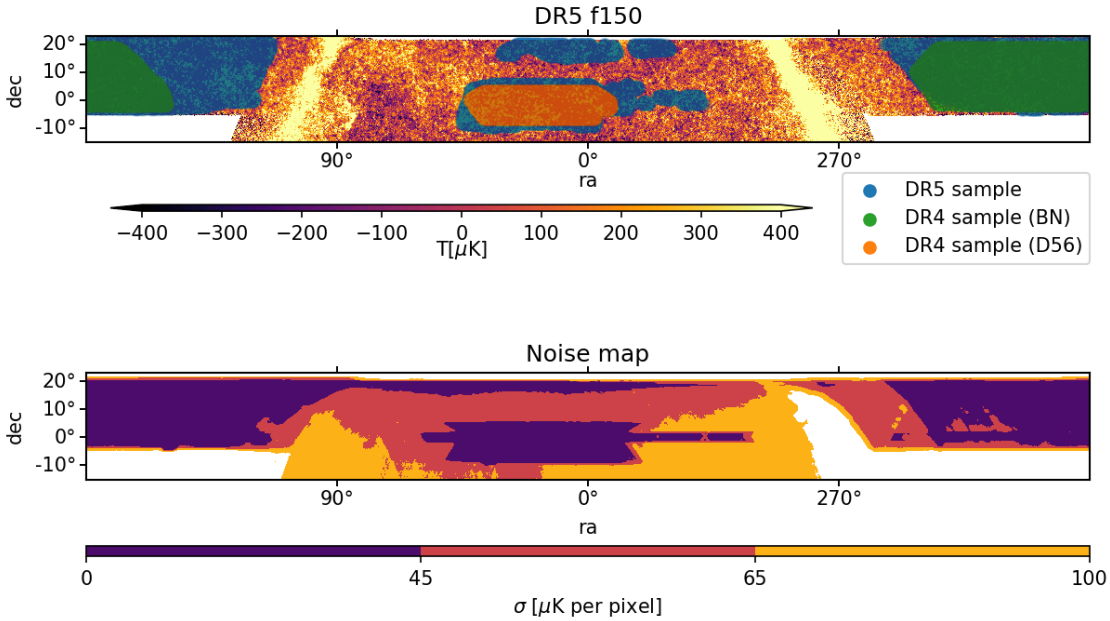

Figure 5.2: Top: The ACT + *Planck* map used for the DR5 f150 analysis in V21 with the overlapping 343,647 SDSS DR15 selected sources plotted in blue over 3,700 sq. deg., and the BN and D56 areas covered by the ILC maps plotted in green and orange, respectively. Bottom: The inverse white noise variance map associated with the DR5 f150 coadded ACT+*Planck* map highlighting regions representing a noise equivalence of 45 and 65 μK per pixel (with a 0.5 arcmin resolution plate Carré projection), which were used to cut the SDSS sample for the DR5 f150 analysis. The orange and yellow regions of higher noise overlapped with 27% of the DR15 sample. The SDSS sample was cut using the more conservative 45 μK per pixel inverse white noise variance map limit, shown in purple. We performed an equivalent cut for the DR5 f090 map and analysis. Figure is from [264].

5.2 SDSS Data

In both our 2017 and 2021 works, we used sources from the Sloan Digital Sky Survey (SDSS) Baryon Oscillation Spectroscopic Survey (BOSS [66]) to trace the positions of galaxy clusters and groups. SDSS conducts optical and infrared spectroscopy [227, 269] using the 2.5-meter Sloan Foundation Telescope at the Apache Point Observatory in New Mexico [109] and infrared spectroscopy using the du Pont Telescope at Las Campanas Observatory in the Atacama Desert in Chile [44]. SDSS measures galaxies and quasars at z ~ 0.6–3.5 to characterize large scale structure, nearby galaxies using integral field spectroscopy, and large scales of the Galaxy with high resolution near-IR measurements [18]. For our purposes, we use publicaly available catalogs of luminous red galaxies including position, luminosity and redshift information, described below in Sections 5.2.1 and 5.2.2.

5.2.1 DR11 Sample

In DB17, we used the public Large Scale Structure (LSS) DR11 catalog [1]. Sources within a 5 arcmin radius from >15 mJy point sources were cut from the sample, leaving 67,938 objects overlapping with the DR3 map area, with redshifts ranging from 0.05 to 0.8 with an average redshift of 0.48. The luminosities of the sources were calculated based on their r-band Petrosian de-redened magnitudes and a K-correction applied using the kcorrect[2] software [40]. The K-corrected luminosities for the sample ranged from 1.5×10^8 to $1.25\times10^{12} L_\odot$. In addition to the SDSS sources, sources from the redMaPPer [210, 208, 209] SDSS DR8 cata-

[1] http://data.sdss3.org/sas/dr11/boss/lss
[2] http://kcorrect.org

log of galaxy clusters were analyzed for comparison. The redMaPPer algorithm provides a more precise estimate of cluster centers, at the cost of a smaller sample of objects and the inclusion of less precise photometric redshifts as opposed to spectroscopic redshifts of individual luminous red galaxies (LRGs). 31,600 sources overlapped with the coadded ACT DR3 map, of which only 2,242 met a redMaPPer richness cutoff of λ>20 after including a correction factor which accounted for masked clusters and incompleteness [68].

To explore the dependence of the SZ signals on the luminosity of the LRG sample, eight bins were chosen in the range $5.3\times10^{10}L_{odot}$-$11.6\times10^{10}L_{odot}$ (corresponding to the brightest 50,000 and 5,000 sources, respectively). The range was then divided by choosing the most luminous 5,000 sources, and increasing the number of objects per bin in steps of 5,000, or 10,000 for the larger bins. The number of sources per bin used in the tSZ analysis were slightly reduced due to wider submaps discarding some sources at the map edges. The selected luminosity cuts and the number of sources per bin is shown in Table 5.1.

5.2.2 DR15 Sample

In our 2021 work, 602,461 SDSS DR15[3] LRGs overlapping with the DR5 f150 ACT+*Planck* map were selected for use through a luminosity cut, a cut based on the CMB map noise level, point source masks, and a Galactic plane mask. The catalog was downloaded from the SDSS SkyServer using the query presented in Appendix B.1. The luminosities of the sources were calculated based on their (multiband) de-reddened SDSS composite model magnitudes and K-corrected using the kcorrect [40] software according to the luptitude to flux conversion

[3]https://www.sdss.org/dr15/

		kSZ Analysis	tSZ Analysis		
Luminosity cut/$10^{10}L_\odot$	Mass cut ($M_{200}/10^{13}M_\odot$	N	$\langle L\rangle/10^{10}L_\odot$	$\langle z\rangle$	N
$L > 5.30$	$M > 2.8$	50000	46448	0.52	8.22
$L > 6.10$	$M > 3.2$	40000	37190	0.51	8.85
$L > 6.90$	$M > 3.8$	30000	27877	0.50	9.64
$L > 7.40$	$M > 4.2$	25000	23251	0.49	10.13
$L > 7.90$	$M > 4.6$	20000	18586	0.48	10.75
$L > 8.70$	$M > 5.2$	15000	13898	0.48	11.56
$L > 9.80$	$M > 6.1$	10000	9269	0.47	12.73
$L > 11.60$	$M > 7.6$	5000	4650	0.47	14.90
$5.30 < L < 7.90$	$2.8 < M < 4.6$	30000	27880	0.45	6.53
$7.90 < L < 9.80$	$4.6 < M < 6.1$	10000	9299	0.45	8.77

Table 5.1: Luminosity bins, corresponding mass cuts, and number of sources per bin for the DB17 pairwise kSZ analysis, as well as the number of sources, average luminosity per bin, and average redshift per bin for the DB17 tSZ analysis. The number of sources per bin for the tSZ analysis is smaller because of the cropping of map edges required for the larger submaps used in the analysis. Numbers in this table are taken from [68].

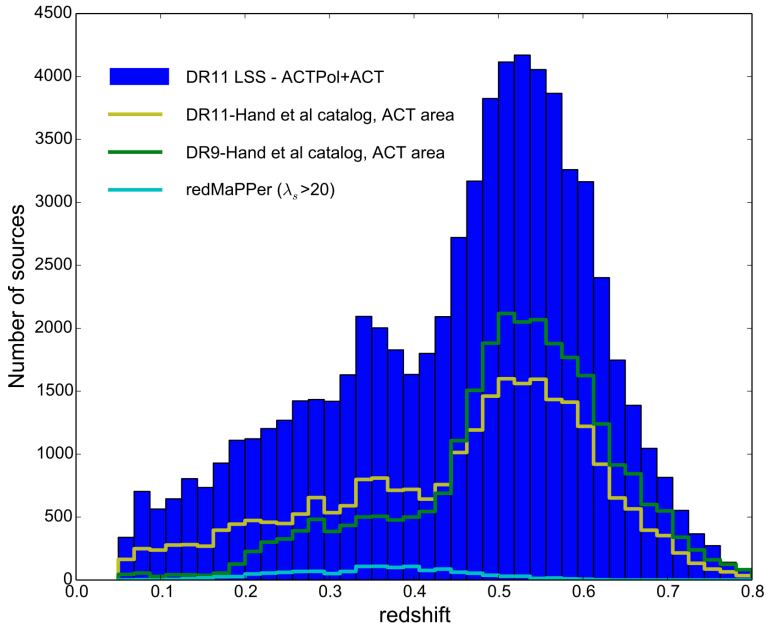

Figure 5.3: A histogram of the redshifts of SDSS DR11 tracer sources used in the DB17 ACT DR3 SZ analysis (dark blue). The overlap of the DR11 catalog with the same area as the DR9 selection used in [112] (green, 27,291 galaxies) for the 220 sq. deg. ACT-only region is shown in yellow (26,357 galaxies). The light blue line shows the much smaller selected redMaPPer sample. Figure is from [68].

outlined in [161]. The DR15 luminosities of the selected sources range from $4.30 \times 10^{10} L_\odot$ to $2.61 \times 10^{12} L_\odot$ with an average luminosity of $7.38 \times 10^{10} L_\odot$. Luminosity bins for joint tSZ and kSZ analyses with C21 were chosen to match two of the luminosity cuts from DB17 ($L = 7.9 \times 10^{10} L_\odot$ and $L = 6.1 \times 10^{10} L_\odot$) as well as one lower luminosity cut ($L = 4.3 \times 10^{10} L_\odot$). The three disjoint bins based on these cuts were selected to have roughly equal spacing, and such that each bin has over 100,000 galaxies that pass cuts for analysis with the DR5 maps (Table 5.2). The cumulative luminosity bins include the highest signal-to-noise SZ measurements, while the disjoint bins enable comparisons between independent bins. Since the tSZ signal-to-noise ratio is higher for high mass halos, we also perform the tSZ analysis for the two highest mass bins from DB17 (L98 and

L116) which are not studied in C21. A plot of the luminosity distribution and bins is shown in Appendix B.2.

After we selected luminosity bins and applied the minimum luminosity cut, which removed 80,162 lower luminosity sources from the sample, we performed an inverse white noise variance cut. Figure 5.2 shows the inverse white noise variance map that was used to explore cuts in a DR14 sample. Initially two different cuts were studied (45 and 65 μK per pixel) (Figure 5.4). The more conservative cut of 45 μK per pixel was selected for all subsequent analyses based on a signal-blind uncertainty analysis which compared the jackknife error bars on the aperture photometry (AP) analysis for the samples cut by 45 μK per pixel, 65 μK per pixel, and no noise cut. The 45 μK per pixel cut removes 27%, or 140,209 sources from the overlapping sample and improves the jackknife error bars as compared to no noise cut (Figure 5.4).

Galactic plane masking was then performed with the mask used in the production of the 2015 *Planck* Compton-*y* map to reduce Galactic contamination [193] (Figure 5.5). The 50% mask was selected to conservatively cut sources from the Galactic plane region of the ACT+*Planck* map, resulting in a cut of 26,521 additional sources from the DR15 sample.

To mask point sources we first used the two source masks developed for Choi et al. 2020 [56]. For the lowest noise D56 region a 15 mJy point source mask was applied, and for the higher noise regions a 100 mJy mask was applied. Together these masks removed an additional 11,922 sources from our sample, leaving us with a final selected sample of 343,647 sources after all masks and cuts are applied.

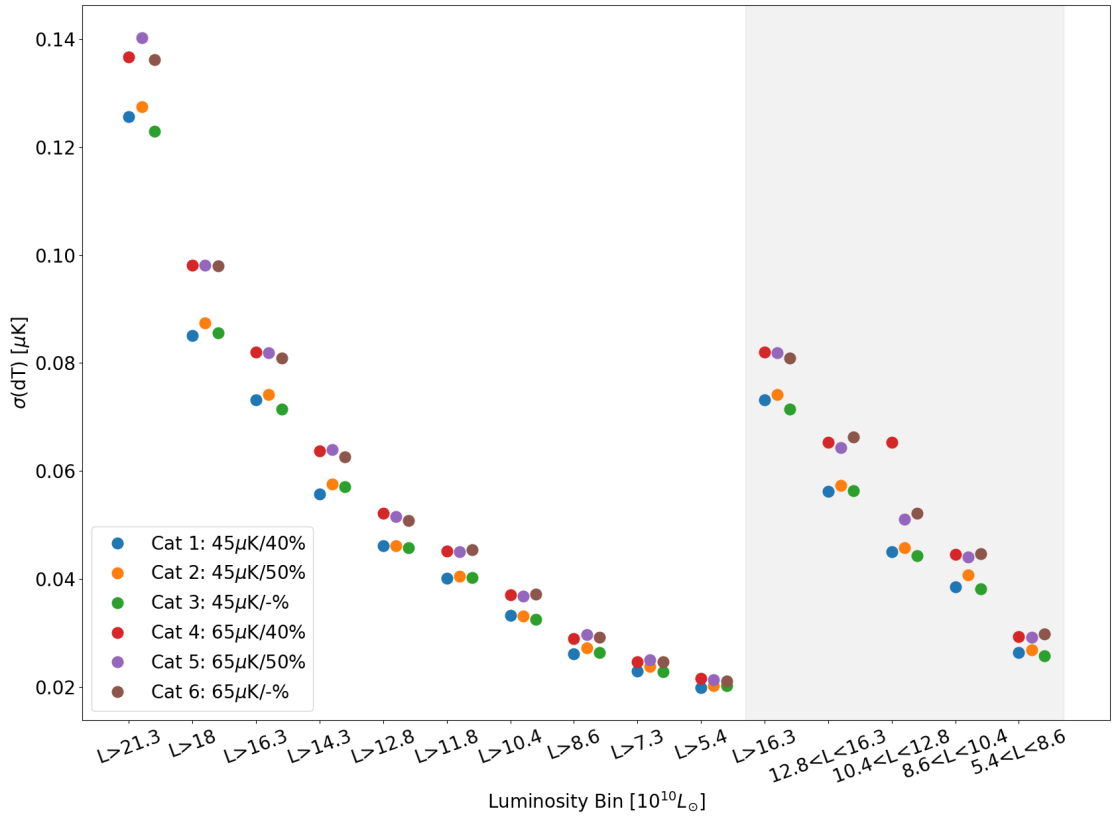

Figure 5.4: A signal-blind comparison of the tSZ analysis in an earlier set of luminosity bins with the previous SDSS DR14 sample, to motivate cuts in the final analysis. A kSZ analysis on these 6 sample catalogs was also performed. The catalogs contained between 313078 and 457916 sources, depending on the combination of cuts, which included a 50% or 40% Galactic plane mask and/or a 45 μK per pixel or 65 μK per pixel inverse white noise variance map cut. The more conservative inverse white noise variance map cut was selected based on this comparison because it improved the jackknife error bars in the tSZ analysis as well as the uncertainty in the kSZ pairwise analysis.

Figure 5.6 shows the redshift distributions of the 343,647 DR15 galaxies overlapping with the ACT+*Planck* map after the luminosity, inverse white noise variance map, Galactic plane mask and point source mask cuts. The 67,938 DR11 sources overlapping with the coadded ACT DR3 map used in our 2017 result (Figure 5.3) are also shown for comparison. The redshifts range from 0.08 to 0.8 with an average reshift of 0.49 for the DR15 catalog.

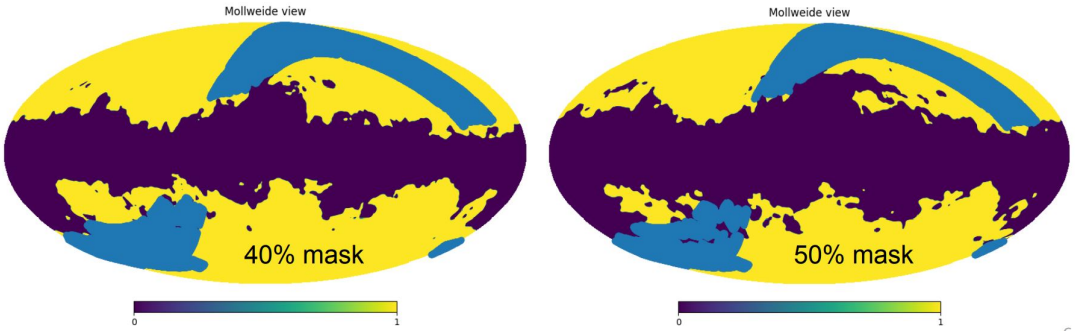

Figure 5.5: The 40% and 50% Galactic plane masks used in the production of the 2015 *Planck* Compton-y map [193], overlapping with the SDSS DR15 catalog (blue points). Regions with mask value 0 (dark purple) are excluded from the analysis. The 50% mask was chosen to conservatively cut sources from the Galactic plane region of our maps, which resulted in a cut of 26,521 sources after the inverse white noise variance cut and luminosity cut.

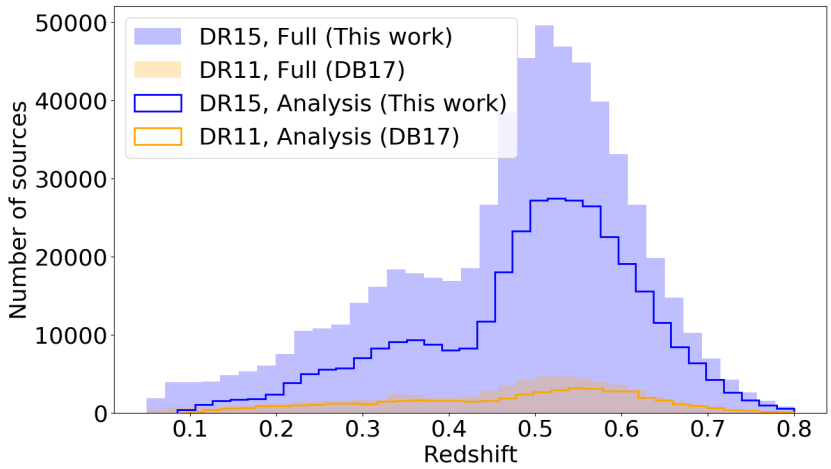

Figure 5.6: The SDSS DR15 redshift distribution for the 602,461 total galaxy sample and selected 343,647 galaxy sample for the analysis in V21 and C21 overlapping with the ACT+*Planck* DR5 map, as compared to the ~9 and ~7 times fewer DR11 galaxies overlapping with the ACT DR3 area and those used for the 2017 result (DB17), respectively. Figure is from [264].

Histograms of the luminosities depicting cuts and bins are provided in Appendix B.2. The properties of each luminosity-selected bin are summarized in Table 5.2. The mean stellar masses are estimated from the mean luminosities

assuming $M_*/L = 3.0$ as predicted by the Chabrier IMF [51] and discussed in [149, 31, 32, 35]. The mean halo masses are derived from the $M_* - M_{vir}$ relation from abundance matching as described in [149]. Abundance matching is a statistical technique to model the correlations between galaxy and halo properties based on mapping galaxies to dark matter halos of the same number density in the universe.

5.3 tSZ Analysis

5.3.1 Average Compton-y Parameter $\bar{y}$

The tSZ temperature signal extracted from maps of the CMB after filtration is proportional to the Compton-y parameter. The Compton-y parameter is the number of photon scatterings occurring with the hot electrons in the halo gas, multiplied by the energy gain per scattering (Section 1.2.1).

To obtain the Compton-y parameter from our tSZ signals we follow the steps detailed in [116]. The tSZ temperature signal is related to the Compton-y parameter via Equation 1.10 (Section 1.2.1). Relativistic corrections are negligible for the SDSS DR11 and DR15 sample masses and can safely be excluded [181]. At an effective frequency of 146.9 GHz, as for the ACT DR3 map, $f_{\rm SZ} = -0.992$. For the coadded DR5 maps, the effective band centers vary based on sky position, so the median values of the SZ-weighted band centers are chosen for the analysis. The appropriately weighted band center frequencies are 97.8 and 149.6 GHz for the DR5 f090 and DR5 f150 maps, respectively, so $f_{\rm SZ,f090} = -1.53$ and $f_{\rm SZ,f150} = -0.958$ [127]. We assume the ACT-based band center frequencies

				DR5 f150, DR5 f090			DR4 ILC		
Bin	Luminosity cut/$10^{10}L_\odot$	$M_{\rm vir}$ cut/$10^{13}M_\odot$	$\langle M_*\rangle/10^{11}M_\odot$	N	$\langle L\rangle/10^{10}L_\odot$	$\langle z\rangle$	N	$\langle L\rangle/10^{10}L_\odot$	$\langle z\rangle$
L43*	$L > 4.30$	$M > 0.52$	2.21	343647	7.4	0.49	190551	7.4	0.50
L61*	$L > 6.10$	$M > 1.00$	2.61	213070	8.7	0.51	118852	8.7	0.51
L79*	$L > 7.90$	$M > 1.66$	3.17	103159	10.6	0.53	57828	10.6	0.54
L98	$L > 9.80$	$M > 2.59$	3.84	46956	12.8	0.56	26308	12.8	0.57
L116	$L > 11.60$	$M > 3.70$	4.50	23504	15.0	0.58	13277	15.0	0.59
L43D*	$4.30 < L < 6.10$	$0.52 < M < 1.00$	1.57	130577	5.2	0.48	71699	5.2	0.48
L61D*	$6.10 < L < 7.90$	$1.00 < M < 1.66$	2.08	109911	6.9	0.48	61024	6.9	0.48
L79D	$7.90 < L < 9.80$	$1.66 < M < 2.59$	2.61	56203	8.7	0.51	31520	8.7	0.52
L98D	$9.8 < L < 11.60$	$2.59 < M < 3.70$	3.18	23452	10.6	0.54	13031	10.6	0.55

Table 5.2: Luminosity bin labels (the *bins are jointly analyzed in V21 and C21) and cuts, equivalent halo mass cuts, average stellar mass per bin, Number of sources (N), average luminosity ($\langle L\rangle$), and average redshift ($\langle z\rangle$) per luminosity bin for the final DR15 samples used in the DR5 f150, DR5 f090, and ILC Compton-y map analyses. These samples have the noise cut, point source masks and Galactic plane mask applied. The samples differ between the coadded and ILC maps due to the difference in footprints of the two maps, with the ILC maps covering a smaller area on the sky. Table is from [264].

because the ACT measurements dominate over those from *Planck* at our scales [175]. These frequencies are associated with a 2.4 GHz uncertainty, and detailed bandpass considerations could carry a larger impact (at the few percent level). However, each of these has a small effect on $\bar{y}$ compared to our statistical uncertainties.

5.3.2 $\bar{y} - \tau$ Relationship

A strong relationship exists between the Compton-y parameter of a halo and its optical depth. In simulations with AGN feedback, Battaglia [25] finds the relationship between $\bar{y}$ and optical depth to be

$$\ln(\bar{\tau}) = \ln(\tau_0) + m \ln(\bar{y}/10^{-5}) \tag{5.1}$$

where $\ln(\tau_0) = -6.40$ and $m = 0.49$ at z = 0.5 for an average area with radius 1.8′, a close approximation to the filter scales used in both our ACT tSZ analyses. We use this to estimate $\bar{\tau}$ from our tSZ $\bar{y}$ measurements. The systematic error bars on $\bar{\tau}$ from the $\bar{y}$-$\bar{\tau}$ relationship are calculated in V21 by using the Monte Carlo method taking into account the estimated 4% systematic uncertainty on $\ln(\tau_0)$ and 8% on m, which were estimated in [25] by taking the largest relative differences between the radiative cooling and AGN feedback models used for Equation 5.1. In DB17, a max/min approach to estimating the systematic uncertainties on $\bar{\tau}$ is adopted as a conservative approach which returns slightly larger uncertainties than standard error propagation.

5.3.3 tSZ Signals from ACT DR3 and SDSS DR11

In DB17, we adopted the same matched filtering approach as used in Hasselfield et al. [116], which is based on a Universal Pressure Profile [22] with a fixed scale of $\theta_{500} = 5.9'$. After the filter was applied to the CMB map (Section 5.1.1), the sources from the DR11 catalog were binned using the same luminosity cuts as those used for the kSZ analysis (Table 5.2). Within each luminosity bin, a 10.5′ by 10.5′ submap centered on each SDSS source was repixelized from 0.5′ per pixel to 3.75″ per pixel. The temperature signal associated with each source is taken to be the central pixel value in units of μK. These source signals are averaged within each luminosity bin to obtain a stacked tSZ signal per bin, $_{tSZ}$. The uncertainty associated with each temperature signal is obtained by taking the standard deviation of the pixels within an annulus of inner radius $R_1 = 3'$ and an outer radius of $\sqrt{2}R_1$. This 3′ size of this annulus is a conservative estimate of the local noise in the map. This approach has the advantage of not requiring the modeling of variations of the noise across the map. We verified that the distribution of the standard deviation values is similar for annuli around the sources and for annuli selected in source free regions, implying that, regardless of the presence of sources, there can be non-negligible variations in the noise across the map. We also verified that the error increases monotonically up to 3 arcmin and is stable for larger rings. For each source, $y(\theta = 0)$ is obtained from the central pixel temperature signal via Equation 1.10.

The angular averaged Compton parameter $\bar{y}$ is determined for each source by integrating over the generalized Navarro-Frenk-White (GNFW) pressure profile [176],

Luminosity cut/$10^{10}L_\odot$	$\delta T_{\rm tSZ}$ (μK)	$y_0/10^{-7}$	$\bar{y}_{1.8}/10^{-7}$
$L > 5.30$	-0.52 ± 0.16	1.91 ± 0.58	0.88 ± 0.27
$L > 6.10$	-0.65 ± 0.18	2.41 ± 0.65	1.11 ± 0.30
$L > 6.90$	-0.79 ± 0.20	2.92 ± 0.75	1.34 ± 0.34
$L > 7.40$	-0.90 ± 0.22	3.32 ± 0.82	1.51 ± 0.37
$L > 7.90$	-0.91 ± 0.25	3.35 ± 0.92	1.52 ± 0.42
$L > 8.70$	-1.23 ± 0.29	4.52 ± 1.06	2.05 ± 0.48
$L > 9.80$	-1.67 ± 0.35	6.17 ± 1.29	2.78 ± 0.58
$L > 11.60$	-3.70 ± 0.49	13.60 ± 1.82	6.09 ± 0.81
$5.30 < L < 7.90$	-0.26 ± 0.20	1.00 ± 0.75	0.45 ± 0.35
$7.90 < L < 9.80$	-0.15 ± 0.35	0.54 ± 1.30	0.25 ± 0.60

Table 5.3: Extracted tSZ temperature signals $\delta T_{\rm tSZ}$, central Compton parameter y_0, and angular averaged $\bar{y}$ for a 1.8 arcmin radius circle for the luminosity ranges and samples in Table 5.1. Results are from [68].

$$y(\theta) \propto \int ds P\Big(\sqrt{s^2 + (R_{500}\theta/\theta_{500})^2}\Big), \tag{5.2}$$

where $\theta_{500} = R_{500}/D_A(z)$, $D_A(z)$ is the angular diameter distance to the source with redshift z and we vary R_{500} to fix $\theta_{500} = 5.9'$. The integral s is along the line of sight, with $P(r)$ being the pressure profile, defined as in [116]. We normalize this integral with the y_0 value of each luminosity bin and calculate an averaged Compton $\bar{y}_\theta$ parameter:

$$\bar{y}_\theta = \frac{2}{\theta^2}\int_0^\theta y(\theta')\theta' d\theta'. \tag{5.3}$$

These results are shown in Table 5.5.

5.3.4 tSZ Signals from ACT DR4 and DR5 and SDSS DR15

In V21, we used aperture photometry (AP) to filter the Compton-y and DR5 f150 maps and extract the tSZ signals by stacking on source-centered submaps. A 2.1′ AP filter is also used in the kSZ analysis in C21. This approach to comparing estimated optical depths is an improvement in consistency over our work in DB17.

We selected submaps of $18' \times 18'$ (about three times larger than the outer diameter of the AP annulus) of pixel size 0.5′, interpolate in the Fourier domain with a pixel size of 0.1′ per pixel, and reprojected to a coordinate system centered at the galaxy center position using pixell[4]. A comparison between different pixelization approaches is discussed in C21 Appendix A, and we used the same approach adopted in C21. On each source-centered submap, we drew an aperture of $R_1 = 2.1'$ located at the central coordinate in RA and DEC provided by the DR15 catalog. The signal associated with the sources is taken to be the average within this aperture, minus the average of the pixels within an annulus of inner radius $R_1 = 2.1'$ and an outer radius of $\sqrt{2}R_1$. The 2.1′ size of this annulus was selected to correspond to ~1.1 Mpc based on the average angular diameter distance for the source sample. An associated weight for each source was assigned by taking the average within a $R_1 = 2.1'$ disk centered on the same source position on a $18' \times 18'$ submap taken from the inverse white noise variance map. This value is used for weighting the signals in the tSZ analysis.

We stacked on the positions of DR15 sources in the nine luminosity bins listed in Table 5.2 to measure the average δT_{SZ} in differential CMB temperature units from the DR5 f090 and DR5 f150 maps, and the average Compton-y for

[4]https://github.com/simonsobs/pixell

the DR4 ILC map. The round number luminosity cuts discussed in Section B.2 were chosen to yield five cumulative and disjoint luminosity bins, before any cuts were made to the DR15 sample, or any analyses were run. The weighted averages of the stacked submaps for each bin are shown in Figure 5.7, and the radial averages of these submaps are plotted in Figure 5.8. The signal associated with each source in a bin was taken to be the average of the $\langle \text{disk} \rangle - \langle \text{ring} \rangle$ values per source, weighted by the associated average inverse variance weight per source. The presence of dust emission on angular scales comparable to or less than the beam size is visible in all the maps analyzed, but is most prominent in the DR5 f150 map (Figure 5.7). We studied the impact of discarding the pixels within the beam radius from our analysis. This "core-excised" AP method removes the SZ signal within the beam radius along with the dust emission; it has a small (generally $< 1\sigma$) effect on the tSZ signals (Figure 5.9), so it was not adopted for the final analysis. The 2.1′ AP signals were then averaged in each bin to obtain a stacked tSZ signal, $\delta T_{\rm tSZ}$. The uncertainty associated with the stacked tSZ signal for each bin was obtained using a jackknife estimation method over the sources with 2,000 iterations per bin.

We corrected the $\delta T_{\rm tSZ}$ and $\bar{y}$ estimates obtained from the DR5 f090 map to account for the larger DR5 f090 beam (FWHM=2.1′) compared to the DR5 f150 map (FWHM=1.3′) [175]. We also corrected the $\bar{y}$ estimates from the DR4 ILC map which has an effective beam corresponding to a 1.6′ FWHM Gaussian [163]. We computed the beam correction factors as follows: we considered a fiducial pressure profile for the average virial mass (M_{vir}) in each bin [26]; we derived three estimates of the Compton-y signal in a 2.1′ AP filter, convolved with the f150 and f090 beams from [175] and with a 1.6′ FWHM Gaussian beam, us-

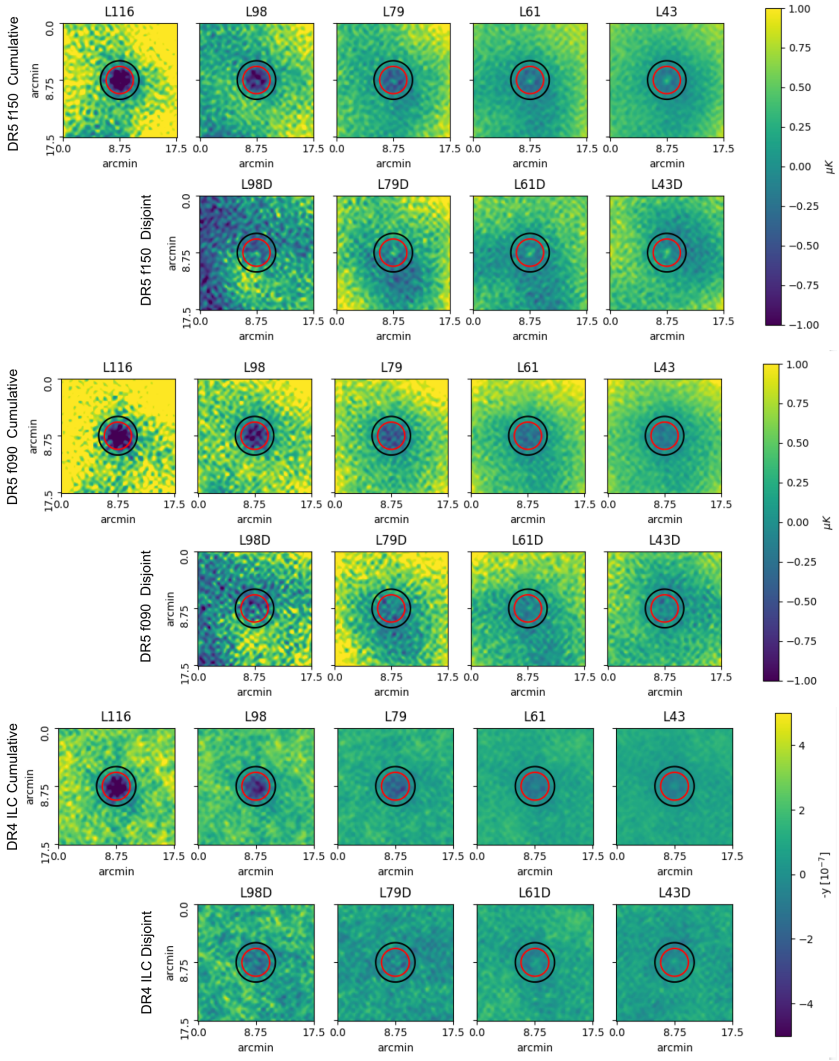

Figure 5.7: Stacked raw submaps for the five cumulative (top) and four disjoint (bottom) luminosity bins as defined in Table 5.2, for the DR5 f150 map (top two rows), the DR5 f090 map (middle two rows) and the DR4 ILC Compton-y maps (bottom two rows, in negative units of y to better compare to the coadded maps). The submaps represent the weighted average submaps of the sources in a given bin, where the weight for each source is taken to be the average value inside the accompanying $R_1 = 2.1$ submap in the inverse white noise variance map. The sub-0.5′-scale structure in the submaps is an artifact of the sub-pixel interpolation and is not physical. The maps are normalized with the average value within the AP annulus, such that the mean of the pixels in the annulus in these maps is equal to zero. The apertures used for the tSZ and kSZ AP are drawn, where $R_1 = 2.1'$ (red) and $\sqrt{2}R_1$ (black). Radial averages of these submaps are plotted in Figure 5.8. A central bright spot due to dust on approximately the beam scale can be seen across luminosity bins in the DR5 f150 submaps, but not the DR5 f090 submaps. Dust contamination of the DR4 ILC maps is more subtle, but can be noticed in radial average plots (Figure 5.8). Figure is from [264].

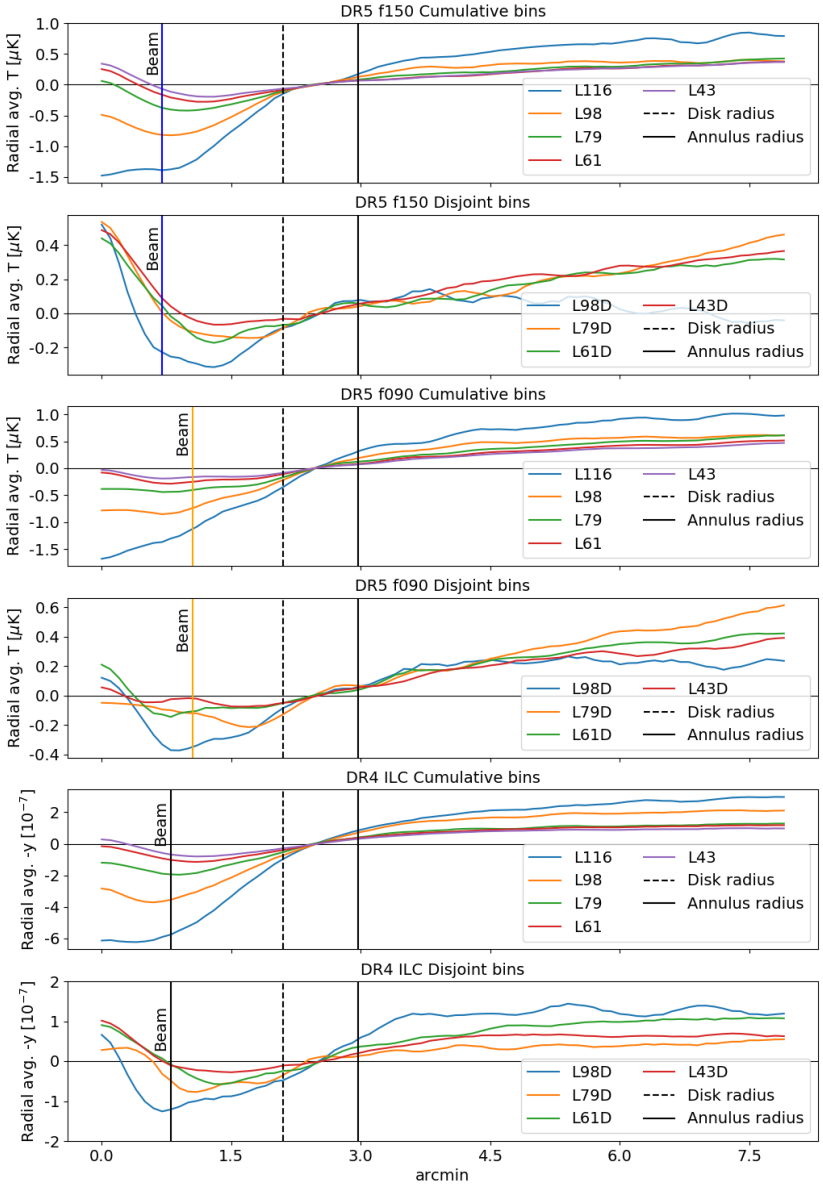

Figure 5.8: Radial average of the stacked submaps, which have been repixelized to 0.1′ per pixel, normalized to the average annulus value, for each luminosity bin, for the DR5 f150 and DR5 f090 coadded maps as well as the DR4 ILC map, shown for illustrative purposes only. The native units of the DR5 f150 and DR5 f090 maps are in μK and the DR4 ILC maps in y. Negative y is plotted here to compare with the decrements present in temperature. The aperture photometry disk radius is plotted as a vertical black dashed line, and the annulus outer radius is plotted as a vertical solid black line. The beam radius is plotted as a blue vertical line for DR5 f150, an orange vertical line for DR5 f090, and a black vertical line for the effective DR4 ILC beam. A central "bright spot" is observed in nearly all but the most luminous bin, and is attributed to dust emission. Due to this effect, we studied the core-excised AP approach for the DR5 f150 and DR5 f090 analysis. Figure is from [264].

ing `Mop-c GT` [5] (see [21] for a detailed description on how the projection from pressure to Compton-y profile and the beam convolution are implemented). We found an AP beam correction of 31% for the DR5 f090 measurements, and a beam correction of -5% for the DR4 ILC measurements. Thus, the DR5 f090 $\delta T_{\rm tSZ}$ measurements are multiplied by 1.3, which propagates into the DR5 f090 Compton-y estimates and resulting analyses, and the DR4 ILC $\bar{y}$ measurements are multiplied by 0.95. The value for the correction changes negligibly across luminosity bins, and is insensitive to our estimate of M_{vir} (the change in factor is $\sim 1\%$ if we vary M_{vir} in our mass range). While Figures 5.7 and 5.8 show the raw data, the DR5 f090 and DR4 ILC data in the rest of the work are multiplied by these factors. We note that because the f150 beam is not exactly Gaussian, but features side lobes [98], we get a negative (< 1) ILC correction, contrary to what we would expect given the larger ILC FWHM.

One potential tSZ signal contamination is the light emitted from star-forming SDSS galaxies in the optical/UV that is absorbed by dust grains and re-emitted in the infrared/sub-mm. To account for this, we used data from the *Herschel* Astrophysical TeraHertz Large Area Survey (H-ATLAS) [80] to infer the amount of dust emission at 150 GHz and 98 GHz, following the approach in Amodeo et al. [21]. The details of this correction are in [264]. These corrections are applied to the tSZ signals per bin from the DR5 f150 and DR5 f090 maps (Figure 5.9). Because the error bars on the dust estimates are asymmetric, the largest values for each data point are selected for the more conservative estimate of $\bar{y}/\sigma(\bar{y})$ (Figures 5.9,5.11).

For each luminosity bin, $\bar{y}$ was obtained from the AP temperature signal $\delta T_{\rm tSZ}$ via Equation (1.10). A jackknife approach was used to estimate the uncertainties

[5] https://github.com/samodeo/Mop-c-GT

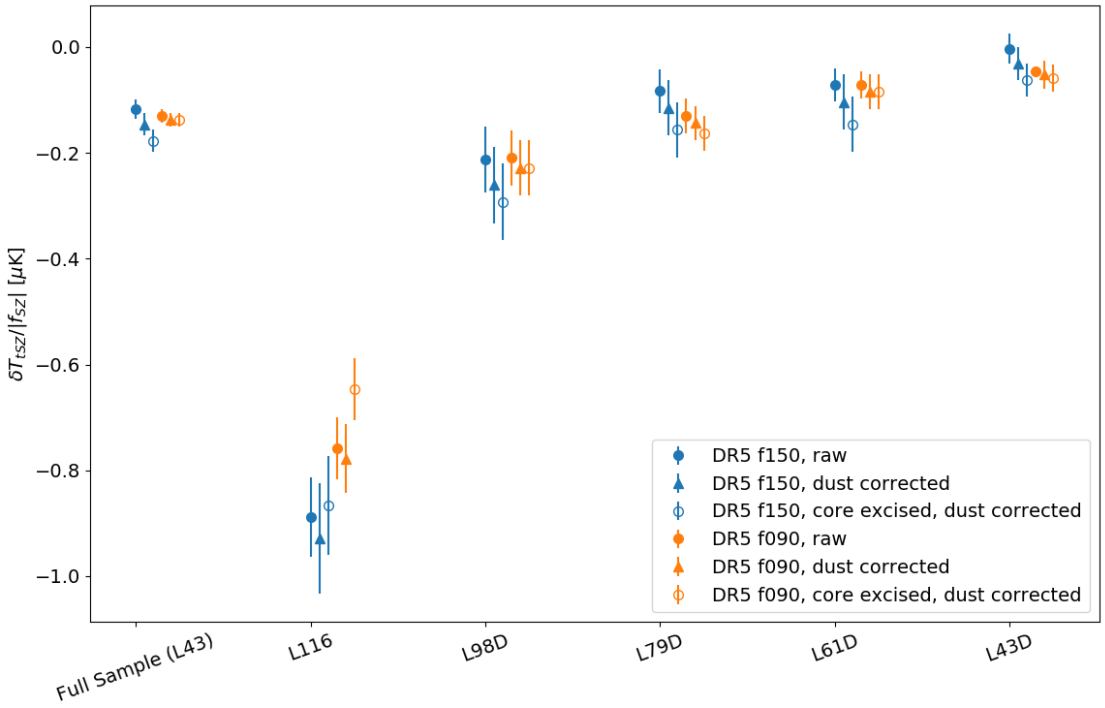

Figure 5.9: Aperture photometry tSZ signals in units of temperature rescaled by f_{SZ} (Equation 1.11) for disjoint luminosity bins and the full analysis sample, with 1σ jackknife estimated uncertainties, for the DR5 f150 and DR5 f090 maps. Raw results using the 2.1′ radius are compared to results after *Herschel* dust correction and the removal of the pixels within a beam-scale radius (0.7′ for the DR5 f150 map and 1.1′ for the DR5 f090 map). The DR5 f090 results shown have been beam corrected. The *Herschel* dust correction has a small effect on the temperature signals and lowers signal-to-noise for the DR5 f090 map due to the relatively large error bars on the dust estimates which are propagated into the uncertainties on tSZ signal. The "core-excised" AP approach removes a noticeable amount of tSZ signal in the L116 bin, as there is less dust contamination apparent on the beam scale in the stacked submaps for this bin as compared to the lower luminosity bins (Figure 5.8). For the most part, it has less than a 1σ effect on the tSZ signals, and is not included in the rest of this analysis. The dust corrected (filled triangle) results are propagated through to our comparisons of optical depth estimates. Figure is from [264].

associated with the binned tSZ signals and the covariance matrix for the kSZ analysis. The jackknife estimator for the standard error in the mean value of X is

	DR5 f150		DR5 f090		DR4 ILC
Bin	$\delta T_{tSZ,corr.}(\mu K)$	$\bar{y}/10^{-7}$	$\delta T_{tSZ,corr.}(\mu K)$	$\bar{y}/10^{-7}$	$\bar{y}/10^{-7}$
L43	-0.14 ± 0.02	0.53 ± 0.09	-0.21 ± 0.02	0.51 ± 0.06	0.54 ± 0.08
L61	-0.21 ± 0.03	0.79 ± 0.11	-0.29 ± 0.03	0.70 ± 0.07	0.78 ± 0.10
L79$^+$	-0.32 ± 0.03	1.22 ± 0.13	-0.47 ± 0.04	1.12 ± 0.11	1.28 ± 0.14
L98	-0.57 ± 0.06	2.18 ± 0.22	-0.77 ± 0.06	1.84 ± 0.15	2.19 ± 0.22
L116	-0.89 ± 0.10	3.42 ± 0.37	-1.19 ± 0.10	2.86 ± 0.24	3.52 ± 0.34
L43D$^+$	-0.03 ± 0.03	0.11 ± 0.13	-0.08 ± 0.04	0.20 ± 0.09	0.13 ± 0.11
L61D$^+$	-0.10 ± 0.05	0.39 ± 0.18	-0.13 ± 0.05	0.31 ± 0.11	0.28 ± 0.12
L79D	-0.11 ± 0.05	0.41 ± 0.18	-0.22 ± 0.05	0.53 ± 0.13	0.46 ± 0.16
L98D	-0.25 ± 0.07	0.97 ± 0.27	-0.35 ± 0.08	0.85 ± 0.19	0.78 ± 0.28

Table 5.4: Thermal SZ results from the DR5 f150, DR5 f090, and DR4 ILC map analyses, along with 1σ jackknife uncertainty estimates. Dust-corrected stacked tSZ signals δT_{tSZ} and $\bar{y}$ are given for the two coadded temperature maps, and $\bar{y}$ for the DR4 ILC Compton-y map. For the DR5 f150 map, the *Herschel* dust correction is applied, and the uncertainties associated with these corrections are propagated into the cited jackknife uncertainties. For the DR5 f090 map, the *Herschel* dust correction and the f090 beam correction scaling factor are applied. The $\bar{y}$ results from the disjoint bins shared with C21 (marked as $^+$bins) are shown in Figure 5.16.

$$SE_{jackknife} = \sqrt{\frac{n-1}{n}\sum(\chi_{-i} - \chi_{(.)})^2} \tag{5.4}$$

where $\chi_{(.)} = \sum\chi_i/N$ [167]. To use the estimator, we split the sample of sources into N smaller subsamples and removed one subsample at a time, calculating the weighted average for each bin on the summed $N-1$ subsamples to obtain N realizations of the computation. The jackknife method has the advantage of being self-contained and not requiring external information such as simulated CMB maps. We varied N to check the convergence of the jackknife algorithm, selecting the value that provided a stable significance against variations of N. For the tSZ analysis, a choice of $N = 2000$ was conservative (Figure 5.10).

Table 5.4 presents values of δT_{tSZ} for each luminosity bin along with the av-

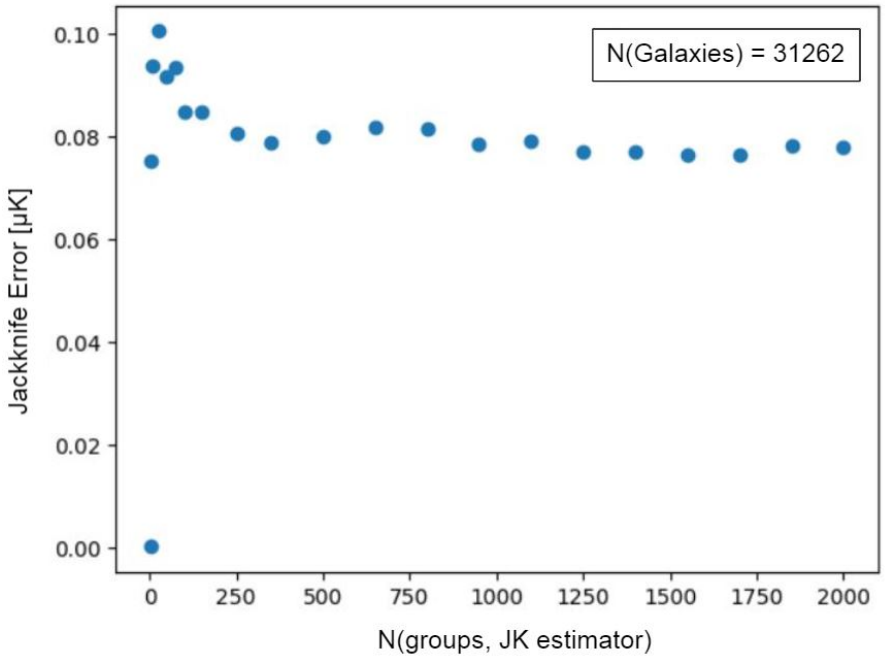

Figure 5.10: Varying the number of subsamples in the jackknife estimator (Equation 5.4) to check the convergence of the jackknife algorithm, using the positions of 31,262 SDSS DR14 galaxies on a coadded full sky (ACT MBAC + ACTPol S13-S16 day+night + *Planck*) map. This catalog and map were intermediary datasets not used in the final analysis, but were used to tune our pipeline and analysis approach. $N = 2000$ was chosen to provide a conservatively stable significance against variations of N.

eraged Compton $\bar{y}$ parameter we calculated using the tSZ signal. These results are beam and dust corrected using our *Herschel*-based estimates, and assume one source per filter. The signal-to-noise ratios for the tSZ measurements are up to 10 for the DR5 f150 map, 12 for the DR5 f090 map, and 10 for the ILC map, with the highest signal-to-noise in the L98 bin for the coadded maps, and the L116 bin for the ILC map. Before the *Herschel* dust corrections were applied and the uncertainties from those corrections propagated into the statistical tSZ uncertainty estimates, the highest signal-to-noise was seen in the highest luminosity bin (L116) for the coadded maps as well, which is as expected. The average Compton $\bar{y}$ from the tSZ signals in the three maps is presented in Figure 5.11

along with signal-to-noise per disjoint bin. The $\bar{y}$ measurements are consistent across the maps we analyzed.

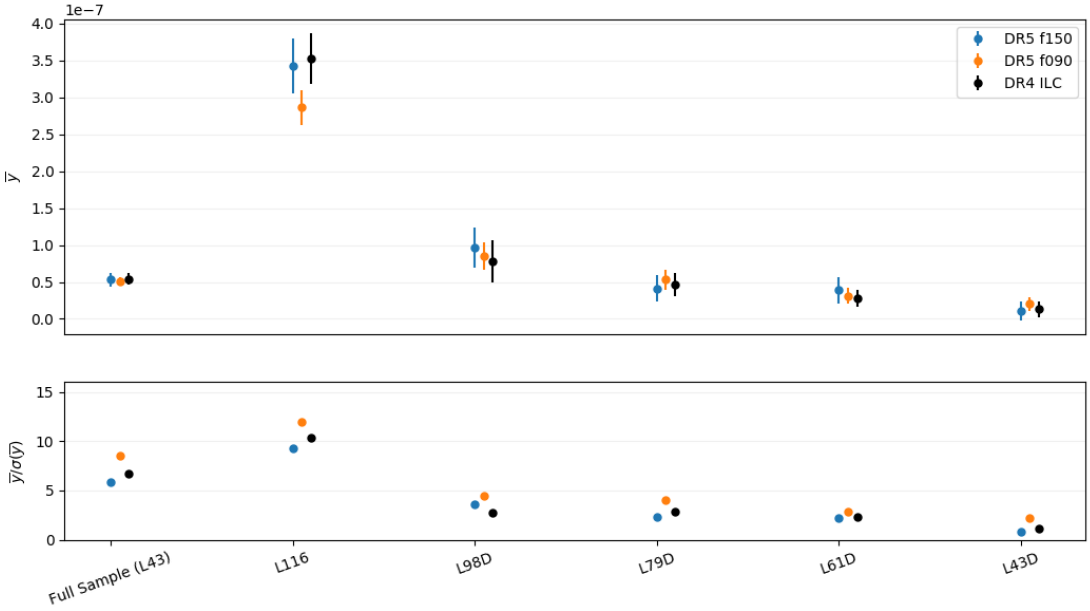

Figure 5.11: Average Compton-y in the 2.1′ aperture for the five disjoint (highest luminosity bin L116 and bin labels with suffix "D") luminosity bins and the full source sample ($L > 4.3 \times 10^{10} L_{\odot}$), with jackknife estimated uncertainties, for the DR5 f150 and DR5 f090 maps after dust and beam correction, and the DR4 ILC Compton-y map after beam correction. The lower panel shows the signals divided by their associated uncertainties. The significance of the tSZ effect observed generally decreases for less luminous sources, as expected. The results from each of the three maps are consistent. Figure is from [264].

Null Test

A null test was performed by stacking the ILC sample on a simulated CMB-only map. This test served as a check of our pipeline and jacknife estimates. The same pipeline used in the ILC analysis was used to measure the Compton-y parameter in the simulated CMB map for all luminosity bins in Table 5.2 (Figure 5.12), print stacked submaps as in Figure 5.7 (Figure 5.13), and plot radial aver-

ages as in Figure 5.8. The Compton-y results for the simulated CMB map were consistent with zero for all luminosity bins (Figure 5.12). The stacked submaps were also consistent with the same noise level as estimated using the jackknife uncertainty estimations.

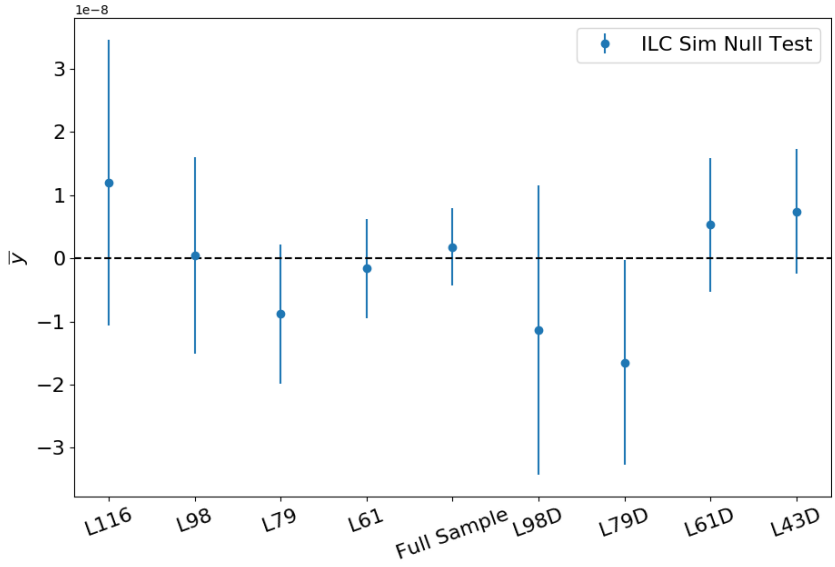

Figure 5.12: The same pipeline and sample used for the ILC map analysis as applied to a simulated CMB map as a null test for the tSZ pipeline. The Compton-y results are consistent with zero for all luminosity bins.

5.3.5 tSZ Systematics

Several systematic effects can affect SZ measurements. Systematics for the kSZ measurements are discussed in DB17 and C21, including tracer galaxy miscentering, map filtering, and imperfect removal of other effects such as the tSZ effect itself.

For the thermal SZ effect, a potential systematic is emission from dusty star-forming galaxies. At the frequencies used in our ACT DR3, DR4, and DR5 anal-

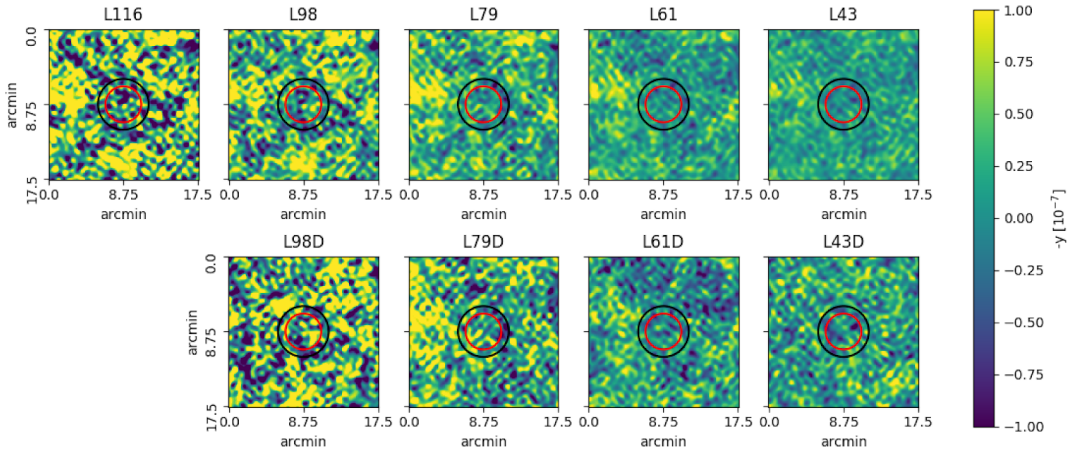

Figure 5.13: Stacked submaps from the same pipeline and sample used for the ILC map analysis as applied to a simulated CMB map as a null test for the tSZ pipeline. There is no signal observed, and radial average plots return the same noise level as estimated with jackknife uncertainty estimates (Figure 5.12).

yses, this dust emission is not negligible [106, 195]. Data at 220 GHz, where the tSZ effect vanishes, can be used to estimate the dust contribution and remove it from the measured temperature signals with an appropriate temperature scaling. In DB17, while a 220 GHz map was not available covering the full coadded map, a 220 GHz map for the noisier ACT-only region was shown to increase the value of the estimated tSZ signal by about 20% for luminosities above $7.9{\times}10^{10} L_{\odot}$ and up to 50% for the lower luminosity bin, where the tSZ signal is weaker.

As discussed in Section 5.3.4, we corrected our measurements in V21 for dusty star-forming galaxy emission by using data from *Herschel*. In the raw data, we observed a central "bright spot" in several luminosity bins in all maps, most notably the DR5 f150 map. We attributed this to additional dust contamination at approximately the beam scale in the stacked submaps (Figure 5.7), as shown in the radial averages presented in Figure 5.8. This apparent dust contamination is particularly present in the DR5 f150 map and is stronger than the

emission estimated from *Herschel*. The apparent angular scale, comparable to the beam size, suggests a compact source. We explored the effect of this excess emission by using a core-excised AP approach for the DR5 maps, using an aperture photometry filter which excluded the central disk on the beam scale (Section 5.3.4). We do not include the core-excised AP approach in our reported results or optical depth comparisons due to the small (generally $< 1\sigma$) impact on the tSZ signals, to avoid biasing our results by removing the central portion of the tSZ signal, and to best compare with the results from C21. Thus, while the *Herschel* dust correction accounts for some of the dust present in the DR5 f150 and DR5 f090 maps, this correction is imperfect, and some contamination remains from source galaxy emission. The effects of the dust correction steps taken on the DR5 f150 and DR5 f090 analyses can be seen in Figure 5.9.

Another potential cause of increased uncertainty in the tSZ measurements is dust and synchrotron emission from our own galaxy. To account for this, we applied the same 50% Galactic plane mask as used in the production of the 2015 *Planck* all-sky Compton-y maps [193] in our work in V21 (Figure 5.5). This cut eliminated 16,977 sources after all other cuts are considered, or 6% of our final sample, and was found to have a negligible impact on our signal compared to not applying the mask. We did not expect that synchrotron emission from the SDSS galaxies themselves had a significant impact on our discussion in V21 based on the core excised comparison shown in Figure 5.9. Future work could improve upon our results by modeling and removing dust and synchrotron emission from the LRGs.

Our $\bar{y}$ estimates in V21 include a contribution from neighboring halos, known as the two-halo term (e.g. [126]), which biases them high when assum-

ing we have only one halo per source. Compared to the [25] simulations, our sample includes lower mass halos and our measurements include a beam, so they will have a larger two-halo contribution. We estimate this contribution using `Mop-c GT` (see Appendix A of [21] for details on the implementation) and we find that our $\bar{y}$ values are biased high by a factor between 2% and 10% in the luminosity bins of interest. The two-halo bias does not significantly affect the V21 results, but will need to be accounted for in future higher signal-to-noise analyses.

The $\bar{y}$-$\bar{\tau}$ relationship (Equation 5.1) also carries associated systematics. In addition to the quoted systematic uncertainty between different hydrodynamical simulations, we conjectured in DB17 that there is also uncertainty in extrapolating from the larger masses in the hydrodynamical simulations to the lower mass objects in the DR11 sample used in DB17 (Section 5.5). New hydrodynamical simulations of lower mass clusters and groups would help address this concern.

In both analyses we used the best fit relation provided by Battaglia [25] for a redshift z=0.5. This is a reasonable choice, because, as shown in Tables 5.1 and 5.2, the average redshift of all the luminosity bins is close to 0.5. In DB17, we checked the redshift dependence of the $\bar{y} - \bar{\tau}$ conversion by repeating the analysis for the best fit values provided by Battaglia [25] for z = 0.3 and z = 0.7. We found variations in the value of $\bar{\tau}$ in the range 6–20%. These variations are still within 1–2 of our estimates but suggest that future larger surveys, which will be able to split the cluster sample into redshift bins, will need to account for the redshift dependence of the $\bar{y} - \bar{\tau}$ relation.

Luminosity cut/$10^{10}L_\odot$	$\bar{\tau}_{1.8,\,\mathrm{kSZ}}/10^{-4}$	$\bar{\tau}_{1.8,\,\mathrm{tSZ}}/10^{-4}$	$\sigma_{\mathrm{sys.}}$
$L > 5.30$	0.84 ± 0.20	1.64 ± 0.24	±0.49
$L > 6.10$	0.78 ± 0.21	1.83 ± 0.24	±0.54
$L > 6.90$	0.99 ± 0.28	2.01 ± 0.25	±0.58
$L > 7.40$	1.17 ± 0.31	2.13 ± 0.26	±0.60
$L > 7.90$	1.46 ± 0.36	2.14 ± 0.29	±0.60
$L > 8.70$	1.66 ± 0.43	2.57 ± 0.28	±0.68
$L > 9.80$	1.13 ± 0.60	2.87 ± 0.29	±0.78
$L > 11.60$	1.22 ± 0.82	4.22 ± 0.28	±1.11
$5.30 < L < 7.90$	0.89 ± 0.37	1.17 ± 0.45	±0.40
$7.90 < L < 9.80$	1.42 ± 0.68	0.88 ± 1.04	±0.21

Table 5.5: Best fit optical depths from the pairwise kSZ signal as a function of luminosity cut, and the estimated optical depths for the same sample from the tSZ measurements for comparison. The bottom part of the table shows the disjoint luminosity ranges, and values from these two samples plus the $L > 9.8 \times 10^{10} L_\odot$ sample are plotted for comparison in Figure 5.5. The 1σ uncertainties on the kSZ tau estimates are from simulations. The 1σ uncertainties on the tSZ optical depth estimates are from propagated jackknife uncertainties, and the $\sigma_{\mathrm{sys.}}$ values are from the systematic uncertainties present in the hydrodynamical simulation relationship (Section 5.3.2). Values are from [68].

5.3.6 Optical Depth

In each analysis, the average Compton $\bar{y}$ value per luminosity bin is converted to an estimate of area-averaged optical depth $\bar{\tau}$ via Equation 5.1. These values are presented in Table 5.5 for the ACT DR3 analysis and in Table 5.7 for the ACT DR4 and DR5 analysis. The listed 1-σ uncertainties are derived from the max/min approach and Monte Carlo methods described in Section 5.3.2.

5.3.7 Theoretical Optical Depth

For comparison with our measurements in V21, we calculate theoretical estimates for the mean optical depths $\bar{\tau}_{\mathrm{theory}}$ for each of the luminosity bins. We

Luminosity cut/$10^{10}L_{\odot}$	$\bar{\tau}_{\rm theory}/10^{-4}$
L43**	1.39
L61	1.77
L79+	2.42
L98	3.35
L116	4.44
L43D+	0.70
L61D+	1.06
L79D	1.53
L98D	2.09

Table 5.6: Theoretical estimates for mean optical depth (to calculate $f_{\rm c}$, as described in Section 5.3.7) for each luminosity bin in V21. Luminosity bins are described in Table 5.2. Values are from [264].

follow the derivation in [25] using an NFW profile to estimate the optical depth in a given aperture,

$$\bar{\tau}_{\rm theory} = \sigma_{\rm T} x_{\rm e} X_{\rm H} (1 - f_{\star}) f_{\rm b} \frac{M_{\rm vir}(< \theta_{2.1'})}{d_A^2 m_p}. \tag{5.5}$$

Here $\sigma_{\rm T}$ is the Thomson cross-section, $x_{\rm e}$ is the electron fraction defined as $x_{\rm e} = (X_{\rm H} + 1)/(2X_{\rm H})$, $X_{\rm H}$ is the primordial hydrogen mass fraction ($X_{\rm H} = 0.76$), $f_{\star}$ is the stellar mass fraction of the halo, $f_{\rm b}$ is the universal baryon fraction ($\Omega_{\rm b}/\Omega_{\rm M}$), $m_{\rm p}$ is the proton mass, and d_A is the angular diameter distance to mean redshift of our sample. The parameter value for $f_{\rm b} = 0.157$ is set from the cosmological parameters we choose. The value for $f_{\star}$ is inferred from the stellar mass-halo mass relation from abundance matching as described in [149]. We defined the parameter $f_{\rm c} = \bar{\tau}_{obs}/\bar{\tau}_{\rm theory}$ to compare the estimated $\bar{\tau}$ values from V21 (Table 5.7) to the theoretically predicted values. This parameter represents the fraction of theoretically predicted optical depth obtained by the two SZ measurements, and is of interest to compare the consistency of the two optical depth estimate methods.

	DR5 f150				
Bin	$\bar{\tau}_{\rm tSZ}$ $[10^{-4}]$	$\sigma_{\rm sys.}$ $[10^{-4}]$	$f_{\rm c,tSZ}$ ± (stat., sys.)	$\bar{\tau}_{\rm kSZ}$ [C21] $[10^{-4}]$	$f_{\rm c,kSZ}$
L43**	1.28 ± 0.10	0.27	0.92 ± (0.07, 0.20)	0.54 ± 0.09	0.39 ± 0.06
L61	1.55 ± 0.11	0.30	0.88 ± (0.06, 0.17)	0.69 ± 0.11	0.39 ± 0.06
L79+	1.92 ± 0.10	0.34	0.79 ± (0.04, 0.14)	0.88 ± 0.18	0.36 ± 0.07
L98	2.55 ± 0.12	0.39	0.76 ± (0.04, 0.12)		
L116	3.18 ± 0.17	0.43	0.72 ± (0.04, 0.10)		
L43D+	0.59 ± 0.35	0.17	0.85 ± (0.50, 0.24)	0.46 ± 0.24	0.66 ± 0.34
L61D+	1.10 ± 0.25	0.25	1.04 ± (0.24, 0.23)	0.72 ± 0.26	0.68 ± 0.25
L79D	1.12 ± 0.24	0.25	0.74 ± (0.16, 0.16)		
L98D	1.71 ± 0.23	0.33	0.82 ± (0.11, 0.16)		
	DR5 f090				
Bin	$\bar{\tau}_{\rm tSZ}$ $[10^{-4}]$	$\sigma_{\rm sys.}$ $[10^{-4}]$	$f_{\rm c,tSZ}$ ± (stat., sys.)	$\bar{\tau}_{\rm kSZ}$ [C21] $[10^{-4}]$	$f_{\rm c,kSZ}$
L43**	1.25 ± 0.07	0.27	0.89 ± (0.05, 0.19)	0.65 ± 0.13	0.47 ± 0.09
L61	1.46 ± 0.07	0.29	0.82 ± (0.04, 0.16)	0.82 ± 0.17	0.46 ± 0.10
L79+	1.84 ± 0.08	0.32	0.76 ± (0.03, 0.13)	0.79 ± 0.27	0.33 ± 0.11
L98	2.35 ± 0.10	0.37	0.70 ± (0.03, 0.11)		
L116	2.91 ± 0.12	0.41	0.66 ± (0.03, 0.09)		
L43D+	0.79 ± 0.18	0.20	1.14 ± (0.25, 0.29)	0.83 ± 0.34	1.19 ± 0.49
L61D+	0.98 ± 0.18	0.23	0.92 ± (0.17, 0.22)	1.07 ± 0.35	1.01 ± 0.33
L79D	1.27 ± 0.15	0.27	0.83 ± (0.10, 0.18)		
L98D	1.60 ± 0.18	0.30	0.77 ± (0.09, 0.15)		
	DR4 ILC				
Bin	$\bar{\tau}_{\rm tSZ}$ $[10^{-4}]$	$\sigma_{\rm sys.}$ $[10^{-4}]$	$f_{\rm c,tSZ}$ ± (stat., sys.)	$\bar{\tau}_{\rm kSZ}$ [C21] $[10^{-4}]$	$f_{\rm c,kSZ}$
L43**	1.29 ± 0.09	0.27	0.92 ± (0.07, 0.19)	0.47 ± 0.12	0.34 ± 0.09
L61	1.54 ± 0.09	0.30	0.87 ± (0.05, 0.17)	0.74 ± 0.15	0.42 ± 0.08
L79+	1.96 ± 0.11	0.34	0.81 ± (0.04, 0.14)	0.78 ± 0.23	0.32 ± 0.10
L98	2.55 ± 0.13	0.39	0.76 ± (0.04, 0.12)		
L116	3.22 ± 0.15	0.43	0.73 ± (0.03, 0.10)		
L43D+	0.64 ± 0.26	0.17	0.91 ± (0.37, 0.25)	0.18 ± 0.32	0.26 ± 0.46
L61D+	0.93 ± 0.20	0.22	0.88 ± (0.19, 0.21)	0.69 ± 0.34	0.65 ± 0.32
L79D	1.19 ± 0.20	0.26	0.78 ± (0.13, 0.17)		
L98D	1.54 ± 0.27	0.30	0.74 ± (0.13, 0.14)		

Table 5.7: Optical depth estimates from the tSZ effect and fraction of theoretical estimates for mean optical depths (f_c, Section 5.3.7, calculated from values presented in Table 5.6) for each luminosity bin and analyzed map in V21/C21. The fractions for the full galaxy sample (**bin) are shown in Figure 5.15, and kSZ results from the three disjoint bins shared with C21 (+bins) are shown in Figure 5.16. Values are from [264].

5.4 kSZ Analysis

As described in Section 1.2.2, the mean pairwise momentum of groups and clusters as a function of their comoving separation distance is negative at and around separations of 25-50 Mpc, implying that they are moving towards one another on average due to gravity [111, 180, 140, 222]. While the 3-dimensional momentum of the groups is not easily measurable, the mean pairwise momentum can be still estimated from the line-of-sight component of the momenta [89]. The kSZ signal of a given cluster is directly proportional to this line-of-sight momentum: $\delta T_{\rm kSZ,i} \propto -\mathbf{p}_i \cdot \mathbf{r}_i$, where the unstated multiplicative factors depend on the properties of the cluster (density profile, including angular extent in the sky) and on the pixel scale and angular resolution of the CMB experiment. This was the same approach taken in DB17, where the same pairwise estimator was applied to the ACT DR3 map and the SDSS DR11 sample presented in Table 5.1.

In both C21 and DB17, he significance of the kSZ measurement is determined by a fit to the analytic prediction of linear perturbation theory for the pairwise velocity [111, 180, 140, 222, 37, 172, 171], rescaled by the factor $-\bar{\tau}T_{\rm CMB}/c$, where $\bar{\tau}$, the average halo optical depth of the galaxy sample used for the pairwise momentum estimator, is the free parameter of the fit.

C21 presented a value of $\bar{\tau} = (0.69 \pm 0.11) \times 10^{-4}$ as the highest signal-to-noise best fit average optical depth. It was derived from the mean pairwise momentum for the full sample of 343,647 sources and DR5 f150 map using bootstrap uncertainty estimates of the pairwise correlation covariance matrix. In C21, we found that the analytical signal model is a good fit to the data with a best fit χ^2 of 10 for 17 degrees of freedom. Selected best fit optical depths from the mean

pairwise momentum fits and bootstrap estimated signal-to-noise are reported in Table 5.7, and shown in Figures 5.15 and 5.16, along with the results derived here. The statistical uncertainties on tSZ estimated optical depth presented in Table 5.7 are propagated from the tSZ AP jackknife uncertainty estimates and *Hershcel* dust corrections (Section 5.3.4). The systematic uncertainties presented in Table 5.7 are estimated using the Monte Carlo method taking into account the estimated systematic uncertainties in the $\bar{y}$-$\bar{\tau}$ relationship from simulations (Equation 5.1). Selected $\bar{\tau}$ estimates from the pairwise kSZ effect from C21 with bootstrap uncertainties are listed along with f_c for comparison.

In DB17, we estimated the covariance matrix of the mean pairwise momentum using microwave sky simulations, jackknife evaluation, and bootstrap estimates, and the most conservative simulation-based errors give signal-to-noise estimates between 3.6 and 4.1 for varying galaxy luminosity cuts [68]. For the highest signal-to-noise bin, we obtained a best fit optical depth of $\bar{\tau} = (1.46 \pm 0.36) \times 10^{-4}$. The best fit optical depths from the mean pairwise momentum fits and simulations-estimated signal-to-noise are reported in Table 5.5, and compared with the tSZ-derived optical depth estimates in Figure 5.5.

5.5 Optical Depth Comparisons

ACT DR3

In DB17, we compare the kSZ optical depth results (Section 5.4) to those obtained from tSZ measurements and find a slope $m_{1.8} = 1.60 \pm 0.49(\text{stat}) \pm 0.59(\text{sys})$ (Figure 5.5), where the systematic uncertainty is related to the uncertainties on

the best fit parameters from the $\bar{y} - \bar{\tau}$ relation. The resulting slope is within 1.3σ and 1σ of unity, considering the statistical and systematic uncertainties respectively, suggesting that the tSZ and kSZ optical depth estimates are consistent given current uncertainties, and that this approach is promising for extracting pairwise velocities from pairwise momentum measurements.

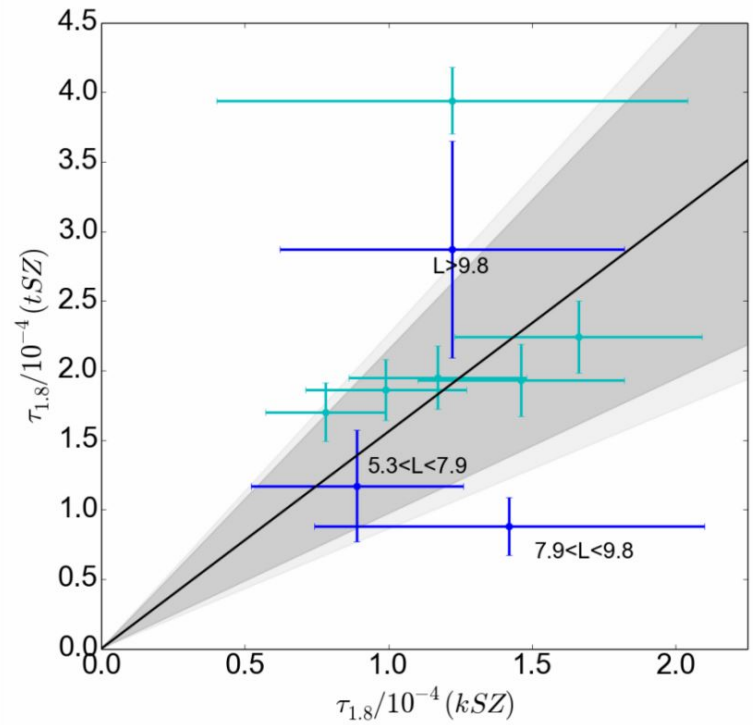

Figure 5.14: Best fit line for the tSZ and kSZ optical depth measurements from DB17. The fit is only performed to the dark blue points, which correspond to the three independent luminosity bins in the DR11 sample (second row and last two rows in Table 5.1) indicated by the labels (in units of $10^{10} L_{\odot}$). The cyan points correspond to the other cumulative bins. We find a slope of $m_{1.8} = 1.60 \pm 0.49(\text{stat}) \pm 0.59(\text{sys})$. The gray areas represent the 1σ statistical (dark) and systematic (light) uncertainty ranges. Figure is from [68].

ACT DR4 and DR5

Optical depth estimates from the two SZ effects are presented in Section 5.5 Table 5.7 along with comparisons to theory. Figure 5.15 presents the fraction of theoretically predicted optical depth (f_c) for the three independent joint analysis bins and the full sample, a representation of the baryon fraction we observe within the AP radius for those source samples. The tSZ and kSZ estimates are consistent within 1σ for the two lower mass disjoint bins (L61D and L43D), while they differ at 2-3σ in the highest mass bin (L79), which is also the best constrained. This difference drives 2-3σ differences between the tSZ and kSZ results in the cumulative bins. We look forward to comparing the two tracers in more detail in future work with even more sensitive datasets. The comparisons with theoretical estimates of the optical depth suggest that between one third and all of the predicted baryons lie within the aperture size of radius 2.1′, or 1.1 Mpc (for a mean redshift of z = 0.55) studied in this analysis. However, because uncertainties in the luminosity-mass relation for DR15 (Section 5.3.7) are difficult to accurately propagate through to $\bar{\tau}_{\rm theory}$, it is challenging to draw strong conclusions about baryon content based on our estimates of f_c. For future high signal-to-noise measurements, careful treatment of the uncertainties, discussed in [149], will be necessary for accurate interpretation of these SZ results. Here, the f_c values are used for making comparisons between the SZ estimates and studying trends.

Figure 5.16 shows a comparison of $\bar{\tau}$ estimates from kSZ measurements and average Compton-y from tSZ measurements to the power-law scaling relation using an AGN feedback model simulation relation (Equation 5.1) [25]. We expect significant covariance between the data from the different maps. Two of the

three disjoint analysis bins are in agreement with the model, while the highest mass bin (L79) is an outlier. This appears to be driven by low kSZ $\bar{\tau}$ estimates for this bin (Figure 5.15).

The two-halo contribution to our tSZ measurements, discussed in Section 5.3.5, does not affect these results. Propagating our $\bar{y}$ corrections to $\bar{\tau}_{tSZ}$ and then to $f_{c,\mathrm{tSZ}}$ (filled circles in Fig. 5.16), we get lower tSZ fractions by a factor of 4% for the L43D bin and less for the other bins.

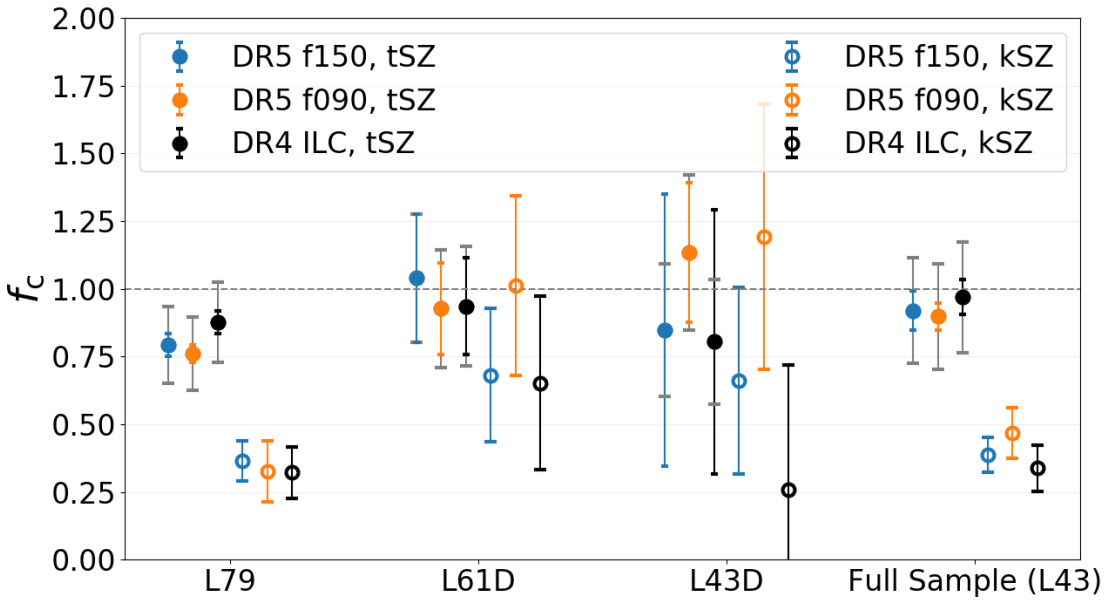

Figure 5.15: Fraction of the theoretically predicted optical depth (f_c) for the full DR15 sample. The estimates are extracted from tSZ measurements (filled circles) from three different maps (DR5 f150: blue, DR5 f090: orange, and ILC: black) and kSZ measurements from the same maps, as described in C21 (open circles). The tSZ measurements are converted to optical depth estimates using a scaling relationship from hydrodynamic simulations [25]. The tSZ jackknife uncertainties are plotted in color, and the systematic uncertainties from the simulation-based scaling relationship are plotted as grey bars. The plotted kSZ uncertainties are from bootstrap estimates. The kSZ and tSZ results agree within 1σ in the L61D and L43D bins, while in the highest signal-to-noise L79 bin they differ at 2-3σ. This results in the 2-3σ difference observed in the full sample, L43. The difference between the kSZ and tSZ results is discussed in Section 5.5. The kSZ results are lowest for the L79 bin. Figure is from [264].

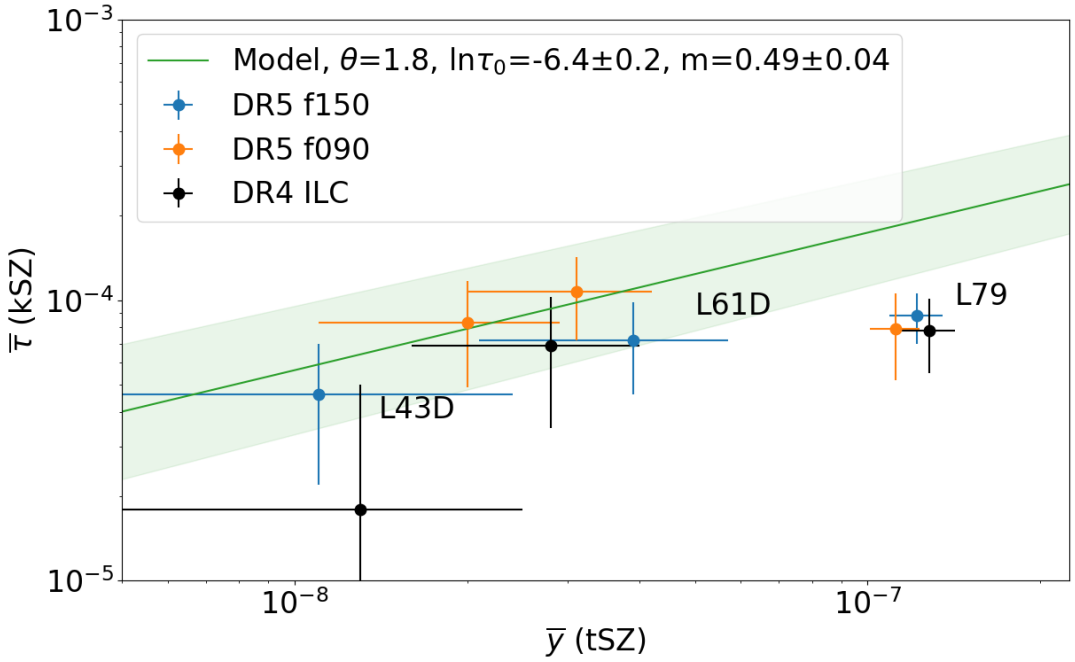

Figure 5.16: Optical depth fits from kSZ signals versus average Compton-y from the tSZ measurements for the three jointly analyzed disjoint luminosity bins with statistical error bars from jackknife estimates (bootstrap estimated uncertainties for the kSZ, see C21). The scaling relation between $\bar{\tau}$ and $\bar{y}$ from hydrodynamical simulations with aperture $\Theta = 1.8'$ (the closest scaling relation in [25] to our 2.1′ aperture) is plotted as the green model curve (Equation 5.1) with the 1σ uncertainty envelope shaded. The tSZ and kSZ results in the L43D and L61D luminosity bins are consistent with the model, while the kSZ results in the L79 bin fall below the model line. Figure is from [264].

5.6 Discussion

We have presented estimates of halo optical depths from measurements of the tSZ effect made on ACT DR3, DR4 and DR5 maps in combination with data from *Planck* and LRG tracers from the SDSS BOSS DR11 and DR15 catalogs. By combining these measurements with the kSZ measurements from the same datasets, we compare estimates of optical depths from the two SZ effects and make progress towards empirical $\bar{y} - \bar{\tau}$ relationships from the SZ effects. The tSZ results in V21 are consistent with those in DB17, with smaller uncertainties.

The details of the kSZ analysis that differ between V21 and DB17 are discussed in C21. And although our galaxy samples are different than those in Hand et al. 2011 [112], our results are statistically consistent with those results for bins with similar average luminosity. We improved our approach in our later work, V21, compared to DB17, by analyzing the CMB map with the same AP filter for both the kSZ and tSZ analysis, and removing contaminating dust emission by estimating the contribution from dusty star-forming galaxies using *Herschel* maps and a modified blackbody dust emission model.

In both works, the stacked tSZ signals were converted to an estimate of optical depth through a hydrodynamic simulation scaling model [25], while the pairwise kSZ signals were fit to theoretical predictions to find best fit optical depths. The two methods are independent of one another, and in V21, each of the SZ results is consistent over the three maps analyzed (DR5 f150, DR5 f090, and DR4 ILC). In DB17, we found that the optical depth estimated with tSZ measurements is consistent with the one estimated by fitting the kSZ pairwise momentum measurements to the analytical pairwise velocity. In V21, the results from the tSZ and kSZ measurements agreed with one another within 1σ in the two lower mass disjoint bins, while they differed by 2-3σ in the highest mass bin and thus the cumulative bin.

When comparing to the theoretical optical depth in V21, the kSZ and tSZ optical depth estimates accounted for one third to all of the theoretically predicted baryon content. When comparing the tSZ $\bar{y}$ measurements and kSZ $\bar{\tau}$ results to the hydrodynamic model, two of the three bins analyzed are in agreement with the model.

Using tSZ data appears to be a promising approach for obtaining accurate

estimates of galaxy group and cluster optical depths and eventually estimating the mean pairwise velocity from pairwise momentum measurements, once a better understanding of the relationship between $\bar{y}$ and $\bar{\tau}$ is achieved. Our results help to move us from an era of measurement alone to one of interpretation based on the consistency of previously inaccessible quantities.

With improved data from the complete ACT dataset [119] and current and upcoming projects such as CCAT-prime [233], the Simons Observatory [225], DESI [155], SPT-3G [34] and CMB-S4 [9], we will achieve higher signal-to-noise measurements of the SZ signals and be able to probe the baryon content of galaxy clusters and groups and large-scale structure further. Improved multi-frequency data will enable precise measurements of optical depths and peculiar velocities simultaneously for large samples and for single sources, potentially sensitive enough to measure the missing baryons between groups. With these data, the SZ signals are anticipated to become valuable cosmological probes that are complementary to current observables.

CHAPTER 6

CONCLUSION

Measuring the Sunyaev-Zel'dovich effects in high-resolution, multifrequency maps of the cosmic microwave background will provide valuable information about our universe and the largest gravitationally bound structures within it. With high signal-to-noise measurements of the SZ signals, we will improve constraints in cosmology and particle physics that are complementary to concurrent surveys and laboratory experiments on Earth. These constraints will inform our understanding of dark energy and the sum of the neutrino masses. By probing the baryon content of galaxy clusters and groups, we will learn about their evolution and the distribution of matter in our universe. These measurements will provide unprecedented experimental data to inform our theoretical models of galaxy evolution and feedback mechanisms.

With upcoming observatories like CCAT-prime and the Simons Observatory, we will precisely image the cosmic microwave background and submillimeter sky by opening previously inaccessible windows in frequency and deploying novel cameras with large numbers of sensitive superconducting detectors in state-of-the-art telescopes. Observing large areas of sky which overlap with complementary surveys such as optical galaxy catalogs will provide synergies that will allow statistical methods such as the pairwise kSZ estimator to yield high significance measurements. These projects will advance cosmology and astrophysics while developing technologies for the next generation CMB experiment, CMB-S4, the definitive ground-based CMB project to investigate the nature of our universe.

Future high-resolution maps of the CMB will enable measurements of veloc-

ity fields at large scales, which will constrain the amplitude of matter density fluctuations ($\sigma_8(z)$) and the linear growth factor f [10, 171]. While other observables such as direct measures of galaxy clustering as a function of redshift can in principle yield such constraints, the kSZ effect is able to probe the growth of structure over large volumes and across epochs of our universe's timeline due to its redshift independence [147]. High signal-to-noise kSZ measurements will complement measurements of clustering in galaxy redshift surveys and the weak gravitational lensing of the CMB to synergistically constrain cosmology. Expected constraints on $f\sigma_8$ from CMB-S4 in combination with an upcoming DESI survey are shown in Figure 6.1. An important degeneracy is the optical depth of the galaxy sample used in the analysis, τ_g, which can be broken through measuring redshift-space distortions of the sample, or through X-ray or tSZ measurements of the galaxies themselves like discussed in this dissertation. With ACT data, we have taken steps towards breaking this degeneracy by estimating the halo optical depth of the same sample of galaxies through the tSZ and pairwise kSZ effects, and comparing these measurements in order to extract pairwise velocities in the future [68, 264].

When the sensitivity of kSZ measurements becomes high enough, like is expected from CMB-S4, the kSZ effect will allow for the direct measurement of optical depth profiles ($\tau_g(\theta)$), which is proportional to the gas profile of the galaxy sample. This will enable the calibration of baryon effects on the power spectrum, which are a leading systematic for weak lensing surveys to study dark energy (Figure 6.2) [258, 169].

In this dissertation, we discussed the exciting potential of science with the SZ effects. In pursuit of this goal, we discussed novel cryogenics, detectors, and

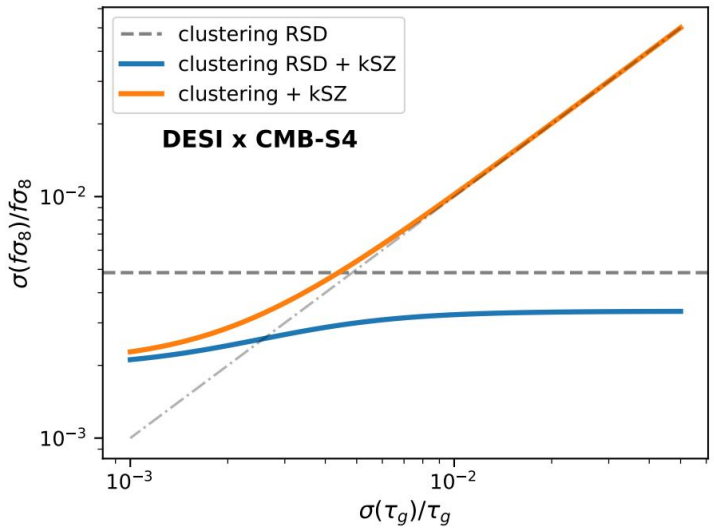

Figure 6.1: Constraints on the linear growth factor × matter amplitude ($f\sigma_8$) from the kSZ effect as a function of the size of the prior on the optical depth of the galaxy sample used in the analysis (τ_g), assuming a single redshift bin centered at z=0.75. The horizontal dashed line shows redshift space distortion measurements from DESI. The kSZ signal from pure galaxy clustering is plotted in orange, while the combination with redshift space distortion information is plotted in blue, yeidling a constraining power of twice that of DESI alone. The kSZ signal will become an instrumental probe for dark energy studies with this future dataset. Figure from [10].

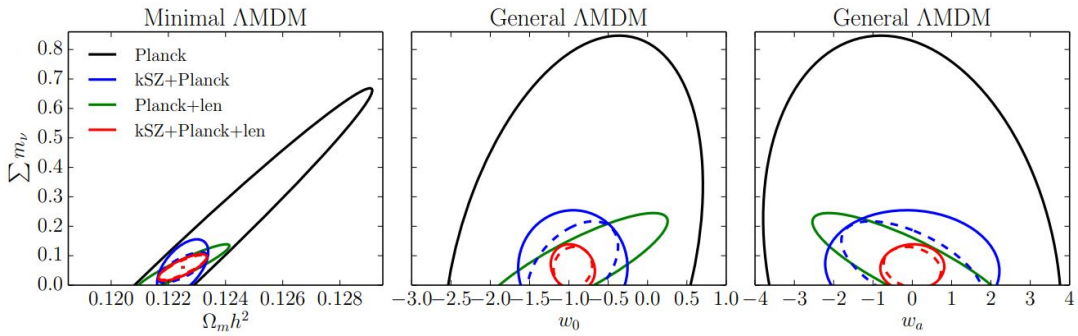

Figure 6.2: Expected constraints on the neutrino mass sum (Σm_ν) versus the matter density ($\Omega_m h^2$) and dark energy equations of state and evolution parameters (w_0 and w_a). Contours shown are 68% confidence levels for combinations of information from *Planck*, kSZ information from CMB-S4, and CMB lensing. Dashed lines include a 1% prior on the average cluster optical depth evolution, $b_\tau(z)$. Figure from [172].

readout for microwave and submillimeter observations.

We presented the design and testing of cryogenic receivers for the Fred Young Submillimeter Telescope. Mod-Cam is a single-module cryogenic testbed for the first-generation science instrument, Prime-Cam. With Mod-Cam we will test and deploy the first instrument module for the CCAT-prime project. These receivers will capitalize on rapid developments in microwave detector technology, deploying microwave kinetic inductance detector (MKID) arrays coupled with imaging Fabry-Perot interferometers for spectroscopic measurements including those for SZ spectral science. We presented the instrument modules that will house the light-focusing and light-filtering elements of the cameras, detailed the detector and readout technologies, discussed how these elements will be optimized for science goals, and gave an overview of the cryogenic systems that will cool these components. We discussed the ongoing tests that will ready Mod-Cam, and, soon, Prime-Cam, for observations at the exceptionally high FYST site in the Atacama.

In addition to the MKIDs on which Mod-Cam will rely, we discussed the transition edge sensors (TESes) that will be used for SO and are baselined for CMB-S4, as well as the principals of their multiplexed readout. Through tests of superconducting film samples and devices, we helped tune the fabrication process of the AlMn TESes to meet the specifications needed for the Simons Observatory. Similar tests provided iterative feedback to Argonne National Laboratory to inform the fabrication process for AlMn TESes for CMB-S4.

Understanding the magnetic sensitivity of these superconducting detectors and readout components on which future experiments rely is important to motivate the magnetic shielding designs of the instrument and detector modules.

Through laboratory experiments, we presented and compared estimates of the magnetic sensitivity of μMUX and TDM SQUIDs as well as AlMn and MoCu TESes, and explored magnetic phenomena in the TES films. These measurements provided an estimate for desired magnetic shielding factors for upcoming experiments. Testing various magnetic shielding materials with NIST μMUX SQUIDs for SO also guided the design of the SO focal planes.

Cameras for the Atacama Cosmology Telescope provided heritage for some of the technologies presented in this work, as well as observations used to develop SZ analysis techniques. We used ACT data from data releases 3, 4 and 5 in conjunction with optical catalogs from BOSS-SDSS data releases 11 and 15 to measure the SZ effects. Our work with ACT DR4 and DR5 improved upon our work with DR3, and helped to develop the pairwise kSZ methods that future analyses and observations will push to a higher sensitivity regime. Measuring both the tSZ and kSZ effects using the same datasets allows us to compare independent estimates of halo optical depth and explore the potential for tSZ measurements to provide optical depth information for kSZ pairwise velocity measurements. Through comparing tSZ and pairwise kSZ measurements, we began to constrain the baryon content of the halos in our optical catalog, and we made progress towards an empirical relationship between optical depth and Compton-y for these galaxies which will inform simulations of their evolution.

Improved measurements of the SZ effect will require large collaborative efforts to further advances in detector and readout technologies and deploy large cryogenic receivers in upcoming microwave and submillimeter telescopes. Laboratory experiments like the ones discussed in this work motivate the design of these technologies, and data analysis progress such as that presented here

guides pipelines for the upcoming datasets. Together, these advances will make SZ measurements an important tool for cosmology in the years to come.

APPENDIX A

CRYOCOOLER TESTBED

The design of a small test cryostat which housed a Cryomech PT 410 cryocooler served as a laboratory testbed and a reference point for the future cryostat designs presented in this thesis. Loading estimates verified by laboratory performance informed the estimates used in the design of Mod-Cam (Section 2.3).

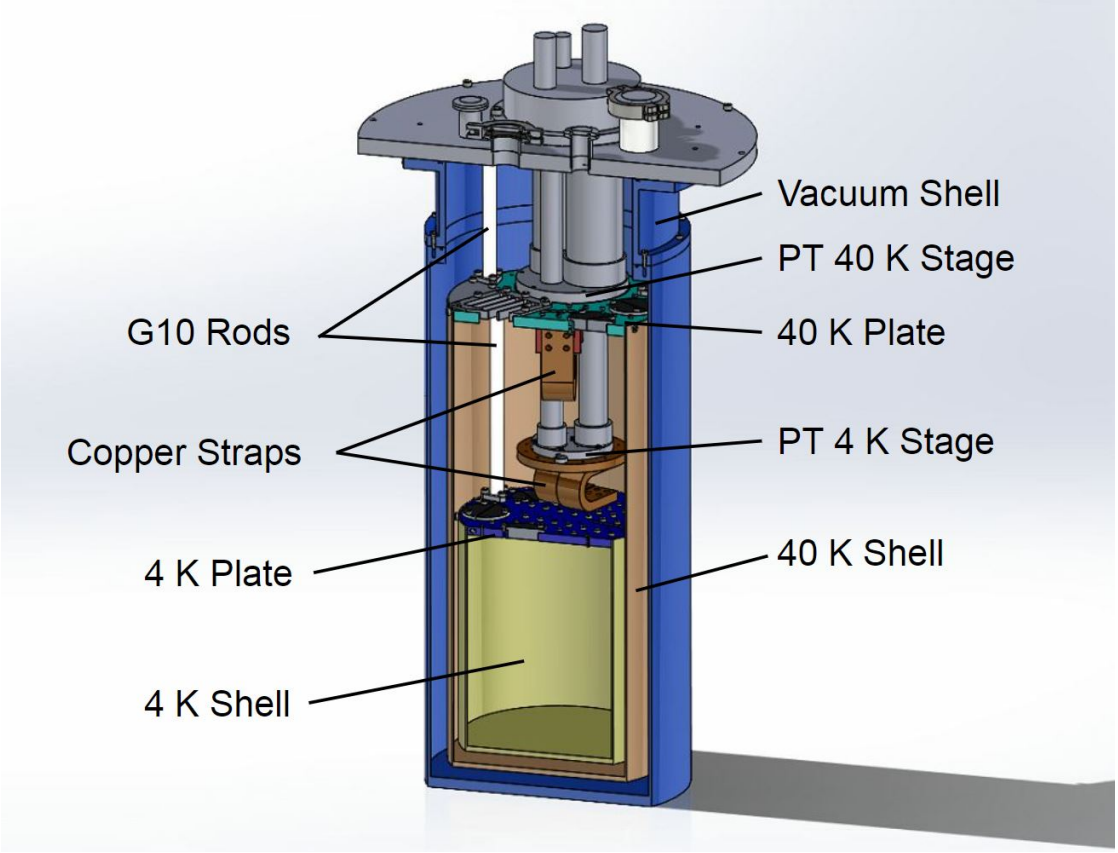

Figure A.1: A labeled diagram of the PT Test Dewar, including the Cryomech PT 410 crycooler with 40 and 4 K stages coupled via OFHC copper straps to 6061-T6 Al 40 and 4 K plates. Off of the cold plates hung 40 and 4 K 6061-T6 Al shells. The cold plates were each thermally isolated via three G10 rods epoxied to 6061-T6 mounting feet. A vacuum shell with multiple ports for wiring and pressure sensors was pumped out using a scroll and turbo pump.

The 12″ diameter, 30″ long cryostat, dubbed the ″PT Test Dewar,″ was fabricated by Precision Cryogenics. It consisted of a vacuum shell and 40 and 4 K stages separated by epoxied G10 rods and coupled to the cold heads of the PT 410 via Bluefors OFHC copper braided straps (Figure A.1). The G10 rods were epoxied with Stycast 2850-FT Epoxy to aluminum mounting feet in an epoxy jig. The loading on the 4 K stage from the three rods mounted to the 40 K stage was estimated to be ~20 mW.

A.1 Loading Estimate

A loading estimate for the PT Test Dewar with only a copper plate attached to the 4 K cold head (Figure A.2) is compared to the initial cooldown performance in which a base temperature of 5.52 K was achieved.

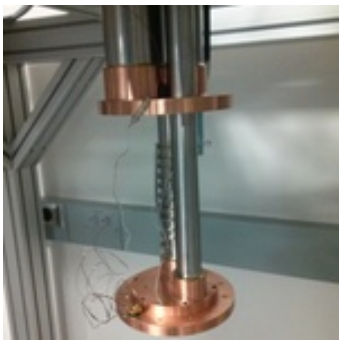

Figure A.2: The first cooldown of the Cryomech PT 410 within the vacuum shell of the PT Test Dewar, with one thermometer attached to a copper plate on the bottom of the 4 K stage.

Heat exchange equilibrium between two blackbodies can be computed as the difference between radiation emitted from the first body and absorbed by the second, and the radiation emitted by the second body and absorbed by the first. This power is given by

$$W = \sigma A_1 F_{12} (T_1^4 - T_2^4) \tag{A.1}$$

where the geometrical view factor F_{12} is the fraction of the total radiation leaving the first body absorbed by the second, σ is the Stefan-Boltzmann constant, A_1 is the area of the first body, and T_1 and T_2 are the temperatures of the first and second bodies, respectively [197]. F_{12} depends on the relative orientation of the two surfaces, with $0 \leq F_{12} \leq 1$, and it can be shown that reciprocity applies, i.e. $A_1 F_{12} = A_2 F_{21}$ [185]. The view factor for our specific geometry won't be calculated here and will be taken to be unity, which assumes parallel plane surfaces and is an obvious overestimation of the radiation from the outer shell intercepted by the copper stage on the PT. Therefore the following calculations will be upper bounds on the loading on the PT stages.

We assume that the outer shell of the dewar is a blackbody with $\epsilon_{shell} = 1.00$, the inner 40 K shell is a grey body with $\epsilon_{aluminum} = 0.07$ and the copper plate on the bottom stage of the PT is a grey body with $\epsilon_{copper} = 0.01$. Then, equation A.1 is modified to be [197]

$$W = \sigma A_1 F_{12} \frac{\epsilon_1 \epsilon_2}{\epsilon_1 + \epsilon_2 - \epsilon_1 \epsilon_2} (T_1^4 - T_2^4). \tag{A.2}$$

We estimate the involved areas to be the walls and bottom of the outer/inner shell (ignoring the top of the dewar due to the view factor) and the walls and bottom of the copper plate. Using 5.000″ diameter, 0.404″ tall copper cylinder dimensions, 9.874″ diameter, 21.260″ tall inner shield dimensions, and 11.750″

diameter, 25.000" tall outer shell dimensions, we obtain $A_{outer} = 0.665\ \mathrm{m}^2$, $A_{inner} = 0.475\ \mathrm{m}^2$, and $A_{copper} = 0.017\ \mathrm{m}^2$. We take room temperature to be 293.00 K, the temperature of the inner shield to be 40.00 K, and the temperature of the copper plate to be 5.52 K, the lowest temperature achieved during the first cooldown of the dewar. Plugging in to equation A.1 we find

$$\mathrm{W}_{\mathrm{outer}\rightarrow\mathrm{copper}} = \sigma \cdot 0.6654[\mathrm{m}^2] \cdot 0.01 \cdot (293^4 - 5.52^4)[\mathrm{K}^2] = \boxed{2.78\,\mathrm{W}} \tag{A.3}$$

for the load on the second stage of the PT when no intermediate shell is installed on the dewar. While this is a rough upper estimate, the Cryomech capacity curve (Figure A.3) for the PT when there is 0 W of loading on the 40 K stage of the PT suggests that this estimate is credible for our recorded base temperature of 5.52 K. Another estimate gives

$$\mathrm{W}_{\mathrm{outer}\rightarrow\mathrm{inner}} = \sigma \cdot 0.6654[\mathrm{m}^2] \cdot 0.07 \cdot (293^4 - 40^4)[\mathrm{K}^2] = \boxed{13.6\,\mathrm{W}} \tag{A.4}$$

for the load on the first stage of the PT if an intermediate shell on the stage is installed and brought to 40 K, ignoring the second stage. This is in rough agreement with what we would expect looking at the capacity curve. Another check,

$$\mathrm{W}_{\mathrm{inner}\rightarrow\mathrm{copper}} = \sigma \cdot 0.4749[\mathrm{m}^2] \cdot 0.01 \cdot (40^4 - 5.52^4)[\mathrm{K}^2] = \boxed{0.4\,\mu\mathrm{W}}, \tag{A.5}$$

shows that the inner shell, once cooled to 40 K, even if modeled as a blackbody, will produce a negligible load on the second stage of the PT.

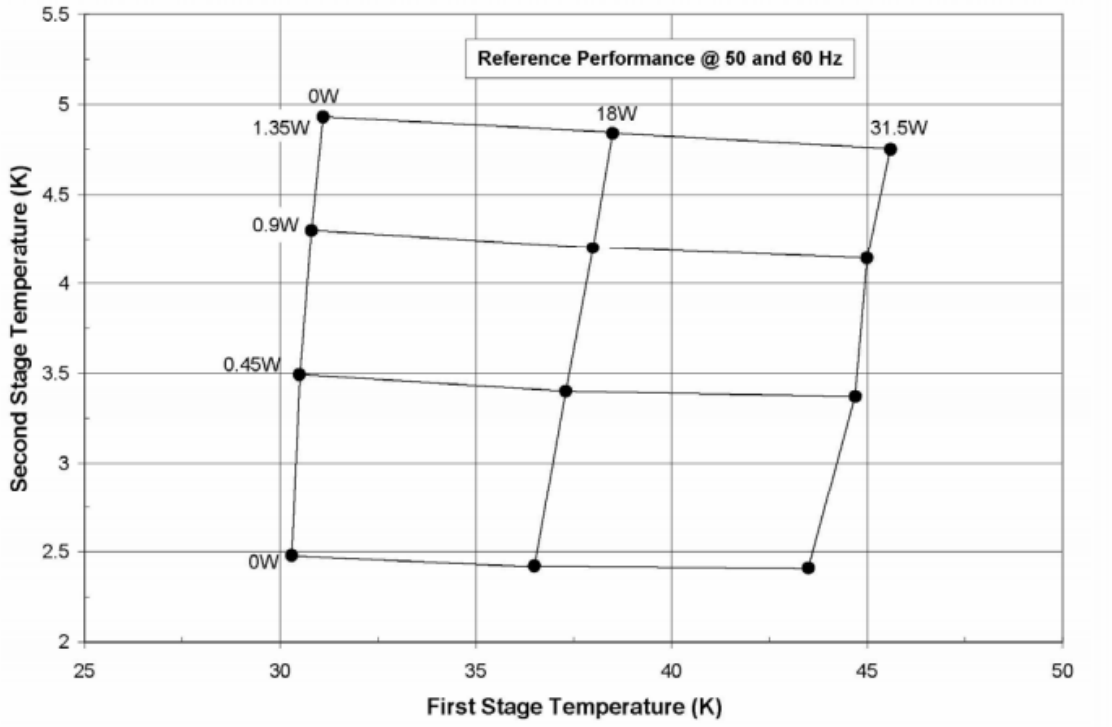

Figure A.3: Capacity curve of the PT 410 cryocooler, courtesy of Cryomech [134]. The first stage temperature is that of the 4 K stage and the second stage temperature is that of the 40 K stage. Achieved temperatures give an indication of the amount of loading present on each stage.

Subsequent tests with the PT Test Dewar in the full configuration with 40 and 4 K shells attached were successful, achieving temperatures below 30 K and ~2.5 K as expected from the loading curves from the first and second stages of the PT, respectively (Figure A.3). Later, students converted the testbed into an optical filter wheel assembly for Fourier Transform Spectrometer measurements.

APPENDIX B

SDSS DR15 CATALOG AND BINNING

B.1 CasJobs SDSS Query

The SDSS data used in V21 [264] and C21 [47] was downloaded from the SDSS Catalog Archive Server (CAS) via the SkyServer website in May of 2019. All of the CMASS and LOWZ galaxies are included in this catalog, in addition to more recently released eBOSS galaxies. We used this approach in defining the catalog to utilize as many SDSS LRGs as possible. The following query returned 602,461 objects. The positions, redshifts, cmodel and Petrosian magnitudes, extinction corrections, and object IDs are recorded for the objects. An RA and DEC cut is applied to target the survey area overlapping with our maps, and the redshifts of the objects are selected to match the range in DB17. "ZWARNING_NOQSO=0" indicates that the automated redshift estimate is reliable for the source. Objects with "zWarning=0" have no known redshift issues. Querying with "sciencePrimary>0" selects the best available unique set of spectra for the objects. Bitmasks are applied to exclude SDSS target flags: "SpecObjAll.TILE>= 10324" excludes incorrectly targeted LOWZ galaxies in early BOSS data, and the i-band fiber magnitude is selected to be the same as in DB17 [68].

```
SELECT
SpecObjAll.ra, SpecObjAll.dec, SpecObjAll.z,
PhotoObjAll.cModelMag_u, PhotoObjAll.cModelMag_g,
    PhotoObjAll.cModelMag_r, PhotoObjAll.cModelMag_i,
    PhotoObjAll.cModelMag_z, PhotoObjAll.cModelMagErr_u,
```

```
    PhotoObjAll.cModelMagErr_g,
PhotoObjAll.cModelMagErr_r, PhotoObjAll.cModelMagErr_i,
    PhotoObjAll.cModelMagErr_z,
PhotoObjAll.petroMag_u, PhotoObjAll.petroMag_g, PhotoObjAll.
    petroMag_r, PhotoObjAll.petroMag_i, PhotoObjAll.
    petroMag_z, PhotoObjAll.petroMagErr_u, PhotoObjAll.
    petroMagErr_g,
PhotoObjAll.petroMagErr_r, PhotoObjAll.petroMagErr_i,
    PhotoObjAll.petroMagErr_z, PhotoObjAll.extinction_u,
    PhotoObjAll.extinction_g, PhotoObjAll.extinction_r,
    PhotoObjAll.extinction_i,
PhotoObjAll.extinction_z, SpecObjAll.bestObjID into
    DR15_actplanck_catalog_wbestObjID_PetrANDcModel_20200902_EMV
     from SpecObjAll, PhotoObjAll, Photoz
 WHERE
((SpecObjAll.bestObjID = PhotoObjAll.objID) and (
    SpecObjAll.bestObjID = Photoz.objID))
and
    ((((SpecObjAll.ra BETWEEN 142.0 AND 180.0) and (
        SpecObjAll.dec BETWEEN -8.3 AND 22.0)) or ((
        SpecObjAll.ra BETWEEN 0.0 AND 142.0) and (SpecObjAll
        .dec BETWEEN -61.5 AND 22.0))
       or ((SpecObjAll.ra BETWEEN 246.0 AND 360.0) and (
          SpecObjAll.dec BETWEEN -61.5 AND 22.0)) or ((
          SpecObjAll.ra BETWEEN 180.0 AND 246.0) and (
          SpecObjAll.dec BETWEEN -8.3 AND 22.0)))
```

```
and (SpecObjAll.ZWARNING_NOQSO = 0) and
(SpecObjAll.zWarning = 0) AND
(SpecObjAll.sciencePrimary>0) and
(SpecObjAll.z>0.049) and
(SpecObjAll.z<0.8) and
((((SpecObjAll.BOSS_TARGET1 & 0x0000000000000001) != 0)
   and
(SpecObjAll.TILE>= 10324)) OR
(((SpecObjAll.BOSS_TARGET1 & 0x0000000000000002)!=0) and
  (PhotoObjAll.fiber2Mag_i<21.5))))
```

B.2 DR15 Luminosity Binning

Luminosity bins for the joint tSZ and kSZ analyses with V21 [264] and C21 [47] were chosen based on luminosity cuts from DB17 (Table 5.1) ($L > 7.9 \times 10^{10} L_{\odot}$ and $L > 6.1 \times 10^{10} L_{\odot}$) as well as one lower luminosity cut, ($L > 4.3 \times 10^{10} L_{\odot}$). The three disjoint bins were selected to have roughly equal spacing, each with ~100,000 galaxies after cutting for analysis with the DR5 maps (Table 5.1). The luminosity cuts are plotted over a histogram of the SDSS samples in Figure 9.

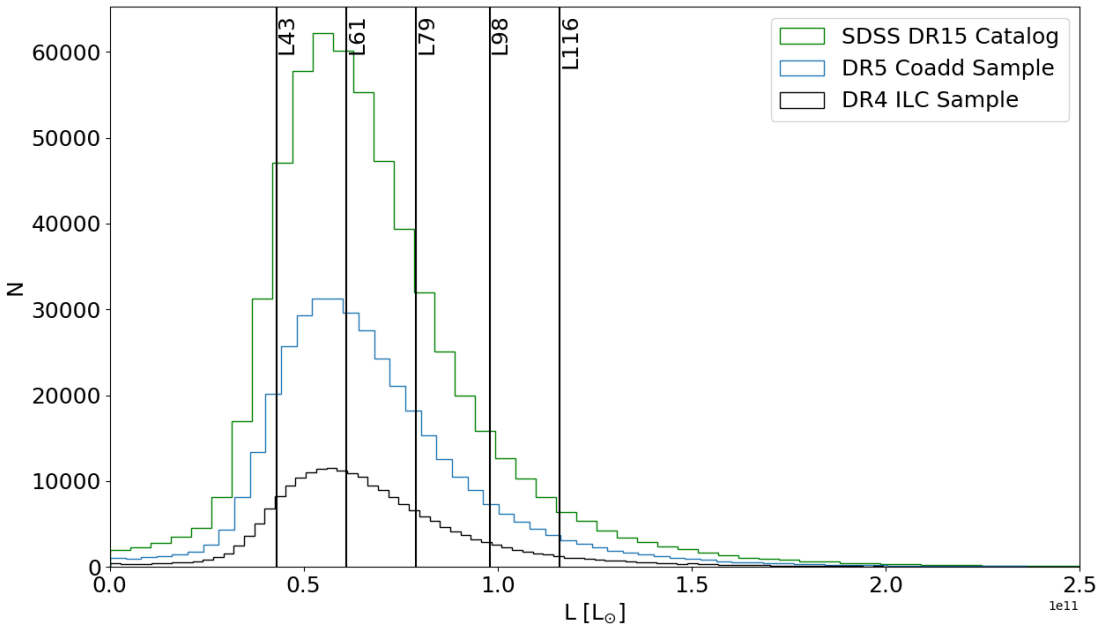

Figure B.1: Luminosity bin cuts for the SDSS DR15 catalog plotted over a histogram of the full sample (green), DR5 f150 and DR5 f090 selected analysis sample (blue), and DR4 ILC sample (black). The bottom three bins were selected to each have over 100,000 galaxies for the joint tSZ and kSZ analyses of the DR5 maps, while being roughly evenly spaced and overlapping with bin selection from the DB17 analysis. The top two bins were added for the tSZ analysis to study higher mass bins that have a strong tSZ signal, while also overlapping with DB17 bins.

BIBLIOGRAPHY

[1] Sadleir, J.E., *Superconducting transition-edge sensor physics*, Ph.D. Thesis, University of Illinois (2010).

[2] T.M. Lanting et al., Appl. Phys. Lett. 86, 112511 (2005).

[3] K.D. Irwin, K.W. Lehnert, Applied Physics Letters 85, 2107 (2004).

[4] J.A.B. Mates, G.C. Hilton, K.D. Irwin, L.R. Vale, K.W. Lehnert, Applied Physics Letters 92, 023514 (2008).

[5] M.D. Niemack, *Towards Dark Energy: Design, Development, and Preliminary Data from ACT*, Ph.D. Thesis, Princeton University (2008).

[6] K. N. Abazajian, P. Adshead, Z. Ahmed, S. W. Allen, D. Alonso, K. S. Arnold, C. Baccigalupi, J. G. Bartlett, N. Battaglia, B. A. Benson, C. A. Bischoff, J. Borrill, V. Buza, E. Calabrese, R. Caldwell, J. E. Carlstrom, C. L. Chang, T. M. Crawford, F.-Y. Cyr-Racine, F. De Bernardis, T. de Haan, S. di Serego Alighieri, J. Dunkley, C. Dvorkin, J. Errard, G. Fabbian, S. Feeney, S. Ferraro, J. P. Filippini, R. Flauger, G. M. Fuller, V. Gluscevic, D. Green, D. Grin, E. Grohs, J. W. Henning, J. C. Hill, R. Hlozek, G. Holder, W. Holzapfel, W. Hu, K. M. Huffenberger, R. Keskitalo, L. Knox, A. Kosowsky, J. Kovac, E. D. Kovetz, C.-L. Kuo, A. Kusaka, M. Le Jeune, A. T. Lee, M. Lilley, M. Loverde, M. S. Madhavacheril, A. Mantz, D. J. E. Marsh, J. McMahon, P. D. Meerburg, J. Meyers, A. D. Miller, J. B. Munoz, H. N. Nguyen, M. D. Niemack, M. Peloso, J. Peloton, L. Pogosian, C. Pryke, M. Raveri, C. L. Reichardt, G. Rocha, A. Rotti, E. Schaan, M. M. Schmittfull, D. Scott, N. Sehgal, S. Shandera, B. D. Sherwin, T. L. Smith, L. Sorbo, G. D. Starkman, K. T. Story, A. van Engelen, J. D. Vieira, S. Watson, N. Whitehorn, and W. L. Kimmy Wu. CMB-S4 Science Book, First Edition. *ArXiv e-prints*, October 2016.

[7] K. N. Abazajian, P. Adshead, Z. Ahmed, et al. CMB-S4 Science Book, First Edition. *ArXiv e-prints*, October 2016. 1610.02743.

[8] K. N. Abazajian, K. Arnold, J. Austermann, B. A. Benson, C. Bischoff, J. Bock, J. R. Bond, J. Borrill, E. Calabrese, J. E. Carlstrom, C. S. Carvalho, C. L. Chang, H. C. Chiang, S. Church, A. Cooray, T. M. Crawford, K. S. Dawson, S. Das, M. J. Devlin, M. Dobbs, S. Dodelson, O. Doré, J. Dunkley, J. Errard, A. Fraisse, J. Gallicchio, N. W. Halverson, S. Hanany, S. R. Hildebrandt, A. Hincks, R. Hlozek, G. Holder, W. L. Holzapfel, K. Honscheid,

W. Hu, J. Hubmayr, K. Irwin, W. C. Jones, M. Kamionkowski, B. Keating, R. Keisler, L. Knox, E. Komatsu, J. Kovac, C.-L. Kuo, C. Lawrence, A. T. Lee, E. Leitch, E. Linder, P. Lubin, J. McMahon, A. Miller, L. Newburgh, M. D. Niemack, H. Nguyen, H. T. Nguyen, L. Page, C. Pryke, C. L. Reichardt, J. E. Ruhl, N. Sehgal, U. Seljak, J. Sievers, E. Silverstein, A. Slosar, K. M. Smith, D. Spergel, S. T. Staggs, A. Stark, R. Stompor, A. G. Vieregg, G. Wang, S. Watson, E. J. Wollack, W. L. K. Wu, K. W. Yoon, and O. Zahn. Neutrino physics from the cosmic microwave background and large scale structure. *Astroparticle Physics*, 63:66–80, March 2015.

[9] K. N. Abazajian et al. Neutrino Physics from the Cosmic Microwave Background and Large Scale Structure. *Astropart. Phys.*, 63:66–80, 2015.

[10] Kevork Abazajian et al. CMB-S4 Science Case, Reference Design, and Project Plan. *arXiv e-prints*, page arXiv:1907.04473, July 2019.

[11] T. M. C. Abbott, M. Aguena, A. Alarcon, S. Allam, S. Allen, J. Annis, S. Avila, D. Bacon, K. Bechtol, A. Bermeo, G. M. Bernstein, E. Bertin, S. Bhargava, S. Bocquet, D. Brooks, D. Brout, E. Buckley-Geer, D. L. Burke, A. Carnero Rosell, M. Carrasco Kind, J. Carretero, F. J. Castander, R. Cawthon, C. Chang, X. Chen, A. Choi, M. Costanzi, M. Crocce, L. N. da Costa, T. M. Davis, J. De Vicente, J. DeRose, S. Desai, H. T. Diehl, J. P. Dietrich, S. Dodelson, P. Doel, A. Drlica-Wagner, K. Eckert, T. F. Eifler, J. Elvin-Poole, J. Estrada, S. Everett, A. E. Evrard, A. Farahi, I. Ferrero, B. Flaugher, P. Fosalba, J. Frieman, J. García-Bellido, M. Gatti, E. Gaztanaga, D. W. Gerdes, T. Giannantonio, P. Giles, S. Grandis, D. Gruen, R. A. Gruendl, J. Gschwend, G. Gutierrez, W. G. Hartley, S. R. Hinton, D. L. Hollowood, K. Honscheid, B. Hoyle, D. Huterer, D. J. James, M. Jarvis, T. Jeltema, M. W. G. Johnson, M. D. Johnson, S. Kent, E. Krause, R. Kron, K. Kuehn, N. Kuropatkin, O. Lahav, T. S. Li, C. Lidman, M. Lima, H. Lin, N. MacCrann, M. A. G. Maia, A. Mantz, J. L. Marshall, P. Martini, J. Mayers, P. Melchior, J. Mena-Fernández, F. Menanteau, R. Miquel, J. J. Mohr, R. C. Nichol, B. Nord, R. L. C. Ogando, A. Palmese, F. Paz-Chinchón, A. A. Plazas, J. Prat, M. M. Rau, A. K. Romer, A. Roodman, P. Rooney, E. Rozo, E. S. Rykoff, M. Sako, S. Samuroff, C. Sánchez, E. Sanchez, A. Saro, V. Scarpine, M. Schubnell, D. Scolnic, S. Serrano, I. Sevilla-Noarbe, E. Sheldon, J. Allyn. Smith, M. Smith, E. Suchyta, M. E. C. Swanson, G. Tarle, D. Thomas, C. To, M. A. Troxel, D. L. Tucker, T. N. Varga, A. von der Linden, A. R. Walker, R. H. Wechsler, J. Weller, R. D. Wilkinson, H. Wu, B. Yanny, Y. Zhang, Z. Zhang, J. Zuntz, and DES Collaboration. Dark Energy Survey Year 1 Results: Cosmological constraints from cluster abundances and weak lensing. , 102(2):023509, July 2020.

[12] M. H. Abitbol et al. CMB-S4 Technology Book, First Edition. *ArXiv e-prints*, June 2017.

[13] Maximilian H. Abitbol, Zeeshan Ahmed, Darcy Barron, et al. CMB-S4 Technology Book, First Edition. *ArXiv e-prints*, June 2017. 1706.02464.

[14] Maximilian H. Abitbol et al. CMB-S4 Technology Book, First Edition. *arXiv e-prints*, 1706.02464, June 2017.

[15] S. Adachi, M. A. O. Aguilar Faúndez, K. Arnold, C. Baccigalupi, D. Barron, D. Beck, F. Bianchini, S. Chapman, K. Cheung, Y. Chinone, K. Crowley, M. Dobbs, H. El Bouhargani, T. Elleflot, J. Errard, G. Fabbian, C. Feng, T. Fujino, N. Galitzki, N. Goeckner-Wald, J. Groh, G. Hall, M. Hasegawa, M. Hazumi, H. Hirose, A. H. Jaffe, O. Jeong, D. Kaneko, N. Katayama, B. Keating, S. Kikuchi, T. Kisner, A. Kusaka, A. T. Lee, D. Leon, E. Linder, L. N. Lowry, F. Matsuda, T. Matsumura, Y. Minami, M. Navaroli, H. Nishino, A. T. P. Pham, D. Poletti, C. L. Reichardt, Y. Segawa, P. Siritanasak, O. Tajima, S. Takakura, S. Takatori, D. Tanabe, G. P. Teply, C. Tsai, C. Vergès, B. Westbrook, Y. Zhou, and Polarbear Collaboration. A Measurement of the CMB E-mode Angular Power Spectrum at Subdegree Scales from 670 Square Degrees of POLARBEAR Data. , 904(1):65, November 2020.

[16] N. Aghanim, M. Douspis, G. Hurier, D. Crichton, et al. PACT. I. Combining ACT and Planck data for improved extraction of tSZ signal. , 632:A47, December 2019.

[17] Nabila Aghanim, Subhabrata Majumdar, and Joseph Silk. Secondary anisotropies of the CMB. *Reports on Progress in Physics*, 71(6):066902, June 2008.

[18] D. S. Aguado et al. The Fifteenth Data Release of the Sloan Digital Sky Surveys: First Release of MaNGA-derived Quantities, Data Visualization Tools, and Stellar Library. , 240(2):23, February 2019.

[19] Aamir M. Ali, Shunsuke Adachi, Kam Arnold, Peter Ashton, Andrew Bazarko, Yuji Chinone, Gabriele Coppi, Lance Corbett, Kevin D. Crowley, Kevin T. Crowley, and et al. Small aperture telescopes for the simons observatory. *Journal of Low Temperature Physics*, 200(5-6):461–471, Apr 2020.

[20] Elham Alipour, Kris Sigurdson, and Christopher M. Hirata. Effects of Rayleigh scattering on the CMB and cosmic structure. *Phys. Rev.*, D91(8):083520, 2015.

[21] Stefania Amodeo et al. The Atacama Cosmology Telescope: Modelling the Gas Thermodynamics in BOSS CMASS galaxies from Kinematic and Thermal Sunyaev-Zel'dovich Measurements. 9 2020.

[22] M. Arnaud, G. W. Pratt, R. Piffaretti, H. Böhringer, J. H. Croston, and E. Pointecouteau. The universal galaxy cluster pressure profile from a representative sample of nearby systems (REXCESS) and the Y_{SZ} - M_{500} relation. *AAP*, 517:A92, July 2010.

[23] J. E. Austermann et al. Millimeter-Wave Polarimeters Using Kinetic Inductance Detectors for TolTEC and Beyond. *ArXiv e-prints*, March 2018. 1803.03280.

[24] Jason Austermann, James Beall, Sean A. Bryan, Brad Dober, Jiansong Gao, Gene Hilton, Johannes Hubmayr, Philip Mauskopf, Christopher McKenney, Sara M. Simon, Joel Ullom, Michael Vissers, and Grant W. Wilson. Large format arrays of kinetic inductance detectors for the TolTEC millimeter-wave imaging polarimeter (Conference Presentation). In *Millimeter, Submillimeter, and Far-Infrared Detectors and Instrumentation for Astronomy IX*, volume 10708, page 107080U. International Society for Optics and Photonics, July 2018.

[25] N. Battaglia. The tau of galaxy clusters. *JCAP*, 8:058, August 2016.

[26] N. Battaglia, J. R. Bond, C. Pfrommer, and J. L. Sievers. On the Cluster Physics of Sunyaev-Zel'dovich and X-Ray Surveys. II. Deconstructing the Thermal SZ Power Spectrum. , 758:75, October 2012.

[27] N. Battaglia, S. Ferraro, E. Schaan, and D. Spergel. Future constraints on halo thermodynamics from combined Sunyaev-Zel'dovich measurements. *ArXiv e-prints*, May 2017. 1705.05881.

[28] E. S. Battistelli, M. Amiri, B. Burger, M. J. Devlin, S. R. Dicker, W. B. Doriese, R. Dünner, R. P. Fisher, J. W. Fowler, M. Halpern, M. Hasselfield, G. C. Hilton, A. D. Hincks, K. D. Irwin, M. Kaul, J. Klein, S. Knotek, J. M. Lau, M. Limon, T. A. Marriage, M. D. Niemack, L. Page, C. D. Reintsema, S. T. Staggs, D. S. Swetz, E. R. Switzer, R. J. Thornton, and Y. Zhao. Automated SQUID tuning procedure for kilo-pixel arrays of TES bolometers on the Atacama Cosmology Telescope. In William D. Duncan, Wayne S. Holland, Stafford Withington, and Jonas Zmuidzinas, editors, *Millimeter and Submillimeter Detectors and Instrumentation for Astronomy IV*, volume 7020 of *Society of Photo-Optical Instrumentation Engineers (SPIE) Conference Series*, page 702028, July 2008.

[29] D. Baumann and L. McAllister. *Inflation and String Theory*. April 2015.

[30] Daniel Baumann. TASI Lectures on Primordial Cosmology. *arXiv e-prints*, page arXiv:1807.03098, July 2018.

[31] Eric F. Bell and Roelof S. de Jong. Stellar Mass-to-Light Ratios and the Tully-Fisher Relation. , 550(1):212–229, Mar 2001.

[32] Eric F. Bell, Daniel H. McIntosh, Neal Katz, and Martin D. Weinberg. The Optical and Near-Infrared Properties of Galaxies. I. Luminosity and Stellar Mass Functions. , 149(2):289–312, Dec 2003.

[33] C. L. Bennett, M. Bay, M. Halpern, G. Hinshaw, C. Jackson, N. Jarosik, A. Kogut, M. Limon, S. S. Meyer, L. Page, D. N. Spergel, G. S. Tucker, D. T. Wilkinson, E. Wollack, and E. L. Wright. The Microwave Anisotropy Probe Mission. , 583(1):1–23, January 2003.

[34] B. A. Benson and et al. SPT-3G: a next-generation cosmic microwave background polarization experiment on the South Pole telescope. *Proc. SPIE Millimeter, Submillimeter, and Far-Infrared Detectors and Instrumentation for Astronomy VII*, 9153:91531P, July 2014.

[35] M. Bernardi, F. Shankar, J. B. Hyde, S. Mei, F. Marulli, and R. K. Sheth. Galaxy luminosities, stellar masses, sizes, velocity dispersions as a function of morphological type. , 404(4):2087–2122, Jun 2010.

[36] Suman Bhattacharya and Arthur Kosowsky. Cosmological Constraints from Galaxy Cluster Velocity Statistics. *Astrophys.J.*, 659:L83–L86, 2007.

[37] Suman Bhattacharya and Arthur Kosowsky. Dark Energy Constraints from Galaxy Cluster Peculiar Velocities. *Phys. Rev. D*, 77:083004, 2008.

[38] BICEP2 Collaboration, Keck Array Collaboration, P. A. R. Ade, Z. Ahmed, R. W. Aikin, K. D. Alexander, D. Barkats, S. J. Benton, C. A. Bischoff, J. J. Bock, R. Bowens-Rubin, J. A. Brevik, I. Buder, E. Bullock, V. Buza, J. Connors, J. Cornelison, B. P. Crill, M. Crumrine, M. Dierickx, L. Duband, C. Dvorkin, J. P. Filippini, S. Fliescher, J. Grayson, G. Hall, M. Halpern, S. Harrison, S. R. Hildebrandt, G. C. Hilton, H. Hui, K. D. Irwin, J. Kang, K. S. Karkare, E. Karpel, J. P. Kaufman, B. G. Keating, S. Kefeli, S. A. Kernasovskiy, J. M. Kovac, C. L. Kuo, N. A. Larsen, K. Lau, E. M. Leitch, M. Lueker, K. G. Megerian, L. Moncelsi, T. Namikawa, C. B. Netterfield, H. T. Nguyen, R. O'Brient, R. W. Ogburn, S. Palladino, C. Pryke, B. Racine,

S. Richter, A. Schillaci, R. Schwarz, C. D. Sheehy, A. Soliman, T. St. Germaine, Z. K. Staniszewski, B. Steinbach, R. V. Sudiwala, G. P. Teply, K. L. Thompson, J. E. Tolan, C. Tucker, A. D. Turner, C. Umiltà, A. G. Vieregg, A. Wandui, A. C. Weber, D. V. Wiebe, J. Willmert, C. L. Wong, W. L. K. Wu, H. Yang, K. W. Yoon, and C. Zhang. Constraints on Primordial Gravitational Waves Using Planck, WMAP, and New BICEP2/Keck Observations through the 2015 Season. , 121(22):221301, November 2018.

[39] S. M. Bilenky. On the origin of majorana neutrino masses, 2020.

[40] Michael R. Blanton and Sam Roweis. K-Corrections and Filter Transformations in the Ultraviolet, Optical, and Near-Infrared. , 133(2):734–754, February 2007.

[41] L. Bleem, B. Stalder, T. de Haan, et al. Galaxy Clusters Discovered via the Sunyaev-Zel'dovich Effect in the 2500-Square-Degree SPT-SZ Survey. , 216(2):27, February 2015.

[42] G. Boato, G. Gallinaro, and C. Rizzuto. Effect of transition-metal impurities on the critical temperature of superconducting al, zn, in, and sn. *Phys. Rev.*, 148:353–361, Aug 1966.

[43] BOSS Collaboration. Cosmological implications of baryon acoustic oscillation measurements. , 92(12):123516, December 2015.

[44] I. S. Bowen and A. H. Vaughan. The optical design of the 40-in. telescope and of the irenee dupont telescope at las campanas observatory, chile. *Appl. Opt.*, 12(7):1430–1435, Jul 1973.

[45] C. M. Bradford, G. J. Stacey, M. R. Swain, et al. SPIFI: a direct-detection imaging spectrometer for submillimeter wavelengths. *Applied Optics*, 41:2561–2574, May 2002.

[46] Philip Bull, Timothy Clifton, and Pedro G. Ferreira. The kSZ effect as a test of general radial inhomogeneity in LTB cosmology. *Phys. Rev.*, D85:024002, 2012.

[47] Victoria Calafut, Patricio A. Gallardo, Eve. M. Vavagiakis, Stefania Amodeo, et al. The Atacama Cosmology Telescope: Detection of the Pairwise Kinematic Sunyaev-Zel'dovich Effect with SDSS DR15 Galaxies. 1 2021.

[48] John E. Carlstrom, Gilbert P. Holder, and Erik D. Reese. Cosmology with the sunyaev-zelâdovich effect. *Annual Review of Astronomy and Astrophysics*, 40(1):643–680, 2002.

[49] Sean M. Carroll. The Cosmological Constant. *Living Reviews in Relativity*, 4(1):1, February 2001.

[50] Renyue Cen and Jeremiah P. Ostriker. Where Are the Baryons? II. Feedback Effects. , 650(2):560–572, October 2006.

[51] Gilles Chabrier. Galactic Stellar and Substellar Initial Mass Function. , 115(809):763–795, July 2003.

[52] Scott C. Chapman et al. A 350 micron camera module for the Prime-Cam instrument on CCAT-prime. In *Society of Photo-Optical Instrumentation Engineers (SPIE) Conference Series*, volume 11453 of *Society of Photo-Optical Instrumentation Engineers (SPIE) Conference Series*, December 2020.

[53] Jonas Chaves-Montero, Carlos Hernandez-Monteagudo, Raul E. Angulo, and J. D. Emberson. Measuring the evolution of intergalactic gas from z=0 to 5 using the kinematic Sunyaev-Zel'dovich effect. *arXiv e-prints*, November 2019.

[54] I. Chiu, J. J. Mohr, M. McDonald, S. Bocquet, et al. Baryon content in a sample of 91 galaxy clusters selected by the south pole telescope at 0.2 ¡z ¡ 1.25. *Monthly Notices of the Royal Astronomical Society*, 478(3):3072–3099, May 2018.

[55] S. K. Choi, J. Austermann, K. Basu, N. Battaglia, F. Bertoldi, D. T. Chung, N. F. Cothard, S. Duff, C. J. Duell, P. A. Gallardo, J. Gao, T. Herter, J. Hubmayr, M. D. Niemack, T. Nikola, D. Riechers, K. Rossi, G. J. Stacey, J. R. Stevens, E. M. Vavagiakis, M. Vissers, and S. Walker. Sensitivity of the Prime-Cam Instrument on the CCAT-Prime Telescope. *Journal of Low Temperature Physics*, 199(3-4):1089–1097, March 2020.

[56] Steve K. Choi et al. The Atacama Cosmology Telescope: A Measurement of the Cosmic Microwave Background Power Spectra at 98 and 150 GHz. 7 2020.

[57] G. Coppi et al. Cooldown strategies and transient thermal simulations for the Simons Observatory. *Proc. SPIE*, (10708-77), 2018.

[58] N. F. Cothard, S. K. Choi, C. J. Duell, T. Herter, J. Hubmayr, J. McMahon, M. D. Niemack, T. Nikola, C. Sierra, G. J. Stacey, E. M. Vavagiakis, E. J. Wollack, and B. Zou. The Design of the CCAT-prime Epoch of Reionization Spectrometer Instrument. *Journal of Low Temperature Physics*, 199(3-4):898–907, January 2020.

[59] N. F. Cothard et al. Optimizing the efficiency of Fabry-Perot interferometers with silicon-substrate mirrors. *Proc. SPIE*, (10706-182), 2018.

[60] Nicholas F. Cothard, Aamir M. Ali, Jason E. Austermann, Steve K. Choi, Kevin T. Crowley, Bradley J. Dober, Cody J. Duell, Shannon M. Duff, Patricio Gallardo, Gene C. Hilton, Shuay-Pwu Patty Ho, Johannes Hubmayr, Michael J. Link, Michael D. Niemack, Rita F. Sonka, Suzanne T. Staggs, Eve M. Vavagiakis, Edward J. Wollack, and Zhilei Xu. Comparing complex impedance and bias step measurements of Simons Observatory transition edge sensors. In *Society of Photo-Optical Instrumentation Engineers (SPIE) Conference Series*, volume 11453 of *Society of Photo-Optical Instrumentation Engineers (SPIE) Conference Series*, page 1145325, December 2020.

[61] Omar Darwish, Mathew S. Madhavacheril, Blake D. Sherwin, Simone Aiola, Nicholas Battaglia, James A. Beall, Daniel T. Becker, J. Richard Bond, Erminia Calabrese, Steve K. Choi, Mark J. Devlin, Jo Dunkley, Rolando Dünner, Simone Ferraro, Anna E. Fox, Patricio A. Gallardo, Yilun Guan, Mark Halpern, Dongwon Han, Matthew Hasselfield, J. Colin Hill, Gene C. Hilton, Matt Hilton, Adam D. Hincks, Shuay-Pwu Patty Ho, J. Hubmayr, John P. Hughes, Brian J. Koopman, Arthur Kosowsky, J. Van Lanen, Thibaut Louis, Marius Lungu, Amanda MacInnis, Loïc Maurin, Jeffrey McMahon, Kavilan Moodley, Sigurd Naess, Toshiya Namikawa, Federico Nati, Laura Newburgh, John P. Nibarger, Michael D. Niemack, Lyman A. Page, Bruce Partridge, Frank J. Qu, Naomi Robertson, Alessandro Schillaci, Benjamin Schmitt, Neelima Sehgal, Cristóbal Sifón, David N. Spergel, Suzanne Staggs, Emilie Storer, Alexander van Engelen, and Edward J. Wollack. The Atacama Cosmology Telescope: a CMB lensing mass map over 2100 square degrees of sky and its cross-correlation with BOSS-CMASS galaxies. , 500(2):2250–2263, January 2021.

[62] Sudeep Das, Thibaut Louis, Michael R. Nolta, et al. The Atacama Cosmology Telescope: temperature and gravitational lensing power spectrum measurements from three seasons of data. , 2014(4):014, April 2014.

[63] R. Datta, C. D. Munson, M. D. Niemack, et al. Large-aperture wide-bandwidth antireflection-coated silicon lenses for millimeter wavelengths. *Applied Optics*, 52:8747, December 2013.

[64] R. Datta, C. D. Munson, M. D. Niemack, J. J. McMahon, J. Britton, E. J. Wollack, J. Beall, M. J. Devlin, J. Fowler, P. Gallardo, J. Hubmayr, K. Irwin, L. Newburgh, J. P. Nibarger, L. Page, M. A. Quijada, B. L. Schmitt, S. T. Staggs, R. Thornton, and L. Zhang. Large-aperture wide-bandwidth antireflection-coated silicon lenses for millimeter wavelengths. *Appl. Opt.*, 52(36):8747–8758, Dec 2013.

[65] M. Davis and P. J. E. Peebles. A survey of galaxy redshifts. V. The two-point position and velocity correlations. , 267:465–482, April 1983.

[66] K. S. Dawson, D. J. Schlegel, et al. The Baryon Oscillation Spectroscopic Survey of SDSS-III. 145:10, January 2013.

[67] Kyle S. Dawson, Schlegel, et al. The Baryon Oscillation Spectroscopic Survey of SDSS-III. , 145(1):10, January 2013.

[68] F. De Bernardis et al. Detection of the pairwise kinematic Sunyaev-Zel'dovich effect with BOSS DR11 and the Atacama Cosmology Telescope. *JCAP*, 1703(03):008, 2017.

[69] Francesco De Bernardis et al. Survey strategy optimization for the Atacama Cosmology Telescope. *SPIE proceedings*, 2016.

[70] Pablo F. de Salas, Stefano Gariazzo, Olga Mena, Christoph A. Ternes, and Mariam Tórtola. Neutrino mass ordering from oscillations and beyond: 2018 status and future prospects. *Frontiers in Astronomy and Space Sciences*, 5, Oct 2018.

[71] Simon DeDeo, David N. Spergel, and Hy Trac. The kinetic Sunyaev-Zel'dovitch effect as a dark energy probe. 2005.

[72] S. W. Deiker, W. Doriese, G. C. Hilton, K. D. Irwin, W. H. Rippard, J. N. Ullom, L. R. Vale, S. T. Ruggiero, A. Williams, and B. A. Young. Superconducting transition edge sensor using dilute almn alloys. 85(11):2137–2139, 2004.

[73] A. C. Deshpande, T. D. Kitching, V. F. Cardone, P. L. Taylor, S. Casas, S. Camera, C. Carbone, M. Kilbinger, V. Pettorino, Z. Sakr, D. Sapone, I. Tutusaus, N. Auricchio, C. Bodendorf, D. Bonino, M. Brescia, V. Capobianco, J. Carretero, M. Castellano, S. Cavuoti, R. Cledassou, G. Congedo, L. Conversi, L. Corcione, M. Cropper, F. Dubath, S. Dusini, G. Fabbian, E. Franceschi, M. Fumana, B. Garilli, F. Grupp, H. Hoekstra, F. Hormuth, H. Israel, K. Jahnke, S. Kermiche, B. Kubik, M. Kunz, F. Lacasa,

S. Ligori, P. B. Lilje, I. Lloro, E. Maiorano, O. Marggraf, R. Massey, S. Mei, M. Meneghetti, G. Meylan, L. Moscardini, C. Padilla, S. Paltani, F. Pasian, S. Pires, G. Polenta, M. Poncet, F. Raison, J. Rhodes, M. Roncarelli, R. Saglia, P. Schneider, A. Secroun, S. Serrano, G. Sirri, J. L. Starck, F. Sureau, A. N. Taylor, I. Tereno, R. Toledo-Moreo, L. Valenziano, Y. Wang, and J. Zoubian. Euclid: The reduced shear approximation and magnification bias for Stage IV cosmic shear experiments. , 636:A95, April 2020.

[74] S. Dicker et al. Cold optical design for Simons Observatory large telescope. *Proc. SPIE*, (10700-122), 2018.

[75] B. Dober et al. Optical Demonstration of THz, Dual-Polarization Sensitive Microwave Kinetic Inductance Detectors. *Journal of Low Temperature Physics*, 184:173–179, July 2016.

[76] B. Dober et al. Microwave SQUID multiplexer demonstration for cosmic microwave background imagers. *Applied Physics Letters*, 111(24):243510, December 2017.

[77] G. Douthit et al. Development of the Fabry-Perot Interferometers for the HIRMES spectrometer on SOFIA. *Proc. SPIE*, (10708-59), 2018.

[78] Cody J. Duell, Eve M. Vavagiakis, Jason Austermann, Scott C. Chapman, Steve K. Choi, Nicholas F. Cothard, Brad Dober, Patricio Gallardo, Jiansong Gao, Christopher Groppi, Terry L. Herter, Gordon J. Stacey, Zachary Huber, Johannes Hubmayr, Doug Johnstone, Yaqiong Li, Philip Mauskopf, Jeff McMahon, Michael D. Niemack, Thomas Nikola, Kayla Rossi, Sara Simon, Adrian K. Sinclair, Michael Vissers, Jordan Wheeler, and Bugao Zou. CCAT-prime: Designs and status of the first light 280 GHz MKID array and mod-cam receiver. In *Society of Photo-Optical Instrumentation Engineers (SPIE) Conference Series*, volume 11453 of *Society of Photo-Optical Instrumentation Engineers (SPIE) Conference Series*, page 114531F, December 2020.

[79] S. M. Duff, J. Austermann, J. A. Beall, D. Becker, R. Datta, P. A. Gallardo, S. W. Henderson, G. C. Hilton, S. P. Ho, J. Hubmayr, B. J. Koopman, D. Li, J. McMahon, F. Nati, M. D. Niemack, C. G. Pappas, M. Salatino, B. L. Schmitt, S. M. Simon, S. T. Staggs, J. R. Stevens, J. Van Lanen, E. M. Vavagiakis, J. T. Ward, and E. J. Wollack. Advanced actpol multichroic polarimeter array fabrication process for 150 mm wafers. *Journal of Low Temperature Physics*, 184(3):634–641, 2016.

[80] S. Eales et al. The Herschel ATLAS. , 122(891):499, May 2010.

[81] EBEX Collaboration, Asad Aboobaker, Peter Ade, Derek Araujo, François Aubin, Carlo Baccigalupi, Chaoyun Bao, Daniel Chapman, Joy Didier, Matt Dobbs, Will Grainger, Shaul Hanany, Kyle Helson, Seth Hillbrand, Johannes Hubmayr, Andrew Jaffe, Bradley Johnson, Terry Jones, Jeff Klein, Andrei Korotkov, Adrian Lee, Lorne Levinson, Michele Limon, Kevin MacDermid, Amber D. Miller, Michael Milligan, Lorenzo Moncelsi, Enzo Pascale, Kate Raach, Britt Reichborn-Kjennerud, Ilan Sagiv, Carole Tucker, Gregory S. Tucker, Benjamin Westbrook, Karl Young, and Kyle Zilic. The EBEX Balloon-borne Experiment—Gondola, Attitude Control, and Control Software. , 239(1):9, November 2018.

[82] G. Efstathiou, J. R. Bond, and S. D. M. White. COBE background radiation anisotropies and large-scale structure in the Universe. *Monthly Notices of the Royal Astronomical Society*, 258(1):1P–6P, 09 1992.

[83] J. Ekin and Oxford University Press. *Experimental Techniques for Low-Temperature Measurements: Cryostat Design, Material Properties and Superconductor Critical-Current Testing*. OUP Oxford, 2006.

[84] J. Erler, K. Basu, J. Chluba, and F. Bertoldi. Planck's view on the spectrum of the Sunyaev-Zeldovich effect. *Mon. Not. Roy. Astron. Soc*, 476:3360–3381, May 2018.

[85] Thomas Essinger-Hileman, Aamir Ali, Mandana Amiri, John W. Appel, Derek Araujo, Charles L. Bennett, Fletcher Boone, Manwei Chan, Hsiao-Mei Cho, David T. Chuss, Felipe Colazo, Erik Crowe, Kevin Denis, Rolando Dünner, Joseph Eimer, Dominik Gothe, Mark Halpern, Kathleen Harrington, Gene C. Hilton, Gary F. Hinshaw, Caroline Huang, Kent Irwin, Glenn Jones, John Karakla, Alan J. Kogut, David Larson, Michele Limon, Lindsay Lowry, Tobias Marriage, Nicholas Mehrle, Amber D. Miller, Nathan Miller, Samuel H. Moseley, Giles Novak, Carl Reintsema, Karwan Rostem, Thomas Stevenson, Deborah Towner, Kongpop U-Yen, Emily Wagner, Duncan Watts, Edward J. Wollack, Zhilei Xu, and Lingzhen Zeng. Class: the cosmology large angular scale surveyor. 9153:91531I–91531I–23, 2014.

[86] Simone Ferraro, J. Colin Hill, Nick Battaglia, Jia Liu, and David N. Spergel. Kinematic sunyaev-zel'dovich effect with projected fields. ii. prospects, challenges, and comparison with simulations. *Phys. Rev. D*, 94:123526, Dec 2016.

[87] P. G. Ferreira and et al. Measuring Ω with Galaxy Streaming Velocities. In Ana M. Mourão, Mário Pimenta, and Paulo Sá, editors, *New Worlds in Astroparticle Physics II*, page 292, January 1999.

[88] P. G. Ferreira, R. Juszkiewicz, H. A. Feldman, M. Davis, and Andrew H. Jaffe. Streaming velocities as a dynamical estimator of omega. *Astrophys. J.*, 515:L1–L4, 1999.

[89] P. G. Ferreira, R. Juszkiewicz, H. A. Feldman, et al. Streaming velocities as a dynamical estimator of omega. *ApJ*, 515:L1–L4, 1999.

[90] D. Flanigan, B. R. Johnson, M. H. Abitbol, S. Bryan, R. Cantor, P. Day, G. Jones, P. Mauskopf, H. McCarrick, A. Miller, and J. Zmuidzinas. Magnetic field dependence of the internal quality factor and noise performance of lumped-element kinetic inductance detectors. *Applied Physics Letters*, 109(14):143503, October 2016.

[91] Samuel Flender, Lindsey Bleem, Hal Finkel, Salman Habib, Katrin Heitmann, and Gilbert Holder. Simulations of the Pairwise Kinematic Sunyaev-Zeldovich Signal. 2015.

[92] Masataka Fukugita and P. J. E. Peebles. The Cosmic Energy Inventory. , 616(2):643–668, December 2004.

[93] Brittany J. Fuzia et al. The Atacama Cosmology Telescope: SZ-based masses and dust emission from IR-selected cluster candidates in the SHELA survey. January 2020.

[94] N. Galitzki et al. The Simons Observatory cryogenic cameras. *Proc. SPIE*, (10708-3), 2018.

[95] Nicholas Galitzki, Peter Ade, Francesco E. Angilè, Peter Ashton, Jason Austermann, Tashalee Billings, George Che, Hsiao-Mei Cho, Kristina Davis, Mark Devlin, Simon Dicker, Bradley J. Dober, Laura M. Fissel, Yasuo Fukui, Jiansong Gao, Samuel Gordon, Christopher E. Groppi, Seth Hillbrand, Gene C. Hilton, Johannes Hubmayr, Kent D. Irwin, Jeffrey Klein, Dale Li, Zhi-Yun Li, Nathan P. Lourie, Ian Lowe, Hamdi Mani, Peter G. Martin, Philip Mauskopf, Christopher McKenney, Federico Nati, Giles Novak, Enzo Pascale, Giampaolo Pisano, Fabio P. Santos, Douglas Scott, Adrian Sinclair, Juan D. Soler, Carole Tucker, Matthew Underhill, Michael Vissers, and Paul Williams. Instrumental performance and results from testing of the BLAST-TNG receiver, submillimeter optics, and

MKID detector arrays. In Wayne S. Holland and Jonas Zmuidzinas, editors, *Millimeter, Submillimeter, and Far-Infrared Detectors and Instrumentation for Astronomy VIII*, volume 9914, pages 108 – 118. International Society for Optics and Photonics, SPIE, 2016.

[96] P. A. Gallardo et al. Studies of Systematic Uncertainties for Simons Observatory: Optical Effects and Sensitivity Considerations. *Proc. SPIE*, (10708-133), 2018.

[97] P. A. Gallardo, B. J. Koopman, N. F. Cothard, S. M. M. Bruno, G. Cortes-Medellin, G. Marchetti, K. H. Miller, B. Mockler, M. D. Niemack, G. Stacey, and E. J. Wollack. Deep reactive ion etched anti-reflection coatings for sub-millimeter silicon optics. *Applied Optics*, 56:2796, April 2017.

[98] Patricio A. Gallardo, Nicholas F. Cothard, Roberto Puddu, Rolando Dünner, Brian J. Koopman, Michael D. Niemack, Sara M. Simon, and Edward J. Wollack. Far sidelobes from baffles and telescope support structures in the Atacama Cosmology Telescope. In Jonas Zmuidzinas and Jian-Rong Gao, editors, *Millimeter, Submillimeter, and Far-Infrared Detectors and Instrumentation for Astronomy IX*, volume 10708 of *Society of Photo-Optical Instrumentation Engineers (SPIE) Conference Series*, page 107082L, July 2018.

[99] Eric Gawiser and Joseph Silk. The cosmic microwave background radiation. *Physics Reports*, 333-334:245–267, Aug 2000.

[100] E. M. George, C. L. Reichardt, K. A. Aird, B. A. Benson, L. E. Bleem, J. E. Carlstrom, C. L. Chang, H. M. Cho, T. M. Crawford, A. T. Crites, T. de Haan, M. A. Dobbs, J. Dudley, N. W. Halverson, N. L. Harrington, G. P. Holder, W. L. Holzapfel, Z. Hou, J. D. Hrubes, R. Keisler, L. Knox, A. T. Lee, E. M. Leitch, M. Lueker, D. Luong-Van, J. J. McMahon, J. Mehl, S. S. Meyer, M. Millea, L. M. Mocanu, J. J. Mohr, T. E. Montroy, S. Padin, T. Plagge, C. Pryke, J. E. Ruhl, K. K. Schaffer, L. Shaw, E. Shirokoff, H. G. Spieler, Z. Staniszewski, A. A. Stark, K. T. Story, A. van Engelen, K. Vanderlinde, J. D. Vieira, R. Williamson, and O. Zahn. A Measurement of Secondary Cosmic Microwave Background Anisotropies from the 2500 Square-degree SPT-SZ Survey. , 799(2):177, February 2015.

[101] D.G. Gilmore. *Spacecraft Thermal Control Handbook. Vol. 1: Fundamental Technologies*. The Aerospace Corporation Press, California, 2002.

[102] S. Gordon, B. Dober, A. Sinclair, S. Rowe, S. Bryan, P. Mauskopf, J. Austermann, M. Devlin, S. Dicker, J. Gao, G. C. Hilton, J. Hubmayr, G. Jones,

J. Klein, N. P. Lourie, C. McKenney, F. Nati, J. D. Soler, M. Strader, and M. Vissers. An Open Source, FPGA-Based LeKID Readout for BLAST-TNG: Pre-Flight Results. *Journal of Astronomical Instrumentation*, 5:1641003, March 2016.

[103] E. A. Grace. *Detector characterization, optimization, and operation for ACTPol*. PhD thesis, Princeton University, 2016.

[104] E. A. Grace, J. Beall, H. M. Cho, M. J. Devlin, A. Fox, G. Hilton, J. Hubmayr, K. Irwin, J. Klein, D. Li, M. Lungu, L. B. Newburgh, J. Nibarger, M. D. Niemack, J. McMahon, L. A. Page, C. Pappas, B. L. Schmitt, S. T. Staggs, J. Van Lanen, and E. Wollack. Characterization and performance of a kilo-tes sub-array for actpol. *Journal of Low Temperature Physics*, 176(5-6):705–711, 2014.

[105] Megan B. Gralla et al. A measurement of the millimetre emission and the Sunyaev-Zel'dovich effect associated with low-frequency radio sources. , 445(1):460–478, November 2014.

[106] Johnny P. Greco, J. Colin Hill, David N. Spergel, and Nicholas Battaglia. The Stacked Thermal Sunyaev–zel'dovich Signal of Locally Brightest Galaxies in Planck Full Mission Data: Evidence for Galaxy Feedback? *ApJ*, 808(2):151, 2015.

[107] Particle Data Group. Review of Particle Physics. *Progress of Theoretical and Experimental Physics*, 2020(8), 08 2020. 083C01.

[108] R. Gualtieri, J. P. Filippini, P. A. R. Ade, M. Amiri, S. J. Benton, A. S. Bergman, R. Bihary, J. J. Bock, J. R. Bond, S. A. Bryan, H. C. Chiang, C. R. Contaldi, O. Doré, A. J. Duivenvoorden, H. K. Eriksen, M. Farhang, L. M. Fissel, A. A. Fraisse, K. Freese, M. Galloway, A. E. Gambrel, N. N. Gandilo, K. Ganga, R. V. Gramillano, J. E. Gudmundsson, M. Halpern, J. Hartley, M. Hasselfield, G. Hilton, W. Holmes, V. V. Hristov, Z. Huang, K. D. Irwin, W. C. Jones, C. L. Kuo, Z. D. Kermish, S. Li, P. V. Mason, K. Megerian, L. Moncelsi, T. A. Morford, J. M. Nagy, C. B. Netterfield, M. Nolta, B. Osherson, I. L. Padilla, B. Racine, A. S. Rahlin, C. Reintsema, J. E. Ruhl, M. C. Runyan, T. M. Ruud, J. A. Shariff, J. D. Soler, X. Song, A. Trangsrud, C. Tucker, R. S. Tucker, A. D. Turner, J. F. van der List, A. C. Weber, I. K. Wehus, D. V. Wiebe, and E. Y. Young. SPIDER: CMB Polarimetry from the Edge of Space. *Journal of Low Temperature Physics*, 193(5-6):1112–1121, December 2018.

[109] James E. Gunn et al. The 2.5 m Telescope of the Sloan Digital Sky Survey. , 131(4):2332–2359, April 2006.

[110] C. Hagedorn, R. N. Mohapatra, E. Molinaro, C. C. Nishi, and S. T. Petcov. Cp violation in the lepton sector and implications for leptogenesis. *International Journal of Modern Physics A*, 33(05n06):1842006, Feb 2018.

[111] A. J. S. Hamilton, P. Kumar, E. Lu, and A. Matthews. Reconstructing the primordial spectrum of fluctuations of the universe from the observed nonlinear clustering of galaxies. , 374:L1–L4, June 1991.

[112] N. Hand et al. The Atacama Cosmology Telescope: Detection of Sunyaev-Zel'Dovich Decrement in Groups and Clusters Associated with Luminous Red Galaxies. , 736(1):39, July 2011.

[113] Nick Hand et al. Evidence of Galaxy Cluster Motions with the Kinematic Sunyaev-Zel'dovich Effect. *Phys. Rev. Lett.*, 109:041101, 2012.

[114] K. Harrington, T. Marriage, A. Ali, J. W. Appel, C. L. Bennett, F. Boone, M. Brewer, M. Chan, D. T. Chuss, F. Colazo, S. Dahal, K. Denis, R. Dünner, J. Eimer, T. Essinger-Hileman, P. Fluxa, M. Halpern, G. Hilton, G. F. Hinshaw, J. Hubmayr, J. Iuliano, J. Karakla, J. McMahon, N. T. Miller, S. H. Moseley, G. Palma, L. Parker, M. Petroff, B. Pradenas, K. Rostem, M. Sagliocca, D. Valle, D. Watts, E. Wollack, Z. Xu, and L. Zeng. The Cosmology Large Angular Scale Surveyor. 9914:99141K, July 2016.

[115] Farbod Hassani, Julian Adamek, and Martin Kunz. Clustering dark energy imprints on cosmological observables of the gravitational field. , 500(4):4514–4529, January 2021.

[116] Matthew Hasselfield et al. The Atacama Cosmology Telescope: Sunyaev-Zel'dovich selected galaxyclusters at 148 GHz from three seasons of data. *JCAP*, 1307:008, 2013.

[117] Erin Healy, Aamir M. Ali, Kam Arnold, Jason E. Austermann, James A. Beall, Sarah Marie Bruno, Steve K. Choi, Jake Connors, Nicholas F. Cothard, Bradley Dober, Shannon M. Duff, Nicholas Galitzki, Gene Hilton, Shuay-Pwu Patty Ho, Johannes Hubmayr, Bradley R. Johnson, Yaqiong Li, Michael J. Link, Tammy J. Lucas, Heather McCarrick, Michael D. Niemack, Maximiliano Silva-Feaver, Rita F. Sonka, Suzanne Staggs, Eve M. Vavagiakis, Michael R. Vissers, Yuhan Wang, Edward J. Wollack, Zhilei Xu, Benjamin Westbrook, and Kaiwen Zheng. Assembly

development for the Simons Observatory focal plane readout module. In Jonas Zmuidzinas and Jian-Rong Gao, editors, *Millimeter, Submillimeter, and Far-Infrared Detectors and Instrumentation for Astronomy X*, volume 11453, pages 224 – 235. International Society for Optics and Photonics, SPIE, 2020.

[118] S. W. Henderson, R. Allison, J. Austermann, T. Baildon, N. Battaglia, J. A. Beall, D. Becker, F. De Bernardis, J. R. Bond, E. Calabrese, S. K. Choi, K. P. Coughlin, K.T. Crowley, R. Datta, M. J. Devlin, S. M. Duff, R. Dunner, J. Dunkley, A. van Engelen, P. A. Gallardo, E. Grace, M. Hasselfield, F. Hills, G. C. Hilton, A. D. Hincks, R. Hlozek, S. P. Ho, J. Hubmayr, K. Huffenberger, J. P. Hughes, K. D. Irwin, B. J. Koopman, A. B. Kosowsky, D. Li, J. McMahon, C. Munson, F. Nati, L. Newburgh, M. D. Niemack, P. Niraula, L. A. Page, C. G. Pappas, M. Salatino, A. Schillaci, B. L. Schmitt, N. Sehgal, B. D. Sherwin, J. L. Sievers, S. M. Simon, D. N. Spergel, S. T. Staggs, J. R. Stevens, R. Thornton, J. Van Lanen, E. M. Vavagiakis, J. T. Ward, and E. J. Wollack. Advanced actpol cryogenic detector arrays and readout. *Journal of Low Temperature Physics*, 184(3-4):772–779, 2015.

[119] S. W. Henderson et al. Advanced ACTPol Cryogenic Detector Arrays and Readout. *Journal of Low Temperature Physics*, 184(3-4):772–779, August 2016.

[120] S. W. Henderson et al. Highly-multiplexed microwave SQUID readout using the SLAC microresonator radio frequency (SMuRF) electronics for future CMB and sub-millimeter surveys. *Proc. SPIE*, (10708-43), 2018.

[121] S. W. Henderson, J. R. Stevens, M. Amiri, J. Austermann, J. A. Beall, S. Chaudhuri, H.-M. Cho, S. K. Choi, N. F. Cothard, K. T. Crowley, S. M. Duff, C. P. Fitzgerald, P. A. Gallardo, M. Halpern, M. Hasselfield, G. Hilton, S.-P. P. Ho, J. Hubmayr, K. D. Irwin, B. J. Koopman, D. Li, Y. Li, J. McMahon, F. Nati, M. Niemack, C. D. Reintsema, M. Salatino, A. Schillaci, B. L. Schmitt, S. M. Simon, S. T. Staggs, E. M. Vavagiakis, and J. T. Ward. Readout of two-kilopixel transition-edge sensor arrays for Advanced ACTPol. In *Millimeter, Submillimeter, and Far-Infrared Detectors and Instrumentation for Astronomy VIII*, volume 9914 of *Proc. SPIE*, page 99141G, July 2016.

[122] Doug Henke, Doug Johnstone, Lewis B. G. Knee, Scott Chapman, Colin Ross, Michel Fich, Thomas Nikola, Steve K. Choi, Michael D. Niemack, Stephen C. Parshley, Gordon J. Stacey, and Eve Vavagiakis. Optical design study for the 860 GHz first-light camera module of CCAT-p. In *Society of Photo-Optical Instrumentation Engineers (SPIE) Conference Series*, volume

11453 of *Society of Photo-Optical Instrumentation Engineers (SPIE) Conference Series*, page 114532K, December 2020.

[123] J. W. Henning, J. T. Sayre, C. L. Reichardt, P. A. R. Ade, A. J. Anderson, J. E. Austermann, J. A. Beall, A. N. Bender, B. A. Benson, L. E. Bleem, J. E. Carlstrom, C. L. Chang, H. C. Chiang, H. M. Cho, R. Citron, C. Corbett Moran, T. M. Crawford, A. T. Crites, T. de Haan, M. A. Dobbs, W. Everett, J. Gallicchio, E. M. George, A. Gilbert, N. W. Halverson, N. Harrington, G. C. Hilton, G. P. Holder, W. L. Holzapfel, S. Hoover, Z. Hou, J. D. Hrubes, N. Huang, J. Hubmayr, K. D. Irwin, R. Keisler, L. Knox, A. T. Lee, E. M. Leitch, D. Li, A. Lowitz, A. Manzotti, J. J. McMahon, S. S. Meyer, L. Mocanu, J. Montgomery, A. Nadolski, T. Natoli, J. P. Nibarger, V. Novosad, S. Padin, C. Pryke, J. E. Ruhl, B. R. Saliwanchik, K. K. Schaffer, C. Sievers, G. Smecher, A. A. Stark, K. T. Story, C. Tucker, K. Vanderlinde, T. Veach, J. D. Vieira, G. Wang, N. Whitehorn, W. L. K. Wu, and V. Yefremenko. Measurements of the Temperature and E-mode Polarization of the CMB from 500 Square Degrees of SPTpol Data. , 852(2):97, January 2018.

[124] C. Hill et al. BoloCalc: a sensitivity calculator for the design of Simons Observatory. *Proc. SPIE*, (10708-137), 2018.

[125] J. C. Hill, S. Ferraro, N. Battaglia, J. Liu, and D. N. Spergel. Kinematic Sunyaev-Zel'dovich Effect with Projected Fields: A Novel Probe of the Baryon Distribution with Planck, WMAP, and WISE Data. *Physical Review Letters*, 117(5):051301, July 2016.

[126] J. Colin Hill, Eric J. Baxter, Adam Lidz, Johnny P. Greco, and Bhuvnesh Jain. Two-halo term in stacked thermal Sunyaev-Zel'dovich measurements: Implications for self-similarity. , 97(8):083501, April 2018.

[127] M. Hilton et al. The Atacama Cosmology Telescope: A Catalog of ¿ 4000 Sunyaev-Zel'dovich Galaxy Clusters. page arXiv:2009.11043, September 2020.

[128] M. Hilton, M. Hasselfield, C. Sifón, N. Battaglia, et al. The Atacama Cosmology Telescope: The Two-Season ACTPol Sunyaev-Zel'dovich Effect Selected Cluster Catalog. *ApJS*, January 2018.

[129] G. Hinshaw, A. J. Banday, C. L. Bennett, K. M. Gorski, A. Kogut, G. F. Smoot, and E. L. Wright. Band Power Spectra in the COBE DMR Four-Year Anisotropy Maps. , 464:L17, June 1996.

[130] S. Ho, S. DeDeo, and D.N. Spergel. Finding the Missing Baryons Using CMB as a Backlight. March 2009.

[131] Shuay-Pwu Patty Ho, Jason Austermann, James A. Beall, Steve K. Choi, Nicholas F. Cothard, Kevin T. Crowley, Rahul Datta, Mark J. Devlin, Shannon M. Duff, Patricio A. Gallardo, Matthew Hasselfield, Shawn W. Henderson, Gene Hilton, Johannes Hubmayr, Brian J. Koopman, Yaqiong Li, Jeffrey McMahon, Michael D. Niemack, Maria Salatino, Sara M. Simon, Suzanne T. Staggs, Jonathan T. Ward, Joel N. Ullom, Eve M. Vavagiakis, and Edward J. Wollack. Highly uniform 150 mm diameter multichroic polarimeter array deployed for cmb detection. *Proc. SPIE*, 9914:9914 – 9914 – 15, 2017.

[132] Shuay-Pwu Patty Ho et al. Highly uniform 150 mm diameter multichroic polarimeter array deployed for CMB detection. In Wayne S. Holland and Jonas Zmuidzinas, editors, *Millimeter, Submillimeter, and Far-Infrared Detectors and Instrumentation for Astronomy VIII*, volume 9914, pages 301 – 315. International Society for Optics and Photonics, SPIE, 2017.

[133] https://map.gsfc.nasa.gov/media/101080/index.html.

[134] https://www.cryomech.com/.

[135] Wayne Hu and Naoshi Sugiyama. Small scale integrated sachs-wolfe effect. *Phys. Rev. D*, 50:627–631, Jul 1994.

[136] K.D. Irwin and G.C. Hilton. *Transition-Edge Sensors*. Springer Berlin Heidelberg, Berlin, Heidelberg, 2005.

[137] Naoki Itoh, Satoshi Nozawa, and Yasuharu Kohyama. Relativistic Corrections to the Sunyaev-Zeldovich Effect for Clusters of Galaxies. III. Polarization Effect. , 533(2):588–593, April 2000.

[138] E. Shirokoff J. D. Wheeler, S. Hailey-Dunsheath et al. SuperSpec: the on-chip spectrometer: characterization of a full 300 channel filterbank. Number 10708-23, 2018.

[139] Roman Juszkiewicz, Volker Springel, and Ruth Durrer. Dynamics of Pairwise Motions. , 518(1):L25–L28, June 1999.

[140] Roman Juszkiewicz, Volker Springel, and Ruth Durrer. Dynamics of pairwise motions. *ApJ*, 518:L25–L28, 1999.

[141] Nick Kaiser. Clustering in real space and in redshift space. , 227:1–21, July 1987.

[142] A. Kashlinsky and F. Atrio-Barandela. Measuring cosmological bulk flows via the kinematic sunyaev-zeldovich effect in the upcoming cosmic microwave background maps. *Astrophys. J.*, 536:L67, 2000.

[143] A. Kashlinsky, F. Atrio-Barandela, H. Ebeling, A. Edge, and D. Kocevski. A new measurement of the bulk flow of X-ray luminous clusters of galaxies. *Astrophys. J.*, 712:L81–L85, 2010.

[144] Brian G. Keating, Peter A. R. Ade, James J. Bock, Eric Hivon, William L. Holzapfel, Andrew E. Lange, Hien Nguyen, and Ki Won Yoon. BICEP: a large angular scale CMB polarimeter. In Silvano Fineschi, editor, *Polarimetry in Astronomy*, volume 4843 of *Society of Photo-Optical Instrumentation Engineers (SPIE) Conference Series*, pages 284–295, February 2003.

[145] B. J. Koopman, N. F. Cothard, et al. Advanced ACTPol Low-Frequency Array: Readout and Characterization of Prototype 27 and 39 GHz Transition Edge Sensors. *Journal of Low Temperature Physics*, 193(5-6):1103–1111, December 2018.

[146] Brian J. Koopman, Jack Lashner, Lauren J. Saunders, Matthew Hasselfield, Tanay Bhandarkar, Sanah Bhimani, Steve K. Choi, Cody J. Duell, Nicholas Galitzki, Kathleen Harrington, Adam D. Hincks, Shuay-Pwu Patty Ho, Laura Newburgh, Christian L. Reichardt, Joseph Seibert, Jacob Spisak, Benjamin Westbrook, Zhilei Xu, and Ningfeng Zhu. The Simons Observatory: overview of data acquisition, control, monitoring, and computer infrastructure. In *Society of Photo-Optical Instrumentation Engineers (SPIE) Conference Series*, volume 11452 of *Society of Photo-Optical Instrumentation Engineers (SPIE) Conference Series*, page 1145208, December 2020.

[147] Arthur Kosowsky and Suman Bhattacharya. A Future Test of Gravitation Using Galaxy Cluster Velocities. *Phys. Rev.*, D80:062003, 2009.

[148] E. D. Kovetz, M. P. Viero, A. Lidz, et al. Line-Intensity Mapping: 2017 Status Report. *ArXiv e-prints*, September 2017. 1709.09066.

[149] A.V. Kravtsov, A.A. Vikhlinin, and A.V. Meshcheryakov. Stellar Mass – Halo Mass Relation and Star Formation Efficiency in High-Mass Halos. *Astron. Lett.*, 44:8–34, 2018.

[150] A. Kutyrev et al. HIRMES: the third generation instrument for SOFIA. *Proc. SPIE*, (10708-22), 2018.

[151] D. Larson, J. Dunkley, G. Hinshaw, E. Komatsu, M. R. Nolta, C. L. Bennett, B. Gold, M. Halpern, R. S. Hill, N. Jarosik, A. Kogut, M. Limon, S. S. Meyer, N. Odegard, L. Page, K. M. Smith, D. N. Spergel, G. S. Tucker, J. L. Weiland, E. Wollack, and E. L. Wright. Seven-year Wilkinson Microwave Anisotropy Probe (WMAP) Observations: Power Spectra and WMAP-derived Parameters. , 192(2):16, February 2011.

[152] H. M. Latvakoski. *High Spatial Resolution Mid and Far-Infrared Imaging of the Galactic Center*. PhD thesis, Cornell University, 1997.

[153] H. M. Latvakoski, G. J. Stacey, G. E. Gull, and T. L. Hayward. Kuiper Widefield Infrared Camera Far-Infrared Imaging of the Galactic Center: The Circumnuclear Disk Revealed. *Ap. J.*, 511:761–773, February 1999.

[154] G. Lavaux, N. Afshordi, and M. J. Hudson. First measurement of the bulk flow of nearby galaxies using the cosmic microwave background. , 430:1617–1635, April 2013.

[155] Michael Levi, Lori E. Allen, Raichoor, et al. The Dark Energy Spectroscopic Instrument (DESI). In *Bulletin of the American Astronomical Society*, volume 51, page 57, September 2019.

[156] Antony Lewis and Anthony Challinor. Weak gravitational lensing of the CMB. , 429(1):1–65, June 2006.

[157] D. Li et al. AlMn Transition Edge Sensors for Advanced ACTPol. *Journal of Low Temperature Physics*, 184:66–73, 2016.

[158] Yaqiong Li et al. Assembly and Integration Process of the High-Density Detector Array Readout Modules for the Simons Observatory. *Journal of Low Temperature Physics*, 199(3-4):985–993, March 2020.

[159] Eric V. Linder. Cosmic growth history and expansion history. , 72(4):043529, August 2005.

[160] LSST Dark Energy Science Collaboration. Large Synoptic Survey Telescope: Dark Energy Science Collaboration. *arXiv e-prints*, page arXiv:1211.0310, November 2012.

[161] Robert H. Lupton, James E. Gunn, and Alexander S. Szalay. A Modified Magnitude System that Produces Well-Behaved Magnitudes, Colors, and Errors Even for Low Signal-to-Noise Ratio Measurements. , 118(3):1406–1410, September 1999.

[162] Yin-Zhe Ma and Gong-Bo Zhao. Dark energy imprints on the kinematic Sunyaev-Zel'dovich signal. *Physics Letters B*, 735:402–411, July 2014.

[163] Mathew S. Madhavacheril, J. Colin Hill, Sigurd Næss, et al. Atacama Cosmology Telescope: Component-separated maps of CMB temperature and the thermal Sunyaev-Zel'dovich effect. , 102(2):023534, July 2020.

[164] Tobias A. Marriage et al. The Atacama Cosmology Telescope: Sunyaev-Zel'dovich-Selected Galaxy Clusters at 148 GHz in the 2008 Survey. , 737(2):61, August 2011.

[165] J. C. Mather, D. J. Fixsen, R. A. Shafer, C. Mosier, and D. T. Wilkinson. Calibrator Design for the COBE Far-Infrared Absolute Spectrophotometer (FIRAS). , 512(2):511–520, February 1999.

[166] B. A. Mazin. Microwave Kinetic Inductance Detectors: The First Decade. In B. Young, B. Cabrera, and A. Miller, editors, *American Institute of Physics Conference Series*, volume 1185 of *American Institute of Physics Conference Series*, pages 135–142, December 2009.

[167] Avery McIntosh. The Jackknife Estimation Method. *arXiv:1606.00497 [stat]*, June 2016. arXiv: 1606.00497.

[168] A. Mittal, F. de Bernardis, and M. D. Niemack. Optimizing measurements of cluster velocities and temperatures for CCAT-prime and future surveys. *ArXiv e-prints*, August 2017. 1708.06365.

[169] Irshad Mohammed, Davide Martizzi, Romain Teyssier, and Adam Amara. Baryonic effects on weak-lensing two-point statistics and its cosmological implications. *arXiv e-prints*, page arXiv:1410.6826, October 2014.

[170] Tony Mroczkowski et al. A High-resolution SZ View of the Warm-Hot Universe. , 51(3):124, May 2019.

[171] Eva-Maria Mueller, Francesco de Bernardis, Rachel Bean, and Michael D.

Niemack. Constraints on gravity and dark energy from the pairwise kinematic Sunyaev-Zeldovich effect. *ApJ*, 808(1):47, 2015.

[172] Eva-Maria Mueller, Francesco de Bernardis, Rachel Bean, and Michael D. Niemack. Constraints on massive neutrinos from the pairwise kinematic Sunyaev-Zel'dovich effect. , 92(6):063501, September 2015.

[173] Eva-Maria Mueller, Francesco de Bernardis, Rachel Bean, and Michael D. Niemack. Constraints on massive neutrinos from the pairwise kinematic sunyaev-zel'dovich effect. 92:063501, Sep 2015.

[174] S. Naess, M. Hasselfield, J. McMahon, M. D. Niemack, et al. The Atacama Cosmology Telescope: CMB polarization at 200 l 9000. 10:7, October 2014.

[175] Sigurd Naess et al. The Atacama Cosmology Telescope: arcminute-resolution maps of 18,000 square degrees of the microwave sky from ACT 2008-2018 data combined with Planck. 7 2020.

[176] Daisuke Nagai, Andrey V. Kravtsov, and Alexey Vikhlinin. Effects of Galaxy Formation on Thermodynamics of the Intracluster Medium. *ApJ*, 668:1–14, 2007.

[177] NASA/JPL-Caltech/ESA.

[178] Fabrizio Nicastro, Smita Mathur, and Martin Elvis. Missing baryons and the warm-hot intergalactic medium. *Science (New York, N.Y.)*, 319(5859):55–57, January 2008.

[179] M. D. Niemack et al. ACTPol: a polarization-sensitive receiver for the Atacama Cosmology Telescope. In *Millimeter, Submillimeter, and Far-Infrared Detectors and Instrumentation for Astronomy V*, volume 7741 of *Proc. SPIE*, page 77411S, July 2010.

[180] R. Nityananda and T. Padmanabhan. Scaling Properties of Nonlinear Gravitational Clustering. *Mon. Not. Roy. Astron. Soc.*, 271:976, December 1994.

[181] S. Nozawa, N. Itoh, Y. Suda, and Y. Ohhata. An improved formula for the relativistic corrections to the kinematical Sunyaev-Zeldovich effect for clusters of galaxies. *Nuovo Cimento B Serie*, 121(5):487–500, May 2006.

[182] T. E. Oberst. *Submillimeter spectroscopy of the Carina Nebula: Observations, operations and upgrades of the South Pole Imaging Fabry-Perot Interferometer*. PhD thesis, Cornell University, 2009.

[183] J. Orlowski-Scherer et al. Simons Observatory large aperture receiver simulation overview . *Proc. SPIE*, (10708-132), 2018.

[184] Y. Oyama, K. Kohri, and M. Hazumi. Constraints on the neutrino parameters by future cosmological 21 cm line and precise CMB polarization observations. *JCAP*, 2:008, February 2016.

[185] V Parma. Cryostat Design. *arXiv e-prints*, page arXiv:1501.07154, January 2015.

[186] S. Parshley et al. CCAT-prime: A Novel Telescope for Sub-millimeter Astronomy. *Proc. SPIE*, (10700-220), 2018.

[187] R. B. Patterson. Prospects for Measurement of the Neutrino Mass Hierarchy. *Annual Review of Nuclear and Particle Science*, 65:177–192, October 2015.

[188] John A. Peacock. *Cosmological Physics*. 1999.

[189] A. A. Penzias and R. W. Wilson. A Measurement of Excess Antenna Temperature at 4080 Mc/s. , 142:419–421, July 1965.

[190] Will J. Percival, Shaun Cole, Daniel J. Eisenstein, Robert C. Nichol, John A. Peacock, Adrian C. Pope, and Alexander S. Szalay. Measuring the Baryon Acoustic Oscillation scale using the Sloan Digital Sky Survey and 2dF Galaxy Redshift Survey. , 381(3):1053–1066, November 2007.

[191] Pavel Fileviez Perez, Clara Murgui, and Alexis D. Plascencia. Baryogenesis via leptogenesis: Spontaneous b and l violation, 2021.

[192] S. Perlmutter, G. Aldering, G. Goldhaber, R. A. Knop, P. Nugent, P. G. Castro, S. Deustua, S. Fabbro, A. Goobar, D. E. Groom, I. M. Hook, A. G. Kim, M. Y. Kim, J. C. Lee, N. J. Nunes, R. Pain, C. R. Pennypacker, R. Quimby, C. Lidman, R. S. Ellis, M. Irwin, R. G. McMahon, P. Ruiz-Lapuente, N. Walton, B. Schaefer, B. J. Boyle, A. V. Filippenko, T. Matheson, A. S. Fruchter, N. Panagia, H. J. M. Newberg, W. J. Couch, and The Supernova Cosmology Project. Measurements of Ω and Λ from 42 High-Redshift Supernovae. , 517(2):565–586, June 1999.

[193] Planck Collaboration. Planck 2015 results. XXII. A map of the thermal Sunyaev-Zeldovich effect. , 594:A22, September 2016.

[194] Planck Collaboration. Planck 2018 results. I. Overview and the cosmological legacy of Planck. , 641:A1, September 2020.

[195] Planck Collaboration, P. A. R. Ade, N. Aghanim, M. Arnaud, M. Ashdown, F. Atrio-Barandela, J. Aumont, C. Baccigalupi, A. Balbi, A. J. Banday, et al. Planck intermediate results. XI. The gas content of dark matter halos: the Sunyaev-Zeldovich-stellar mass relation for locally brightest galaxies. *AAP*, 557:A52, September 2013.

[196] Planck Collaboration, P. A. R. Ade, N. Aghanim, M. Arnaud, M. Ashdown, J. Aumont, C. Baccigalupi, A. J. Banday, R. B. Barreiro, J. G. Bartlett, and et al. Planck 2015 results. XXIV. Cosmology from Sunyaev-Zeldovich cluster counts. *Astronomy and Astrophysics*, 594:A24, September 2016.

[197] F. Pobell. *Matter and Methods at Low Temperatures*. Springer Berlin Heidelberg, 2007.

[198] A. Poglitsch, J. W. Beeman, N. Geis, et al. The MPE/UCB far-infrared imaging Fabry-Perot interferometer (FIFI). *International Journal of Infrared and Millimeter Waves*, 12:859–884, August 1991.

[199] POLARBEAR Collaboration, P. A. R. Ade, M. Aguilar, Y. Akiba, K. Arnold, C. Baccigalupi, D. Barron, D. Beck, F. Bianchini, D. Boettger, J. Borrill, S. Chapman, Y. Chinone, K. Crowley, A. Cukierman, R. Dünner, M. Dobbs, A. Ducout, T. Elleflot, J. Errard, G. Fabbian, S. M. Feeney, C. Feng, T. Fujino, N. Galitzki, A. Gilbert, N. Goeckner-Wald, J. C. Groh, G. Hall, N. Halverson, T. Hamada, M. Hasegawa, M. Hazumi, C. A. Hill, L. Howe, Y. Inoue, G. Jaehnig, A. H. Jaffe, O. Jeong, D. Kaneko, N. Katayama, B. Keating, R. Keskitalo, T. Kisner, N. Krachmalnicoff, A. Kusaka, M. Le Jeune, A. T. Lee, E. M. Leitch, D. Leon, E. Linder, L. Lowry, F. Matsuda, T. Matsumura, Y. Minami, J. Montgomery, M. Navaroli, H. Nishino, H. Paar, J. Peloton, A. T. P. Pham, D. Poletti, G. Puglisi, C. L. Reichardt, P. L. Richards, C. Ross, Y. Segawa, B. D. Sherwin, M. Silva-Feaver, P. Siritanasak, N. Stebor, R. Stompor, A. Suzuki, O. Tajima, S. Takakura, S. Takatori, D. Tanabe, G. P. Teply, T. Tomaru, C. Tucker, N. Whitehorn, and A. Zahn. A Measurement of the Cosmic Microwave Background B-mode Polarization Power Spectrum at Subdegree Scales from Two Years of polarbear Data. , 848(2):121, October 2017.

[200] C. M. Posada et al. Fabrication of large dual-polarized multichroic TES

bolometer arrays for CMB measurements with the SPT-3G camera. *Superconductor Science Technology*, 28(9):094002, September 2015.

[201] E. E. Quealy. *The POLARBEAR Cosmic Microwave Background Polarization Experiment and Anti-Reflection Coatings for Millimeter Wave Observations*. PhD thesis, University of California, Berkeley, 2012.

[202] S. J. E. Radford and J. B. Peterson. Submillimeter Atmospheric Transparency at Mauna Kea, at the South Pole, and at Chajnantor. *Pub. Astron. Soc. Pacific*, 128(7):075001, July 2016.

[203] Bilhuda Rasheed, Neta Bahcall, and Paul Bode. Searching for the missing baryons in clusters. *Proceedings of the National Academy of Sciences*, 108(9):3487–3492, 2011.

[204] M. J. Rees and D. W. Sciama. Large-scale Density Inhomogeneities in the Universe. , 217(5128):511–516, February 1968.

[205] P. Richter, B. D. Savage, T. M. Tripp, and K. R. Sembach. Hunting for the missing baryons in the warm-hot intergalactic medium. *IAU Colloq. 199: Probing Galaxies through Quasar Absorption Lines*, pages 469–471, March 2005.

[206] D. A. Riechers. Astronomy: New distance record for galaxies. *Nature*, 502:459–460, October 2013.

[207] Adam G. Riess, Alexei V. Filippenko, Peter Challis, Alejandro Clocchiatti, Alan Diercks, Peter M. Garnavich, Ron L. Gilliland, Craig J. Hogan, Saurabh Jha, Robert P. Kirshner, B. Leibundgut, M. M. Phillips, David Reiss, Brian P. Schmidt, Robert A. Schommer, R. Chris Smith, J. Spyromilio, Christopher Stubbs, Nicholas B. Suntzeff, and John Tonry. Observational Evidence from Supernovae for an Accelerating Universe and a Cosmological Constant. , 116(3):1009–1038, September 1998.

[208] Eduardo Rozo and Eli S. Rykoff. redMaPPer II: X-ray and SZ Performance Benchmarks for the SDSS Catalog. *ApJ*, 783:80, 2014.

[209] Eduardo Rozo, Eli S. Rykoff, James G. Bartlett, and Jean B. Melin. redMaPPer – III. A detailed comparison of the Planck 2013 and SDSS DR8 redMaPPer cluster catalogues. *Mon. Not. Roy. Astron. Soc.*, 450(1):592–605, 2015.

[210] E. S. Rykoff et al. redMaPPer I: Algorithm and SDSS DR8 Catalog. *ApJ*, 785:104, 2014.

[211] R. K. Sachs and A. M. Wolfe. Perturbations of a Cosmological Model and Angular Variations of the Microwave Background. , 147:73, January 1967.

[212] R. K. Sachs and A. M. Wolfe. Perturbations of a Cosmological Model and Angular Variations of the Microwave Background. , 147:73, January 1967.

[213] J. E. Sadleir, S. J. Smith, S. R. Bandler, J. A. Chervenak, and J. R. Clem. Longitudinal Proximity Effects in Superconducting Transition-Edge Sensors. *Physical Review Letters*, 104(4):047003, January 2010.

[214] Mayuri Sathyanarayana Rao, Maximiliano Silva-Feaver, et al. Simons Observatory Microwave SQUID Multiplexing Readout: Cryogenic RF Amplifier and Coaxial Chain Design. *Journal of Low Temperature Physics*, 199(3-4):807–816, March 2020.

[215] J. T. Sayre, C. L. Reichardt, J. W. Henning, P. A. R. Ade, A. J. Anderson, J. E. Austermann, J. S. Avva, J. A. Beall, A. N. Bender, B. A. Benson, F. Bianchini, L. E. Bleem, J. E. Carlstrom, C. L. Chang, P. Chaubal, H. C. Chiang, R. Citron, C. Corbett Moran, T. M. Crawford, A. T. Crites, T. de Haan, M. A. Dobbs, W. Everett, J. Gallicchio, E. M. George, A. Gilbert, N. Gupta, N. W. Halverson, N. Harrington, G. C. Hilton, G. P. Holder, W. L. Holzapfel, J. D. Hrubes, N. Huang, J. Hubmayr, K. D. Irwin, L. Knox, A. T. Lee, D. Li, A. Lowitz, J. J. McMahon, S. S. Meyer, L. M. Mocanu, J. Montgomery, A. Nadolski, T. Natoli, J. P. Nibarger, G. Noble, V. Novosad, S. Padin, S. Patil, C. Pryke, J. E. Ruhl, B. R. Saliwanchik, K. K. Schaffer, C. Sievers, G. Smecher, A. A. Stark, C. Tucker, K. Vanderlinde, T. Veach, J. D. Vieira, G. Wang, N. Whitehorn, W. L. K. Wu, V. Yefremenko, and SPTpol Collaboration. Measurements of B -mode polarization of the cosmic microwave background from 500 square degrees of SPTpol data. , 101(12):122003, June 2020.

[216] E. Schaan et al. Evidence for the kinematic Sunyaev-Zel'dovich effect with the Atacama Cosmology Telescope and velocity reconstruction from the Baryon Oscillation Spectroscopic Survey. *Phys. Rev. D*, 93, April 2016.

[217] Emmanuel Schaan et al. Evidence for the kinematic Sunyaev-Zel'dovich effect with the Atacama Cosmology Telescope and velocity reconstruction from the Baryon Oscillation Spectroscopic Survey. *Phys. Rev.*, D93(8):082002, 2016.

[218] Emmanuel Schaan et al. The Atacama Cosmology Telescope: Combined kinematic and thermal Sunyaev-Zel'dovich measurements from BOSS CMASS and LOWZ halos. 9 2020.

[219] Robert J. Scherrer. Mapping the Chevallier-Polarski-Linder parametrization onto physical dark energy Models. , 92(4):043001, August 2015.

[220] A. Schillaci, P. A. R. Ade, Z. Ahmed, M. Amiri, D. Barkats, R. Basu Thakur, C. A. Bischoff, J. J. Bock, H. Boenish, E. Bullock, V. Buza, J. Cheshire, J. Connors, J. Cornelison, M. Crumrine, A. Cukierman, M. Dierickx, L. Duband, S. Fatigoni, J. P. Filippini, G. Hall, M. Halpern, S. Harrison, S. Henderson, S. R. Hildebrandt, G. C. Hilton, H. Hui, K. D. Irwin, J. Kang, K. S. Karkare, E. Karpel, S. Kefeli, J. M. Kovac, C. L. Kuo, K. Lau, K. G. Megerian, L. Moncelsi, T. Namikawa, H. T. Nguyen, R. O'Brient, S. Palladino, N. Precup, T. Prouve, C. Pryke, B. Racine, C. D. Reintsema, S. Richter, B. L. Schmitt, R. Schwarz, C. D. Sheehy, A. Soliman, T. St. Germaine, B. Steinbach, R. V. Sudiwala, K. L. Thompson, C. Tucker, A. D. Turner, C. Umiltà, A. G. Vieregg, A. Wandui, A. C. Weber, D. V. Wiebe, J. Willmert, W. L. K. Wu, E. Yang, K. W. Yoon, E. Young, C. Yu, and C. Zhang. Design and Performance of the First BICEP Array Receiver. *Journal of Low Temperature Physics*, 199(3-4):976–984, February 2020.

[221] D. R. Schmidt, H. Cho, J. Hubmayr, P. Lowell, M. D. Niemack, G. C. O'Neil, J. N. Ullom, K. W. Yoon, K. D. Irwin, W. L. Holzapfel, M. Lueker, E. M. George, and E. Shirokoff. Al-mn transition edge sensors for cosmic microwave background polarimeters. *IEEE Transactions on Applied Superconductivity*, 21(3):196–198, 2011.

[222] Ravi K. Sheth, Antonaldo Diaferio, L. Hui, and Roman Scoccimarro. On the streaming motions of haloes and galaxies. *Mon. Not. Roy. Astron. Soc.*, 326:463–472, 2001.

[223] J. Michael Shull, Britton D. Smith, and Charles W. Danforth. The Baryon Census in a Multiphase Intergalactic Medium: 30% of the Baryons May Still be Missing. , 759(1):23, November 2012.

[224] Joseph Silk. Cosmic Black-Body Radiation and Galaxy Formation. , 151:459, February 1968.

[225] Simons Observatory Collaboration. The Simons Observatory: science goals and forecasts. , 2019(2):056, February 2019.

[226] A K Sinclair, T Browning, L R Miles, T L Jamison, R Stephenson, J Hoh,

S Bryan, P D Mauskopf, J Smith, D Bradley, and B Mazin. Development of a Reconfigurable Readout for Superconducting Arrays (Conference Poster). In *Proceedings of the 18th International Workshop on Low Temperature Detectors*. Journal of Low Temperature Physics, July 2019.

[227] Stephen A. Smee et al. The Multi-object, Fiber-fed Spectrographs for the Sloan Digital Sky Survey and the Baryon Oscillation Spectroscopic Survey. , 146(2):32, August 2013.

[228] S. J. Smith, J. S. Adams, C. N. Bailey, S. R. Bandler, S. E. Busch, J. A. Chervenak, M. E. Eckart, F. M. Finkbeiner, C. A. Kilbourne, R. L. Kelley, S.-J. Lee, J.-P. Porst, F. S. Porter, and J. E. Sadleir. Implications of weak-link behavior on the performance of Mo/Au bilayer transition-edge sensors. *Journal of Applied Physics*, 114(7):074513–074513–24, August 2013.

[229] G. F. Smoot, M. V. Gorenstein, and R. A. Muller. Detection of Anisotropy in the Cosmic Blackbody Radiation. , 39(14):898–901, October 1977.

[230] J. A. Sobrin et al. Design and characterization of the SPT-3G receiver. In Jonas Zmuidzinas and Jian-Rong Gao, editors, *Millimeter, Submillimeter, and Far-Infrared Detectors and Instrumentation for Astronomy IX*, volume 10708, pages 187 – 197. International Society for Optics and Photonics, SPIE, 2018.

[231] D. Spergel, N. Gehrels, J. Breckinridge, M. Donahue, A. Dressler, B. S. Gaudi, T. Greene, O. Guyon, C. Hirata, J. Kalirai, N. J. Kasdin, W. Moos, S. Perlmutter, M. Postman, B. Rauscher, J. Rhodes, Y. Wang, D. Weinberg, J. Centrella, W. Traub, C. Baltay, J. Colbert, D. Bennett, A. Kiessling, B. Macintosh, J. Merten, M. Mortonson, M. Penny, E. Rozo, D. Savransky, K. Stapelfeldt, Y. Zu, C. Baker, E. Cheng, D. Content, J. Dooley, M. Foote, R. Goullioud, K. Grady, C. Jackson, J. Kruk, M. Levine, M. Melton, C. Peddie, J. Ruffa, and S. Shaklan. Wide-Field InfraRed Survey Telescope-Astrophysics Focused Telescope Assets WFIRST-AFTA Final Report. *arXiv e-prints*, page arXiv:1305.5422, May 2013.

[232] D. N. Spergel, R. Bean, O. Doré, M. R. Nolta, C. L. Bennett, J. Dunkley, G. Hinshaw, N. Jarosik, E. Komatsu, L. Page, H. V. Peiris, L. Verde, M. Halpern, R. S. Hill, A. Kogut, M. Limon, S. S. Meyer, N. Odegard, G. S. Tucker, J. L. Weiland, E. Wollack, and E. L. Wright. Three-Year Wilkinson Microwave Anisotropy Probe (WMAP) Observations: Implications for Cosmology. , 170(2):377–408, June 2007.

[233] G. J. Stacey et al. CCAT-Prime: science with an ultra-widefield submil-

limeter observatory on Cerro Chajnantor. *Proc. SPIE Ground-based and Airborne Telescopes VII*, 10700:107001M, July 2018.

[234] G. J. Stacey, N. Geis, R. Genzel, et al. The 158 micron C II line - A measure of global star formation activity in galaxies. *Ap. J.*, 373:423–444, June 1991.

[235] S. M. Stanchfield, P. A. R. Ade, J. Aguirre, J. A. Brevik, H. M. Cho, R. Datta, M. J. Devlin, S. R. Dicker, B. Dober, D. Egan, P. Ford, G. Hilton, J. Hubmayr, K. D. Irwin, P. Marganian, B. S. Mason, J. A. B. Mates, J. McMahon, M. Mello, T. Mroczkowski, C. Romero, C. Tucker, L. Vale, S. White, M. Whitehead, and A. H. Young. Development of a Microwave SQUID-Multiplexed TES Array for MUSTANG-2. *Journal of Low Temperature Physics*, 184(1-2):460–465, July 2016.

[236] Z. Staniszewski et al. Galaxy Clusters Discovered with a Sunyaev-Zel'dovich Effect Survey. , 701(1):32–41, August 2009.

[237] J. R. Stevens. *Measuring the Cosmic Microwave Background Radiation from Chile*. PhD thesis, Cornell University, 2020.

[238] Jason R. Stevens, Nicholas F. Cothard, Eve M. Vavagiakis, et al. Characterization of Transition Edge Sensors for the Simons Observatory. *Journal of Low Temperature Physics*, 199(3-4):672–680, February 2020.

[239] T. Su et al. On the redshift distribution and physical properties of ACT-selected DSFGs. , 464(1):968–984, January 2017.

[240] H. Sugai et al. Updated Design of the CMB Polarization Experiment Satellite LiteBIRD. *Journal of Low Temperature Physics*, 199(3-4):1107–1117, January 2020.

[241] N. S. Sugiyama, T. Okumura, and D. N. Spergel. Will kinematic Sunyaev-Zel'dovich measurements enhance the science return from galaxy redshift surveys? , 1:057, January 2017.

[242] Naoshi Sugiyama. Introduction to temperature anisotropies of Cosmic Microwave Background radiation. *Progress of Theoretical and Experimental Physics*, 2014(6), 06 2014. 06B101.

[243] R. A. Sunyaev and Ya. B. Zeldovich. The Observations of Relic Radiation as a Test of the Nature of X-Ray Radiation from the Clusters of Galaxies. *Comments on Astrophysics and Space Physics*, 4:173, November 1972.

[244] A. Suzuki. *Multichroic Bolometric Detector Architecture for Cosmic Microwave Background Polarimetry Experiments*. PhD thesis, University of California, Berkeley, 2013.

[245] A. Suzuki, P. Ade, Y. Akiba, C. Aleman, K. Arnold, C. Baccigalupi, B. Barch, D. Barron, A. Bender, D. Boettger, J. Borrill, S. Chapman, Y. Chinone, A. Cukierman, M. Dobbs, A. Ducout, R. Dunner, T. Elleflot, J. Errard, G. Fabbian, S. Feeney, C. Feng, T. Fujino, G. Fuller, A. Gilbert, N. Goeckner-Wald, J. Groh, T. D. Haan, G. Hall, N. Halverson, T. Hamada, M. Hasegawa, K. Hattori, M. Hazumi, C. Hill, W. Holzapfel, Y. Hori, L. Howe, Y. Inoue, F. Irie, G. Jaehnig, A. Jaffe, O. Jeong, N. Katayama, J. Kaufman, K. Kazemzadeh, B. Keating, Z. Kermish, R. Keskitalo, T. Kisner, A. Kusaka, M. L. Jeune, A. Lee, D. Leon, E. Linder, L. Lowry, F. Matsuda, T. Matsumura, N. Miller, K. Mizukami, J. Montgomery, M. Navaroli, H. Nishino, J. Peloton, D. Poletti, G. Puglisi, G. Rebeiz, C. Raum, C. Reichardt, P. Richards, C. Ross, K. Rotermund, Y. Segawa, B. Sherwin, I. Shirley, P. Siritanasak, N. Stebor, R. Stompor, J. Suzuki, O. Tajima, S. Takada, S. Takakura, S. Takatori, A. Tikhomirov, T. Tomaru, B. Westbrook, N. Whitehorn, T. Yamashita, A. Zahn, and O. Zahn. The Polarbear-2 and the Simons Array Experiments. *Journal of Low Temperature Physics*, 184:805–810, August 2016.

[246] Aritoki Suzuki, Chris Bebek, Maurice Garcia-Sciveres, Stephen Holland, Akito Kusaka, Adrian T. Lee, Nicholas Palaio, Natalie Roe, and Leo Steinmetz. Commercialization of Micro-fabrication of Antenna-Coupled Transition Edge Sensor Bolometer Detectors for Studies of the Cosmic Microwave Background. *Journal of Low Temperature Physics*, 193(5-6):744–751, December 2018.

[247] Aritoki Suzuki, Nicholas Cothard, Adrian T. Lee, Michael D. Niemack, Christopher Raum, Mario Renzullo, Trevor Sasse, Jason Stevens, Patrick Truitt, Eve Vavagiakis, John Vivalda, Benjamin Westrook, and Daniel Yohannes. Commercially Fabricated Antenna-Coupled Transition Edge Sensor Bolometer Detectors for Next-Generation Cosmic Microwave Background Polarimetry Experiment. *Journal of Low Temperature Physics*, 199(3-4):1158–1166, January 2020.

[248] Hideki Tanimura, Saleem Zaroubi, and Nabila Aghanim. Direct detection of the kinetic Sunyaev-Zel'dovich effect in galaxy clusters. *Astron. Astrophys.*, 645:A112, 2021.

[249] Max Tegmark et al. Cosmological parameters from sdss and wmap. *Phys. Rev. D*, 69:103501, May 2004.

[250] Max Tegmark et al. Cosmological constraints from the SDSS luminous red galaxies. , 74(12):123507, December 2006.

[251] Herter Terry, Nicholas Battaglia, Kaustuv Basu, Benjamin Beringue, Frank Bertoldi, Scott Chapman, Steve Choi, Nicholas Cothard, Dongwoo Chung, Jens Erler, Michel Fich, Simon Foreman, Patricio Gallardo, Jiansong Gao, Urs Graf, Martha Haynes, Terry Herter, Gene Hilton, Johannes Hubmayr, Doug Johnstone, Eiichiro Komatsu, Benjamin Magnelli, Phil Mauskopf, Jeffrey McMahon, Daan Meerburg, Joel Meyers, Avirukt Mittal, Michael Niemack, Thomas Nikola, Stephen Parshley, Dominik Riechers, Gordon Stacey, Juergen Stutzki, Eve Vavagiakis, Marco Viero, and Michael Vissers. The CCAT-Prime Submillimeter Observatory. In *Bulletin of the American Astronomical Society*, volume 51, page 213, September 2019.

[252] R. J. Thornton, P. A. R. Ade, C. Allen, M. Amiri, J. W. Appel, E. S. Battistelli, B. Burger, J. A. Chervenak, M. J. Devlin, S. R. Dicker, W. B. Doriese, T. Essinger-Hileman, R. P. Fisher, J. W. Fowler, M. Halpern, P. C. Hargrave, M. Hasselfield, G. C. Hilton, A. D. Hincks, K. D. Irwin, N. Jarosik, M. Kaul, J. Klein, J. M. Lau, M. Limon, T. A. Marriage, K. L. Martocci, P. Mauskopf, S. H. Moseley, M. D. Niemack, L. Page, L. P. Parker, J. Reidel, C. D. Reintsema, S. T. Staggs, O. R. Stryzak, D. S. Swetz, E. R. Switzer, C. Tucker, E. J. Wollack, and Y. Zhao. Opto-mechanical design and performance of a compact three-frequency camera for the millimeter bolometer array camera on the atacama cosmology telescope. *Proc. SPIE*, 7020:7020 – 7020 – 10, 2008.

[253] R. J. Thornton et al. The Atacama Cosmology Telescope: The Polarization-sensitive ACTPol Instrument. *ApJs*, 227:21, December 2016.

[254] R. J. Thornton et al. The Atacama Cosmology Telescope: The Polarization-sensitive ACTPol Instrument. *ApJS*, 227(2):21, December 2016.

[255] C. E. Tucker and P. A. R. Ade. Thermal filtering for large aperture cryogenic detector arrays. In *Society of Photo-Optical Instrumentation Engineers (SPIE) Conference Series*, volume 6275 of *Proc. SPIE*, page 62750T, June 2006.

[256] J. N. Ullom and D. A. Bennett. Review of superconducting transition-edge sensors for x-ray and gamma-ray spectroscopy. *Superconductor Science Technology*, 28(8):084003, August 2015.

[257] J. N. Ullom and D. A. Bennett. Review of superconducting transition-edge

sensors for x-ray and gamma-ray spectroscopy. *Superconductor Science and Technology*, 28(8):084003, 2015.

[258] Marcel P. van Daalen, Joop Schaye, C. M. Booth, and Claudio Dalla Vecchia. The effects of galaxy formation on the matter power spectrum: a challenge for precision cosmology. , 415(4):3649–3665, August 2011.

[259] Alexander van Engelen, Blake D. Sherwin, Neelima Sehgal, Graeme E. Addison, Rupert Allison, Nick Battaglia, Francesco de Bernardis, J. Richard Bond, Erminia Calabrese, Kevin Coughlin, Devin Crichton, Rahul Datta, Mark J. Devlin, Joanna Dunkley, Rolando Dünner, Patricio Gallardo, Emily Grace, Megan Gralla, Amir Hajian, Matthew Hasselfield, Shawn Henderson, J. Colin Hill, Matt Hilton, Adam D. Hincks, Renée Hlozek, Kevin M. Huffenberger, John P. Hughes, Brian Koopman, Arthur Kosowsky, Thibaut Louis, Marius Lungu, Mathew Madhavacheril, Loïc Maurin, Jeff McMahon, Kavilan Moodley, Charles Munson, Sigurd Naess, Federico Nati, Laura Newburgh, Michael D. Niemack, Michael R. Nolta, Lyman A. Page, Christine Pappas, Bruce Partridge, Benjamin L. Schmitt, Jonathan L. Sievers, Sara Simon, David N. Spergel, Suzanne T. Staggs, Eric R. Switzer, Jonathan T. Ward, and Edward J. Wollack. The Atacama Cosmology Telescope: Lensing of CMB Temperature and Polarization Derived from Cosmic Infrared Background Cross-correlation. , 808(1):7, July 2015.

[260] E. M. Vavagiakis, Z. Ahmed, A. Ali, K. Basu, N. Battaglia, F. Bertoldi, R. Bond, R. Bustos, S. C. Chapman, D. Chung, G. Coppi, N. F. Cothard, S. Dicker, C. J. Duell, S. M. Duff, J. Erler, M. Fich, N. Galitzki, P. A. Gallardo, S. W. Henderson, T. L. Herter, G. Hilton, J. Hubmayr, K. D. Irwin, B. J. Koopman, J. McMahon, N. Murray, M. D. Niemack, T. Nikola, M. Nolta, J. Orlowski-Scherer, S. C. Parshley, D. A. Riechers, K. Rossi, D. Scott, C. Sierra, M. Silva-Feaver, S. M. Simon, G. J. Stacey, J. R. Stevens, J. N. Ullom, M. R. Vissers, S. Walker, E. J. Wollack, Z. Xu, and N. Zhu. Prime-Cam: a first-light instrument for the CCAT-prime telescope. In Jonas Zmuidzinas and Jian-Rong Gao, editors, *Millimeter, Submillimeter, and Far-Infrared Detectors and Instrumentation for Astronomy IX*, volume 10708 of *Society of Photo-Optical Instrumentation Engineers (SPIE) Conference Series*, page 107081U, July 2018.

[261] E. M. Vavagiakis, N. F. Cothard, J. R. Stevens, C. L. Chang, M. D. Niemack, G. Wang, V. G. Yefremenko, and J. Zhang. Developing AlMn Films for Argonne TES Fabrication. *Journal of Low Temperature Physics*, 199(1-2):408–415, April 2020.

[262] E. M. Vavagiakis, S. W. Henderson, K. Zheng, H. M. Cho, N. F. Cothard, B. Dober, S. M. Duff, P. A. Gallardo, G. Hilton, J. Hubmayr, K. D. Irwin, B. J. Koopman, D. Li, F. Nati, M. D. Niemack, C. D. Reintsema, S. Simon, J. R. Stevens, A. Suzuki, and B. Westbrook. Magnetic Sensitivity of AlMn TESes and Shielding Considerations for Next-Generation CMB Surveys. *Journal of Low Temperature Physics*, 193(3-4):288–297, November 2018.

[263] Eve Vavagiakis, Zeeshan Ahmed, Aamir Ali, Kamugisha Arnold, Jason Austermann, Sarah Bruno, Steve Choi, Jake Connors, Nicholas Cothard, Simon Dicker, Bradley Dober, Shannon Duff, Valentina Fanfani, Erin Healy, Shawn Henderson, Patty Ho, Duc-Thuong Hoang, Gene Hilton, Johannes Hubmayr, and Ningfeng Zhu. The simons observatory: Magnetic sensitivity measurements of microwave squid multiplexers. *IEEE Transactions on Applied Superconductivity*, PP:1–1, 03 2021.

[264] Eve M. Vavagiakis, Patricio A. Gallardo, Victoria Calafut, Stefania Amodeo, et al. The Atacama Cosmology Telescope: Probing the Baryon Content of SDSS DR15 Galaxies with the Thermal and Kinematic Sunyaev-Zel'dovich Effects. 1 2021.

[265] Limin Wang and Paul J. Steinhardt. Cluster Abundance Constraints for Cosmological Models with a Time-varying, Spatially Inhomogeneous Energy Component with Negative Pressure. , 508(2):483–490, December 1998.

[266] J. T. Ward et al. Mechanical designs and development of TES bolometer detector arrays for the Advanced ACTPol experiment. In *Millimeter, Submillimeter, and Far-Infrared Detectors and Instrumentation for Astronomy VIII*, volume 9914 of *Proc. SPIE*, page 991437, July 2016.

[267] S. Weinberg. *Cosmology*. Cosmology. OUP Oxford, 2008.

[268] Steven Weinberg. The cosmological constant problem. *Reviews of Modern Physics*, 61(1):1–23, January 1989.

[269] J. C. Wilson et al. The Apache Point Observatory Galactic Evolution Experiment (APOGEE) Spectrographs. , 131(999):055001, May 2019.

[270] Zhilei Xu, Tanay Bhandarkar, Gabriele Coppi, Anna Kofman, John L. Orlowski-Scherer, Ningfeng Zhu, Aamir M. Ali, Kam Arnold, Jason E. Austermann, Steve K. Choi, Jake Connors, Nicholas F. Cothard, Mark Devlin, Simon Dicker, Bradley Dober, Shannon M. Duff, Giulio Fabbian, Nicholas Galitzki, Saianeesh Haridas, Katheleen Harrington, Erin

Healy, Shuay-Pwu Patty Ho, Johannes Hubmayr, Jeffrey Iuliano, Jack Lashner, Yaqiong Li, Michele Limon, Brian J. Koopman, Heather McCarrick, Jenna Moore, Federico Nati, Michael D. Niemack, Christian L. Reichardt, Karen Sarmiento, Joseph Seibert, Maximiliano Silva-Feaver, Rita F. Sonka, Suzanne Staggs, Robert J. Thornton, Eve M. Vavagiakis, Michael R. Vissers, Samantha Walker, Yuhan Wang, Edward J. Wollack, and Kaiwen Zheng. The Simons Observatory: the Large Aperture Telescope Receiver (LATR) integration and validation results. In *Society of Photo-Optical Instrumentation Engineers (SPIE) Conference Series*, volume 11453 of *Society of Photo-Optical Instrumentation Engineers (SPIE) Conference Series*, page 1145315, December 2020.

[271] Ya. B. Zeldovich and R. A. Sunyaev. The Interaction of Matter and Radiation in a Hot-Model Universe. , 4(3):301–316, July 1969.

[272] N. Zhu et al. Simons Observatory large aperture telescope receiver design overview. *Proc. SPIE*, (10708-79), 2018.

[273] Ningfeng Zhu, Tanay Bhandarkar, Gabriele Coppi, Anna M. Kofman, John L. Orlowski-Scherer, Zhilei Xu, Shunsuke Adachi, Peter Ade, Simone Aiola, Jason Austermann, Andrew O. Bazarko, James A. Beall, Sanah Bhimani, J. Richard Bond, Grace E. Chesmore, Steve K. Choi, Jake Connors, Nicholas F. Cothard, Mark Devlin, Simon Dicker, Bradley Dober, Cody J. Duell, Shannon M. Duff, Rolando Dünner, Giulio Fabbian, Nicholas Galitzki, Patricio A. Gallardo, Joseph E. Golec, Saianeesh K. Haridas, Kathleen Harrington, Erin Healy, Shuay-Pwu Patty Ho, Zachary B. Huber, Johannes Hubmayr, Jeffrey Iuliano, Bradley R. Johnson, Brian Keatin, Kenji Kiuchi, Brian J. Koopman, Jack Lashner, Adrian T. Lee, Yaqiong Li, Michele Limon, Michael Link, Tammy J Lucas, Heather McCarrick, Jenna Moore, Federico Nati, Laura B. Newburgh, Michael D. Niemack, Elena Pierpaoli, Michael J. Randall, Karen Perez Sarmiento, Lauren J. Saunders, Joseph Seibert, Carlos Sierra, Rita Sonka, Jacob Spisak, Shreya Sutariya, Osamu Tajima, Grant P. Teply, Robert J. Thornton, Tran Tsan, Carole Tucker, Joel Ullom, Eve M. Vavagiakis, Michael R. Vissers, Samantha Walker, Benjamin Westbrook, Edward J. Wollack, and Mario Zannoni. The Simons Observatory Large Aperture Telescope Receiver. *arXiv e-prints*, page arXiv:2103.02747, March 2021.